Alma Mater Studiorum
Università degli Studi di Bologna

Facoltà di Scienze Matematiche, Fisiche e Naturali

Dipartimento di Astronomia

DOTTORATO DI RICERCA IN ASTRONOMIA

Ciclo XXII

ANALYSIS OF THE NUCLEAR PROPERTIES OF BRIGHTEST CLUSTER GALAXIES AND COMPARISON WITH "NORMAL" RADIO GALAXIES.

Dottoranda:

ELISABETTA LIUZZO

Coordinatore:
Chiar.mo Prof.
LAURO MOSCARDINI

Relatore:
Chiar.mo Prof.
GABRIELE GIOVANNINI

Co-relatore:
Dr. **MARCELLO GIROLETTI**

Settore Scientifico Disciplinare: Area 02 - Scienze Fisiche

FIS/05 Astronomia e Astrofisica

Esame Finale Anno 2010

QUESTA TESI E' STATA SVOLTA

NELL'AMBITO DELLE ATTIVITA' DI RICERCA

DELL' ISTITUTO DI RADIOASTRONOMIA

DELL' ISTITUTO NAZIONALE DI ASTROFISICA

(BOLOGNA)

Contents

Abstract **i**

1 General properties of BCGs **1**

1.1 Observational properties. 1

1.1.1 Morphological types. 1

1.1.2 Position in the cluster. 5

1.1.3 Radii and Surface brightness. 5

1.1.4 Size-luminosity relation. 7

1.1.5 Ellipticity. 9

1.1.6 Dynamical mass. 9

1.1.7 The Fundamental Plane. 10

1.1.8 Faber−Jackson relation. 12

1.1.9 Stellar populations. 14

1.1.10 Emission line properties. 16

1.2 Theories on the origin of BCGs. 20

1.2.1 Cooling Flow. 20

1.2.2 Galactic cannibalism. 22

1.2.3 Galaxy merging. 23

1.3 Radio loud BCGs. 28

1.3.1 The cooling flow problem. 31

2 Pc scale properties of BCGs **37**

2.1 The definition of a complete sample of BCGs. 37

2.2 The data set. 40

2.2.1 The data reduction. 40

2.3 Notes on Individual Sources. 42

2.3.1 NGC708 (B2 0149+35) in Abell 262. 42
2.3.2 NGC910 in Abell 347. 43
2.3.3 3C 75 in Abell 400 44
2.3.4 UGC2489 in Abell 407. 46
2.3.5 UGC3274 in Abell 539. 48
2.3.6 NGC2329 in Abell 569. 48
2.3.7 CGCG 261-059 in Abell 576. 51
2.3.8 NGC 2832 in Abell 779. 53
2.3.9 NGC3550 in Abell 1185. 53
2.3.10 4C 29.41 in Abell 1213. 54
2.3.11 IC 2738 in A1228. 56
2.3.12 IC 712 and IC 708 in Abell 1314. 56
2.3.13 NGC3842 and 3C 264 in Abell 1367. 60
2.3.14 NGC4874 in Abell 1656. 63
2.3.15 UGC10143 in Abell 2147. 65
2.3.16 UGC10187 in A2152. 67
2.3.17 NGC6086 in Abell 2162. 67
2.3.18 NGC6173 in A2197. 67
2.3.19 3C 338 in Abell 2199. 69
2.3.20 3C 465 in Abell 2634. 71
2.3.21 NGC7768 in Abell 2666. 73
2.4 Parsec-scale morphology. 74
2.4.1 Two-sided morphology. 74
2.4.2 One-sided morphology. 75
2.4.3 Unresolved sources. 80
2.4.4 Undetected sources. 80
2.5 Statistical considerations for the complete sample. 81
2.6 The extended sample. 84

3 Peculiar cases of BCGs **89**
3.1 4C 26.42 in Abell 1795. 89
3.1.1 Introduction. 89
3.1.2 New VLBA Observations: data reduction. 94
3.1.3 The parsec scale structure. 95

3.1.4 Modelfit results. 96
3.1.5 The parsec-scale spectrum 100
3.1.6 Jet dynamics 101
3.1.7 The physical conditions at equipartition 102
3.1.8 Discussion on the parsec and kpc scale radio morphology. . . . 104
3.2 Hydra A in Abell 780. 107
3.2.1 Introduction. 107
3.2.2 The radio structure. 107
3.3 3C 84 in Abell 426 (Perseus Cluster). 113
3.3.1 Introduction. 113
3.3.2 The radio structure. 116

4 The comparison sample: BCS **125**
4.1 The aim of the BCS study. 125
4.2 The Sample. 126
4.3 New observations and Data Reduction. 131
4.3.1 VLBA Observations at 5 GHz 131
4.3.2 VLBA Observations at 1.6 GHz 133
4.4 Notes on sources. 137
4.4.1 Sources of special interest 137
4.4.2 Notes on other observed sources. 148
4.5 Results for the BCS sample. 186
4.5.1 Source Morphology 186
4.5.2 Missing flux in parsec scale structures 190
4.5.3 Jet velocity and orientation 191

5 Conclusions **193**
5.1 BCG versus BCS sample. 193
5.2 Jet velocity for one sided structures. 195
5.3 Jet velocity for two-sided structures. 195
5.4 Mildly relativistic jets: how to produce them? 198
5.4.1 The jet propagation model of Rossi et al. 2008. 198
5.4.2 Dense surrounding medium in cool core clusters. 202
5.5 Final conclusions for BCG sample. 205

Appendix **207**

Bibliography **213**

Acknowledgments **235**

Abstract

The aim of this PhD thesis is the study of the nuclear properties of radio loud AGN. Multiple and/or recent mergers in the host galaxy and/or the presence of cool core in galaxy clusters can play a role in the formation and evolution of the radio source. Being a unique class of objects (Lin & Mohr 2004), we focus on Brightest Cluster Galaxies (BCGs). We investigate their parsec scale radio emission with VLBI (Very Long Baseline Interferometer) observations. From literature or new data , we collect and analyze VLBA (Very Long Baseline) observations at 5 GHz of a complete sample of BCGs and "normal" radio galaxies (Bologna Complete Sample , BCS). Results on nuclear properties of BCGs are coming from the comparison with the results for the BCS sample.
The Chapters of this thesis are organized as follows:

- In the Introduction, Chap. 1, we give an overview of general properties of BCGs. Morphological types, position in the cluster, radii and surface brightness, stellar population, emission line and Fundamental Plane are for example presented in details. We summarize also the principal theories (cooling flow, galactic cannibalism and galaxy merging) on the origin of these objects. Finally, we describe how BCGs are special sources in radio band and we discuss their role in the cooling flow problem.

- In Chap. 2, we define a complete sample of BCG selecting all BCGs in nearby Abell clusters (distance class <3). No constraints on cluster conditions and/or BCG radio power are imposed. We report notes for all 27 source of the sample discussing new VLBA observations for 23 of them. We present statistical results on their parsec scale morphology. Finally, we define an extended sample of BCGs. The main results from this Chapter can be also found in Liuzzo et al. 2010.

- In Chap. 3, we analyze three peculiar BCGs of our sample that lie in cool core clusters: 4C 26.42 in Abell 1795, Hydra A in Abell 780 and 3C 84 in Perseus cluster (Abell 426). In particular, for 4C 26.42 we present multiepochs new VLBA observations at 1.6, 5, 8.4 and 22 GHz. We study its parsec scale structure and spectrum, its jet dynamics and we discuss the parsec and kpc scale morphology. The main results for this source can be also found in Liuzzo et al. 2009a.

- In Chap. 4, we present the BCS sample, a comparison sample for our BCG study. This sample is unbiased with respect to the orientation of the nuclear relativistic jet being selected at low frequency. It is composed by 94 sources. In Giovannini et al. 2005 VLBI observations for an initial group of 53 sources having bright nuclear emission are discussed. Here we present new VLBA observations at 5 GHz for 26 radio galaxies with a core flux density $S_{5GHz} > 5$ mJy, 23 of them observed for the first time at mas resolution. We also present new VLBA observations at 1.6 GHz for 10 radio galaxies in order to study their extended nuclear emission. For all sources we report parsec-scale observations and discuss in detail their structures and properties. The main results from this chapter can be also found in Liuzzo et al. 2009b.

- In the Conclusions, Chap. 5, we compare results obtained from the study of BCG and BCS sample on their parsec scale radio emission. We present preliminary conclusion to explain the different nuclear properties found for BCG to respect "normal" properties. The main results of this chapter is also shown in Liuzzo et al. 2010.

- In the Appendix, we report some information on the VLBI technique and VLBA instrument from which our data set derives and we specify the definition of the core dominance and the jet sidedness used through our work.

Chapter 1

General properties of Brightest Clusters Galaxies (BCGs)

1.1 Observational properties.

1.1.1 Morphological types.

The most extensive morphological classification of Brigthest Cluster Galaxies (BCGs) is from the catalog of Struble and Rood (1984). Upon examining luminosity distributions, it is found that BCGs are generally distributed into three morphological types: gE (giant ellipticals), D and cD. A normal elliptical is represented by a smooth set of surface photometric profiles. On the low mass end of the sequence these profiles are exponential in shape (Binggeli, Sandage and Tarenghi 1984).On the high mass end these profiles become approximately $r^{1/4}$ shaped. The transition from exponential to power-law is smooth and a template profiles for ellipticals is avalaible in Schombert (1987). In a normal elliptical sequence, gE are the most luminous. They are a natural extension of the elliptical sequence, being roughly $r^{1/4}$ in appearance, and lie on the same fundamental plane of structural and kinematic properties (Djorgovski & Davis 1987) as normal ellipticals. On the other hand, the D class galaxies, similar in luminosity, size and mean surface brightness as gE's, display special properties with respect to normal ellipticals on the fundamental plane. For example, their surface brightness profiles are more extended at a characteristic radius than normal ellipticals causing a shallower profile slope. The cD class is recognized by D-like interiors plus a large, low surface brightness (μ = 26 to 27 mag arcsec^{-2}) envelope (Oemler 1976). All three types are shown in Fig. 1.1 where a surface brightness profiles for the four classes of normal elliptical, giant elliptical, D and cD galaxies are reported.

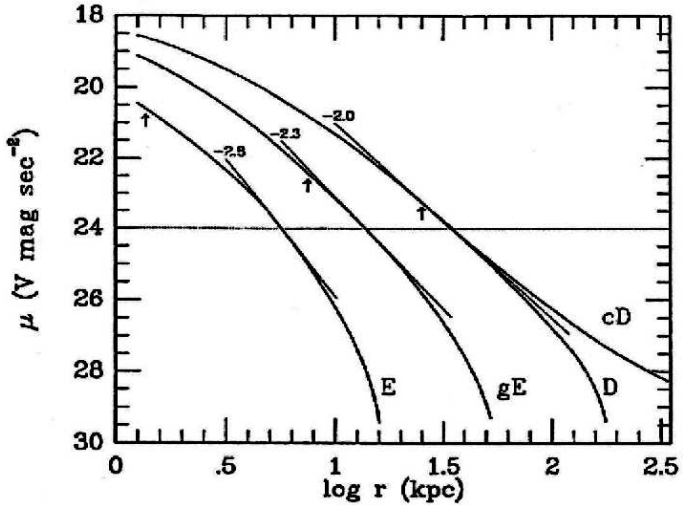

Figure 1.1: Surface brightness profiles (Tonry 1987) for the four classes of BCGs: normal elliptical, gE, D and cD. For more details and discussion on arrows, dotted line and tangent lines see Tonry 1987.

Individual examples of surface brightness profiles of all these morphological classes can be found in Schombert (1987). Most notable of these examples are some "classical" cD galaxies, such as the BCG in A2029, which, although being a very large D galaxy, does not have the extended envelopes that associates it with the cD class. Extreme cD examples are seen with the BCG in A1413 ($L_{env} = 7 \times 10^{11}$ $L_\odot$ where L_{env} is the luminosity of the envelope and $L_\odot$ the solar luminosity) (Fig.1.2) and with the BCG in the southern cluster Shapley 8 ($L_{env} = 2 \times 10^{12}$ $L_\odot$).

Homology merger theory (Hausman & Ostriker 1978) predicts that cD galaxies should have depressed central surface brightnesses; however, as noted by Oemler (1976), most D and cD galaxies have high central surface brightnesses (central refers to the inner 2 kpc, not a core value). Nonetheless, there does exist a sub-sample of cD galaxies with depressed central surface brightness (e.g., A85 and NGC 6166, Schombert 1987). These objects are rare, but it is interesting to note that most are associated with emission lines, IR emission and other evidence of recent star formation in their cores.

Several characteristics are common to BCGs evidenced through comparison of their surface brightness types. The first is that almost all BCGs are of the D or cD class. This is true for poor clusters (Thuan and Romanishin 1981) as well as rich clusters (Schombert 1987).

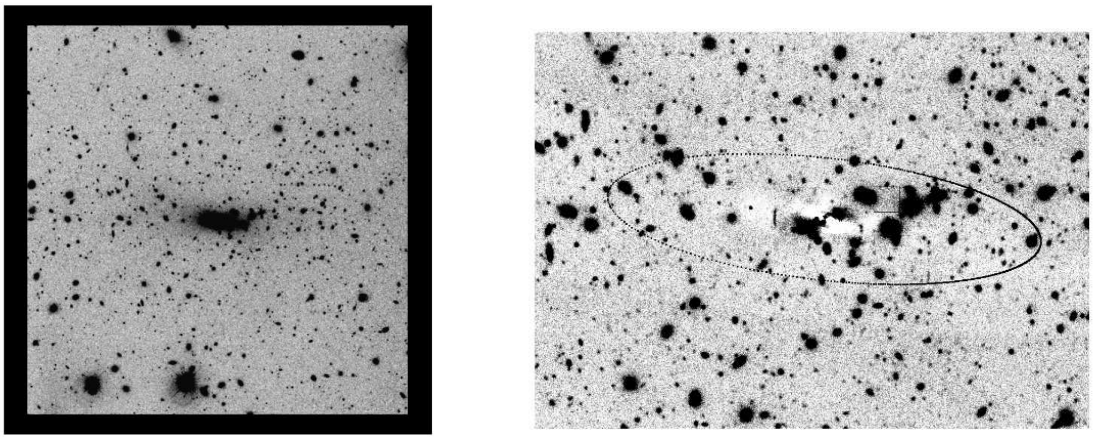

Figure 1.2: Deep optical imaging of the cD cluster Abell 1413 from Feldmeier et al. (2002). The left panel shows the full $10\,'' \times 10''$ view of the cluster, while the right panel shows a close up of the clusters once a smooth elliptical fit to the cD cluster envelope has been removed. The oval shows the radius inside which the model has been subtracted.

1.2.1.1 cD galaxies.

It is important to note that not all D or cD galaxies are BCGs; however, no D or cD type galaxies have been found in the field despite an extended search of bright, field ellipticals from redshift surveys (Schombert 1987). Moreover, they are all positioned on local cluster density enhancements (Beers and Geller 1983).

The enormous size of their extended envelopes implies that the outer regions must be strongly influenced by the cluster potential and that they reflect the dynamics of the cluster orbits rather than the kinematics of underlying galaxies (Dressler et al. 1979). Information about the cD envelope yields knowledge of the cluster potential near the center of rich cluster. In fact, a correlation (Fig.1.3) between L_{env} and the richness of the cluster N_{Abell} exixts (Schombert 1988). It is a direct measure of the depth of the cluster potential and a strong indicator that cD envelopes are directly linked to the evolution of the cluster potential. Of course the reverse situation must also considered; cD envelopes induce more rapid cluster evolution and, thus, the envelope itself may be responsible for the high X-ray luminosity and deeper potential (Schombert 1988).

A weak correlation between the luminosity of the cD envelope L_{env} and the luminosity of the underlying galaxy L_{gal} is also found (Schombert 1988). This suggests a parallel process between cD envelope formation and the growth of the parent elliptical (Fig. 1.3).

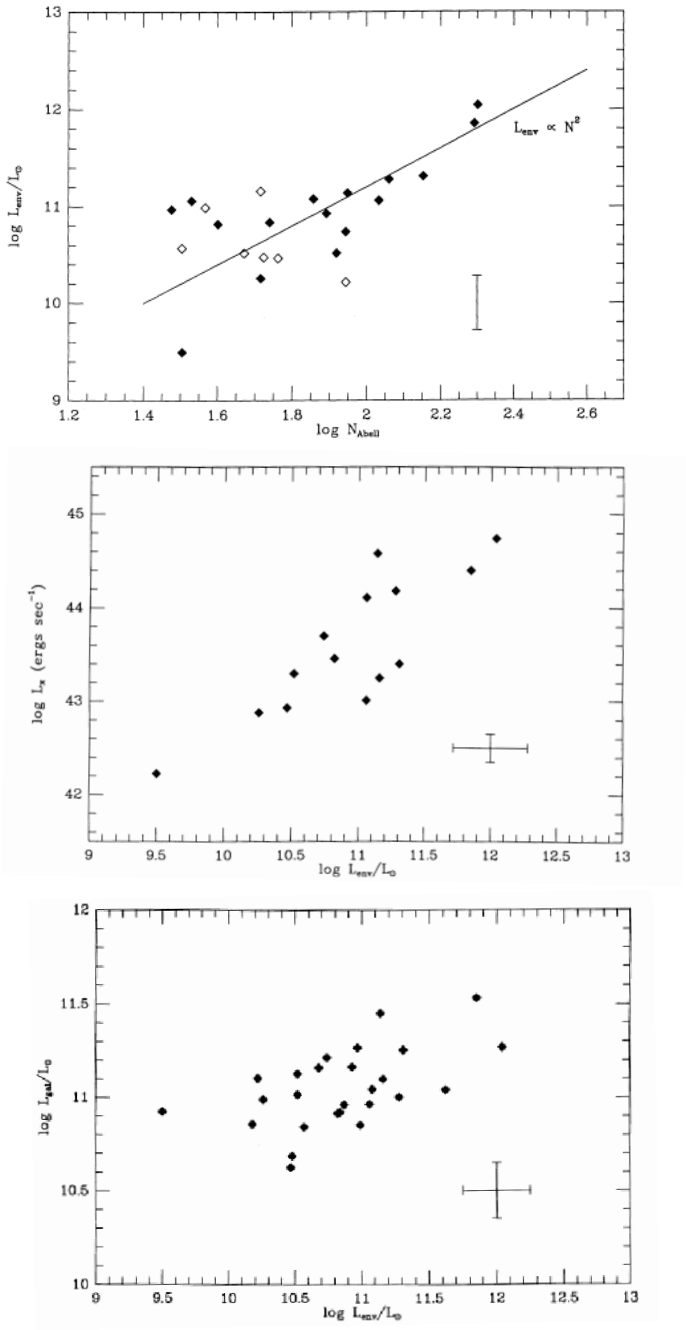

Figure 1.3: On the top: Envelope luminosity L_{env} versus cluster richness represented by galaxy counts N_{Abell}. The solid line indicates the predicted relation from models of Malumuth and Richstone 1984. Solid symbols are for regular clusters and open one for irregular clusters (Schombert 1988). In the center: Total cluster X-ray luminosity L_X versus luminosity of the envelope L_{env} (Schombert 1988). On the bottom: The luminosity of the underlying galaxy L_{gal} versus the luminosity of the cD envelope L_{env} in solar unit (Schombert 1988). Typical error bars are indicated.

1.1.2 Position in the cluster.

BCGs are located at cluster centers (Matthews, Morgan & Schmidt 1964) and they are located at the peak of the cluster X-ray emission (Rhee & Latour 1991). In Fig. 1.4 is reported the X-ray optical study of 26 Abell Clusters at redshift < 0.1 made by Rhee and Latour (1991). They found a very good agreement between the centroid of X-ray emission and the position of the BCG. This result is an important issue to analyse whether the BCG are at rest in the center on the potential well of the cluster. Oegerle and Hill (2001) concluded that, in the velocity space, BCGs typically sit near the rest frame of the clusters.

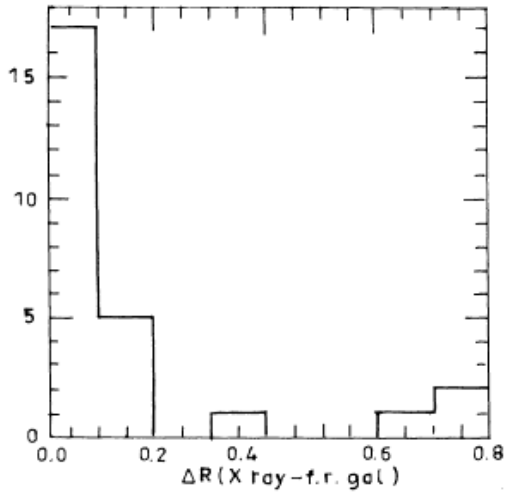

Figure 1.4: Histogram taken from Rhee & Latour (1991) of the difference (in Mpc) between the center of X-ray emission of the cluster and the position of the corresponding BCG of 26 nearby Abell Clusters (see text).

1.1.3 Radii and Surface brightness.

Being essentially gE, D and cD galaxies, the most striking characteristic of the BCGs is their enormous extent (>100 kpc, see Fig. 1.1). Their profiles also display a wide variety of shapes than do the cluster ellipticals. In general, the light distribution of the inner parts is similar to that of a normal giant elliptical. In fact, whether it is physically meanningful or not, Oemler (1976) decomposed these profiles into that of a normal elliptical plus an extended low-surface-brigthness halo. The core radii of BCGs may be compared with those of normal galaxies, like it is made in Fig.1.5, where the BCGs are plotted as crosses.

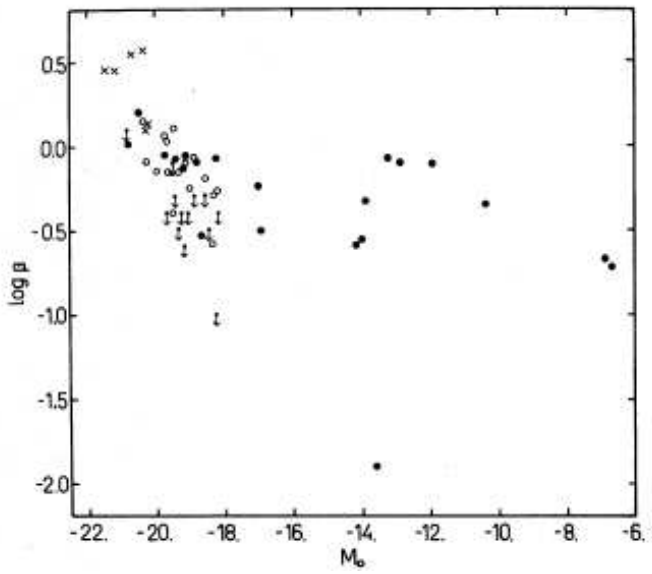

Figure 1.5: From Oemler (1976): The log of the core radii of galaxies (in kpc) versus their absolute reduced magnitudes. Crosses represent BCGs, filled and open circles indicate galaxies listed in Oemler (1976)

The first comparative study of the structure of giant ellipticals and cD galaxies was by Oemler (1976), which concentrated on the differences between BGCs and the normal ellipticals in nearby clusters.

One of the first surface photometry survey of nearby elliptical galaxies was done by King (1978), who measured the surface brighteness profiles of 25 ellipticals. Kormendy (1977) interpreted King's profiles by fitting the $r^{1/4}$ law de Vaucouleurs (1948) to the data. The $r^{1/4}$ law is expressied as

$$\text{Log I} = \text{Log I}_e \text{ - } 3.33\ [(\text{r}/\text{r}_e)^{1/4} \text{ -1}]$$

where r_e is the effective radius (defined as the radius which contains one half of the total light of the galaxy) and I_e is the surface brightness (in intensity units) at r_e. In order to better describe the envelopes of ellipticals, Oemler (1976) fitted surface brighteness profiles to an exponentially truncated Hubble law of the form

$$\text{I} = \frac{I_0 e^{(r/\alpha)^{-2}}}{(r+\beta)^2}$$

where α describes the exponential falloff and β is the Hubble law core radius. I_0 is the reduced intensity (a number which represents a core-independent and envelope -independent parameter describing the power-law section of a galaxy profile) and it is related to the Hubble law central surface brigthness, S_0, by $\text{I}_0 = \text{S}_0\beta^2$. Recent

results of Gonzalez et al. 2005 demonstrate that the Sersic profile $r^{1/n}$ provides a dramatic improvement relative to the $r^{1/4}$ profile.

A survey of BCGs in poor clusters was completed by Thuan & Romanishin (1981). They found that BCGs in poor clusters are missing the extended envelopes discovered by Oemler (1976) and they tend to be brigther amd more diffuse than giant ellipticals in rich cluster. They deduced that, because of the lack of envelopes in poor clusters, the origin of the envelopes in rich cluster is a result of stripped matter falling onto the centrally located cD galaxy. On the other hand, the merger rate of galaxies in poor clusters should be higher than the rate in rich clusters because of the lower velocity dispersions. A higher merger rate could also be one possible explanation for why poor cluster cD galaxies are more diffuse than a typical giant ellipticals.

Concerning the nature of this excess luminosity at large radii, Schombert 1987 argued that the extended light is physically distinct from the central galaxy. In this picture, the excess light component is thought to arise from a population of intracluster stars produced by the tidal stripping and disruption of cluster galaxies (Dressler et al. 1979). Simulations predict that this intracluster light (ICL) is composed of old stars that are dynamically distinct from the stars in the BCG (Murante et al. 2004) and this production of intracluster stars is an ongoing process (Willman et al. 2004). If correct, this model implies that the properties of the ICL, including its fractional contribution to the total cluster luminosity and its spatial distribution, are sensitive probes of the physical processes that drive cluster formation and the evolution of cluster galaxies.

1.1.4 Size-luminosity relation.

The size and luminosities of elliptical galaxies have been shown (Fig. 1.6) to obey the proportional scaling with an exponent $\alpha \sim 0.6$ (Bernardi et al. 2003a, 2003b, 2003c, 2003d, 2007). However, at the massive end, this relation steepens (Lauer et al. 2007).

Bernardi et al. 2007 argue this steepening is caused by an increasing fraction of BCGs, which have larger radii compared with the elliptical galaxies. Desroches et al. 2007 find the steepening is not solely attributed to contamination from a population of galaxies with intrinsically larger radii (BCGs).

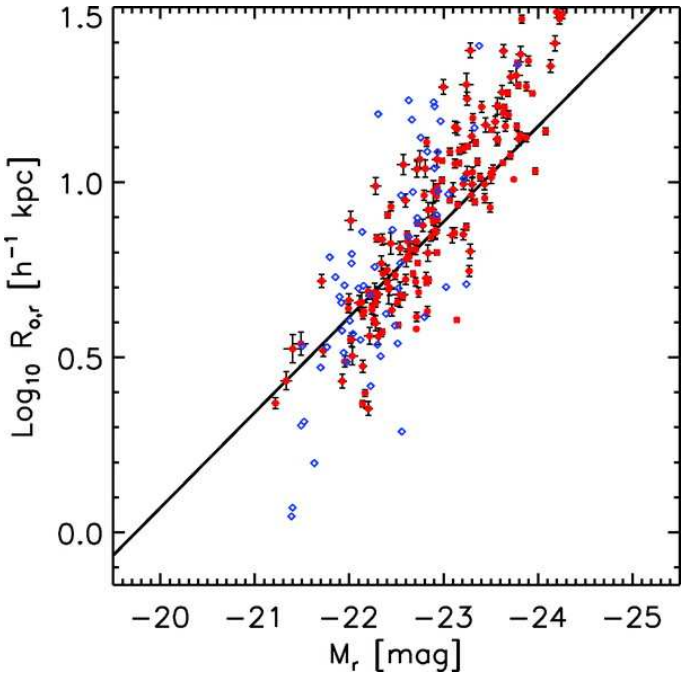

Figure 1.6: From results of Bernardi et al. 2007 : BCGs define steeper size-luminosity relation (symbols) than does the bulk of the early-type galaxy population (solid line). Open diamonds and filled circles represent BCGs with spiral and E/S0 morphologies, respectively.

Von der Linden et al. 2007 demonstrate that BCGs are larger than non BCGs at all luminosities or stellar masses. Symmetric linear fits to the individual data points yield very similar exponents for the radius−luminosity relation for the BCG sample and the comparison sample. They found α =0.65±0.02 for the BCG sample and α =0.63±0.02 for the non-BCG sample. However, they also find that the relation displays curvature, i.e. it steepens with luminosity. The range of α that they found is broadly consistent with that of Desroches et al. 2007. Thus, they do not find the significantly steeper relations claimed by Bernardi et al. 2007 and Lauer et al. 2007. The problem concerning the steepening is open. Von der Linden et al. 2007 speculate that one possible source for the discrepancy could be the different definitions of size used in the different studies. Moreover, they show that both these samples of BCGs are contaminated by non-BCGs. Such contamination from non-BCGs is likely to be most important at lower luminosities, and will thus mimic a steeper slope.

1.1.5 Ellipticity.

The majority of BCGs are round (Fig.1.7) as the non-BCGs sources (von der Linden et al. 2007) , with axis ratios typically b/a> 0.8.

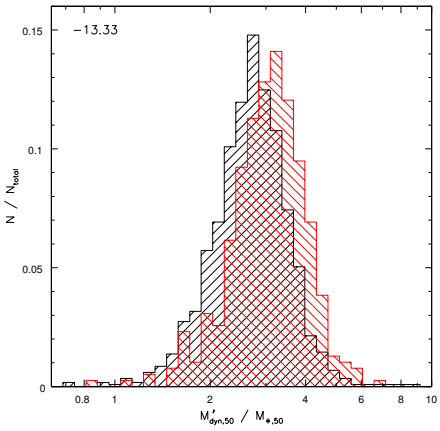

Figure 1.7: From von der Linden et al. 2007; distribution of axis ratio. Blue histogram is for BCG sample and red one represents non- BCG sample.

It should be noted, however, that Porter et al. 1991 found that the ellipticity of BCGs increases (Fig. 1.8) as a function of the radius at which it is measured.

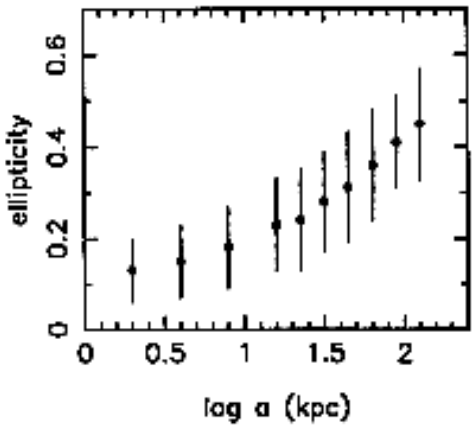

Figure 1.8: Ellipticity of BCGs as a function of the radius at wich it is measured (Porter et al. 1991).

1.1.6 Dynamical mass.

The larger radii and higher velocity dispersions of BCGs imply that they have larger dynamical-to-stellar mass ratios than non-BCGs. The dynamical mass $M_{dyn,50}$

within R_{50} (radius containing 50 per cent of the Petrosian flux) can be derived via a projection of the scalar virial theorem on to observable quantities:

$$M_{dyn,50} = c_2 \frac{\sigma_v^2 R_{50}}{G}$$

where c_2 depends on the profiles of both the dark matter and the luminous matter components. If the dark matter follows an NFW profile (Navarro, Frenk White 1997), and the luminous matter a Hernquist (1990) profile, then $c_2 = (1.65)^2$ (Padmanabhan et al. 2004). Results of von der Linden et al. 2007 find that the ratio of dynamical mass to stellar mass is indeed considerably larger for BCGs (Fig. 1.9).

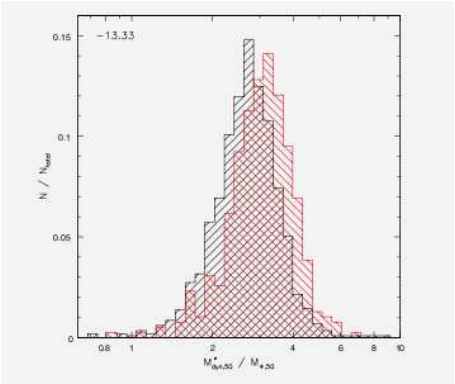

Figure 1.9: From von der Linden et al. 2007: The ratio of dynamical mass to stellar mass (within $R_{50)}$ for the BCGs (red) and the comparison sample non-BCGs (black). They have assumed that $c_2 = (1.65)^2$.

This difference is likely the consequence of the position of BCGs at, or near, the centres of galaxy clusters. As a result, there is a greater contribution from the dark matter halo to the dynamical mass of the BCG.

1.1.7 The Fundamental Plane.

Early-type galaxies seem to be well described by a two-parameter set of equations, as is evidenced by the Fundamental Plane: they lie on a plane in a coordinate system defined by the logarithmic values of velocity dispersion σ_v, effective radius and average surface brightness within the effective radius (Djorgovski & Davis 1987). The plane is typically expressed as :

$$R_e \propto \sigma_v^a I_e^{-b}$$

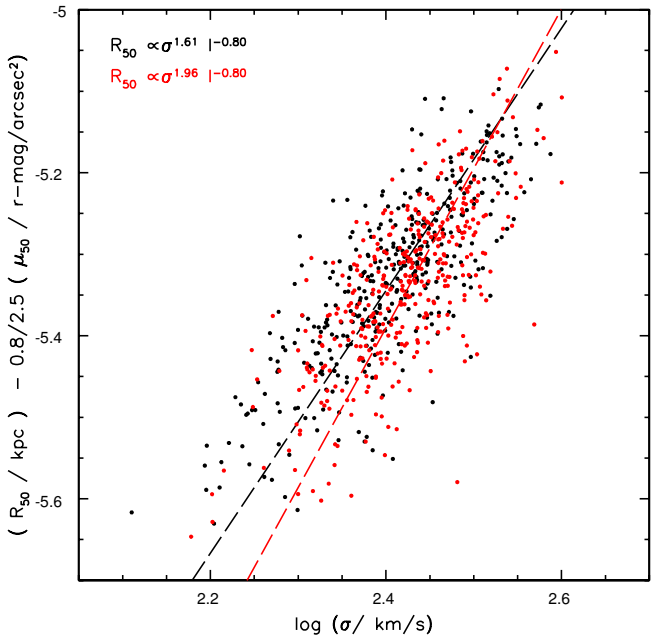

Figure 1.10: From von der Linden et al. 2007: Projection along the Fundamental Plane BCGs (red) and the non-BCGs galaxies (black). The dashed lines show the respective best fit for a, keeping b= 0.8 .

While there is agreement that b$\sim$ 0.8, the parameter a is dependent on filter bands and it may also be sensitive to a variety of selection effects and the precise definitions of σ_v, R_e and I_e. Typical values of a$\sim$1.2 - 1.6 are quoted in the literature (Bernardi et al. 2003c). Fig.1.10 represents the projection along the Fundamental Plane BCGs (red) and non-BCGs (black). The dashed lines show the respective best fit for a keeping b=0.8. For the BCGs, a is significantly larger, indicating that BCGs do not lie on the same Fundamental Plane of 'normal' ellipticals. It is interesting to note that predominantly the small, low velocity dispersion BCGs deviate from the generic Fundamental Plane.

The Fundamental Plane relation is essentially an expression of the virial theorem. The deviation of the observed Fundamental Plane from the theoretical one (a= 2 and b= 1) is referred to as the 'tilt' of the Fundamental Plane. If we define

$$M_* = c_1 L \text{ and } L = 2\,\pi I_{50} R_{50}$$

the tilt implies that $[(c_2/c_1)\ (M_*/M_{dyn,50})]$ varies for different elliptical galaxies. The proportionality constant c_1 is an expression of the stellar mass-to-light ratio and varies for different stellar populations. Moreover, c_2 depends on the profile shapes

of both the luminous and the dark matter components. If c_2 were constant, elliptical galaxies would be structurally homologous systems. There are contradictory results in the literature as to whether it is predominantly non-homology or variation in $L/M_{dyn,50}$ that is responsible for the tilt of the Fundamental Plane. Linden et al. 2007 found that $(L/(M_{dyn,50}/c_2))$ varies little. This implies that the BCG Fundamental Plane is closer to the expectations of the virial theorem (a= 2 and b= 1). Moreover, it is for low-mass galaxies that BCGs differ most from non-BCGs. The similarity between BCGs and non-BCGs at high stellar masses implies that the process(es) which cause this ratio to be approximately constant for BCGs also apply to massive non-BCGs. Possibilities include assembly history (e.g. the influence of the orbital elements during dissipationless mergers (Boylan-Kolchin et al. 2006) , and the fact that both BCGs and massive galaxies in general are found in dense environments (Kauffmann et al. 2004).

BGCs define a tight correlation between luminosity and dynamical mass $\propto R_e\sigma^2$ although this correlation is slightly steeper than it is for the bulk of the early-type population (Fig. 1.11). This, with the steeper R_e-L relation, implies that they define a shallower σ-L relation than the bulk of the population (Fig. 1.12). These scaling relations are altered even for objects that are well described by classical de Vaucouleurs profiles . These changes to the scaling relations are consistent with previous and recent work based on smaller samples of local BCGs (Malumuth & Kirshner 1981, 1985; Oegerle & Hoessel 1991; Lauer et al. 2007). The change in slope of the $\sigma-$L relation may be related to studies of curvature in the $M_{bh}-\sigma$ relation. This is because the most massive galaxies are expected to host the most massive black holes. This expectation is based on the strong and tight correlation between M_{bh} and the velocity dispersion σ of the spheroid/bulge that surrounds it: roughly $M_{bh} \propto \sigma^4$ (e.g., Ferrarese & Merritt 2000; Gebhardt et al. 2000; Tremaine et al. 2002). Note that M_{bh} also correlates with the luminosity of the bulge, although this correlation is not as tight (Magorrian et al. 1998).

1.1.8 Faber−Jackson relation.

Several studies suggest that BCGs follow a different relation between luminosity and velocity dispersion than less massive elliptical galaxies (Oegerle & Hoessel 1991; Bernardi et al. 2007; Lauer et al. 2007). Parametrizing this relation as $L\propto\sigma^{\beta}$, the

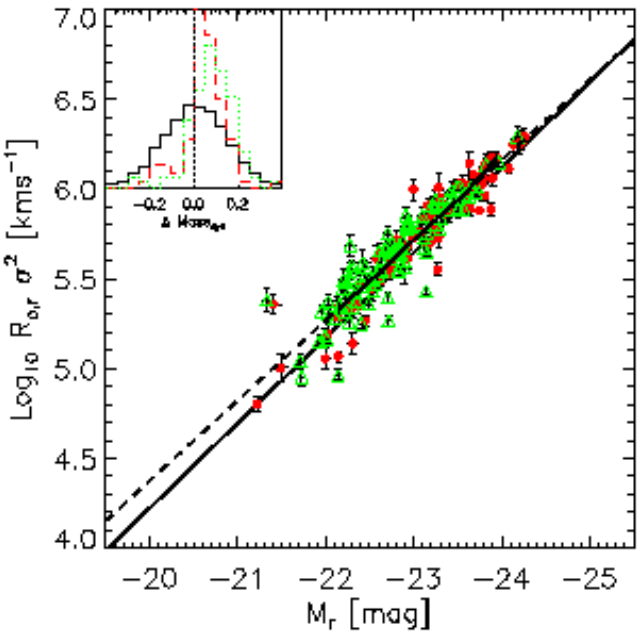

Figure 1.11: From Bernardi et al. 2007: correlation between dynamical mass $R_e\sigma^2$ and luminosity in the bulk of the early-type population (straight solid line) and in the BCG sample (dashed line). Filled circles represent objects that are well described by a de Vaucouleurs profile, and open triangles represent objects that are not. The jagged solid line shows the median value as a function of L. BCGs define a slightly shifted and even tighter correlation between dynamical mass $R_e\sigma^2$ and luminosity than does the bulk of the early-type galaxy population (inset).

canonical value is β= 4 , assuming that $[(c_2/c_1)\ (M_*/M_{dyn,50})\ (1/I_{50})]= d$ is constant and $R_{50}=(1/2\pi G)d\sigma_v^2$. Most measurements reported in the literature are consistent with $\beta\sim$ 4 (e.g. Bernardi et al. 2003b). However, for samples of BCGs (Oegerle & Hoessel 1991) and very massive galaxies (Lauer et al. 2007) , it is found that β>4 , i.e. σ increases less steeply with luminosity than predicted by the standard Faber−Jackson relation.

In Fig. 1.13, it is plotted the Faber−Jackson relation for the BCGs and non-BCGs. Linear fit works both for the BCGs and non-BCGs samples. The slope is compatible with the standard $L\propto\sigma^4$ relation for non-BCGs and σ rises less steeply with luminosity for BCGs (von der Linden et al. 2007). The bottom panel of 1.13 shows that β changes with luminosity, result confimed also by Desroches et al. 2007.

Boylan-Kolchin et al. (2006) found that in simulations of dissipationless mergers, β increases with the eccentricity of the merger orbit. They also argue that BCGs

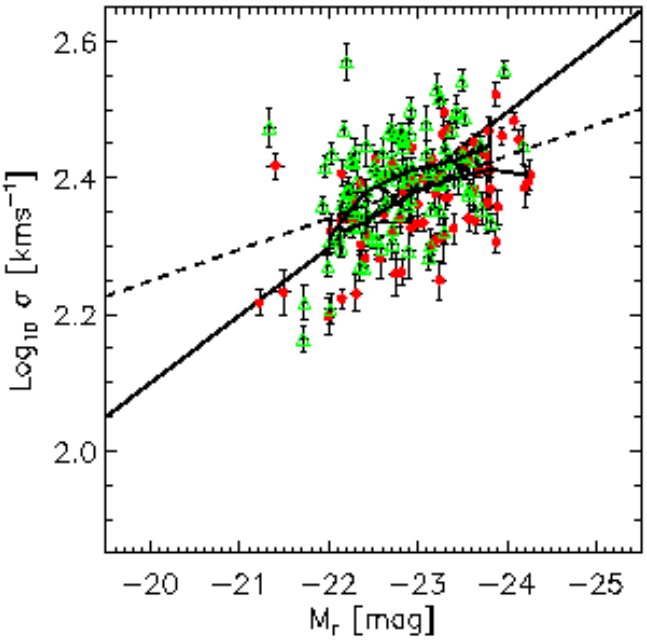

Figure 1.12: From Bernardi et al. 2007: the σ-L relation of BCG sample (filled circles represent objects that are well described by a de Vaucouleurs profile, and open triangles represent objects that are not), which appears to flatten at high luminosities. This flattening may be related to studies of curvature in the $M_{bh}-\sigma$ relation. Straight solid and dashed lines show linear fits to this relation for the early-type galaxy population and for this BCG sample, respectively. Jagged solid lines show the median value as a function of L for objects that are (lower line) and are not (upper line) well fitted by a single de Vaucouleurs profile.

are expected to form through anisotropic merging due to the filamentary structure surrounding galaxy clusters.

Von der Linden et al. 2007 calculated β in function of the cluster mass according to cluster velocity dispersion. They found that β is larger for BCGs in more massive clusters. If the scenario put forward by Boylan-Kolchin et al. (2006) is correct, this might imply that the merger orbit eccentricity increases with cluster mass. Another explanation might be that the number of (dissipationless) mergers is larger for BCGs in more massive clusters.

1.1.9 Stellar populations.

The stellar populations of the BCGs are old (von der Linden et al. 2007), as is generally found for galaxies in this mass range (Kauffmann et al. 2003).

The index [Mgb/<Fe>] is typically used as an indicator of the [α/Fe] ratio

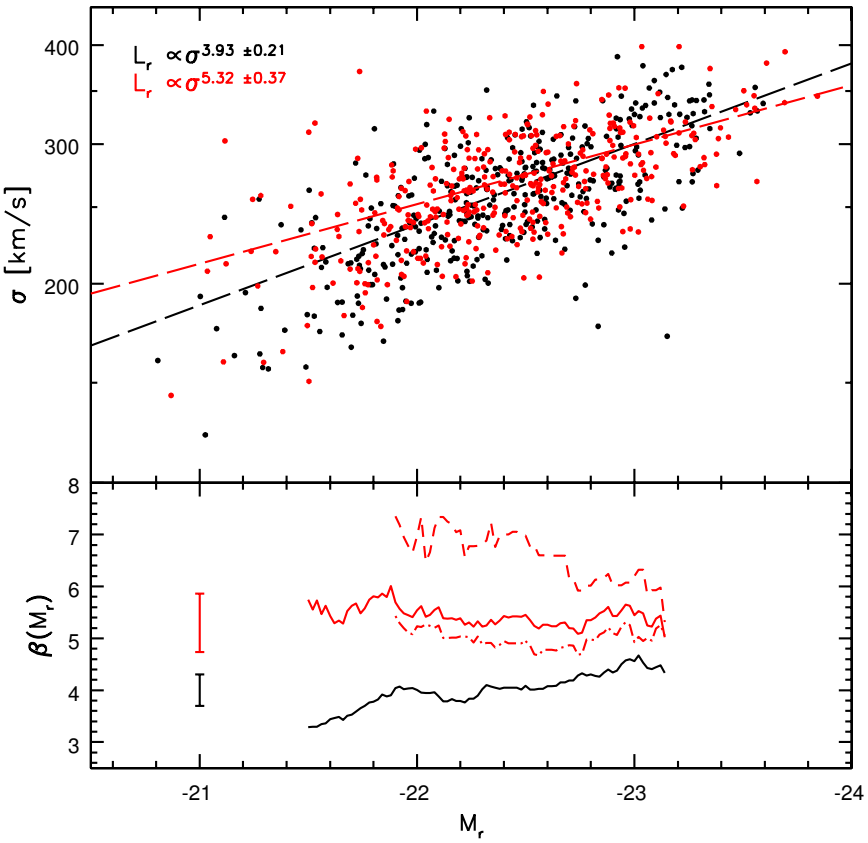

Figure 1.13: From von der Linden et al. 2007: In the top panel, there is represented the FaberJackson relation for BCGs (red) and for the comparison sample of non-BCGs. The dashed lines show the best linear fits to the relations. In the bottom panel, there is plotted the variation of β with Magnitude r M_r. The dashed line shows the subset of these BCGs located in clusters with cluster velocity dispersion $\sigma_{v,cl} > 400$ km s^{-1}, the dashdotted line the subset of BCGs in clusters with $\sigma_{v,cl} < 500$ km s^{-1} . The typical error bars are displayed on the left.

(Thomas et al. 2003). The BCGs have a systematically higher [Mgb/<Fe>] value than non-BCGs, like shown in a Fig. 1.14.

However, this index is known to correlate strongly with velocity dispersion, so this result is not independent of result that BCGs have systematically larger velocity dispersions. Considering [Mgb/<Fe>] as a function of velocity dispersion, for the BCGs this ratio is systematically higher than in non BCGs (von der Linden et al. 2007). Higher [α/Fe] ratios can be interpreted as an indication that star formation in the galaxy occurred over a shorter time-scale (Granato et al. 2004).

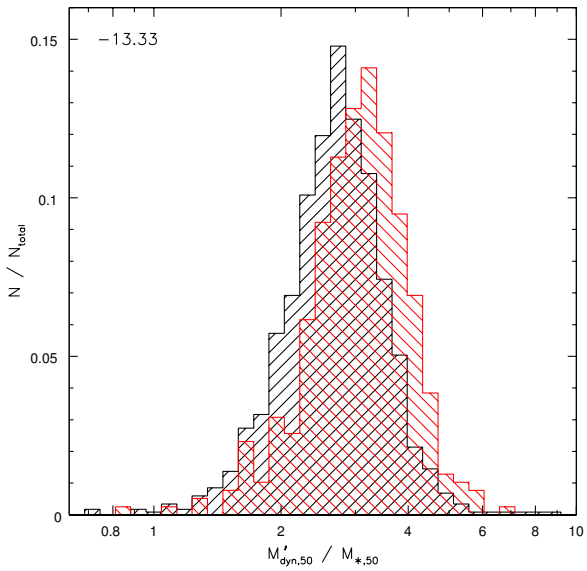

Figure 1.14: From von der Linden et al. 2007: Distributions of the alpha-to-iron index Mgb/Fe for BCG sample (red histogram) and non-BCG sample (black histogram).

1.1.10 Emission line properties.

The strengths of the four emission lines Hα, Hβ, [O III](λ5007Å) and [N II](λ6584Å) are commonly used to classify galaxies according to whether their emission-line luminosity is driven by star formation or AGN activity (Baldwin, Phillips & Terlevich 1981). The emission lines in BCGs are in general weaker than in non-BCGs and it is particularly the high-mass BCGs in which the emission-line strength is suppressed compared to the non BCGs (von der Linden et al. 2007).

Edwards et al. 2007 found that the presence in a cooling flow is higly correlated with the presence of emission lines in BCG. In fact, looking at cluster velocity dispersion (a proxy for dynamical mass) as a function of the bolometric X-ray luminosity, most of the cooling flow clusters have larger X-ray luminosities for their mass, and these clusters are these that have a BCG with line emission. However, in non -cool core clusters, the fraction of emission-line BCGs is low. Hence, this trend is quite different from what is seen in non-BCGs, where almost all of the emission-line galaxies are fainter than $M_k = -25$.

Emission line properties in BCGs in cool core clusters.

Central galaxies of cooling flow clusters have long been known to show luminous line emission, spatially extended in filaments spread over the central 5−60 kpc of the cluster core (e.g. Hu et al. 1985; Johnstone et al. 1987 ; Heckman et al. 1989). The presence of such line emission is dependent on the cluster properties: large line luminosity extended emission-line regions are found in clusters with high cooling flow rates (Johnstone et al. 1987, Allen 1998), and so far such systems have not been found around BCGs in non-cooling flow clusters. Line emission is not, however, ubiquitous in BCGs contained in strong cooling flows (e.g., A2029, A2063 (Crawford et al. 1999) . The emission-line systems tend to be associated with those BCGs which contain a central radio source (Heckman et al. 1989; Crawford 1995) , though again not exclusively (e.g., A1060).

Moreover, only the cooling flow nebulae with a high line luminosity [L(Hα)> 10^{41}ergs^{-1}] are accompanied by an excess ultraviolet/blue continuum (Jonstone, Fabian & Nulsen 1987). Both the line emission and the blue light are extended on scales of 5−60 kpc, and are seen to be spatially coincident from the flattening of the radial gradient of the Mg_2 spectral index within the emission-line regions (Cardiel et al. 1998). The morphology of the blue light also seems (in the few cases imaged) spatially related to that of the contained radio source (McNamara & O'Connell 1993; McNamara 1995; Sarazin et al. 1995b; McNamara et al. 1996a; McNamara 1997). The ultraviolet continuum has been successfully ascribed to massive young star formation, from both the spectra (once intrinsic reddening has been corrected; (Allen 1995)) and from high-resolution images (McNamara et al. 1996, Pinkney et al. 1996). The line ratios observed in these systems have strong Balmer lines relative to forbidden lines such as [O III], [N II] and [S II] (Crawford et al. 1999). A good relation is found between the observed Hα luminosity (again corrected for intrinsic reddening) and that derived from photoionization by the O stars which is predicted to be present from the stellar fit to the dereddened continuum (Allen 1995). Detailed modelling of the BCG spectra (Johnstone & Allen 2002) indicates that the ionizing fluxes required to produce the emission-line ratios and luminosities observed in these systems can be fully accounted for by the observed O-star populations (assuming very hot stars, with T> 40 000 K, and a low mean ionization parameter, U$\sim$4) in a high-metallicity environment (about solar; see also Filippenko & Terlevich 1992

and Allen 1995). Together with the spatial correspondence of the blue light and line emission (Cardiel et al. 1998) , it seems that the most line-luminous cooling flow nebulae are powered by a population of massive hot stars.

Large masses of X-ray-absorbing material are detected in the spectra of cooling flow clusters (White et al. 1991; Allen & Fabian 1997) , indicating that cold clouds can be an end-product of the cooling process. Such clouds might coagulate and condense to form a central reservoir of cold gas. As suggested by the double-lobed blue light morphology of A1795 and A2597, and as hypothesized by several authors (McNamara & O'Connell 1993; Pinkney et al. 1996; McNamara 1997) , the interaction between the outflowing radio plasma and this gas reservoir could induce a massive starburst. The distribution of stellar types inferred is weighted to lower mass stars (Allen 1995) , suggesting that such a starburst is triggered at irregular time-scales. Those galaxies requiring an excess population of just O stars (e.g., those in A291, Z3146, Z8276) may only have one very recent such starburst, whilst others may have aged such that few O stars remain. This scenario predicts that the very luminous systems are created by the combination of a central radio source and a surrounding mass of cold clouds accumulated from the cooling flow both a common consequence of a rich (but non-binary) cluster environment. Thus it is possible a central radio source will not induce star formation and luminous line emission unless the cooling flow has accumulated a reservoir of cold gas. Hence any BCG in a cooling flow cluster that contains a strong radio source, yet no optical anomalies, should also lack evidence for intrinsic absorption in the cluster X-ray spectrum.

The variation in the properties of the cooling flow nebulae form a continuous trend with line luminosity implying a gradual change in the dominance of ionization mechanism (Crawford et al. 1999). The cooling flow galaxies with a lower luminosity emission-line region have stronger forbidden line emission to Balmer line emission ratios (([N II]/Hα)$\sim$2.4 and ([S II]/Hα)$\sim$1, but [O III]/Hβ showing a large spread). Such line intensity ratios are traditionally difficult to explain, and require a steeper ionizing spectrum over 13.6$-$100 eV than can be produced by the O stars present in the higher luminosity systems.

Edwards et al. 2007 investigated also the dependence of line emission with the location of BCG in the cluster with the distance to the X-ray centre. Some BCGs

are found close to the X-ray centre, while others can be found several hundred kpc away. In particular, all of the strongly emitting BCGs are within 50 kpc of the X-ray centre. Moreover, these emitting galaxies are also usually found in a cooling flow cluster. They concluded that only those BCGs that are close to the X-ray centre have significant line emission.

Edwards et al. 2007 tried also to correlate line emission of the BCG with the cluster mass, but no trend is found. However, they observed a clear correlation with the emission-line fraction decreasing with increasing number density, and so BCGs are less likely to show emission lines if they are found in the densest regions of clusters. The fact that it is observed an enhanced emission for those galaxies within the smaller 50-kpc scale of the X-ray centre of cooling flow clusters is therefore likely related directly to the presence of cooling, X-ray gas on small scales, rather than the overall gravitational potential.

1.2 Theories on the origin of BCGs.

BCGs appear to be quite homogenous being big, bright and with remarkably small dispersions in absolute aperture magnitudes compared to the other early-type cluster galaxies (∼0.3 mag, Collins & Mann 1998, Aragon-Salamanca et al. 1998). Therefore, they may be used as standard candles out to large distances. Their attractiveness as standard candles increases if their nature is understood. Photometric galaxy surveys semm to be necessary to identify large numbers of clusters to bigger redshift. This means that large BCG samples will also become available. If their nature is understood, then the BCGs themselves may provide complementary information about cosmological parameters. For example, the Fundamental Plane relation of BCGs can be used to determine the change in surface brigtheness due to stellar evolution with an accuracy of 25% (assuming no dynamical evolution) (Oergerle et al. 1991). However, the slope of Fundamental Plane for BCGs is steeper (see section 1.1.7) than for normal elliptical galaxies. This is one sign of unusual formation histories of BCGs since they are in the most of cases early-types.

In the ollowing, three major theories on the origin of BCGs are presented.

1.2.1 Cooling Flow.

One model proposed for the origin of BCGs is the star formation from cooling flows expected at the centers of clusters (Fabian et al. 1994). The most massive galaxies observed at z>0.5 have many properties that can be interpreted as due to a surrounding cooling hot medium. Cooling flows therefore must play some part in the formation of the most massive galaxies, i.e. the central cluster galaxies. Indeed, any theory of galaxy formation in which gas falls into potential wells, is heated to the virial temperature, and then cools with the possibility $t_{cool} \gtrsim t_{grav}$ (Rees & Ostriker 1977, Silk 1977, White & Frenk 1991) , where t_{cool} is the radiative cooling time due to the observed X-rays and t_{grav} is the gravitational free-fall time, requires cooling flows. In most hierarchical models for structure formation, mass overdensities begin with $t_{cool} < t_{grav}$ and form " normal" stars of which the most massive become supernovae. The energy feedback from these leaves most of the gas uncooled. The supernova ejecta also enriches the gas in metals. It is then incorporated into the next stage of the hierarchy. Many small perturbations do not proceed beyond this condition and

appear as " normal" galaxies and loose groups. In larger preturbations, however, the total mass increases such that the object passes the cooling flow condition. Massive cooling flow are expected in young clusters and massive groups before they merge to form richer clusters. The exact mass level at which this occurs depends on the role and fraction of any nonbaryonic dark matter.

What happens at this stage can be deduced from studies of nearby cooling flows. The gas is multiphase at all radii and it lays down cooled gas according to M(<) $\propto$ r, ($\rho \propto r^{-2}$). Much of the cooled gas is in the form of very cold clouds which may efficiently form low-mass stars. Star formation may therefore switch from the "normal" IMF (Initial Mass Function) which occured during the early phases of the hierachy (giving to the observed galaxy) to an almost exclusively low-mass mode (Thomas & Fabian 1990). A massive isothermal dark halo is thereby assembled (Thomas 1988). While a cooling flow persists, the IMF of any star formation can only be "normal" for a small fracion of the cooled gas, or massive galaxies would appear even more luminous. The dark mass of the central galaxy is continuing to increase from the cooling flow.

Some process is required in order to account for the upper luminosity of the largest galaxies. These are inferred to occur at the boundary where t_{cool}=t_{grav} and some physical process is required to prevent more lumionous galaxies from forming.

The role of cooling flows in galaxy formation has also been studied by Ahsmann & Carr 1988, 1991. They investigated the total mass fraction that can be processed through cluster cooling flows and they again argued that is smallunless significant heating occurs due to supernovae at the early stages of the hierarchy.

If giant galaxies are the result of a cooling-flow, observationally one would expect a soft X-ray background from the radiation of the cooling gas, although absorption in cooled gas may reduce the observed flux by large factors. Line absorption of background quasars by the dense cold clouds in the flow may explain some of the many absorption lines commonly seen in the spectra of distant quasars. The hypothesis predicts that massive protogalaxies will be turbolent, extended mass of rapidly cooling hot gas with a massive embedded population of dense cold clouds. The smallest clouds, or clouds fragments, may mix into the hot gas and produce absorption lines of high ionization, whereas the large cloud may be predominantly neutral and create damped Lyα lines. Lines from individual clouds may be narrow

but the spread from all clouds may be up to 1000 km s $^{-1}$.

If the formation galaxies is due to cooling flow, it is worth taking a careful look at nearby cooling flows to learn how they operate. However, the nearby examples show that much of the action is not directly detectable at visible wavelengths (McNamara & O'connell 1989).

1.2.2 Galactic cannibalism.

Since the realization that close collisions and mergers between galaxies might be common phenomena (Toomre & Toomre 1972) , cD and D galaxies but in general BCGs were widely interpreted as merger products through dynamical friction and tidal stripping. In this theory, the orbits of cluster galaxies are assumed to decay slowly as the orbits of cluster galaxies move through the distributed dark matter that binds the cluster, until their orbital energies are sufficiently low that they can be captured by, and merge with, the "cannibal" at the center. In other words, the most massive objects in any self-gravitating system will gradually spiral towards the bottom of the cluster potential well and lose energy continuously more than less massive bodies. This effect may be viewed as resulting from the attempt of massive cluster members to reach equipartition of energy with the other objects in the part of the cluster they traverse. Under certain conditions the cumulative effect of encounters may be modelled by a frictional force resisting the motion of heavy particles (Chandrasekhar 1943). Such an approach to the problem of two-body relaxation in clusters has the advantage that the orbital evolution of a massive body can be computed relatively easily. In this scenario, bright galaxies spiral to the center of clusters on an equipartion time scale; there are swallowed by a central giant one which becomes BCG.

The galactic cannibalism picture fails when worked out in detail (Merrit et al. 1985, Lauer et al. 1985, Tremaine et al. 1990). In fact, it appears in retrospect that some of the assumption of the early cannibalism models were poorly chosen, and led to rather strong overestimates of the efficiency of this process. The very large growth rates predicted by Hausmann & Ostriker 1978 were based on the assumption that galaxies in clusters are surrounded by massive dark halos. The tidal field resulting from the distributed matter in a cluster is probably sufficiently strong to truncate galaxies almost to their luminous radii (White 1983, Merritt 1984) and N-body

simulations of the clustering process suggest that this truncation is nearly complete by the time a cluster has reached virial equilibrium. Moreover, the dynamical friction timescales are generally too long and so the expected amount of accreted luminosity falls short by an order of magnitude for making BCG's luminosity. At least, the lack of luminosity segregation (i.e. the expected systematic concentration of bright galaxies to the center) is an other argument for which this theory fails. Although it might be argued that cD galaxies themselves are the result of this segregation, it is nevertheless true that the majority of rich clusters contain neither a dominant central galaxy nor any strong evidence of luminosity segregation.

1.2.3 Galaxy merging.

This theory explains the formation of BCGs in a cosmological scenario. In particular, in the hierachical cosmological model, BCGs form through galaxy merging in the early history of the formation of the cluster (Merritt et al. 1985). The strong tendency for BCGs to align with their cluster population (West et al. 1994) seems to be a proof of an origin coinciding with cluster collapse. This model is an attractive one because it predicts for example that the properties of a cD galaxy should be correlated only with its initial (poor cluster) environment, and not necessarily with the properties of the rich cluster that forms later. It also explains why many dense clusters do not contain a dominant central galaxy, even though the time scales for orbital evolution in these clusters are apparently shorter than in other clusters containig cD galaxies. The fact that very bright galaxies sometimes appear in relatively poor environments has been emphasized by White et al. 1978.

According to Dubinski 1998 , most of the work on the formation of giant ellipticals has been based on studies of merging groups of several disk galaxies (Weil & Henquist 1996) or small virialized clusters of spherical galaxies (Bode et al. 1994, Athanassoula et al. 1997). These simulations reveal the high efficiency of dynamical friction in driving merging and the general tendency to produce remnants resembling elliptical galaxies. However, they are phenomenological studies that are still considerably detached from the context of hierarchical collapse in which elliptical galaxies and BCGs probably form.

In this framework, the formation histories of BCGs and ordinary elliptical galaxies are closely linked. Numerical simulations have long predicted that early-

type galaxies, with spheroid-dominated stellar light profiles, are a natural outcome of major galaxy mergers (e.g.,Toomre & Toomre 1972; Barnes & Hernquist 1996; Naab & Burkert 2003). However, both the timing and nature of the violent assembly of early-type galaxies remain frustratingly unclear. Look-back studies have recently become large enough to demonstrate a steady growth in the total stellar mass in the red-sequence galaxy population since $z \sim 1$ (e.g. Bell et al. 2004b; Faber et al. 2006). The majority of these red-sequence galaxies are morphologically early type out to at least $z \sim 0.7$ (Bell et al. 2004a). Indeed, recent works have confirmed a growth in the total stellar mass in morphologically early-type galaxies from $z \sim 1$ to the present day (Cross et al. 2004; Conselice et al. 2005). Interestingly, relatively few blue galaxies bright enough to be the star-forming progenitor of a massive non-star-forming early-type galaxy are observed (Bell et al. 2004b; Faber et al. 2006). Thus, it has been suggested that mergers between non-star-forming early-type galaxies may occur (so-called "dry mergers") and build up the massive early-type galaxy population (Bell et al. 2004b; Faber et al. 2006). Such mergers are observed at least in clustered environments (van Dokkum et al. 1999; Tran et al. 2005). Anyway, it is still unclear how important dry mergers are in driving the evolution of luminous, massive early-type galaxies, averaged over all cosmic environments. In fact, understanding why massive early-type galaxies are red and dead has proved to be difficult. The problem is to arrange for star formation to occur at a higher redshift than the actual assembly of the stars into a single massive galaxy. The most recent galaxy formation models arrange for this to happen by a combination of the dry mergers and active galactic nucleus (AGN) feedback (Hopkins et al. 2006; Croton et al. 2006; De Lucia et al. 2006; Bower et al. 2006). The dry merger hypothesis, as explained above, assumes that the assembly of massive galaxies occurs by merging smaller progenitor systems of old stars without additional star formation (which would otherwise lead to bluer colors). This happens either because the merging units were themselves gas poor, or because AGN feedback has prevented the hot gas reservoirs of the progenitors from cooling and forming stars after the merger. Together, these processes allow massive galaxies to be built from smaller systems while still remaining red.

In particular, combining the results that the dominant factor which determined whether or not a galaxy is radio-loud is its mass and that the distribution of

radio luminosities was found to be the same regardless of the galaxy mass (Best et al. 2005) with a conversion between radio luminosity and the mechanical energy supplied by a jet to its surroundings (as estimated by Birzan et al. 2004), Best et al. (2006) estimated the time-averaged mechanical luminosity output associated with radio source activity for each galaxy, as a function of its mass. They found that, for elliptical galaxies of all masses, the time-averaged radio heating almost exactly balanced the radiative cooling losses from the hot haloes of the ellipticals. They argued that the radio-AGN feedback may therefore play a critical role in galaxy formation, preventing further cooling of gas on to elliptical galaxies and thus explaining why these galaxies are old and red (see also Benson et al. 2003; Scannapieco, Bower et al. 2006; Cattaneo et al. 2006; Croton et al. 2006).

The dry merger hypothesis is most necessary for the most massive galaxies that tend to be the BCGs in clusters and it is important considering the sizes of these BCGs and the other scaling relations. This is because, in a gas -rich ("wet ") merger, gas from the merging components is able to dissipate energy, cool, contract, and eventually make new stars (Barnes & Hernquist 1992, 1996; Mihos & Hernquist 1996). Dry mergers, on the other hand, have no energy-loss mechanism (other than dynamical friction); having suffered less dissipation, their stellar components are not as centrally contracted, so the optical sizes of dry merger products are expected to be larger than if the mergers were wet (e.g., Kormendy 1989; Capelato et al. 1995; Nipoti et al. 2003), although the sizes may also reflect the orbital parameters of the mergers that formed the BCG (e.g., Boylan-Kolchin et al. 2006).

Other confirmations to this model come looking at the Fundamental Plane relation for BCGs. The R_e-L relation of the bulk of the early-type galaxy population is steeper than the correlation between the half-mass radius and the mass of dark matter halos. This is consistent with models in which galaxies in low-mass halos have suffered more dissipation (e.g., Kormendy 1989; Dekel & Cox 2006). If massive galaxies have suffered less dissipation than less massive galaxies, then BCGs have suffered even less dissipation than other massive galaxies of similar luminosities (Bernardi et al. 2007). Although some of the steepening of the R_e-L relation may be due to anisotropic mergers (e.g., Boylan-Kolchin et al. 2006), the larger than expected sizes of BCGs also suggest less dissipation, so they are consistent with the dry merger formation hypothesis. In addition, BCGs show a substantially

smaller scatter around the Fundamental Plane defined by the bulk of the early-type population than does the early-type population itself (see section 1.1.7).

This might indicate that the formation histories of BCGs involve less recent star formation than occurs in early-type galaxies of similar mass. Below average recent star formation rates would be consistent with dry merger formation histories. BCGs define the same g - r color-magnitude relation as the bulk of the early-type population (Bernardi et al. 2007).

Hence, if BCGs form from dry mergers, then BCG progenitors must lie redward of this relation (else the product of the merger would lie blueward of this relation). This suggests that BCG progenitors host older stellar populations than is typical for their luminosities and this may provide an interesting constraint on dry merger models (Bernardi et al. 2007).

Evidence of multiple nuclei BCGs.

Laine et al. (2003) used HST to study a sample of 81 giant elliptical galaxies in order to describe their nuclear morphologies. They found that about half of all BCGs have companions, or a secondary nucleus, located within a projected radius of 10 h^{-1} kpc (H_0= 100 h km s^{-1} Mpc^{-1}) of the luminosity centre of the combined system (Hoessel & Schneider 1985). These 'multiple nuclei' were at one time taken to be the best evidence for models which postulate that massive galaxies are growing at the centres of rich clusters by accreting their less massive neighbours (Hausman & Ostriker 1978). This is the case of brightest cluster galaxy IC 1695 (Fig. 1.15) in Abell 193 (Seigar et al. 2003). This source revealed a triple-nucleus structure. Even if the chance projection of a background or foreground galaxy falling within a projected radius of 10 h^{-1} kpc (H_0= 100 h km s^{-1} Mpc^{-1}) is 10 per cent (Tonry 1984; Hoessel & Schneider 1985) Seigar et al. 2003 studying K band and spectral properties suggest that the three nuclei are gravitationally bound as parts of a common merged, or merging system.

Figure 1.15: HST/WFPC2 F814W I-band image of the centre of IC 1695, BCG of A193 (Seigar et al. 2003). The image shows the triple nucleus in the centre of this galaxy.

1.3 Radio loud BCGs.

BCGs have long been recognized to show different radio properties to other cluster galaxies, being much more likely to be radio-luminous (Fig. 1.16) than other non-dominant cluster ellipticals (e.g. Burns, White & Hough 1981; Valentijn & Bijleveld 1983; Burns 1990). Best et al. (2005) showed that the probability of a galaxy to be a radio-loud AGN was dependent primarily upon its mass, determined either as the stellar mass ($f_{radio-loud} \propto M_{\star}^{2.5}$) , or the black hole mass ($f_{radio-loud} \propto M_{BH}^{1.6}$. As discussed by Best et al. (2005) the difference between the slopes of these two relations arises mainly because of the increasing fraction of disc-dominated galaxies, with small black holes, at stellar masses $M_{\star} \leqslant 10^{11} M_{\odot}$. These host fewer radio-loud AGN, and thus decrease the radio-loud fraction at low stellar masses, leading to a steeper dependence on stellar mass.

Recent results of Best et al. 2007 revealed that BCGs of all stellar masses are more likely to host radio-loud AGN than other galaxies of the same mass. The probability of a BCG hosting a radio-loud AGN scales roughly linearly with stellar mass, which is shallower than the relation for all galaxies. BCGs are an order of magnitude more likely to host radio-loud AGN than other galaxies at stellar masses below $10^{11} M_{\odot}$, but less than a factor of 2 more likely at stellar masses above $5 \times 10^{11} M_{\odot}$. The distribution of radio luminosities of BCGs is independent of the mass of the BCG, and the same as that determined for other galaxies. In fact, only the normalization of the radio luminosity function changes, not its shape (Fig. 1.16).

Moreover, the fraction of BCGs of a given stellar mass which host radio-loud AGN, and the distribution of their radio luminosities, do not depend strongly on the velocity dispersion of their surrounding group or cluster. This means that because BCGs in the richest clusters tend to be more massive than those in poorer clusters, the fraction of BCGs which host radio-loud AGN still turns out to be higher in more massive clusters, but it is the mass of the BCG, rather than the properties of its surroundings, which controls the likelihood of it being radio-loud.

Very often their radio morphology shows evidence of a strong interaction with the surrounding medium: some BCGs have a wide angle tail structure (WAT) very extended on the kiloparsec-scale , like 3C 465 (Fig. 1.17) in A2634, (Sakelliou & Merrifield 1999), or with small size such as NGC4874 (Fig. 1.18) in Coma cluster, (Feretti & Giovannini 1985).

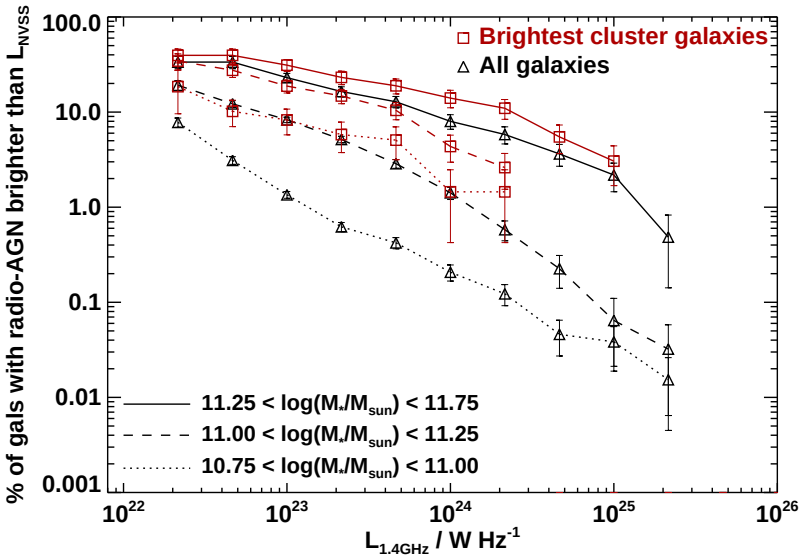

Figure 1.16: The percentage of galaxies which are radio-loud AGN brighter than a given radio luminosity, for 'all galaxies' (black lines) and the subsample of 'BCGs' (red lines) in three different ranges of stellar mass. There is no evidence for any significant difference in the shape of the luminosity functions, either as a function of stellar mass, or between BCGs and all galaxies: only the normalization of the relation changes (Best et al. 2007).

Fig. 1.17 reports the radio map overimposed to X-ray emission of the radiosource 3C 465 which is prototype of WAT (Wide Angle Tail) source. The kiloparsec scale jets are asymmetric. Polarization maps confirm that there is no change in jet dynamics with increasing distance from the core (Venturi et al. 1995). X-ray emission is detected from the active nucleus and the inner radio jet, as well as a small-scale, cool component of thermal emission, a number of the individual galaxies of the host cluster (Abell 2634), and the hotter thermal emission from the cluster (Hardcastle et al. 2005).

Fig. 1.18 contains a radio image overimposed to optical one of NGC4874, one of the two dominant galaxies of the Coma cluster. This is an example of BCG with the radio emission completed embedded in the galaxy.

In other cases, BCGs can have diffuse and amorphous sources, either extended (3C 84 (Fig. 1.19) in Perseus cluster, Pedlar et al. (1990)) or with very small size (e.g., the BCG (Fig. 1.20) in A154, Feretti & Giovannini (1994)).

Fig. 1.19 shows radio image oveimposed to X-ray emission of 3C 84 that is one of the brightest compact radio sources in the sky and it has been studied in some detail by several authors (Vermeulen, Readhead & Backer 1994; Taylor & Vermeulen

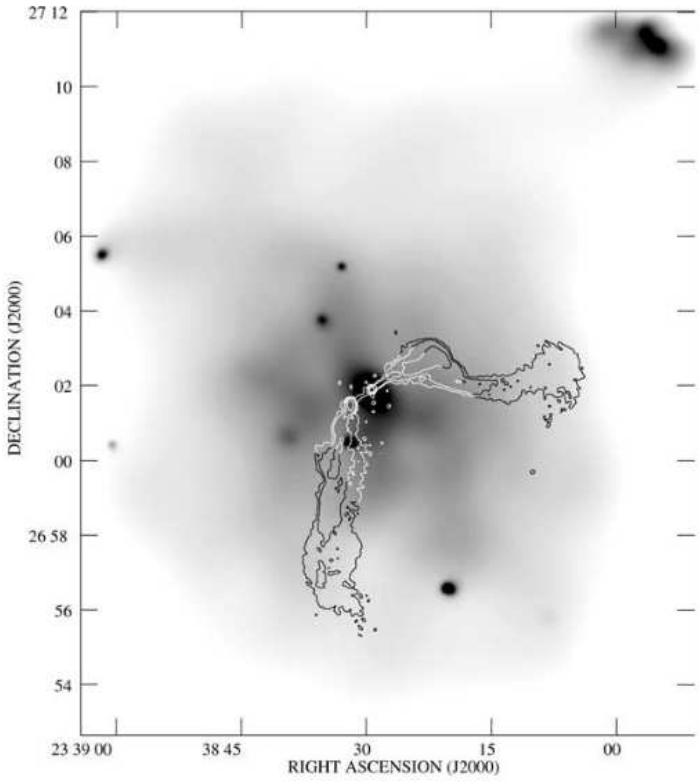

Figure 1.17: Extended X-ray emission from Abell 2634. The grey-scale shows the 0.5−5.0 keV data from XMMNewton. The object to the north-east is the background cluster CL-37. Superposed are contours of the 5.4-arcsec resolution 1.4 GHz VLA map of 3C 465 at 1× (1, 4, 16,) mJy/beam (Hardcastle et al. 2005).

1996; Silver, Taylor & Vermeulen 1998; Walker et al. 2000). In particular, it is known to undergo bursts of activity (Taylor & Vermeulen 1996) that could also drive the observed shocks and sound waves through the cluster. A clear extended radio structure is visible. The radio lobes are coincident with cavities present in the X-ray emitting gas which is sign of important interaction of the radio plasma with the surrounding medium.

In Fig. 1.20 it is presented the VLA radio map at 1.4 GHz of the BCG if Abell 154 which is double source with linear size of only ∼3 kpc (Feretti & Giovannini 1994).

WAT and amorphous sources are rare in the general radio population, but frequently present in BCGs and in particular in BCGs located in cooling core clusters of galaxies.

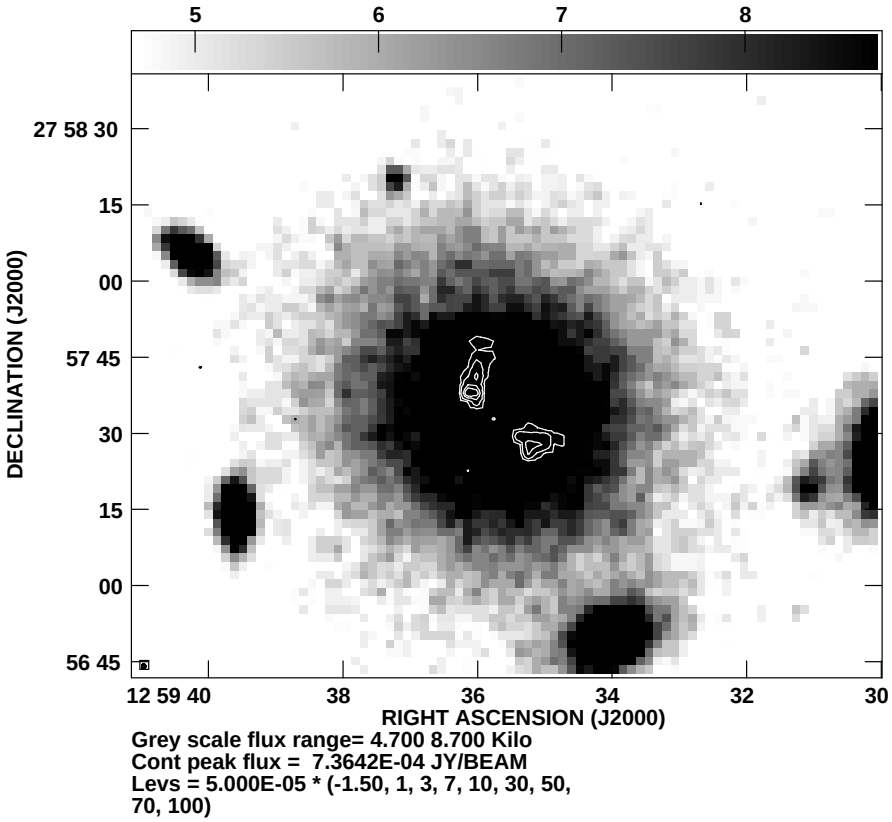

Figure 1.18: First Image (contour) of the NGC4874, BCG of A 1656 overimposed to the optical image (colours).

1.3.1 The cooling flow problem.

Radio loud BCGs has been proposed as a potential solution to the cooling-flow problem. Gas in the central regions of clusters of galaxies often has radiative cooling time-scales very much shorter than the Hubble time and, in the absence of a heating source, a cooling flow would be expected to develop, whereby the temperature in the central regions of the cluster drops and gas flows inwards at rates of up to $\sim$ 1000 $M_\odot$ yr^{-1} (see Fabian 1994, for a review). However, recent XMM-Newton and Chandra observations of cooling-flow clusters have shown that the temperature of cluster cores does not fall below $\sim$ 30 per cent of that at large radii, and that the amount of cooling gas is only about 10 per cent of that predicted for a classical cooling flow (e.g. David et al. 2001; Kaastra et al. 2001; Peterson et al. 2001; Tamura et al. 2001). This implies that some heating source must balance the radiative cooling losses, preventing the gas from cooling further.

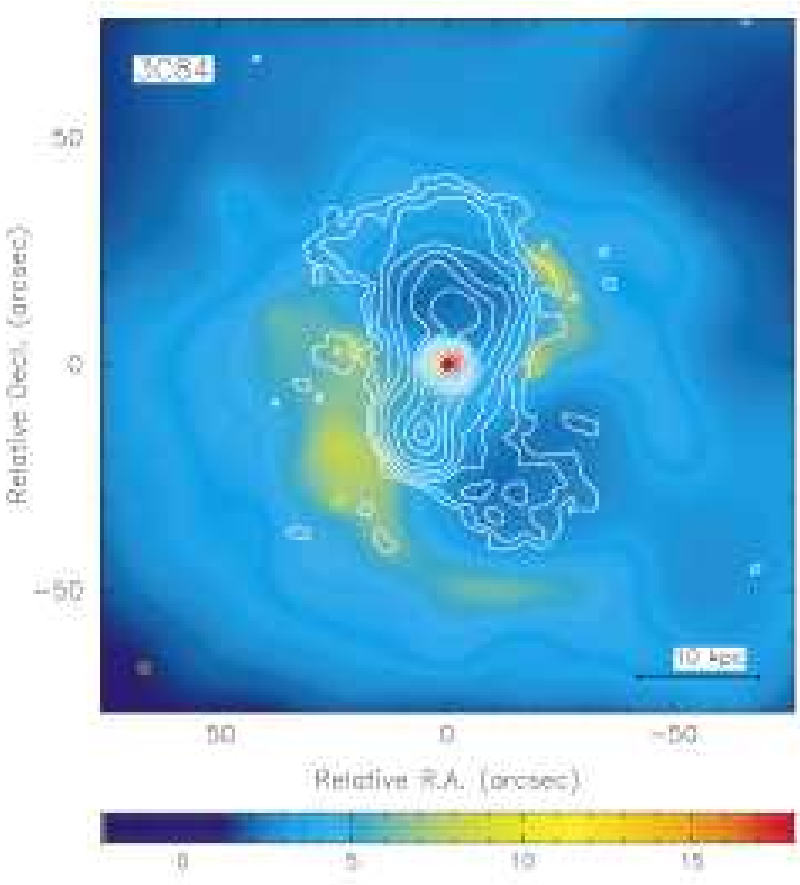

Figure 1.19: VLA observations at a frequency of 1.4 GHz were combined from in the A, B and C configurations overlay to Chandra X-ray observations of Perseus. The resulting radio image has been restored with a 5-arcsec synthesized beam. Contour levels start at 1 mJy/beam and increase by factors of 2 to just below the peak of 21.7 Jy/ beam.

Heating by radio sources associated with the BCGs has gained popularity in recent years, as X-ray observations have revealed bubbles and cavities in the hot intracluster medium of some clusters, coincident with the lobes of the radio sources (e.g. Böhringer et al. 1993; Carilli, Perley & Harris 1994; Fabian et al. 2000; McNamara et al. 2000; Blanton et al. 2001). These are regions where relativistic radio plasma has displaced the intracluster gas, creating a low-density bubble of material in approximate pressure balance with the surrounding medium, which then rises buoyantly and expands. Hydrodynamic simulations have been able to reproduce bubbles with properties similar to those observed (e.g. Churazov et al. 2001; Quilis, Bower & Balogh 2001; Brüggen & Kaiser 2002; Brüggen 2003) and they have also shown that, provided that radio source activity is recurrent, the total energy provided by AGN activity can be sufficient to balance the cooling radiation

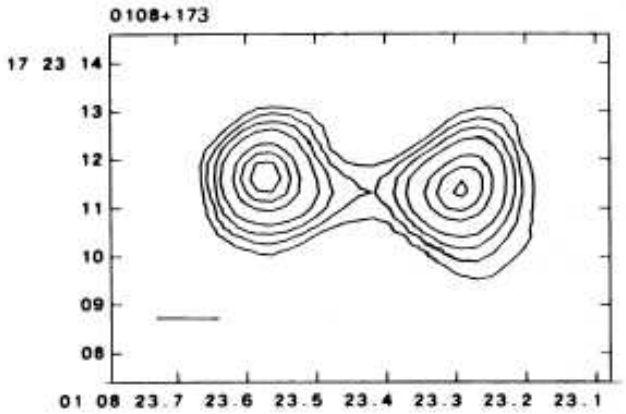

Figure 1.20: VLA radio map at 1.4 GHz of the BCG of Abell 154. Contour levels are (-0.16, 0.16, 0.3, 0.5, 0.6, 1.5, 2, 2.5) mJy/beam. The linear size of the double source is ∼3 kpc (Feretti et al. 1994)

losses through repeated production of jets, buoyant bubbles and associated shocks (e.g. Dalla Vecchia et al. 2004; Brüggen, Ruszkowski & Hallman 2005; Nusser, Silk & Babul 2006). Other authors (e.g. Omma et al. 2004; Brighenti & Mathews 2006) have argued that momentum-driven jets are an alternative means of distributing AGN energy throughout the intracluster medium.

Very deep Chandra observations of the Perseus and Virgo clusters (Fabian et al. 2003, 2006) have revealed the presence of approximately spherical weak shock waves in these clusters, extending out to several tens of kpc radius. Fabian et al. (2003) argued that these 'ripples' (Fig. 1.21) are excited by the expanding radio bubbles, and that dissipation of their energy can provide a quasi-continuous heating of the X-ray gas (see also Ruszkowski, Brüggen & Begelman 2004).

Fujita & Suzuki (2005) and Mathews, Faltenbacher & Brighenti (2006) argued, however, that if all of the wave dissipation occurs at the shock front then too much of the heat is deposited in the inner regions of the cluster, and not enough out at the cooling radius, leading to temperature profiles at variance with observations. Nusser et al. (2006) suggested that a natural solution to this problem is to consider the heating effects of AGN activity from all cluster galaxies, not only BCGs. More recently, Fabian et al. (2006) showed that the shocks occurring in the Perseus cluster are isothermal, meaning that thermal conduction must be important in mediating the shock. They argue that this prevents the accumulation of hot shocked gas in the inner regions, and that the energy of the waves can be dissipated at larger radii

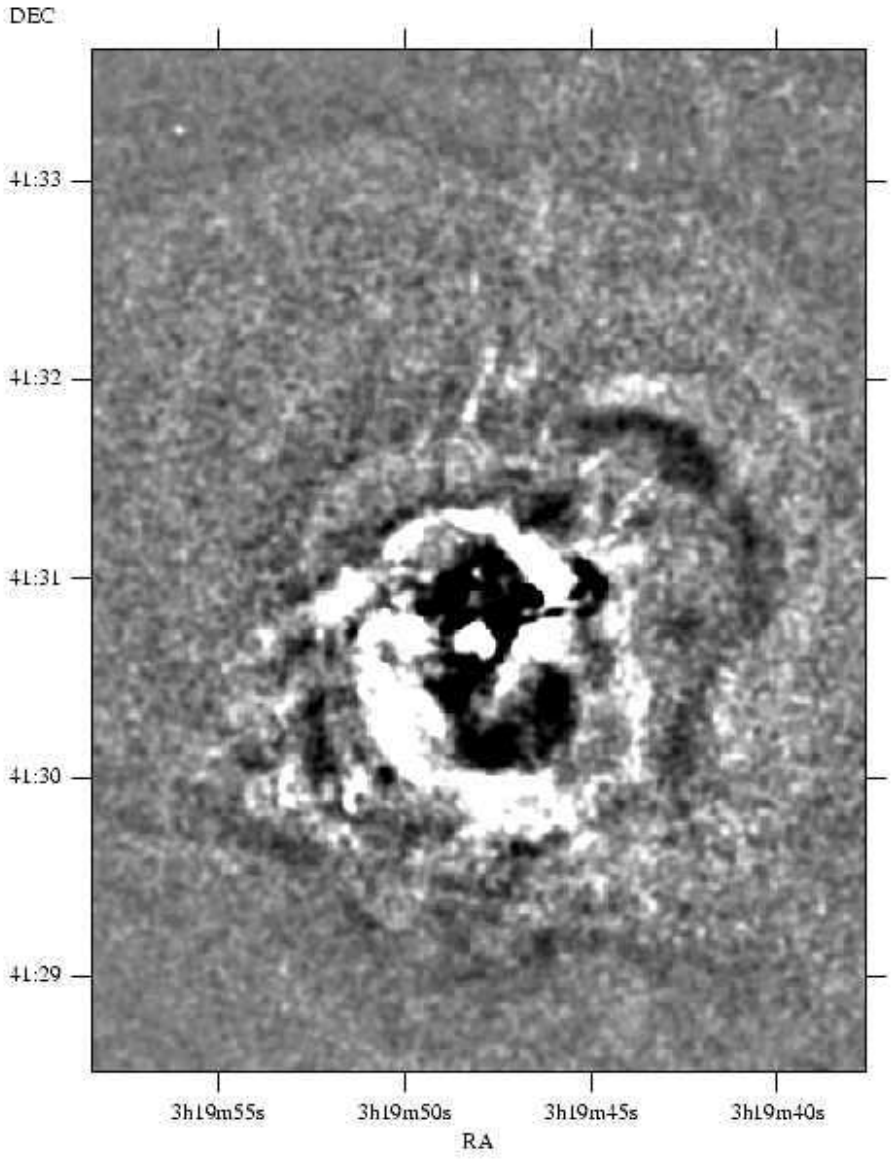

Figure 1.21: Deep-unsharp mask, 0.3–1.5 keV (0.98-arcsec Gaussian smoothed image, with 9.8-arcsec Gaussian smoothed image subtracted) X-ray image of Perseus cluster. Regions brighter than the local average are light; those fainter are dark (Fabian et al. 2003)

by viscous effects.

One critical question for all of these models is whether the heating generated by an episode of radio-loud AGN activity is sufficient, during its lifetime, to offset the radiative cooling losses of the cluster. Viewed in terms of the radio bubbles (which are widely considered to be the driving force behind the shock and sound waves), for some clusters the (pV) energy contained within the evacuated bubbles has been shown to be sufficient to balance the cooling losses, at least for a short period of

time (a few $\times 10^7$ yr ; e.g. Fabian et al. 2003; Bîrzan et al. 2004; Dunn, Fabian & Taylor 2005). However, Bîrzan et al. (2004) showed that this is not true for about half of the clusters they studied (see also Rafferty et al. 2006). Nusser et al. (2006) and others have argued that the mechanical energy injected into the cluster by weak shocks may be up to an order of magnitude larger than pV, which would ease this problem. An alternative possibility is that the heat balance occurs in a quasi-static manner, with recurrent low-luminosity radio activity being punctuated by occasional major eruptions supplying much more energy (Kaiser & Binney 2003).

An other important question is what the duty cycle of this AGN activity is. The duty cycle determines the rate of production of radio bubbles, or equivalently, the time-scale between the sound wave 'ripples', and hence is required to calculate the time-averaged heating rate associated with AGN activity. Burns (1990) showed that as many as 70 per cent of cD galaxies at the centre of cooling-flow clusters are radio-loud, but this result was based on a sample of only 14 such systems, and not all BCGs are cD galaxies.

Best et al. (2006) also concluded that, unless BCGs showed a different mode of radio activity to that of ordinary elliptical galaxies, then they could not provide sufficient heating to balance the cooling in clusters of galaxies. As discussed above, BCGs are found to be radio-luminous much more frequently than other cluster ellipticals, but the strong mass dependence of the radio-loud AGN fraction found by Best et al. (2005) means that this may solely be due to their very much higher masses.

These results support the argument of Best et al. 2005 that low-luminosity radio-loud AGN activity and emission-line AGN activity are independent physical phenomena. It is argued that the radio-loud activity is associated with the cooling of gas from the hot envelopes of elliptical galaxies and, in the case of central cluster galaxies, also from the intracluster medium. Accretion of hot gas from a strong cooling flow is able to explain both the boosted likelihood of BCGs hosting radio-loud AGN, and the different slopes of the mass dependencies of the radio-AGN fractions for BCGs and other galaxies.

Furthermore either the mechanical-to-radio luminosity ratio or the efficiency of converting the mechanical energy of the radio source into heating the intracluster medium must be a factor of $100-1000$ higher in rich clusters than in poor groups in

order that radio-AGN heating balances radiative cooling for systems of all masses. If not, then radio-loud AGN heating either overcompensates the radiative cooling losses in galaxy groups, providing an explanation for the entropy floor, and or falls short of providing enough heat to counterbalance cooling in the richest clusters. Thermal conduction could provide the extra energy required in the richest clusters (Best et al. 2007).

Chapter 2

Parsec scale properties of a complete sample of BCGs

2.1 The definition of a complete sample of BCGs.

We defined an unbiased complete sample selecting all BCGs in nearby (Distance Class [1] lower than 3) Abell clusters with a Declination larger than 0°. All clusters have been included with no selection on the cluster conditions (e.g., cooling) and no selection on the BCG radio power.

We present the sample in Table 2.1. In column 1 we report the name of the Abell cluster, in column 2 the Distance Class (DC), in column 3 the redshift z of the cluster, in column 4 we report the kpc/arcsec conversion for each cluster, in column 5 the name of the BCG, in column 6 and 7 we give the RA and DEC in J2000 coordinates of the BCG. For sources detected by our new observations the nuclear position is derived from our image with an estimated uncertainty ≤ 0.1 mas. For undetected sources ((xn) and sources discussed in the literature), we give in Table 2.1 the available coordinates (see notes for the references). In column 8 we give the angular resolution of maps used to estimate the core coordinates (see notes to the Tab.2.1).

Our complete cluster sample is composed by the BCGs of 23 Abell clusters. The nearest cluster is A262 with redshift = 0.0161 (DC = 1) and the more distant is A1213 with z= 0.0468 (DC = 2). Some BCGs like 3C 84 and 3C 465 are well known and well studied at parsec-scale with publicly available data and we did not obtain new data for them. In Table 2.1, in the last column, we indicate these sources

[1]The subdivision of Abell Clusters in six distance clusters (DC) is based on the apparent magnitude of the tenth brightest galaxy, in accordance with the redshift estimate for the cluster. hence, the distance class provides a coarse measure of distance Schneider (2006)

with (!). We used (*) for binary clusters: where two well defined substructures are present. In these clusters, we give the name of each BCG for the respective sub-clusters. This is the case for A1314, A1367 and A2151. we note also (in the table (**)) that the BCG of A400 is a dumbbell radiosource with two optical nuclei, 3C 75A and 3C 75B. we analyzed the radio emission associated with both. In this way, the BCGs that composed our complete sample are 27 objects.

Table 2.1: **The complete BCG sample.** In column 8 we give the angular resolution of maps used to estimate the core coordinates. we use (v) for the detected objects whose coordinates are taken by the VLBA maps and (!n) for well known radiosources with public VLBI data: (!1) from Taylor et al. (2006), (!2) from Lara et al. (1997); Baum et al. (1997); Lara et al. (1999), (!3) from Gentile et al. (2007) and (!4) from Venturi et al. (1995). We use (xn) for undetected radiosources for which coordinates are taken from : (x1), from NVSS; (x2) from NED ; (x3) from FIRST; (x4) from radio data of Feretti & Giovannini (1994); (x5) from Ledlow & Owen (1995). In the notes: (*) is for binary clusters for which We give the name of BCGs of the two sub-clusters; (**) indicates a dumbbell radiosource for which we consider the radioemission from both optical nuclei.

Abell Cl.	DC	z	kpc/arcsec	BCG	RA_{J2000}	DEC_{J2000}	HPBW	Notes
262	0	0.0161	0.328	NGC708	01 52 46.458	36 09 06.494	0.003″ ,(v)	
347	1	0.0187	0.380	NGC910	02 25 26.77	41 49 27.3	45″ ,(x1)	
400	1	0.0232	0.468	3C75A	02 57 41.650	06 01 20.717	0.0065″ ,(v)	(**)
				3C75B	02 57 41.563	06 01 36.873	0.006″ ,(v)	(**)
407	2	0.0470	0.922	UGC2489	03 01 51.813	35 50 19.587	0.005″ ,(v)	
426	0	0.0176	0.358	3C84	03 19 48.160	41 30 42.104	0.0018″ ,(!1)	
539	2	0.0205	0.415	UGC3274	05 16 38.91	06 25 26.3	45″ ,(x1)	
569	1	0.0196	0.397	NGC2329	07 09 08.006	48 36 55.736	0.0035″ ,(v)	
576	2	0.0381	0.755	CGCG261-059	07 22 06.980	55 52 30.566	0.004″ ,(v)	
779	1	0.0226	0.457	NGC2832	09 19 46.87	33 44 59.6	45″ ,(x1)	
1185	2	0.0304	0.608	NGC3550	11 10 38.50	28 46 04.0	5″ ,(x3)	
1213	2	0.0468	0.918	4C29.41	11 16 34.619	29 15 17.120	0.003″ ,(v)	
1228	1	0.0350	0.697	IC2738	11 21 23.06	34 21 24.0	5″ ,(x3)	
1314	1	0.0341	0.679	IC708	11 33 59.222	49 03 43.428	0.0022″ ,(v)	(*)
				IC712	11 34 49.313	+49 04 40.54	5″ (x3)	(*)
1367	1	0.0215	0.435	NGC3842	11 44 02.161	19 56 59.03	5″ ,(x5)	(*)
				3C264	11 45 05.014	19 36 22.94	0.0035″ ,(!2)	(*)
1656	1	0.0232	0.468	NGC4874	12 59 35.796	27 57 33.259	0.0027″ ,(v)	
2147	1	0.0356	0.708	UGC10143	16 02 17.027	15 58 28.30	5″ ,(x3)	
2151	1	0.0371	0.737	NGC6041	16 04 35.794	17 43 17.551	0.0032″ ,(v)	(*)
				NGC6047	16 05 08.897	+17 43 54.31	5″ ,(x3)	(*)
2152	1	0.0374	0.742	UGC10187	16 05 27.176	16 26 8.4	5″ ,(x3)	
2162	1	0.0320	0.639	NGC6086	16 12 35.59	29 29 04.8	5″ ,(x5)	
2197	1	0.0303	0.606	NGC6173	16 29 44.887	40 48 41.880	0.004″ , (v)	
2199	1	0.0303	0.606	3C338	16 28 38.267	39 33 04.15	0.0014″ ,(!3)	
2634	1	0.0312	0.624	3C465	23 35 58.97	26 45 16.18	0.0025″ ,(!4)	
2666	1	0.0265	0.533	NGC7768	23 50 58.549	27 08 50.416	0.0035″ ,(v)	

2.2 The data set.

2.2.1 The data reduction.

To complete the knowledge of the parsec-scale structure of sources in our sample, we asked and obtained new VLBA (see Appendix) observations at 5 GHz for 23 sources. Observations of 10 BCGs were carried out in 2007 June, while the remaining 13 targets of the complete sample were observed between 2008 February and March (see Table 2.2).

All data have been obtained in phase referencing mode. If the VLBA target source , like us BCGs, is not sufficiently strong for self-calibration or if absolute positional information is needed but geodetic techniques are not used, then VLBA phase referenced observations must be employed (Beasley & Conway 1995).A VLBA phase reference source should be observed frequently and be within a few degrees of the VLBA target region, otherwise differential atmospheric (tropospheric and ionospheric) propagation effects will prevent accurate phase transfer. Most of these candidate phase calibrators now have positional uncertainties below 1 mas.

Each source of our sample was observed for $\sim$3 hours. The data were correlated in Socorro, NM. Postcorrelation processing used the NRAO AIPS package and the Caltech Difmap packages. We follow the same scheme for the data reduction of all data sets. We first applied ionospheric and Earth Orientation Parameters (EOP) corrections. After this, by running VLBACALA we corrected sampler offsets and applied amplitude calibration. With VLBAPANG we corrected the antenna parallactic angles and with VLBAMPCL we removed the instrumental delay residuals. All calibrator data were also globally fringe fitted. After flagging bad data, we obtained good models for the calibrators, which we used to improve the amplitude and phase calibration for the entire data set. Final maps were obtained with DIFMAP by averaging over IFs and in time. After one step of editing, to obtain a good clean model of the source we applied multi-iterations of self-calibration in phase to sources with a correlated flux density > 5 mJy and eventually amplitude self-calibration to sources with signal to noise ratio > 5.

In Table 2.2, we report the image parameters for our final maps. For each source (col.1), we give the epoch of observation (col.2), the calibrator (col.3), the beam size and P.A.(col. 3 and 4), the noise (col.5), the intensity peak (col.6) and the total flux density (col. 7) of final naturally weighted maps. Typically, the error in flux

density resulting from calibration is $\sim 6\%$. On average, the resolution of final maps of 2007 data is better (3×1.5 mas) than 2008 images ($4\times$ 2 mas) as the consequence of more antennas (10 instead of 9) available in observations of 2007 compared to that in 2008 (Saint Croix VLBA antenna was not present). The noise level is $\sim$0.1 mJy/beam, and the detection rate of our new VLBA observations is 12/23 ($\sim$52%). For detected sources, the nuclear source position has been estimated with an error $\leq$1 mas. We have to note that the detection rate is likely influenced by the fact that some BCGs could have an unreliable position derived from arcsecond images. For these sources, we imaged VLBI fields as large as a few arcsecs with no time or/and frequency average allowing us to recover in some cases the nuclear source. More discussion about the detection rate of our BCG sample is given in 2.4.

Table 2.2: Image parameters for naturally weighting maps of new VLBA 5 GHz data.

Epoch yy-mm-dd	BCG	Calibrator	HPBW mas×mas, deg	noise mJy/beam	Peak mJy/beam	Total flux density mJy
2007-06-08	NGC2329	J0712+5033	3.31 x 1.66, 30.20	0.10	62.4	77.1
	NGC708	J0156+3914	2.92 x 1.57, -15.90	0.11	3.2	3.2
2007-06-14	IC708	J1153+4931	2.24 x 1.81, -4.25	0.10	35.5	44.2
	IC712	J1153+4931	2.23 x 1.8, -6.94	0.09	-	-
	NGC3842	J1125+2005	3.05 x 1.81, 2.99	0.14	-	-
	NGC4874	J1257+3229	2.73 x 1.83, -7.18	0.10	7.37	10.1
2007-06-17	NGC6041	J1606+1814	3.20 x 1.70, -6.47	0.09	7.63	7.83
	NGC6047	J1606+1814	3.27 x 1.68, -8.09	0.11	-	-
	UGC10143	J1606+1814	3.28 x 1.70,6.67	0.12	-	-
	UGC10187	J1606+1814	3.31 x 1.7, -7.57	0.11	-	-
2008-02-08	NGC910	J0219+4727	3.73 x 2.23, 29.50	0.10	-	-
	3C75A	J0249+0619	6.40 x 2.21, 25.4	0.13	20.2	22.0
	3C75B	J0249+0619	5.80 x 4.31,19.7	0.13	37.6	44.5
2008-02-09	UGC2489	J0310+3814	4.87 x 2.23, 16.80	0.11	2.6	3.5
2008-02-16	NGC7768	J2347+2719	3.51 x 1.40, -7.15	0.09	0.72	1.3
	UGC3274	J0517+0648	3.51 x 1.53, 0.28	0.08	-	-
2008-02-17	NGC2832	J0919+3324	3.63 x 1.68, 23.10	0.10	-	-
2008-02-22	4C29.41	J1103+3014	3.04 x 1.63, -4.56	0.07	36.7	39.2
2008-02-28	NGC3550	J1103+3014	3.02 x 1.62,-6.37	0.09	-	-
	IC2738	J1127+3620	2.73 x 1.69,- 17.20	0.13	-	-
2008-03-16	CGCG261-059	J0742+5444	4.03 x 1.63, -32.30	0.11	1.9	3.2
	NGC6173	J1652+3902	4.07 x 1.94, -3.03	0.11	1.1	1.3
	NGC6086	J1634+3203	4.78 x 2.20, -2.54	0.11	-	-

2.3 Notes on Individual Sources.

Here we provide a brief description of all the BCGs in our complete sample, together with some information on the large scale structure and cluster conditions. we present contour images for the parsec-scale radio emission for all resolved sources.

2.3.1 NGC708 (B2 0149+35) in Abell 262.

This cluster is one of the most conspicuous condensations in the Pisces-Perseus supercluster. Its redshift is 0.0161. It is a spiral-rich cluster, characterized by the presence of a central X-ray source centered on a D/cD galaxy. Braine & Dupraz (1994) detect molecular gas and suggest that it contains a cooling flow which may contribute to the central X-ray emission. Observations show a double gaseous component.
The BCG has a dust lane almost perpendicular to the direction of its radio emission (Ebneter & Balick 1985), which extends along direction P.A. 70° (Parma et al. 1986). Blanton et al. (2004) discuss the interaction between the cooling gas and the radio source which shows at arcsecond resolution a core with a symmetric structure. In Fig.2.1, an anticorrelation between the radio and X-ray emission is apparent. This is most clearly seen to the east of the cluster center, where the radio lobe has "blown a bubble" in the ICM. The radio lobe fills a region of low surface brightness in the X-ray image and is surrounded by an X-raybright shell of emission. This bubble has an inner diameter of 15 $''$ .5 = 5.2 kpc. The AGN is visible as a point source in the X-ray that is coincident with the radio core. The total 1.4 GHz flux density is 78 mJy (Blanton et al. 2004). This gives a power at 1.4 GHz of $P_{1.4GHz}$=4.7×10^{22} W/Hz, classifying the source as a fairly weak, double-lobed FR I galaxy (Fanaroff & Riley 1974).

At parsec-scale, we observed an unresolved structure with total flux density of 3.2 mJy - about 64% of the arcsecond core flux density. The lack of visible jets and the low core radio power are in agreement with the suggestion that the core is in a low activity phase and that the offset of the radiative cooling is due to several outburst episodes (Clarke et al. 2009).

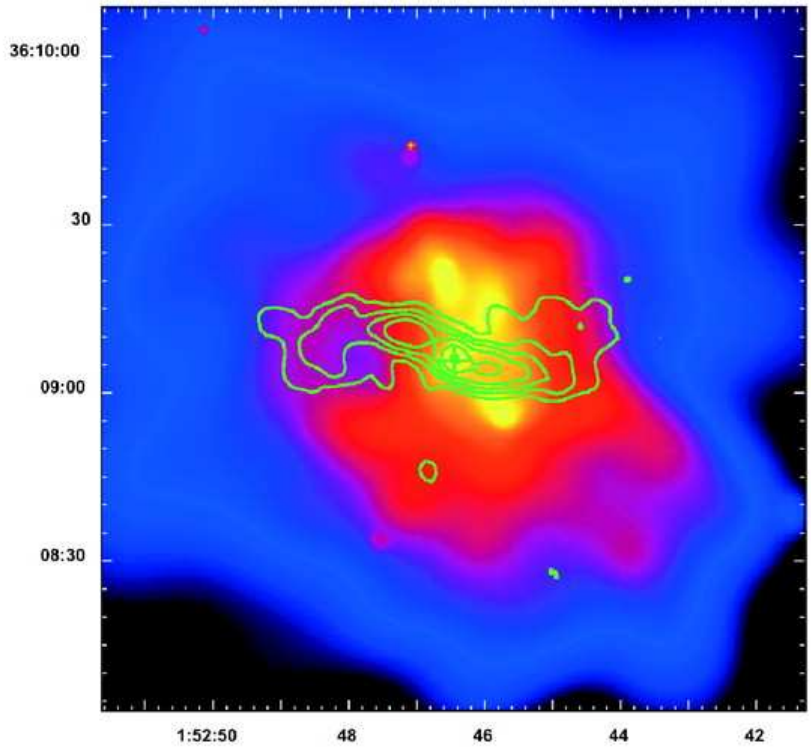

Figure 2.1: From Blanton et al. (2004): Adaptively smoothed Chandra image of the central 125″ × 125″ region of A262 with radio contours at 1.4 GHz (Fabian et al. 2006) overlaid. The radio emission is generally anticoincident with the X-ray emission. This is most clearly seen to the east of the cluster center, where the radio lobe has evacuated a cavity in the X-ray-emitting ICM.

2.3.2 NGC910 in Abell 347.

This cluster at z = 0.0187 has been classified as a small cooling cluster by White et al. (1997). No powerful radio galaxy is seen in its central region. The BCG shows in NVSS images a slightly resolved and faint emission with a flux density of about 2 mJy, that corresponds to a total power $P_{1.4GHz}$=1.6×10^{21}W/Hz.

Our VLBA observations did not detect a radio source to a 5σ limit of < 0.5 mJy/beam.

2.3.3 3C 75 in Abell 400

This cluster has redshift $z = 0.0235$. The central, elliptical-rich population is composed of two subgroups separated by 700 km s^{-1}. These groups are not apparent in the galaxy distribution projected on the sky. From this, we can conclude that a merger is taking place, close to the line-of-sight. Abell 400 does not have a cooling core (Eilek & Owen 2002).

The central BCG galaxy is an interesting case of a dumbbell galaxy, with two components separated by ∼7.2 kpc in projection and 453 km s^{-1} in velocity. Twin radio jets depart from each of the two optical nuclei 3C 75A and 3C 75B (Owen et al. 1985). The two radio sources have similar total radio power at 1.4 GHz (LogP$_{1.4}$∼24.3 Parma et al. (1991)), but different nuclear flux density. The brightest core is 3C 75B in the north with a core flux density at 1.4 GHz S$_{core,1.4}$ ∼37.6 mJy compared to 10.5 mJy for 3C 75A. The large scale radio structure is classified as FRI (Morganti et al. 1993). The jets are strongly bent by the cluster gas and on large scales they intertwine and merge (Fig. 2.2).

The strong asymmetry of the source to the north and east might suggest motion of both nuclei to the southwest relative to the cluster gas. We observed both nuclei, 3C 75A and 3C 75B at mas resolution (see Fig.2.2). At parsec-scale, both radio sources are one sided with the main jet aligned with the kiloparsec structure. 3C 75A is fainter than 3C 75B in agreement with the kpc scale behavior. The nucleus of 3C 75A has a flux density S∼19.9 mJy and the jet has S∼2.14 mJy with an extension of ∼4 mas. The core of 3C 75B has S ∼37.6 mJy and the jet has ∼7 mJy with an extension of ∼14 mas. The high nuclear flux density of 3C 75A in the VLBI image with respect to the arcsecond core flux density at 1.4 GHz suggests a self-absorbed structure and a possible source variability.

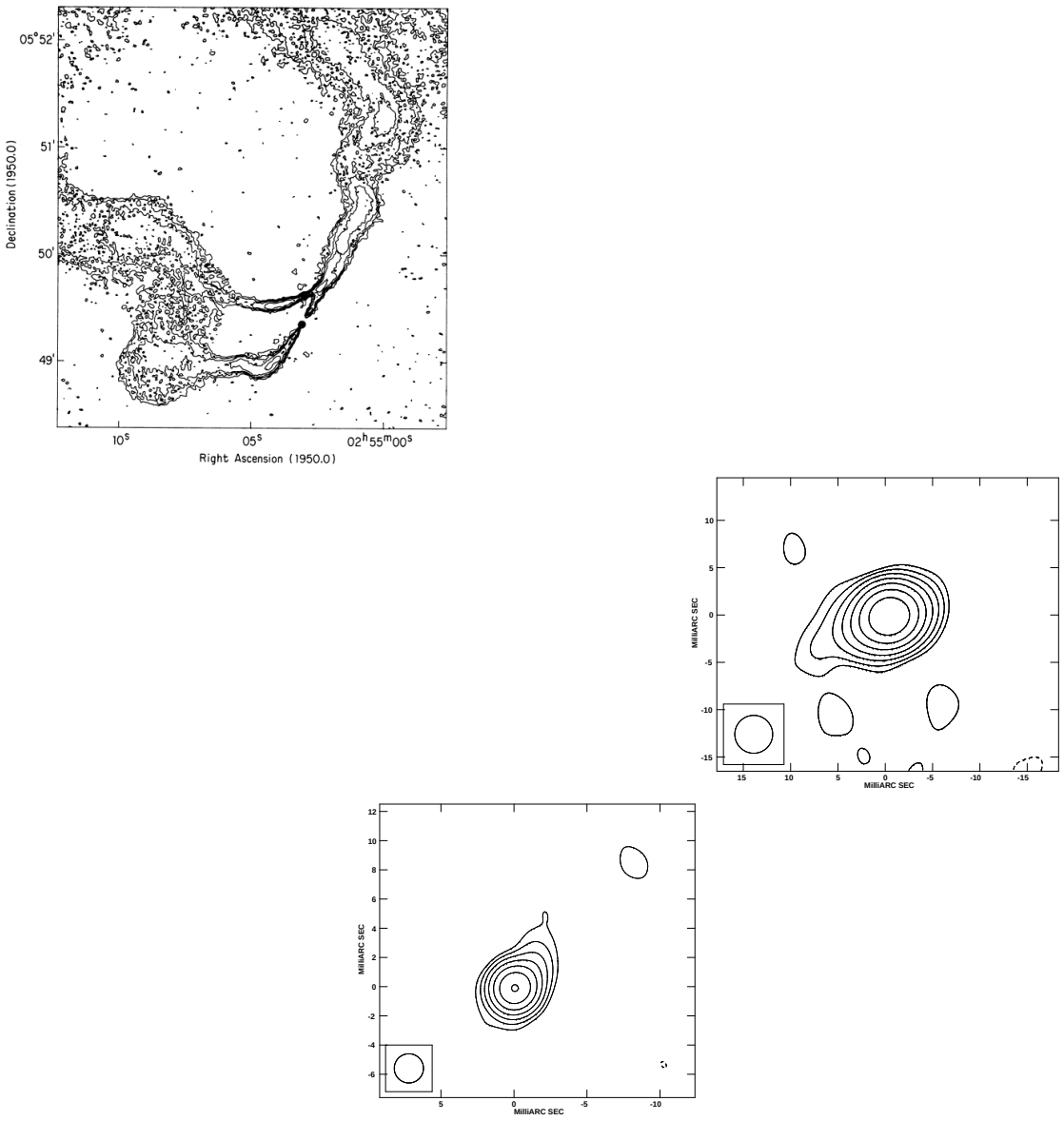

Figure 2.2: The double BCG in the non cool core cluster A400. Left: VLA image at 5 GHz of 3C 75A and 3C 75B from Owen et al. (1985). Contour intervals are (-1, 1, 2, 4, 8. 16, 32, 64, 128, 256, 512) × 0.1 mJy per clean beam. Center: one-sided 5 GHz VLBA tapered image of 3C 75A. Contour levels are -0.3, 0.3, 0.6, 1.2, 2.4, 4.8, 9.6 and 19.2 mJy/beam. The peak flux density is 19.9 mJy/beam, the noise level is 0.1 mJy/beam and the restoring beam is 2 × 2 mas^2, P.A. = 0 °. Right: one-sided 5 GHz VLBA tapered image of 3C 75B. Contour levels are -0.3, 0.3, 0.6, 1.2, 2.4, 4.8, 9.6 and 19.2 mJy/beam. The peak flux density is 37.2 mJy/beam, the noise level is 0.1 mJy/beam and the restoring beam is 4 × 4 mas^2, P.A. = 0 °.

2.3.4 UGC2489 in Abell 407.

No evidence for a cooling core has been found for this cluster. The BCG appears to be embedded in a diffuse optical halo within a region of ∼60kpc in size (Crawford et al. 1999).

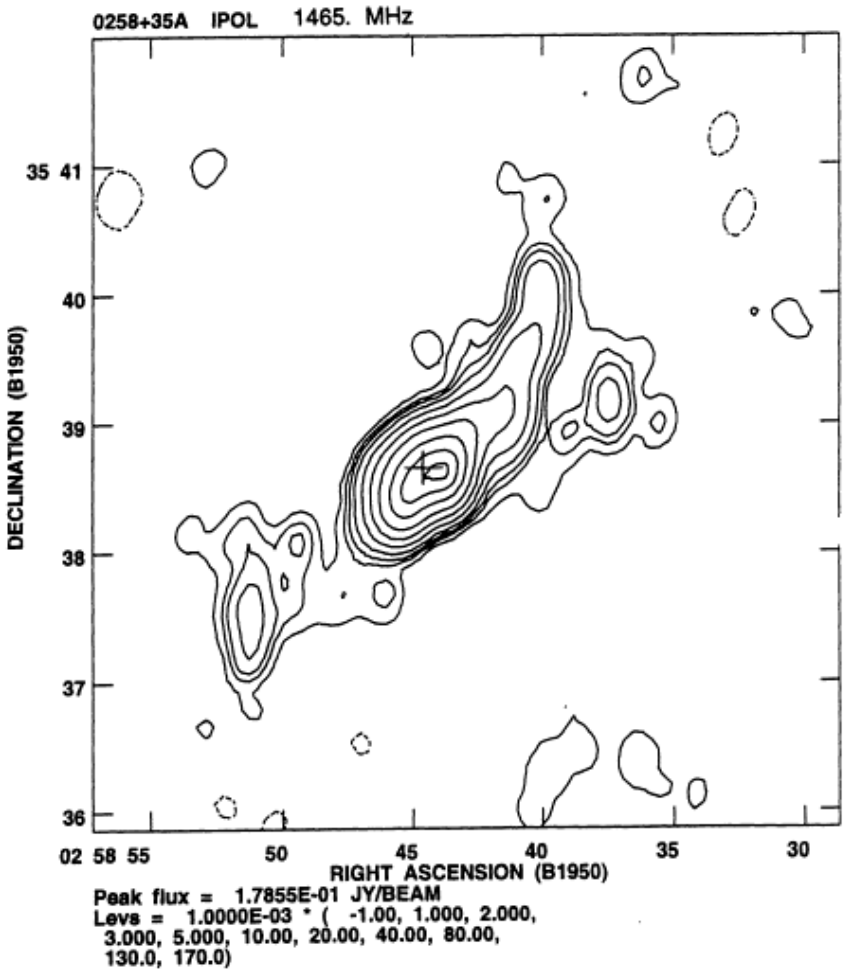

Figure 2.3: VLA image at 20 cm of UGC2489 (Bondi et al. 1993)

.

In radio images at arcsecond resolution it shows a complex extended structure with two lobes and tails oriented East-West (Fig.**??**). The largest angular size is ∼250 arcsec and the total flux density at 20 cm $S_{t,20}$ ∼728 mJy. The core has $S_{c,20}$ ≤10 mJy, the East lobe+tail is ∼110 arcsec extended with $S_{E,20}$∼305 mJy and the West one is brighter ($S_{W,20}$∼ 416 mJy) and larger (∼ 123 arcsec) (Bondi et al. 1993).

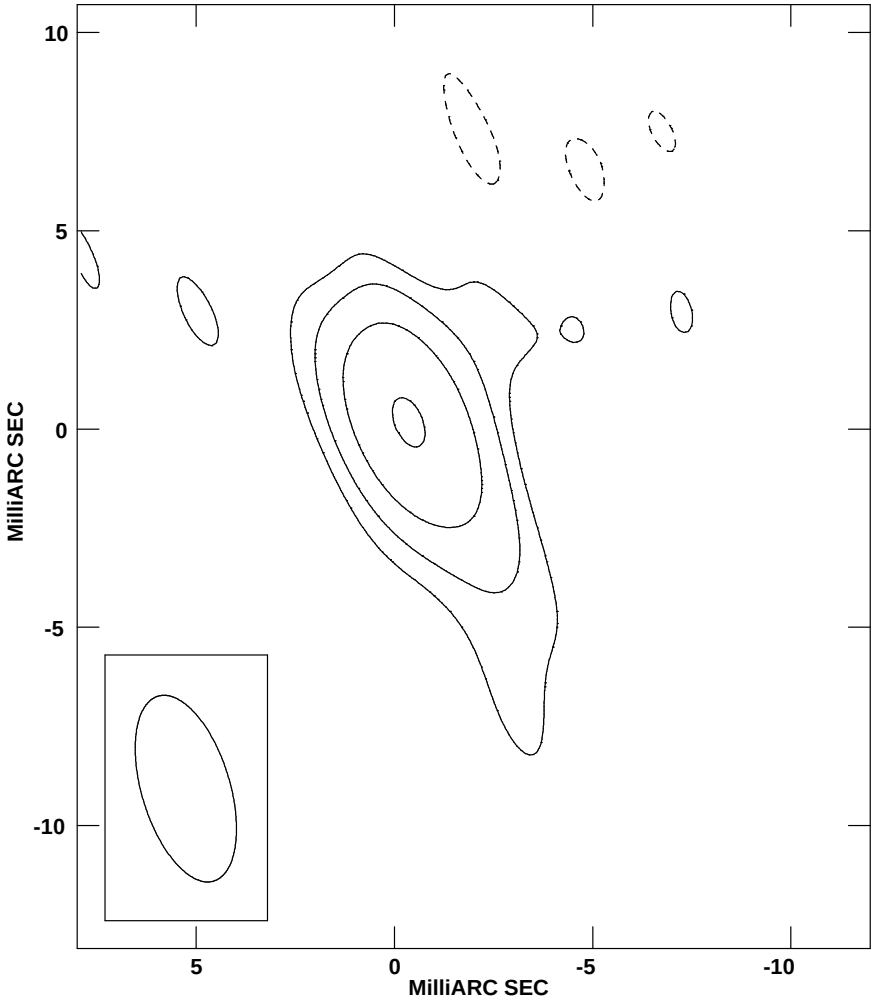

Figure 2.4: The 5 GHz VLBA naturally weighted image of UGC2489, BCG of A407. Contour levels are -0.31, 0.31, 0.62, 1.24 and 2.48 mJy/beam. The peak flux density is 2.6 mJy/beam, the noise level is 0.1 mJy/beam and the restoring beam is 4.87×2.23 mas^2, P.A. = 16.8 °.

At mas scale (fig. 2.4), the source appears one-sided with a core flux density $\sim$2.6 mJy. The jet direction is NW-SE with an extension of 6 mas and flux density $\sim$ 0.9 mJy.

2.3.5 UGC3274 in Abell 539.

This cluster is at z= 0.0205; its internal structure is not clearly understood. Girardi et al. (1997) found that it is composed by two systems, both very extended, separated in velocity by over 4000 km/sec, but spatially overlapped. The BCG in NVSS image is not detected ($\leq$ 1.4 mJy) which corresponds to an upper limit on the total power LogP$\leq$21.1(W/Hz). Our VLBA observations did not detect a radio source to a 5σ limit of $<$ 0.4 mJy/beam.

2.3.6 NGC2329 in Abell 569.

No cooling core has been found in this cluster. The galaxy has an exceptionally blue V-I ($\sim$1.20) color (Verdoes Kleijn et al. 1999). The nucleus is clearly bluer than its surroundings. The nuclear emission is slightly resolved and shows a small extension roughly in the direction of the dust protuberance. The galaxy has a small inclined central dust disk.

NGC2329 has been associated with a wide-angle tail (WAT) radio source with two tails extended for about 4 arcmin (Fig. 2.5).

The total power at 1.4 GHz is LogP=23.48 W/Hz and the core power at 5 GHz is LogP=22.52 W/Hz (Feretti & Giovannini 1985). The extended radio morphology suggests merging.

The VLBA observations at 1.6 GHz of Xu et al. (2000) detect a one-sided morphology with peak flux density $\sim$49.7 mJy/beam and total flux density $\sim$59.1 mJy. The core-jet is elongated in the direction corresponding to the northeastern radio tail. We confirm this morphology in our data. In our images (Fig. 2.6), the core has S$\sim$66.8 mJy, the jet has S$\sim$ 10.3 mJy with an extension of $\sim$ 15 mas. The total spectral index derived from 1.6 and 5 GHz data is $\alpha\sim$ - 0.2.

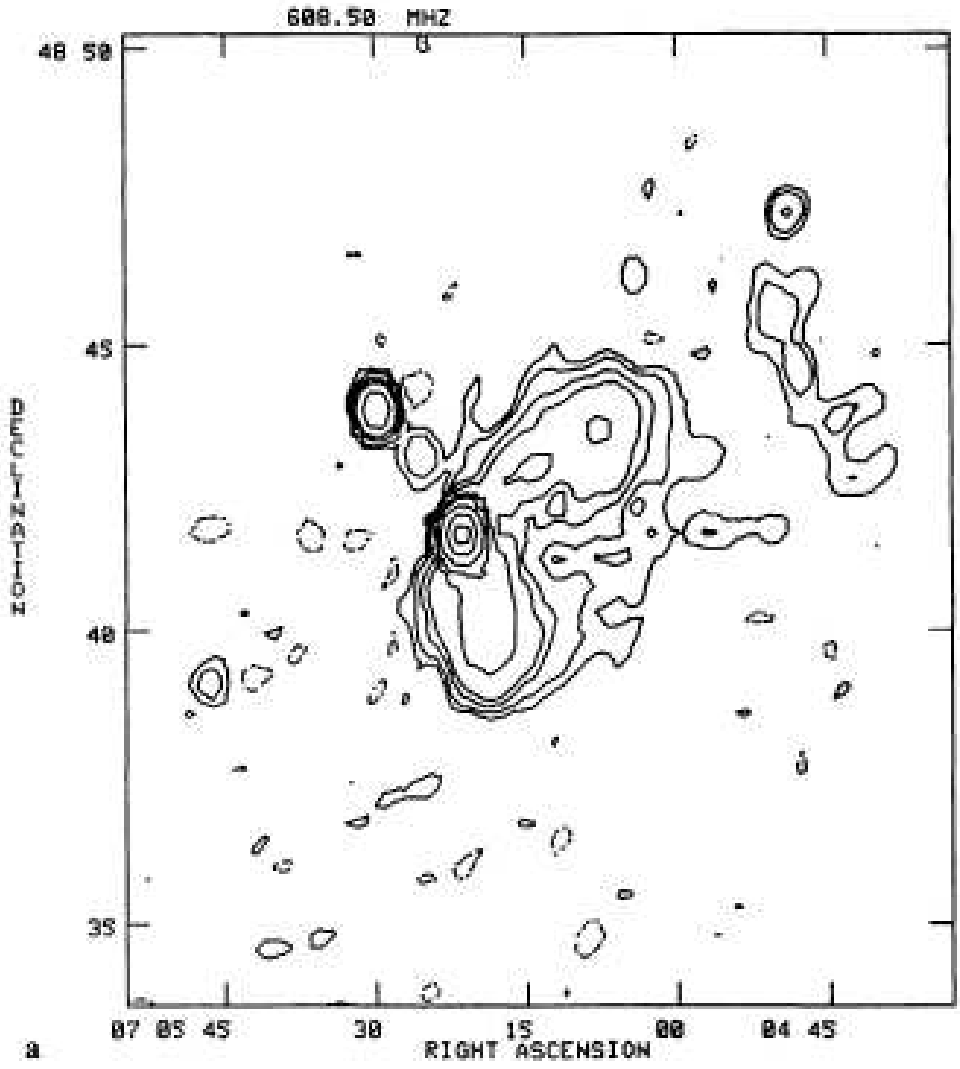

Figure 2.5: WSRT map at 0.6 GHz of NGC2329 (Feretti & Giovannini 1985). Contour levels are : (-2.5, 2.5, 5, 10, 15, 30, 50, 100, 200, 300) mJy/beam. The beam is $31.5'' \times 40''$.

.

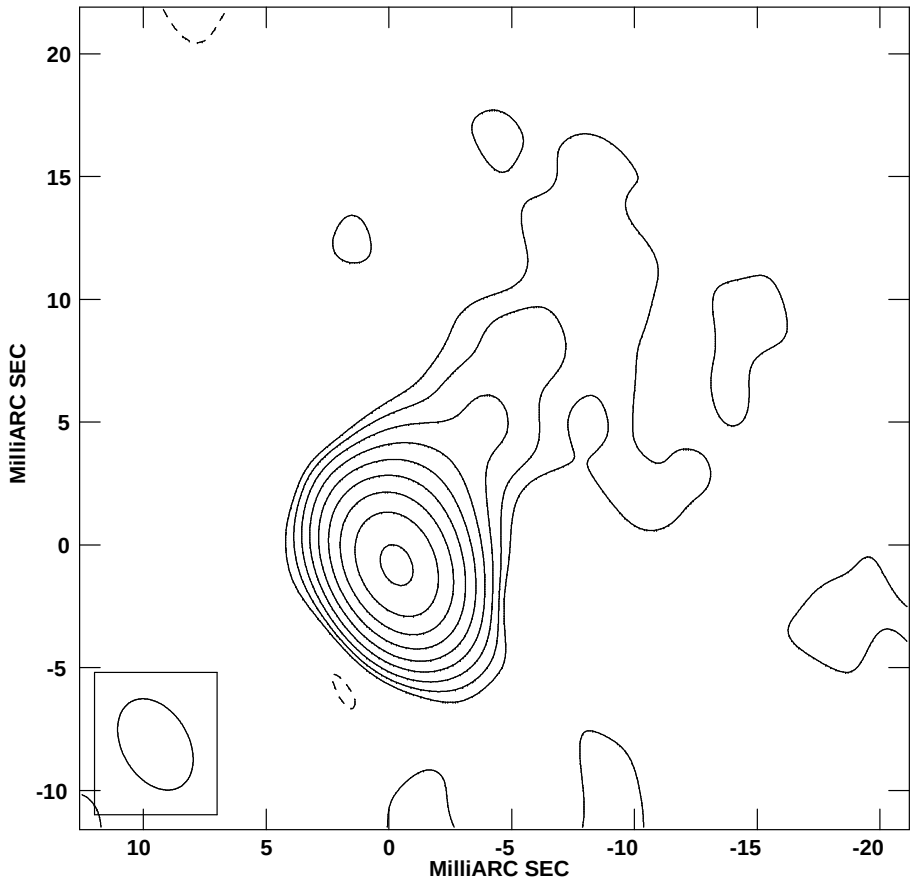

Figure 2.6: 5 GHz VLBA tapered map of NGC2329, BCG of A569. Contour levels are -0.23 0.23 0.46 0.92 1.84 3.68 7.36 14.72 29.44 and 58.88 mJy/beam. The peak flux density is 66.8 mJy/beam, the noise level is 0.08 mJy/beam and the restoring beam is 4.0 × 2.7 mas^2, P.A. = 30 °.

.

2.3.7 CGCG 261-059 in Abell 576.

This cluster is not relaxed. The rise in velocity dispersion of emission-line population towards the cluster core indicates that this population is dynamically aware of the cluster and probably falling into the cluster for the first time. The observations seem to be in favour of the model for which the core of A576 contains the remnants of a lower mass subcluster (Mohr et al. 1996). The BCG is slightly extended in the NVSS image and it shows a mJy level emission. In the FIRST image it appears pointlike with a flux density ~ 3.33 mJy that corresponds to total power LogP=22.04 (W/Hz).

In our parsec-scale map (Fig. 2.7), the source is one sided with a core flux density of 1.87 mJy. The jet has a flux density of 1.37 mJy, and extends for 7 mas in P.A$\tilde{=}\tilde{-}20°$.

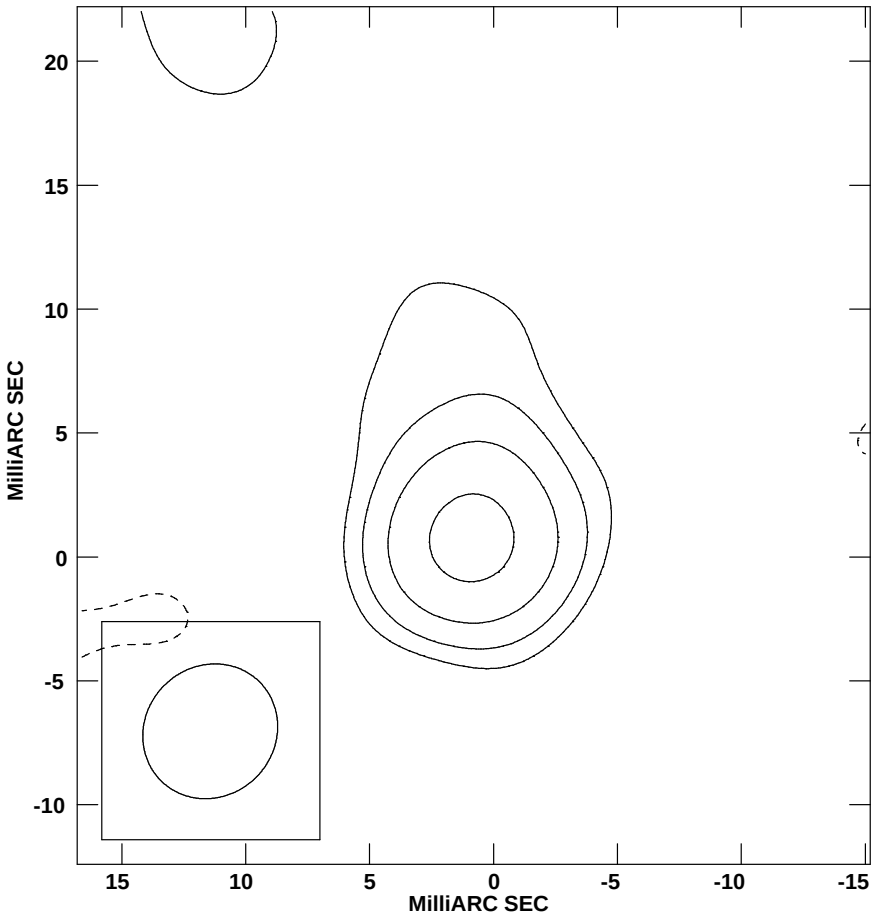

Figure 2.7: The 5 GHz VLBA tapered map of CGCG261-059, BCG of A576. Contour levels are -0.3, 0.3, 0.6, 1.2 and 2.4 mJy/beam. The peak flux density is 3.0 mJy/beam, the noise level is 0.1 mJy/beam and the restoring beam is 5.63 $\times$ 5.24 mas^2, P.A. = -45.19 °.

.

2.3.8 NGC 2832 in Abell 779.

This is a poor cluster, with no evidence of a cooling core from X-ray data (White et al. 1997). In high-resolution ROSAT HRI soft X-ray observations, NGC 2832 shows a strong central emission peak, with some diffuse emission around it. It does not possess an extended cD envelope (**?**). A nearby satellite galaxy, NGC 2831, appears to be tidally interacting with the BCG despite a relative velocity difference of 1692 km s^{-1} (Lauer 1988). No optical emission lines are present in NGC 2832, and it lacks a cooling core (McNamara 1992).

The radio emission associated with the BCG is at the mJy level, unresolved in FIRST images with a flux density $\sim$ 2.36 mJy that corresponds to a total power LogP=21.43(W/Hz). Our VLBA observations did not detect a radio source to a 5σ limit of < 0.5 mJy/beam.

2.3.9 NGC3550 in Abell 1185.

This cluster is at z=0.0304 with no evidence for a cooling core(White et al. 1997). It is undetected in NVSS and FIRST images. In our image, we did not detect any radio emission ≥ 0.45 mJy/beam (5σ).

2.3.10 4C 29.41 in Abell 1213.

This cluster is underluminous in the X-rays, just marginally detected by the Einstein and ROSAT satellites. The X-ray images and optical distribution suggest a non relaxed structure (Jones & Forman 1999). At kiloparsec-scale, this radio source is part of a dumbell galaxy (Trussoni et al. 1997). It is an example of double and symmetric radio source with a bright one-sided jet (Fig. 2.8). It is classified as a FRI radiogalaxy with total power at 1.4 GHz $\mathrm{LogP}_{1.4GHz,t}\sim$ 25.35 and core flux density at 5 GHz of $\mathrm{S}_{5GHz,core} \sim$ 41 mJy. Its linear size is about 81 kpc (Owen & Ledlow 1997).

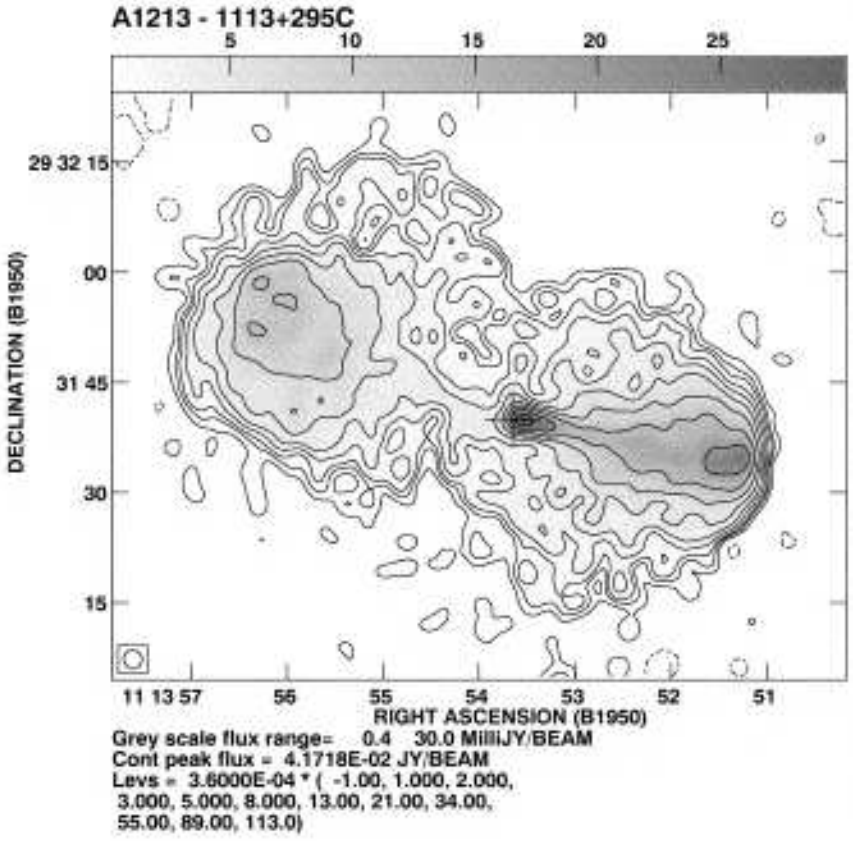

Figure 2.8: Gray-scale/contour map (Owen & Ledlow 1997) at 20 cm for 4C 29.41. The clean beam is shown in a corner of the map. Cross indicates the optical position.

On the mas scale (Fig.2.9), it shows one-sided morphology with the jet aligned with the kiloparsec structure. The core flux density is ∼36.24 mJy, while the jet has $\sim$ 2.5 mJy and is visible out to $\sim$ 12 mas.

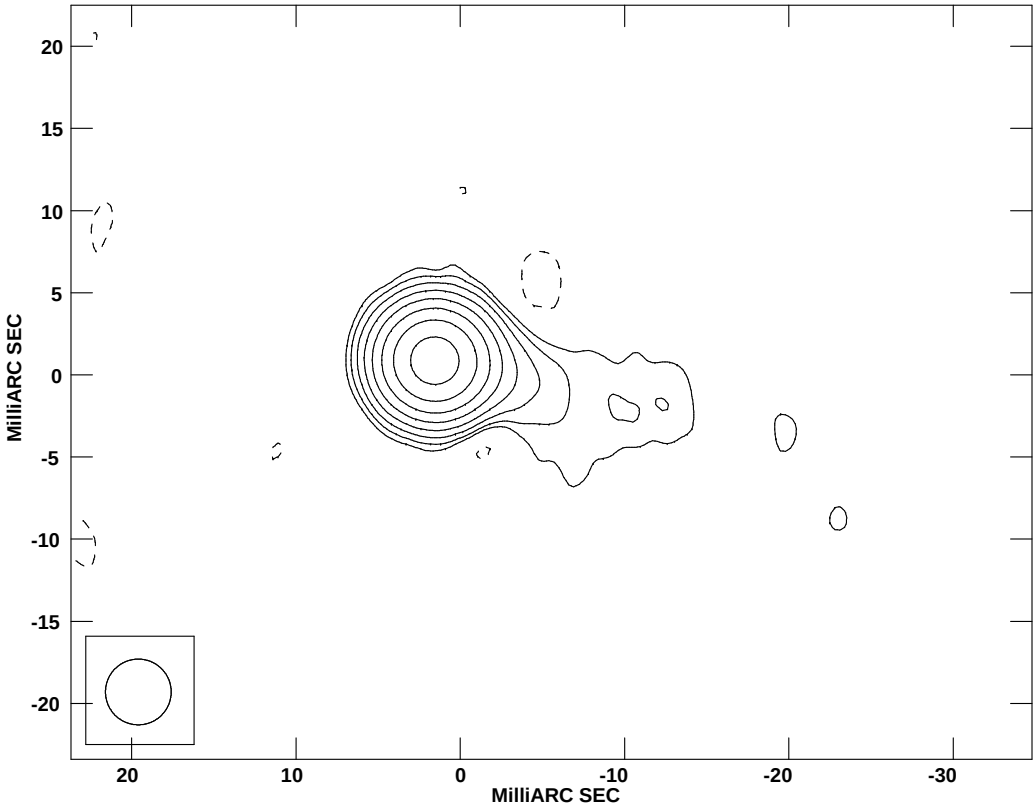

Figure 2.9: The 5 GHz VLBA tapered map of 4C 29.41, BCG of A1213. Contour levels are -0.2, 0.2, 0.4, 0.8, 1.6, 3.2, 6.4, 12.8 and 25.6. mJy/beam. The peak flux density is 36.7 mJy/beam, the noise level is 0.07 mJy/beam and the restoring beam is 4×4 mas^2, P.A. = 0 °.

2.3.11 IC 2738 in A1228.

This cluster is at z= 0.035. No cooling core has been detected (White et al. 1997). Its BCG is undetected in NVSS maps with a power LogP<21.14 (W/Hz). In our image, no detection is present at the 5σ level (0.65 mJy/beam).

2.3.12 IC 712 and IC 708 in Abell 1314.

This cluster is a binary cluster with two main condensations visible in the X-ray images (Fig. 2.10).

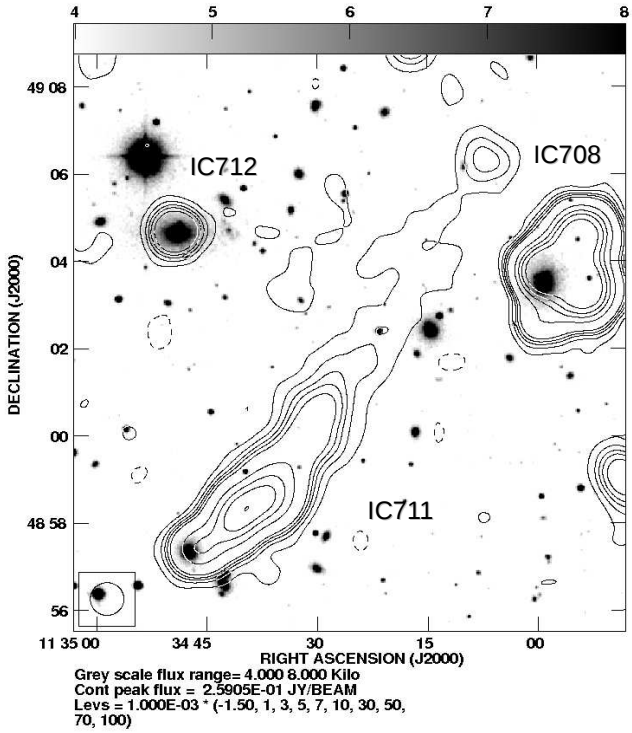

Figure 2.10: Optical image (gray scale) of the two BCGs of A1314 overimposed to radio image (contours map) from NVSS. IC 712 is the BCG of the main condensation and in the figure is the source on the top left. IC708 is the BCG of the second condensation and it is the source on the top right. The source in the middle is IC711, HT within A1314, one of the longest HT known (Vallè & Roger).

This cluster shows very clumpy, elongated X-ray emission, and a strong X-ray centroid shift (Bliton et al. 1998). This elongation is also present in the galaxy distribution, which shows a definite ellipticity, and is oriented mainly E-W (Flin et

al. 1995). IC 712 is the BCG of the main condensation and it shows a WAT structure with a very small linear size ($\sim$ 4.6 kpc) with a total flux density at 1.4 GHz of 26.3 mJy (Giovannini et al. 1994).

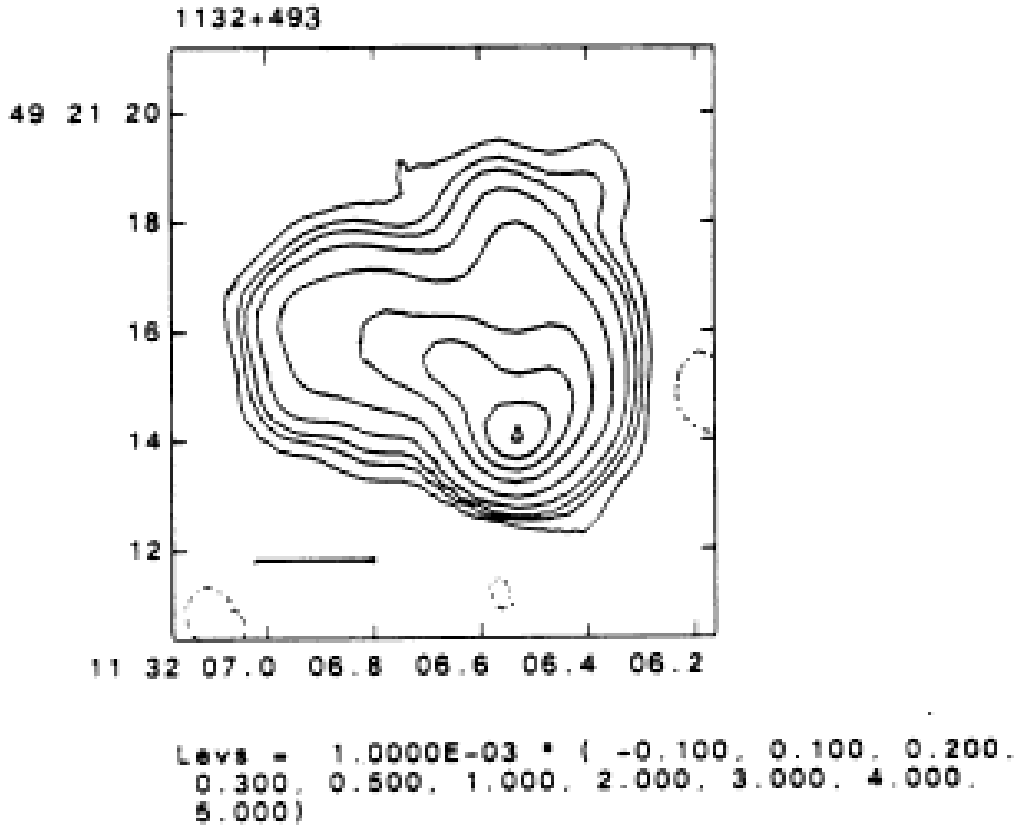

Figure 2.11: VLA image (Feretti & Giovannini 1994) of IC712 at 1.4 GHz. Coordinates are at 1950. The beam is 1.3 $\times$1.3 arcsec^2.

IC 708 is the BCG of the second condensation. It also shows (Fig. 2.12) a WAT structure (Vallee et al. 1979) with a larger size ($\sim$4.5 arcsec), total flux density at 1.4 GHZ $S_{1.4GHz,t}\sim$ 430 mJy and core flux density at 6 cm $S_{5GHz,core}\sim$110 mJy. In our maps, IC 712 is undetected at the 5σ level (<0.45 mJy/ beam). IC 708 (Fig.2.13) shows a one-sided structure with a core flux density S $\sim$38.8 mJy. The jet is aligned with the kiloparsec structure, has S$\sim$ 2.48 mJy and an extension of $\sim$ 16 mas from the core.

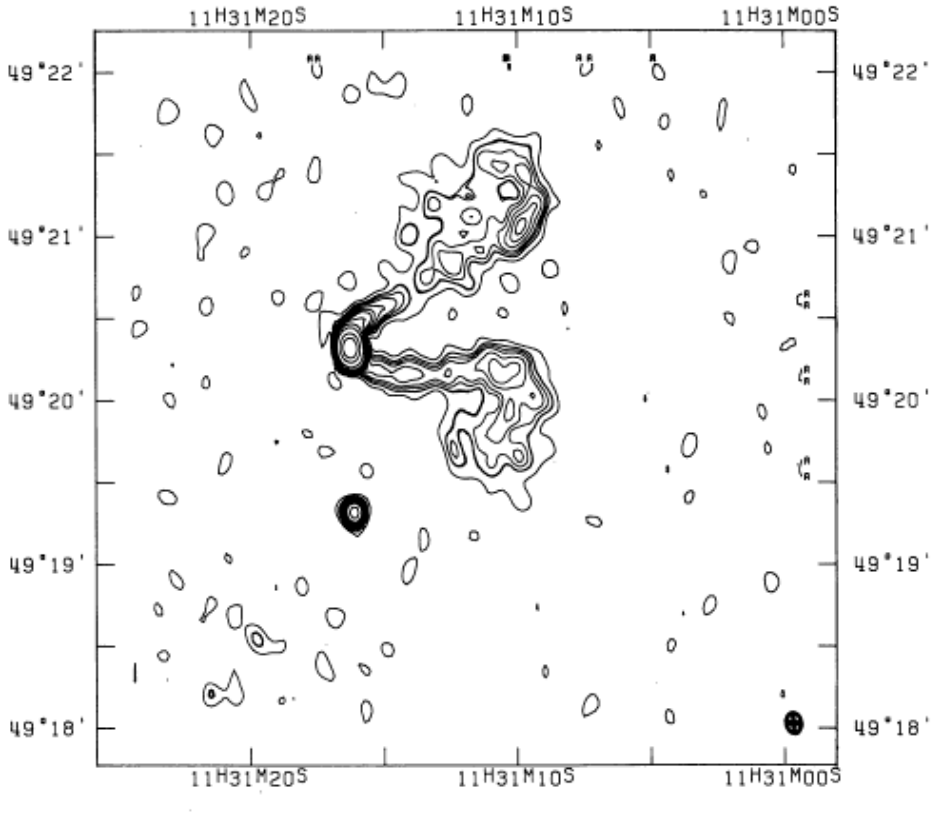

Figure 2.12: Radio image (Vallee et al. 1979) of IC708 obtained with the Westerbork telescope at 6 cm. The ellipse at the bottom right represents the resolution. Contour values are : 1, 2.15, 2.25, 3, 3.75, 5, 6.25, 7.5, 10, 15, 25, 50, 75 mJy/beam. Coordinates are at 1950.

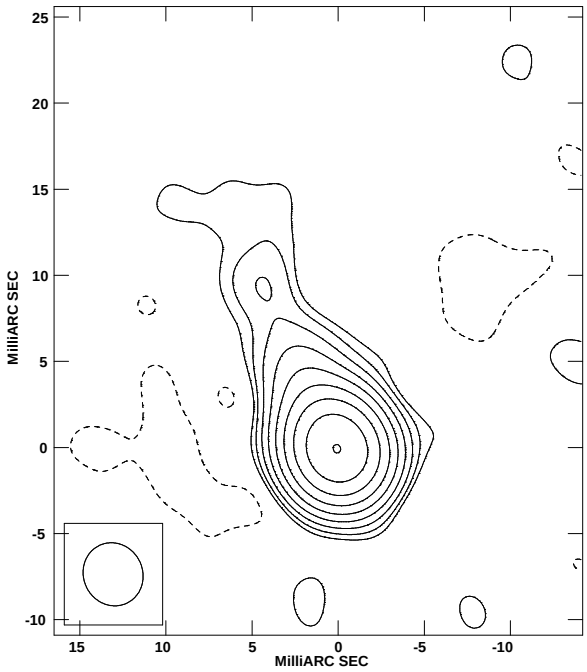

Figure 2.13: The 5 GHz VLBA tapered map of IC708, BCG of the second condensation of the binary cluster A1314. Contour levels are -0.15, 0.15, 0.3, 0.6, 1.2, 2.4, 4.8, 9.6, 19.2 and 38.4 mJy/beam . The peak flux density is 38.8 mJy/beam, the noise level is 0.05 mJy/beam and the restoring beam is 3.71 $\times$ 3.43 mas^2, P.A. = 25.4 °.

2.3.13 NGC3842 and 3C 264 in Abell 1367.

A 1367 is an X-ray-faint and nearby (z=0.0215) galaxy cluster. It has a secondary peak of the X-ray brightness (Donnelly et al. 1998) located approximately 19' offset from the primary brightness peak. This cluster is peculiar in the existence of extended trails of radio emission behind three irregular galaxies in its periphery (Gavazzi & Jaffe 1987). It is a complex cluster currently forming at the intersection of two filaments. NCG3842 and NGC 3862 are the two brightest cluster galaxies.

NGC3842 is a cD galaxy studied in radio band by Feretti & Giovannini (1994). From high resolution VLA radio images, NGC3842 shows a small size WAT structure with angular size of ∼55 arcsec and a flux density of 10.5 mJy corresponding to a total power at 1.4GHz $\mathrm{LogP}_{t,1.4GHz}$=21.72 W/Hz. In our images it appears undetected above 5σ (< 0.7 mJy/beam). NGC3862 is associated with the strong

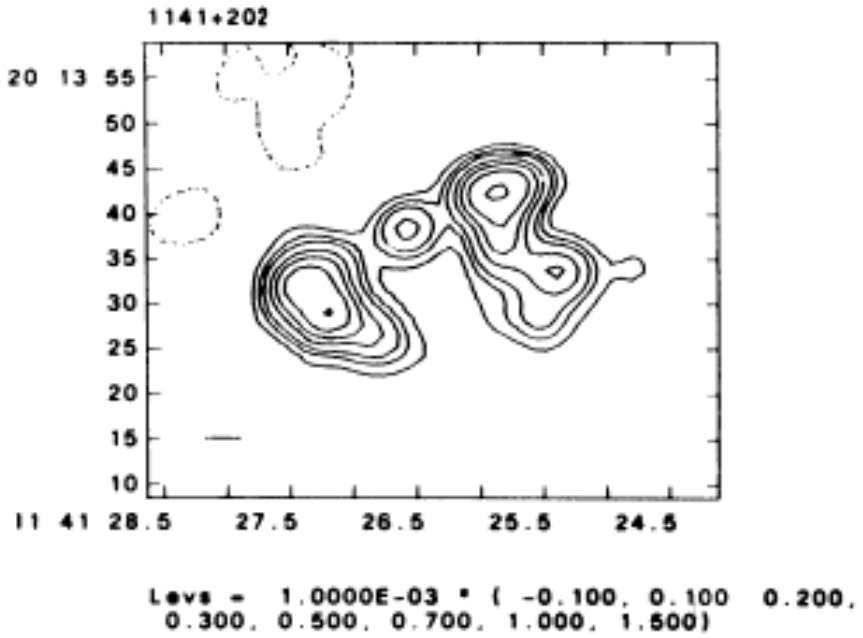

Figure 2.14: VLA image (Feretti & Giovannini 1994) of NGC3842 at 1.4 GHz. Coordinates are at 1950. The beam is 5 ×5 arcsec^2.

radio source 3C 264. In VLA images, it has a total power LogP=24.97 (W/Hz). 3C 264 has a head-tailed morphology at kiloparsec-scales (Fig. 2.15, a prominent core and a wiggling jet extending toward the northeast that ends in a blob of emission

at 28 arcsec (11.5 kpc) from the core (Lara et al. 1997).

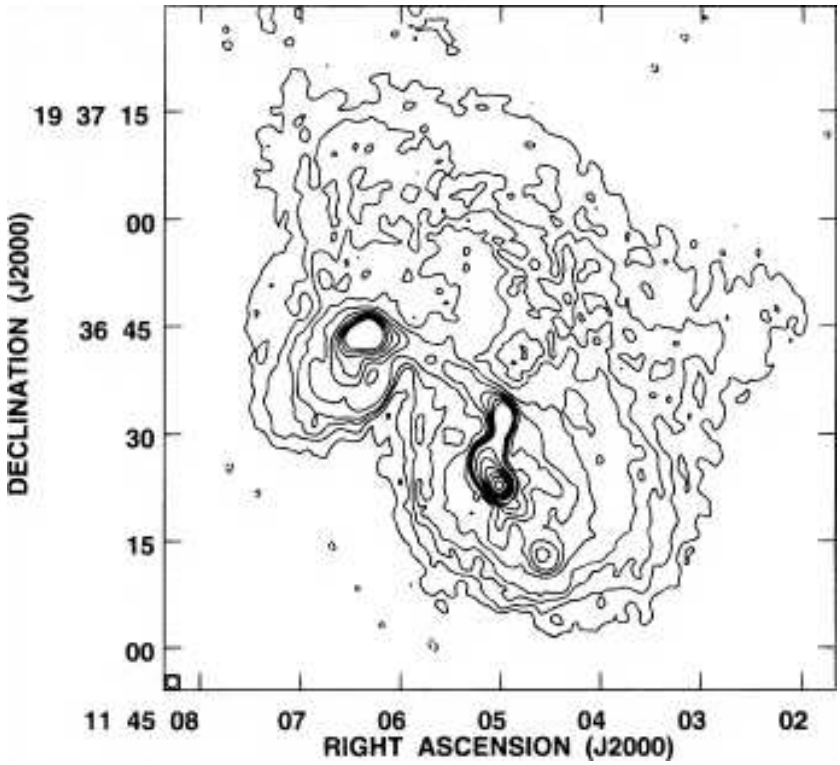

Figure 2.15: VLA image of 3C 264 at 5 GHz (Lara et al. 1997). The restoring beam is an elliptical Gaussian of 1.66″ ×1.61″ in P.A. = -53°. The peak flux density is 287 mJy/beam, and the contours are 2 × 10^4Jy/beam ×(-1, 1, 2, 3, 4, 6, 8, 10, 12, 14, 16, 32, 64, 128, 256, 512, 1024). The rms noise level is 0.06 mJy/beam.

There is evidence of counterjet emission in the southwest direction from the core. Both the jet and counterjet are embedded in a vast and diffuse region of low surface brightness emission which seems to have been dragged toward the north, possibly revealing the existence of a high density intracluster medium. Simultaneous EVN and MERLIN observations at 5.0 GHz by (Lara et al. 1999; Baum et al. 1997) showed for the first time the detailed structure of 3C 264 at sub-kiloparsec-scales. It consists of a one-sided jet with evident variations in its morphological properties with distance: i) the strong core and innermost jet (0-10 pc); ii) a well-collimated and narrow region (10-100 pc); iii) a region with strong widening, kinks and filaments (100-300 pc); iv) a faint and narrow region after a jet deflection (300-400 pc from the core). In particular, in the EVN map at 5 GHz (Lara et al. 1999), the source shows an unresolved core with a peak flux density $\sim$ 0.126 Jy/beam and a smooth one-sided jet extending up to 25 mas from the core along P.A.$\sim$27°.

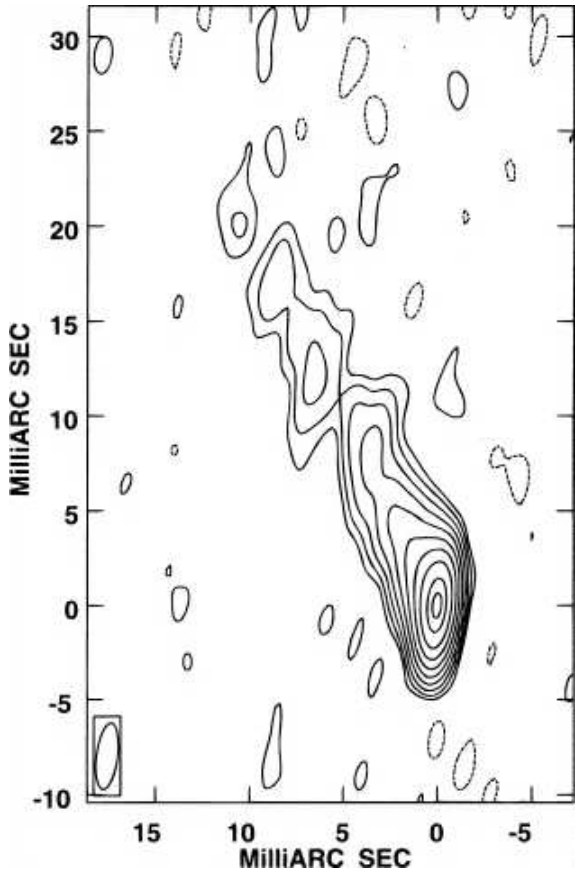

Figure 2.16: VLBI image of 3C 264 at 5 GHz (Lara et al. 1997). The restoring beam is 3.5 mas × 1.11 mas in P.A. = -7.3°. The peak flux density is 121 mJy/beam, and the contours are (-0.25, 0.25, 0.5, 1, 2, 4, 8, 16, 32, 64, and 90% of the peak. The rms noise level is 0.14 mJy/beam.

2.3.14 NGC4874 in Abell 1656.

This is one of the two dominant members of the Coma Cluster (Abell 1656) and considered the Coma BCG. It is a cD galaxy that shows a small size WAT structure. Arcsecond scale properties are discussed in Feretti & Giovannini (1987), where a possible precessing beam model is discussed. On kiloparsec-scales, it has a total flux density at 1.4 GHz of 190 mJy and the core flux density at 6 cm is 1.1 mJy. The radio emission is completely embedded in the optical galaxy. In fact, the radio linear size is 7 kpc.

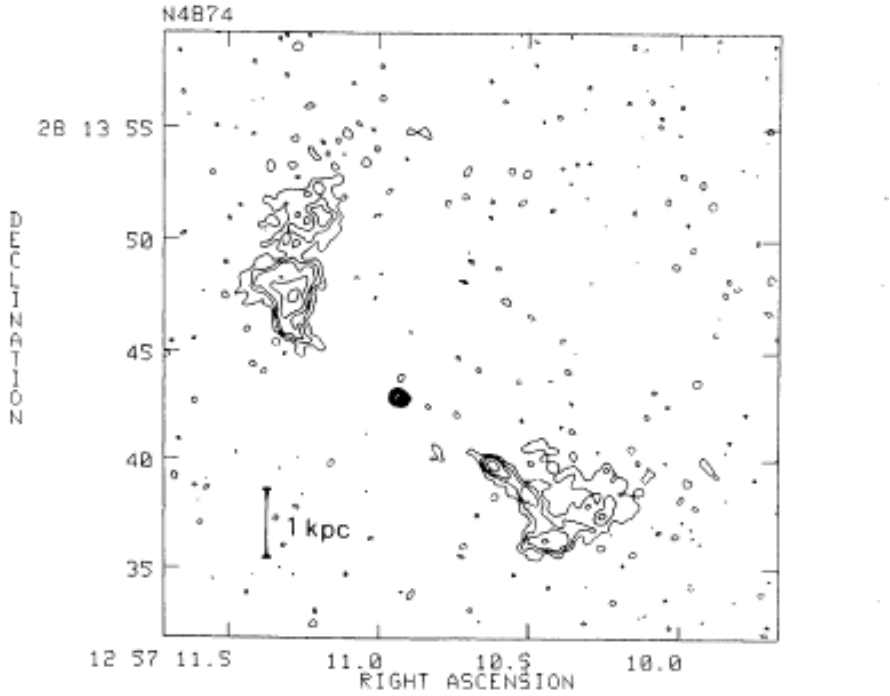

Figure 2.17: Full resolution VLA map (Feretti & Giovannini 1987) of total intensity at 6 cm. Contours level are :-0.1, 0.1, 0.2, 0.3, 0.5, 0.7, 1 mJy/beam. The linear scale is indicated.

In the VLA 1.4 GHz image, a gap of radio emission is present between the core and the SW lobe, while a faint jet connecting the core and the NE lobe is detected. At 5 GHz the jets are detected after gaps of ∼3 arcsec on both sides of the core.

In our VLBA image (Fig. 2.18), the source shows a one-sided structure with a total flux density of 10.1 mJy. The core flux density is 7.27 mJy. The jet has flux density ∼2.83 mJy and it is extended in direction SW (P.A.∼ - 15.4°) with an angular size of ∼ 3 mas.

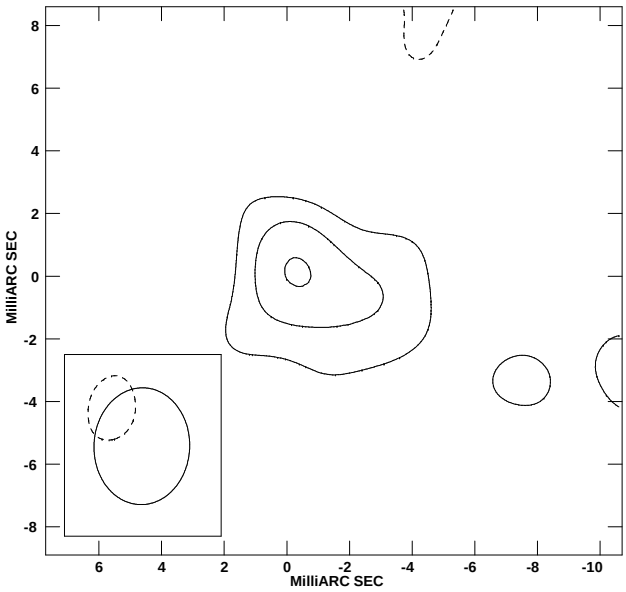

Figure 2.18: The 5 GHz VLBA tapered map of NGC4874, BCG of A1656. Contour levels are -0.24 0.24 0.48 and 0.76 mJy/beam. The peak flux density is 0.8 mJy/beam, the noise level is 0.08 mJy/beam and the restoring beam is 3.73 $\times$ 3.05 mas^2, P.A. = -2.1 $^\circ$.

2.3.15 UGC10143 in Abell 2147.

This cluster shows in the X-ray images, extended elongated emission suggestive of a merger. (Flin & Krywult 2006). The BCG is a cD galaxy with an elongated radio emission apparent in the NVSS image. In the high resolution image from FIRST, it shows a WAT morphology with angular size ∼20 arcsec and total flux density ∼8.03 mJy. At mas scale, we did not detect a radio source: the 5σ limit is < 0.6 mJy/beam.

NGC 6041A and NGC 6047 in Abell 2151. This Abell cluster is also known as the Hercules cluster. It is a highly structured cluster despite an apparently regular velocity distribution of the main field. This cluster should be considered as an ongoing cluster merging (Girardi et al. 1997). This cluster shows two peaks in the X-ray emission (Bird et al. 1995). There is only marginal evidence of soft excess emission in the brightest of the two peaks (Bonamente et al. 2002).

NGC 6041A is the BCG of the first main condensation while NGC 6047 is the brightest galaxy of the second condensation. In the NVSS image, NGC 6041A shows a WAT structure with angular size ∼2.5 arcmin and total flux density ∼ 11.6 mJy. In our VLBA map, it appears unresolved with a total flux density ∼7.83 mJy.

NGC 6047 is classified as an E/S0 and it has a bizarre optical morphology which suggests that it may be a recent merger which has so severely disrupted the dynamics of an HI disk that the gas has lost its kinematic coherence (Dickey 1997). At kiloparsec-scale, NGC 6047 shows an extended FRI structure with a two-sided jet emission (Feretti & Giovannini 1988).

The northern jet is brighter (flux density at 5 GHz ∼13.6 mJy) and more collimated. The total flux density at 1.4 GHz is ∼ 728 mJy and the core flux density at 5 GHz is ∼8.3 mJy. In our maps, it appears undetected above $5\sigma = 0.55$ mJy/beam.

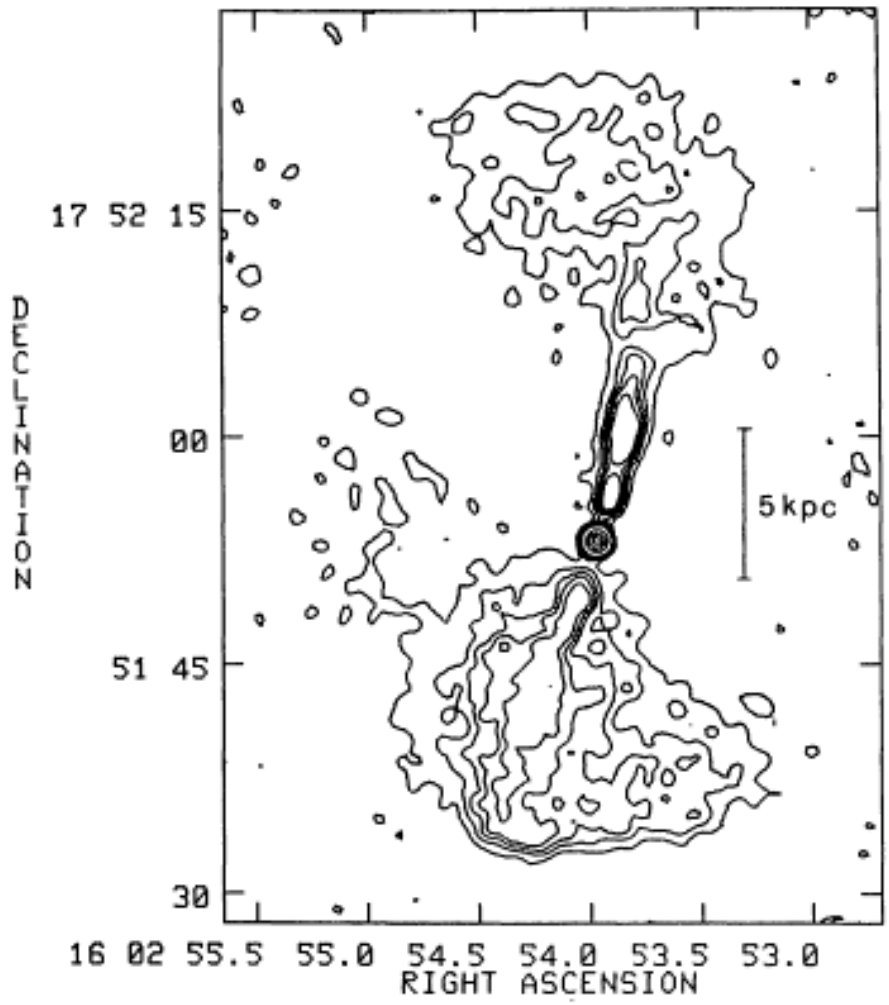

Figure 2.19: Full resolution VLA map of total intensity (Feretti & Giovannini 1988) of NGC6047 at 6 cm. Contour levels are 0.1, 0.3, 0.5, 0.7, 1, 3, 5, 7 mJy/beam. The linear scale is indicated. Coordinates are at 1950.

2.3.16 UGC10187 in A2152.

A2152 is one of the major condensations in the Hercules supercluster together with A2147 and A2151. Its BCG is UGC10187, which is also the brightest of a galaxy pair. In the NVSS this BCG shows an extended ($\sim$ 4 arcmin in NVSS) tailed radio structure with total flux density $\sim$60.3 mJy. In the FIRST image, a gap of $\sim$5 arcsec between the two tails is present and the nuclear source is not visible. In our VLBI image, no detection was found with a 5σ limit < 0.55 mJy/beam.

2.3.17 NGC6086 in Abell 2162.

This Abell cluster is a low X-ray luminosity cluster (Burns et al. 1994). Its BCG is a bright cD galaxy which hosts a double-lobed radio source. In the NVSS image, the total flux density is $\sim$108.7 mJy and its angular size is $\sim$ 3.5 arcmin. In the FIRST image, the radio emission is partly resolved out (only $\sim$60 mJy) and extended over $\sim$2.5 arcmin. No defined structure is observable. The radio spectrum and morphology suggest that it is a relic galaxy where the core radio activity stopped some time ago. Our VLBA observations did not detect a radio source to a 5σ limit of $<$0.55 mJy.

2.3.18 NGC6173 in A2197.

This cluster is one of a few clusters which show an unusual systematic alignment among individual cluster members and it is possible that is linked with A2199 via supercluster structure to the Hercules region (Gregory & Thompson 1984).

The BCG shows mJy level emission ($\sim$7 mJy) unresolved in FIRST images. At mas scale, it appears (Fig. 2.20) one-sided with a total flux density in our VLBA maps of 3.24 mJy. In particular, the core has a flux density of 1.87 mJy and the jet is extended to the east with an angular size $\sim$ 10 mas and flux density $\sim$ 1.37 mJy.

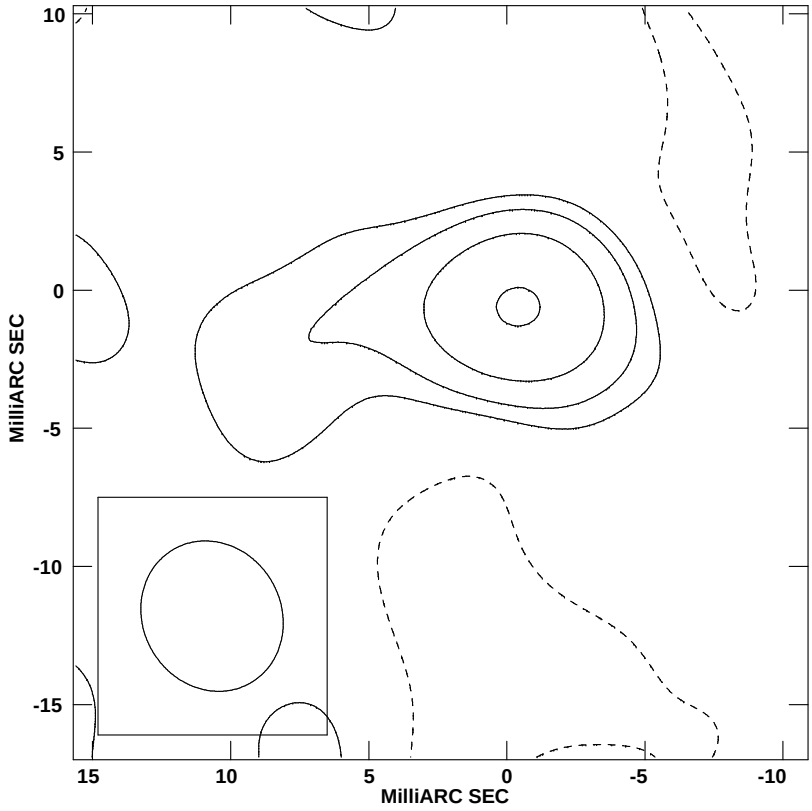

Figure 2.20: The 5 GHz VLBA tapered map of NGC6173, BCG of A2197. Contour levels are -0.19 0.19 0.38 0.76 and 1.52 mJy/beam. The peak flux density is 1.6 mJy/beam, the noise level is 0.06 mJy/beam and the restoring beam is 5.58 $\times$ 5.0 mas^2, P.A. = 30 °.

2.3.19 3C 338 in Abell 2199.

A2199 (z = 0.0304) has a prototypical cooling core. In fact, a Chandra observation of this cluster has detected a point-like source coinciding with the center of the galaxy NGC 6166 (Di Matteo et al. 2001) that is a multiple nuclei cD galaxy. This galaxy hosts the relatively powerful radio source 3C 338, which emits a total power at 330 MHz of LogP∼25.64 W/Hz. This radio source has been known for a few decades to have an unusual structure on both large and small scales (Feretti et al. 1993; Giovannini et al. 1998). It is classified as a FR I radio source and shows central optical [O III] line emission (Fisher et al. 1995).

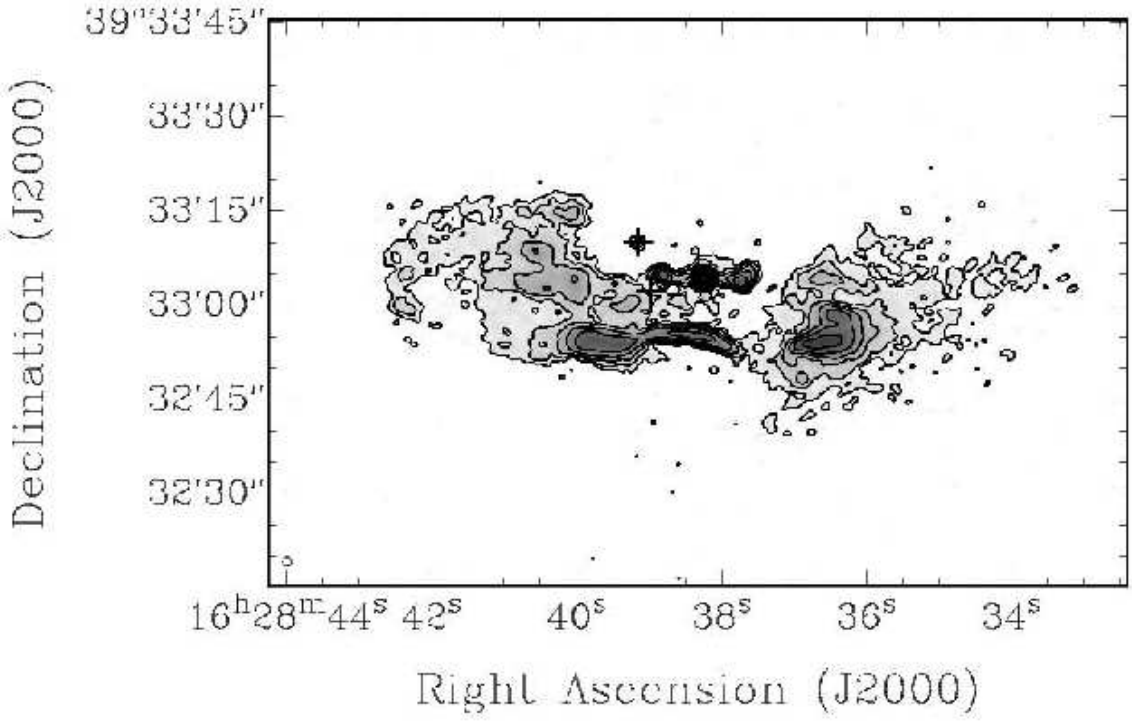

Figure 2.21: Contours of the 8.4 GHz map (Gentile et al. 2007) of 3C 338 from the VLA A, B, BnC, and C configurations at 1.4″ resolution. The synthesized beam is shown in the bottom left corner. Contours levels are 32 (4 σ), 64, 128, 256, ... μJy/beam.

On kiloparsec-scales, 3C 338 (Fig. 2.21) has two symmetric extended radio lobes, characterized by a steep spectrum ($\alpha \sim$ - 1.7) and misaligned with the central emission. The two radio lobes are connected by a bright filamentary structure. Polarimetric observations by Ge & Owen (1994) revealed strong rotation measure gradients across most of the extended emission and inferred the presence of cluster magnetic fields. Both the steep radio spectrum and strong filamentary emission

may be the result of interactions with the dense intracluster medium (Gentile et al. 2007).

On parsec-scales, 3C 338 has a compact radio core with two short (∼10 pc), symmetric jets. In VLBA maps at 5 GHz (Feretti et al. 1993), the parsec-scale structure shows a central dominant feature (the core emission) with flux density ∼ 92 mJy/beam and two symmetric jets. The total flux density is 133 mJy.

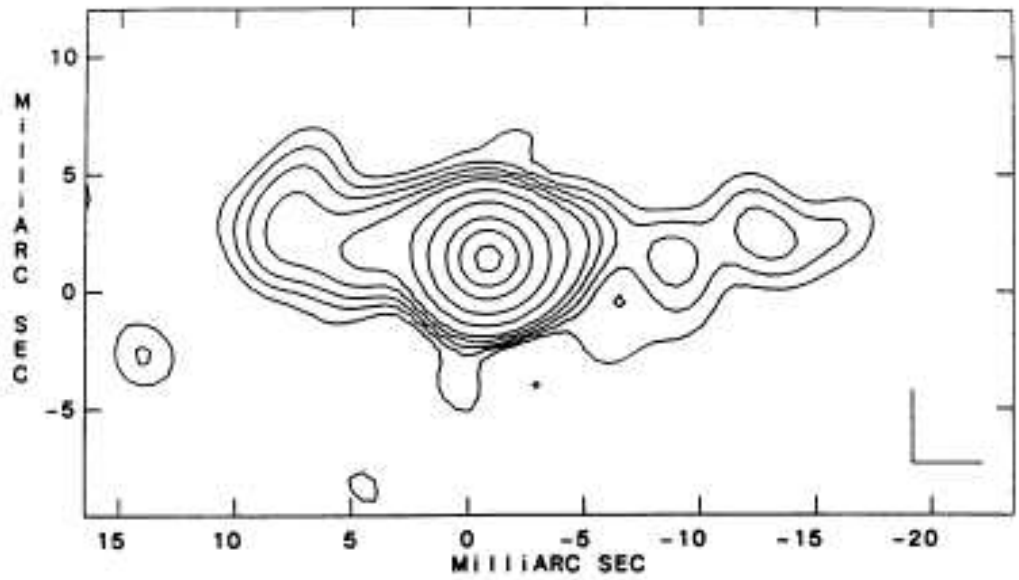

Figure 2.22: VLBI contour map of 3C338 at 5 GHz (Feretti et al. 1993) at the resolution OF 3.2 mas,. The rms noise is 0.4 mJy/beam. Contours are -1.2, 1.2, 1.8, 2.5, 3.5, 5, 10, 20, 40, 60, 80 mJy/beam. Coordinates are at 1950.

The eastern jet shows a couple of low-brightness regions in its center suggesting it could be limb-brightened. The orientation of this structure appears to be very constant in time despite the complex dynamic conditions present in the 3C 338 central regions. Comparing maps obtained at different epochs (Gentile et al. 2007), a change in the parsec-scale morphology is clearly evident, and it is probably correlated with the arcsecond core flux density variability. The structural changes suggest the presence of proper motion with $\beta\sim0.4$ h^{-1} on both sides of the core (Gentile et al. 2007). These properties suggest that the extended emission in 3C 338 is a relic structure not related to the present nuclear activity (Giovannini et al. 1998).

2.3.20 3C 465 in Abell 2634.

A2634 (z=0.0322) does not show evidence of a cooling core. Its BCG is 3C 465 that is associated with the giant D galaxy NGC 7720. The optical host galaxy exhibits distorted isophotes with two gravitationally bound nuclei surrounded by a common envelope (Venturi et al. 1995). Weak broad H_α and high-ionization emission-lines suggest the presence of faint activity in the optical nucleus. In the radio band, this source has a WAT morphology (Fig. 2.23). Its total power at 408 MHz is LogP=25.3.

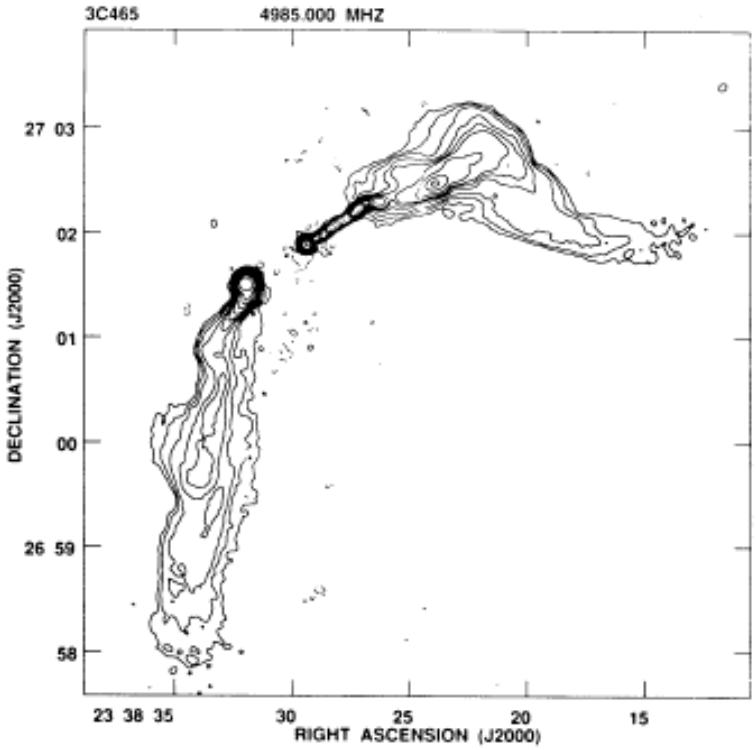

Figure 2.23: 5 GHz VLA C array total intensity map of 3C 465 (Venturi et al. 1995). The peak flux is 242 mJy/beam. Contour levels are -0.2, 0.2, 0.5, 1., 2, 3, 4, 6, 10, 15, 20, 30, 50, 100 and 200 mJy/beam. The restoring beam is 3.87 ×3. 54 arcsec^2 in P.A. = -80.7°. The noise in the map is 0.05 mJy/beam.

The radio jet, the spots and the low-brightness tails are strongly polarized. On parsec-scales the source is one-sided with the jet on the same side as the main kiloparsec-scale structure. At 5 GHz, from VLBA data (Venturi et al. 1995), the core flux density is 168 mJy and the total flux density is 237 mJy (Fig. 2.24).

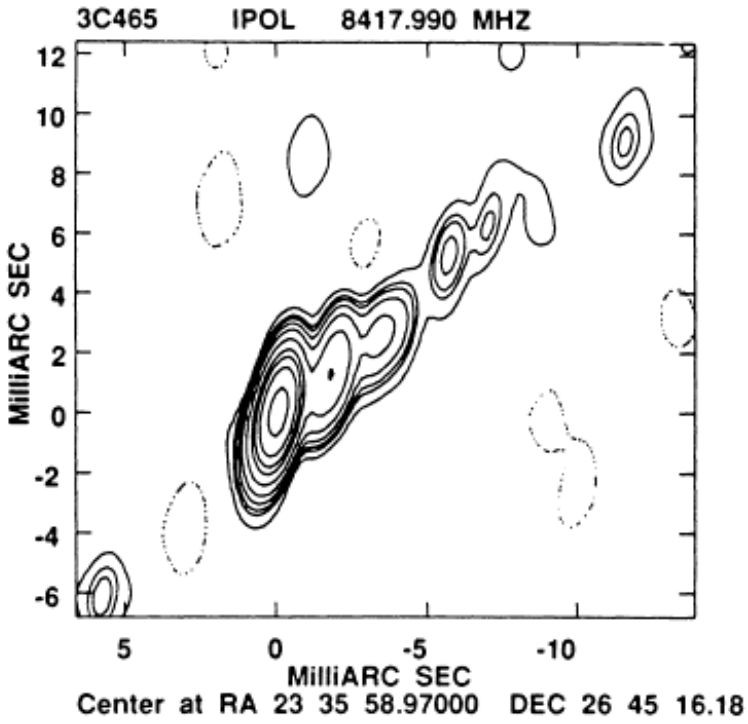

Figure 2.24: Contour plot of 3C 465 on VLBI scale at 8.4 GHz. The peak flux is 132 mJy/beam. Contour levels are -0.75, 0.75, 1.5, 2, 3, 5, 10, 20, 30, 50 and 100 mJy/beam. The restoring beam is 2.52 $\times$0.87 arcsec^2 in P.A. = -9.7°. The noise in the map is 0.35 mJy/beam.

2.3.21 NGC7768 in Abell 2666.

Scodeggio et al. (1995) did not find any evidence of substructures in the central cluster region. Its BCG is a cD galaxy in the center of the cluster. It contains a dusty nuclear disk approximately aligned with the major axis of the galaxy (Grillmair et al. 1994) and radio emission at the mJy level ($\sim$2 mJy that corresponds to LogP=21.50 W/Hz).

In our VLBA data (Fig. 2.25), it shows a one sided structure with a core flux density S $\sim$0.72 mJy and total flux density $\sim$1.31 mJy. The jet is oriented in direction NW-SE, it has $S \sim 0.59$ mJy and an extension of ~ 4 mas from the core.

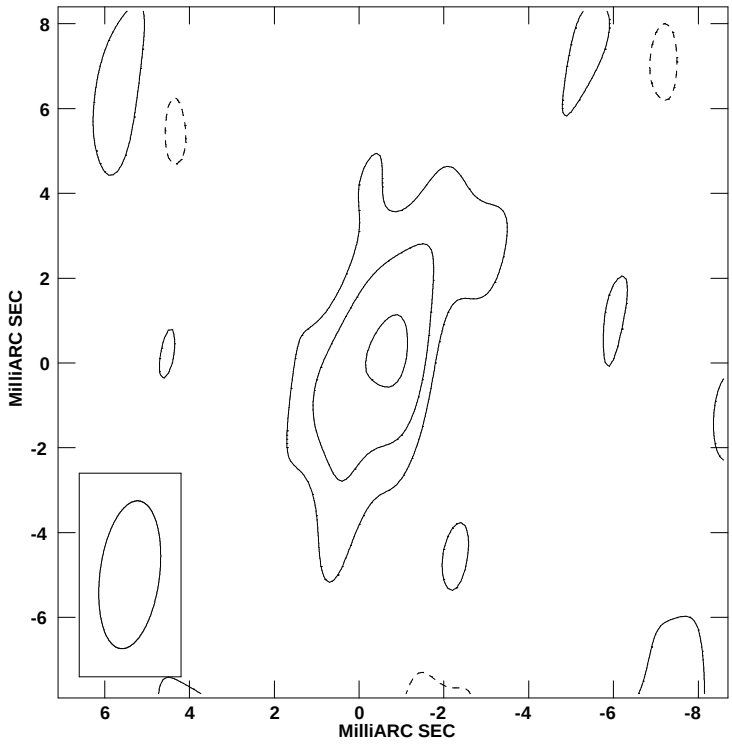

Figure 2.25: The 5 GHz VLBA naturally weighting map of NGC7768, BCG of A2666. Contour levels are -0.17 0.17 0.34 and 0.64 mJy/beam. The peak flux density is 0.72 mJy/beam, the noise level is 0.09 mJy/beam and the restoring beam is 3.51 $\times$ 1.40 mas^2, P.A. = -7.15 °.

2.4 Parsec-scale morphology.

Our complete sample is composed of 27 BCGs, 23 have been observed for the first time with VLBA by us and for the remaining objects radio information at mas scale are available from literature.

Table 2.3 presents parsec-scale and arcsecond radio properties for all our BCGs (complete sample and extended sample, see 2.6).

We give the name of the BCG (col.1), the parsec-scale morphology (col.2 : core (c), one sided (1s) or two sided (2s) jet structure), the jet/counterjet surface brightness ratio (see Appendix) (col.3), $\beta \mathrm{co}\theta$ (col.4), the arcsecond core flux density $S_{c,5}$ at 5 Ghz (col.5), the arcsecond core power $\mathrm{LogP}_{c,5}$ at 5 GHz (col.6), the total arcsecond flux density $S_{t,408}$ (col.7) and the total arcsecond power $\mathrm{LogP}_{t,408}$ (col.8) at 408 MHz, the total VLBI flux density and arcsecond core flux density ratio $S_{VLBI}/S_{c,5}$ at 5 GHz (col. 9), the core dominance (see section 5.2 and Appendix) (col.10). The last column is for the notes. In particular: $S_{t,408}$: 1) From NVSS with α ∼0.5, 2) from Parma et al. (1991) with α ∼0.5; 3) from Pedlar et al. (1990) where α ∼0.5, 4) from Bondi et al. (1993), 5) from Feretti & Giovannini (1985), 6) from Owen & Ledlow (1997) with $\alpha \sim 0.5$, 7) from Vallee et al. (1979) where α ∼0.6, 8) from Feretti & Giovannini (1994), 9) from Giovannini et al. (2001) and NED information with α ∼0.5, 10) from Feretti & Giovannini (1987) with α ∼0.5, 11) from Owen & Ledlow (1997), 12)from Taylor et al. (2002) and NED information, 13) from Venturi et al. (1995),), 14) from Taylor et al. (1990); Taylor (1996), 15) from Liuzzo et al. (2009a), 16) from Venturi et al. (2004), 17) from Augusto et al. (2006) and from NED with α ∼0.5 (408 MHz) and α ∼0 (5 GHz), 18) from Taylor et al. (1999) and NED information and 19) from Taylor et al. (2006) assuming α=0.5. S_c is for the arcsecond core flux density at 5 GHz and S_{VLBI} is a correlated flux density at 5 GHz in our VLBI data.

2.4.1 Two-sided morphology.

In our sample, two sources, 3C 84 and 3C 338, show two-sided structure. For both radio sources, the most supported explanation suggests that their properties can be explained if they consist of two oppositely directed, symmetric, and mildly relativistic jets at a modest angle to the line of sight (Walker et al. (1994); Dhawan et al. (1998) for 3C 84 and Giovannini et al. (1998); Gentile et al. (2007) for 3C 338).

Both 3C 84 and 3C 338 lie at the center of cool core clusters. The Perseus cluster, Abell 426, in particular is the most X-ray luminous cluster in the nearby universe, and the prototypical 'cooling core' cluster. Moreover, these two sources show evidence of a restarted activity. In 3C 338 there is evidence of restarted radio activity with an extended relic emission and a small-scale young structures (Giovannini et al. 1998). Features suggesting the recurrent jet activity of the central engine are present also in 3C 84. At low resolution (frequencies below 5 GHz), the southern jet extends continuously from the core out to ∼100 mas (Taylor 1996), indicating that 3C 84 had previous outbursts. Also, there are multiple lobe-like structures at arcminute scale (Pedlar et al. 1990). Moreover, the synchrotron age of inner lobe (Nagai et al. 2009) and the observed inner proper motions (Asada et al. 2009) is consistent with the scenario that the inner lobe formed by the 1959 outburst (Nesterov et al. 1995).

As discussed in previous section 3C 84 appears one-sided at 86 GHz in the inner 2.5-3 mas ($\leq$ 1 pc) and symmetric (two sided) at $\sim$ 4-5 mas ($\geq$1.5 pc) from the core as evident in the 22 GHz images by Taylor et al. (2006). The jet/counterjet ratio is >35 at 43 GHz at 0.5 mas (∼0.15 pc) and ∼1 at 5 mas (∼1.5 pc) suggesting a strong jet deceleration. This result cannot be due to free-free absorption effect (Walker et al. 2000) since the one sidedness is visible in the high resolution high frequency image. We note that a similar structure can be detected only here because of the good linear resolution due to the low redshift of 3C 84.

2.4.2 One-sided morphology.

In our complete sample 12 BCGs show one-sided parsec-scale structures. The percentage (45%) is in agreement with the percentage of one-sided FRI radio galaxies found in a complete sample of radio galaxies (Liuzzo et al. 2009b): 23/51 (45%). We note that all 12 BCGs lie in non-cool core clusters.

The values of the jet/counter-jet ratios for the sources of our complete sample are given in Table 3. We used these values together with the core dominance information to estimate the angle and jet velocity (Giovannini et al. 2001). Results are uncertain but consistent with an asymmetry because of Doppler boosting effects.

Moreover, we note that in all resolved BCG sample sources the parsec scale jet is aligned with the arcsecond structure indicating that no complex strong change in

the angular momentum of the accreted gas, and no restarted activity with different inclination of the accretion disk and or central BH precession occur.

Table 2.3: **Parameters for BCGs (see the text).**

BCG	Cluster structure	pc ratio	j/cj	$\beta\cos\theta$ mJy	$S_{c,5}$ W/Hz	$LogP_{c,5}$ mJy	$S_{t,408}$ W/Hz	$LoP_{t,408}$ $S_{c,5GHz}(\%)$	S_{VLBI}/ dominance	core	notes
NGC708	A262	c	-	-	5	21.47	364	23.33	60	0.26	5
NGC910	A347	n.d.	-	2	-	-	-	-	<25	-	5
3C75A	A400	1s	≥6.2	≥0.35	6	21.87	190	23.37	100	0.60	1
3C75B	A400	1s	≥ 4.6	≥0.3	20	22.39	190	23.37	100	2	1
3C84	A426	2s	2	0.14	28.17×10^3	25.29	51.68×10^3	25.56	80	70.79	2
UGC3274	A539	n.d.	-	-	<1.4	-	-	-	-	-	5
UGC2489	A407	1s	≥2.8	≥0.2	4	22.32	2.83×10^3	25.17	90	0.13	3
NGC2329	A569	1s	≥4.5	≥0.29	160	23.14	1300	24.05	50	4.3	4
CGCG261-059	A576	1s	≥1.8	≥0.12	1.5	21.71	6.54	22.34	100	1.8	5
NGC2832	A779	n.d.	-	-	2.4	-	-	-	<21	-	5
NGC3550	A1185	n.d.	-	-	<1.4	-	-	-	-	-	5
4C29.41	A1213	1s	≥3.8	≥0.26	41	23.33	135.2	23.84	100	8.71	6

Table 2.3 continued

BCG	Cluster structure	pc ratio	j/cj	$\beta\cos\theta$ mJy	$S_{c,5}$ W/Hz	$LogP_{c,5}$ mJy	$S_{t,408}$ W/Hz	$LoP_{t,408}$ $S_{c,5GHz}(\%)$	S_{VLBI}/ dominance	core	notes
IC2738	A1228	n.d.	-	-	-	-	-	-	-	-	5
IC708	A1314	1s	$\geq$6.5	$\geq$0.36	110	23.47	901.1	24.39	40	5.62	7
IC712	A1314	n.d.	-	-	14.02	22.58	48.72	23.12	<3	4.37	11
NGC3842	A1367	n.d.	-	-	9	22.98	101.88	23.03	<8	0.36	11
3C264	A1367	1s	$\geq$6	$\geq$0.34	200	23.32	17×10^3	25.25	100	1.17	8
NGC4874	A1656	1s	$\geq$1.6	$\geq$0.09	1.1	21.13	351.96	23.63	100	0.08	9
UGC10143	n.d.	-	-	<2	<21.77	14.87	22.64	-	<1.35	5	
NGC6041A	A2151	c	-	-	$\leq$0.9	$\leq$21.92	21.5	22.84	100	1.45	5
NGC6047	A2151	n.d.	-	-	8.3	22.42	1960	24.80	<7	0.28	12
UGC10187	A2152	n.d.	-	-	<2	<21.81	111.7	23.56	-	<0.41	5
NGC6086	A2162	n.d.	-	-	<1	<21.37	201.35	23.68	-	<0.12	5
NGC6173	A2197	1s	$\geq$1.4	$\geq$0.07	3.7	21.89	12.97	22.44	40	2.40	5

Table 2.3 continued

BCG	Cluster structure	pc ratio	j/cj	$\beta\cos\theta$ mJy	$S_{c,5}$ W/Hz	$LogP_{c,5}$ mJy	$S_{t,408}$ W/Hz	$LoP_{t,408}$ $S_{c,5GHz}(\%)$	S_{VLBI}/ dominance	core	notes
3C338	A2199	2s	2.2	0.16	480	24.01	18.12×10^3	25.59	30	3.47	10
3C465	A2634	1s	$\geq$20	$\geq$0.54	246	23.74	10.38×10^3	25.37	100	2.57	8
NGC7768	A2666	1s	$\geq$1.1	$\geq$0.02	0.74	21.08	2.6	21.62	100	1.17	5
B2 0836+29II	A690	1s	$\geq$20	$\geq$0.54	131	24.31	1139	25.24	100	11.20	13
Hydra A	A780	2s	1.2	0.04	168	24.08	132×10^3	26.98	100	0.58	14
4C 26.42	A1795	2s	1.4	0.07	53	23.71	3153	25.48	80	2.04	15
3C 317	A2052	2s	1.5	0.08	310	23.93	132×10^3	26.56	100	0.72	16
B2151+174	A2390	2s	4	0.27	164	25.40	538	25.92	100	53	17
PKS 2322-123	A2597	2s	1.2	0.04	59.3	24.0	7.2×10^3	26.11	80	1.66	18
PKS 1246-410	A3526	1s	$\geq$9	0.34	64.4	22.27	2463	23.86	30	0.76	19

2.4.3 Unresolved sources.

At milliarcsecond resolution, two radio sources of our complete sample appear unresolved: NGC708 in the cooling cluster A262 and NGC6041A in the merging cluster A2151. We note that, for NGC 708, the core dominance, defined as the ratio between the observed and the estimated core radio power according to the relation given in Giovannini et al. (2001) (see also Liuzzo et al. (2009b)) is very low (0.25) suggesting that the nuclear activity is in a low phase and it is for this reason that the jets are not visible. NGC6041A is a faint source (LogP $\sim$22.57 (W/Hz) at 1.4 GHz) and the parsec-scale jets -if any- are probably too weak to be detected with the present sensitivity.

2.4.4 Undetected sources.

In our new VLBA observations, 11 BCGs are undetected below 5σ. This percentage is high but still significantly lower that in non-BCG ellipticals. The nature of the undetected BCGs is varied and they can be grouped as follows:

- radio quiet sources (5/11): this is the case for UGC3274, NGC2832, NGC3550, IC2738 and NGC910 that do not show any radio emission at arcsecond resolution;

- radioquiet core (4/11) in a radio galaxy: in these sources the central AGN was active in the past, but is radio quiet at the time of observations. This is the case for NGC6086, a candidate relic radio galaxy, for the WAT NGC3842 where the arcsecond core is very faint ($\sim$0.26 mJy), for UGC10143 and for UGC10187 where the nuclear source is not detected by the VLA radio images. As expected in these sources the core dominance is low;

- peculiar sources (2/11): NCG 6047 and IC712. In VLA maps, these sources show radio emission from the core but they appear undetected in our VLBA maps. This could be due to an extreme variability of the core emission. Alternatively, these sources could have a complex structure on scales between these allowed by VLBA and VLA with a pc scale low surface brightness that we are not able to map with our VLBA data. In these cases, more sensitive VLBA observations, EVLA observations at high frequencies, or e-Merlin observations will be important to properly study these structures.

2.5 Statistical considerations for the complete sample.

Here, we report some statistical results for our complete sample of BCGs.

- The detection rate of our new VLBA observations is 52% and, adding literature parsec-scale information of the well studied radiosources, the total detection rate at mas resolution of our complete sample is 59%(16/27). In particular, 45%(12/27) are one-sided, 7%(2/27) have a two-sided morphology, 7%(2/27) show point-like structure, and 41%(11/27) are undetected.

- We note that in our complete sample we have 23 clusters of galaxies, and only 5 of them (22%) have been defined cooling core clusters. This percentage is lower than values found in literature: e.g. Hudson et al. (2009) found that 44% of galaxy clusters have strong cool cores. However we note that their statistic is based on X-ray flux limited samples, while our sample has no selection effects on the X-ray luminosity. If we apply the same constraints of Hudson et al. (2009) to our sample we will have only 9 clusters, and 3 of them (33%) with a strong cool core, in agreement (note the small numbers) with literature data.

- We compare the total flux at VLBA scales with the core arcsecond flux density (Tab. 3). Over all data, among 16 detected sources, we find that 11/16 (70%) have a correlated flux density larger than 80% of the arcsecond flux density. This means that in these sources we imaged most of the mas scale structure and so we can properly connect the parsec to the kiloparsec structures. In contrast, for 5/16 (30%), a significant fraction of the arcsecond core flux density is missing in the VLBA images. This suggests variability or the presence of significant structures between $\sim$ 10 mas and 1 arcsecond that the VLBA can miss due to the lack of short baselines. To properly study these structures, future observations with the EVLA at high frequency or with the e-MERLIN array will be necessary.

- We derive the distribution of the total radio luminosities at 1.4 GHz obtained from NVSS (Condon et al. 1998) and FIRST (Becker et al. 1995) and the RLF (Radio Luminosity Function) of the radio loud sources in our complete sample. We compare our sample properties with the results of Best et al. (2007) for their complete sample of BCGs. Because of the lack of spectroscopic information of

our BCGs, we are not able to distinguish between radio emission due to star formation and due to AGN activity. Following Best et al. (2007), we compared only sources with LogL≥22.3 and we assumed that the detected radio emission of our BCGs is from central AGN. We found that in our complete sample the probability of BCGs to be radio loud with LogL≥22.3 is ∼87%. This is consistent with the results of Best et al. (2007). We consider this result as evidence that our small sample is representative of the general properties of BCGs.

- Among the sources of our complete sample, there are two cases, 3C 84 and 3C 338, where there is evidence for restarted activity in the radio emission associated with the BCG. Both 3C 84 and 3C 338 lie in Abell clusters that show a presence of a cool core.

  In the case of 3C 84, Nagai et al. (2009) and Agudo et al. (2005) used multifrequency VLBA observations to constrain the timescale of the restarted activity. In particular, Agudo et al. (2005) derived a kinematic age and Nagai et al. (2009) estimated the synchrotron age of the radiosource. Both authors found a resulting age which is consistent with the scenario that the inner ∼15 mas feature is formed by the recent outburst in 1959. At low frequencies, the southern jet extends continuously from the core out to ∼ 100 mas, suggesting that 3C 84 has had multiples outbursts. Also there are multiple lobe-like structures at arcminute scales that suggest a recurrent jet activity of the central engine.

  For 3C 338, due to the peculiar morphology and arcsecond core flux variability, Giovannini et al. (1998) suggest that the extended emission is older and unrelated to the present nuclear activity (see also Gentile et al. (2007)).

- Looking at the kiloparsec morphologies of our BCG sources, a well known literature results are confirmed. WAT sources are found in non cool core clusters. In fact, it has been argued that cluster mergers can produce the ICM ram pressure necessary to shape WAT sources (Burns et al. 1994; Pinkney 1995; Gomez et al. 1997; Sakelliou & Merrifield 2000). Moreover, elongations of a cluster's X-ray emission along the line that bisects the WAT (Gomez et al. 1997), significant offset (≥100 kpc) of the WAT from the X-ray centroid

(Sakelliou & Merrifield 2000), and the presence of X-ray substructure (Burns et al. 1994; Gomez et al. 1997) have all been observed in WAT-hosting clusters, and are assumed to be indicators of a recent cluster merger. Simulations have shown that relative velocities of the ICM, great enough to bend WATs, are produced in mergers, and persist on timescales greater than the lifetime of the radio sources (107-108 yr) (Roettiger et al. 1993, 1996; Loken et al. 1995; Ricker & Sarazin 2001). Large velocities relative to the ICM resulting from cluster mergers may not be required to bend the WAT, if a model of high flow velocity and low density is assumed within the radio lobes (Burns & Balonek 1982; Eilek et al. 1984; O'Donoghue et al. 1990; Pinkney 1995; Hardcastle et al. 2005).

Concerning BCGs in cool core clusters, as discussed also by Burn et al 1990, most the sources are extended or they have jetlike structure (e.g. 4C 26.42 in Abell 1795). Some, such as 3C 338 in Abell 2199 do not have detectable jets. In general, they either poorly collimated, roughly bipolar structure or amorphous core- halo morphologies (e.g. Abell 2052, Perseus cluster, etc see Tab. 2.4).

2.6 The extended sample.

Looking at X-ray emission of the Abell clusters in our complete sample, clusters are divided in cool core and non cool clusters (Tab.4). However, at parsec-scale, we note that the two two-sided structure (3C 84 and 3C 338) are both found in cool core clusters (A 426 and A 2199) and one-sided sources are all observed in non cool core clusters. A comparison between BCGs in cooling and non-cooling clusters suggests a difference in the properties of the parsec-scale structures, but numbers are too small to properly discuss it. To improve our statistics, we performed a search in the literature and archive data looking for VLBI data of BCG in Abell clusters that have detailed information about the cluster dynamic (X-ray emission) and radio emission at mas and arcsec resolution. In order to obtain an extended BCG list, we added to our complete sample the following sources:

- **B2 0836+29II in A690** (O'Donoghue et al. 1990; Giovannini et al. 2005);
- **Hydra A in A780** (Taylor 1996; Wise et al. 2007);
- **4C 26.42 in A1795** (Liuzzo et al. 2009a; Salomé & Combes 2004);
- **3C317 in A2052** (Venturi et al. 2004);
- **B2151+174 in A2390** (Augusto et al. 2006);
- **PKS 2322-123 in A2597** (Morris & Fabian 2005; Taylor et al. 1999)
- **PKS 1246-410 (NGC4696) in A3526** (Taylor et al. 2006)

In Tab.2.4 we provide our results concerning the morphology for the extended sample. In the first column, we report the Abell cluster of BCG of our sample, in column 2, we indicate Y if the Abell cluster shows a cool core, N if it doesn't, in column 3 there are the value of central mass accretion rate of the cluster taken from the literature, in column 4 there are the names of BCGs. Column 5 is for the large scale morphology of the BCG: we use WAT for Wide Angle Tail radiosource, Tail rs for Head Tail radiosource, MSO for medium symmetric object. In column 6, we mark the parsec-scale structure: one sided, two sided, core (unresolved) or n.d. for the non detections. In the last column, we give the references for the mas scale structure when the source is yet well studied at mas scale in literature and for values of Mass accretion rate given in column 3.

Table 2.4: **Results for the extended sample (see the text).**

Abell Cluster	cool core	M_{accr} $M_\odot$/yr	BCG	Large scale	VLBI	Ref.
A400	N	$0.0^{+28.3}_{-0.0}$	3C75A	WAT	one sided	White et al. (1997)
	N	$0.0^{+28.3}_{-0.0}$	3C75B	WAT	one sided	White et al. (1997)
A407	N	$4.6^{+11.8}_{-4.6}$	UGC2489	Tail rs	one sided	White et al. (1997)
A539	N	$2.1^{+6.8}_{-2.1}$	UGC3274	radio quiet	n.d.	White et al. (1997)
A569	N	$>5.2^{+0.0}_{->4.2}$	NGC2329	WAT	one sided	White et al. (1997)
A576	N	17^{+47}_{-17}	CGCG261-059	Tail rs	one sided	White et al. (1997)
A690	N	$0.0^{+15.3}_{-0.0}$	B2 0836+29 II	WAT	one sided	Giovannini et al. (2005); White et al. (1997)
A779	N	$3.1^{+1.1}_{-1.1}$	NGC2832	radio quiet	n.d.	White et al. (1997)
A1185	N	$0.0^{+1.5}_{-0.0}$	NGC3550	radio quiet	n.d.	White et al. (1997)
A1213	N	$0.0^{+11.5}_{-0.0}$	4C29.41	FRI	one sided	White et al. (1997)
A1228	N	—-	IC2738	radio quiet	n.d.	-
A1314	N	$0.0^{+3.0}_{-0.0}$	IC708	WAT	one sided	White et al. (1997)
	N	$0.0^{+3.0}_{-0.0}$	IC712	small WAT	n.d.	White et al. (1997)
A1367	N	$2.3^{+6.8}_{-2.3}$	NGC3842	small WAT	n.d.	White et al. (1997)
	N	$2.3^{+6.8}_{-2.3}$	3C264	HT	one sided	Lara et al. (1999); White et al. (1997)
A1656	N	$0.0^{+1.0}_{-0.0}$	NGC4874	small WAT	one sided	White et al. (1997)
A2147	N	$0.0^{+14.5}_{-0.0}$	UGC10143	small WAT	n.d.	White et al. (1997)

Table 2.4 continued

Abell Cluster	cool core	M_{accr} $M_\odot$/yr	BCG	Large scale	VLBI	Ref.
A2151	N	$6.3^{+26.3}_{-3.2}$	NGC6041	small WAT	core	White et al. (1997)
	N	$6.3^{+26.3}_{-3.2}$	NGC6047	compact core+symmetric jets	n.d.	White et al. (1997)
A2162	N	—-	NGC6086	FRI, relic source	n.d	-
A2197	N	$2.4^{+3.0}_{-2.4}$	NGC6173	point source	one sided	White et al. (1997)
A2634	N	$0.0^{+1.5}_{-0.0}$	3C465	WAT	one sided	Venturi et al. (1995); White et al. (1997)
A2666	N	$0.0^{+2.6}_{-0.0}$	NGC7768	Tail rs	one sided	White et al. (1997)
A3526	N	$5.2^{+0.3}_{-0.3}$	PKS 1246-410	small tailed rs	one-sided	Taylor et al. (2006); Hudson et al. (2009)
A262	Y	$9.4^{+21.2}_{-4.4}$	NGC708	double-no core,jets	core	White et al. (1997)
A347	Y	$7.8^{+3.5}_{-2.7}$	NGC910	radio quiet	n.d.	White et al. (1997)
A426	Y	$291^{+>-7}_{-58}$	3C84	Compact core+Halo	two sided	Taylor et al. (2006); White et al. (1997)
A780	Y	222^{+98}_{-132}	Hydra A	double	two sided	Taylor (1996); White et al. (1997)
A1795	Y	321^{+166}_{-213}	4C26.42	double	two sided	Liuzzo et al. (2009a); White et al. (1997)
A2052	Y	94^{+84}_{-37}	3C317	bright core+halo (FRI)	two sided	Venturi et al. (2004); White et al. (1997)
A2152	Y	20^{+13}_{-20}	UGC10187	Tail rs	n.d.	White et al. (1997)
A2199	Y	97^{+9}_{-31}	3C338	double restarted	two sided	White et al. (1997); Feretti et al. (1993)
A2390	Y	247^{+43}_{-91}	B2151+174	MSO	two sided	Augusto et al. (2006); Allen et al. (2001)
A2597	Y	501^{+58}_{-512}	PKS 2322-123	asymmetric radiosource (FRI)	two sided	Taylor et al. (1999); Chen et al. (2007)

The extended sample is composed of 34 BCGs: 10 are in cool core clusters and 24 are in non cool core clusters. Tab.2.5 summarizes statistically properties of the complete and the extended sample.

Table 2.5: **BCG counts in the complete (nearby) sample and expanded one**. We report the number of BCG according to the cluster morphology and parsec-scale morphology. Note that most of the undetected sources in VLBA observations are in BCG that are radio quiet (or faint) in VLA observations.

Sample	Cluster morphology	Number	two-sided	one-sided	point	N.D.
Complete	cool core	5	2 (40%)	–	1	2
	non cool core	22	–	12 (55%)	1	9
Expanded	cool core	10	7 (70%)	–	1	2
	non cool core	24	–	14 (58%)	1	9

In the expanded sample, we find in cool core clusters:

- 70% two-sided sources;
- 20% non detected sources;
- 10 % unresolved structures.

Instead, in non cool core clusters, BCGs show:

- 58% one-sided morphology;
- 38% non detected sources;
- 4% unresolved structures.

We have to note that at parsec scale two sided structures are found only in cluster with mass accretion rate > 90 $M_{\odot}$/yr. Moreover, among the cool core clusters A 262 , A 347 and A 2152 are small cooling flow clusters having a lower Mass accretion rate (Tab. 2.4). Their BCGs at parsec scale show no detections (NGC 910 and UGC10187) or core structure (NGC708). This seems to suggest that an interpretation of our results based only on cool core / non cool core clusters could be too simple. Better investigation on the correlation between the parsec scale morphology and the dynamical status of the cluster (mass accretion rate, etc) is needed (see Chapter 5).

Chapter 3

Peculiar cases of BCGs.

3.1 4C 26.42 in Abell 1795.

3.1.1 Introduction.

The radio galaxy 4C 26.42 (B2 1346+26) is identified with a very luminous cD galaxy (M_v=-23) at z=0.0633. This cD galaxy is the brightest member of the rich cluster Abell 1795. In X-rays, A1795 shows a relaxed structure and it is one of the most powerful clusters of galaxies known, with a luminosity of $\sim$8.5 $\times$ 10^{44} ergs s^{-1} in the 0.5-4.5 keV band. More recent study indicate that the central region is undergoing significant cooling (Tab. 3.5). Ettori et al. 2002 also found that the shape of the potential is in agreement with the motion of the central dominant galaxy, and suggests that the central cluster region is not relaxed. It has a strong central peak of cooler gas and this evidence of "cooling flow" (Baum et al. 1992) is supported by the presence of strong emission-line nebulosity (Capetti et al. 2000; Fabian et al. 1994) around the central cD galaxy along with excess blue light. The blue light is probably due to massive stars (McNamara et al. 1996b) with some contribution from young globular stars (Holtzman et al. 1996).

Salomé & Combes (2003) studied in detail the CO emission for 4C 26.42. The observations have been done with the IRAM interferometer, with 3.2 $''$ and 1.8 $''$ spatial resolution at the CO(1-0) and CO(2-1) lines respectively. The velocity of the cD is redshifted by 374 km/s with respect to the mean velocity of the galaxies inside 200 kpc (Hill et al. 1988; Oegerle & Hill 1994).

The resulting integrated maps in the two CO lines are shown in Fig. 3.1.

A velocity gradient of the cold gas is revealed, that shows it is falling on the central galaxy and may provide the AGN fueling material which is consistent with

an AGN regulated cooling flow scenario. The kinematics of the molecular gas in A1795 is shown in Figs. 3.2 and 3.3.

Position-velocity diagrams are presented for the two CO lines along the axis of maximum emission (PA = 27°) through the centre of the cD galaxy. There are two separated trends in velocity in both the CO(1-0) and CO(2-1) lines. One is centered on the galaxy position at zero velocity. The other is 5″ North-West from the radio source position and is at -300/350 km s^{-1} relative to the galaxy velocity. There is also a regular gradient from the galaxy centre towards the North-West (5″). The velocities measured in the CO brightest regions are coinciding with those in H_α by van Breugel et al. (1984) and Anton (1993), supporting the association between the cold gas and the hot gas/optical structures. The peak of H_α emission does not follow the peculiar velocity of the cD galaxy in the cluster, but is centred on the cluster mean velocity (-350 km/s), i.e. the mean velocity of the galaxies inside 200 kpc, while it reaches the cD velocity at the galaxy position. The kinematics of the cold gas and the H_α line emitting gas is compatible with the cooling flow scenario. At the North-West position, coincident with the brightest X-ray region, the gas is cooling within the cluster potential. Near the cD, the flow is captured by the cD potential (and the inner gas have a velocity close to that of the galaxy, with a wider range of velocities).

High Faraday rotation measures (exceeding ∼2000 rad m^{-2}) are found in 4C 26.42 in high resolution (0.6 arcsec) VLA images (Ge & Owen 1993). The magnitude and scale of the RM are consistent with a hot (∼10^8) and dense (∼0.03 cm^{-3}) X-ray emitting gas. The strength of the magnetic field is probably between 20 and 100 μG, depending on the degree of ordering.

From Very Large Array (VLA) observations, 4C26.42 is known to have an FR I, Z-shaped small (2″×12″) radio morphology (van Breugel et al. 1984), with a kpc total power at 0.4 GHz $\mathrm{Log}P_{\mathrm{tot,\,0.4\,GHz}}$=25.47 W/Hz and a core power at 5 GHz $\mathrm{Log}P_{\mathrm{core,\,5\,GHz}}$= 23.70 W/Hz (Giovannini et al. 2005).

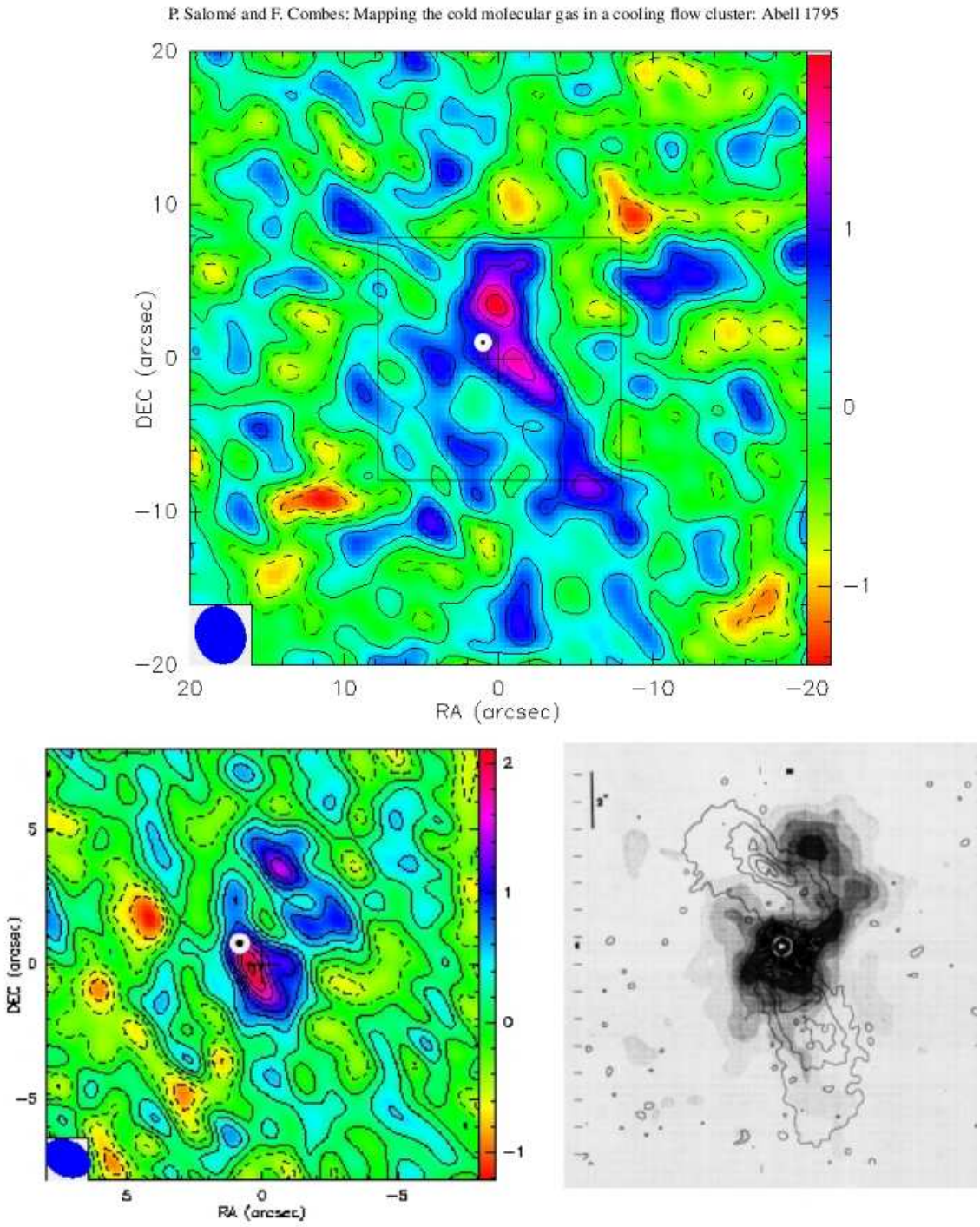

Figure 3.1: Top: CO(1-0) integrated emission (Salomé & Combes (2003)). Linear contours are drawn from -3σ to 6σ spaced by 1 σ = 0.36 Jy/beam km s^{-1}. Dashed lines are for negative contours. The beam is plotted in the bottom left corner. The black box indicate the size of the CO(2-1) integrated map presented in the bottom left. Contours are from -3σ to 8σ spaced by 1 σ = 0.26 Jy/beam km s^{-1}. The white disk indicate the radio source position. Bottom right: H_α + [NII] line emission in grey scale, overlaid the 6 cm continuum emission from 4C 26.42 radio lobes (van Breugel et al. 1984).

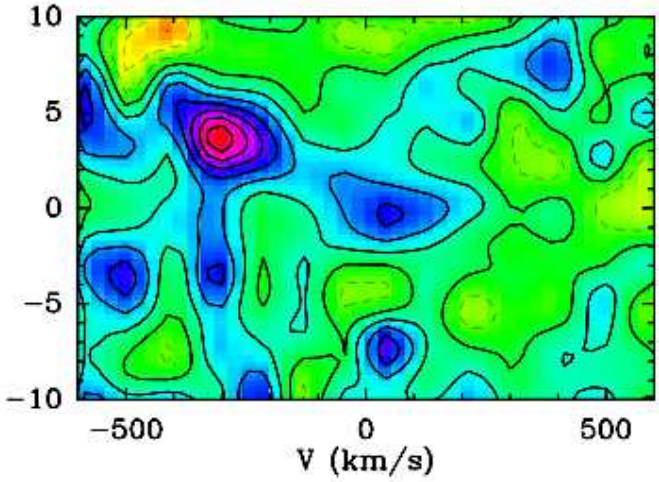

Figure 3.2: Position-velocity diagram in CO(1-0) emission line (Salomé & Combes (2003)), the positions are along a slit of 5 ″ width (integrated), centered on the galaxy position and aligned with the maximum of emission (PA = 27°).

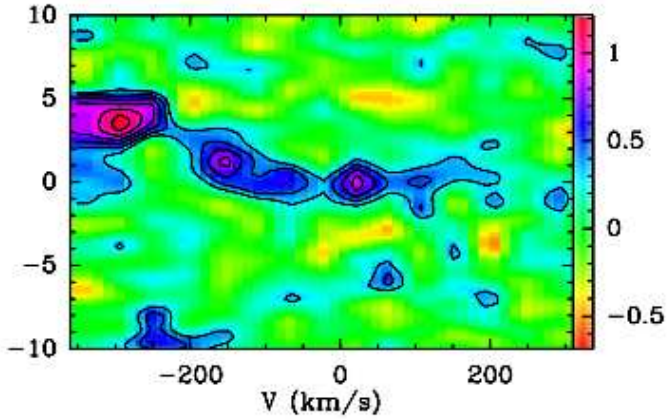

Figure 3.3: Position-velocity map in CO(2-1) emission line (Salomé & Combes (2003)) in the same region as in Fig. 3.2.

On the parsec-scale, Giovannini et al. (2005) observed 4C 26.42 at 5 GHz with the Very Long Baseline Array (VLBA). They found a faint peculiar structure with a total flux density of $\sim$8 mJy, but the observations were inconclusive because of its low brightness. To better investigate this peculiar BCG in a cool core cluster, we asked and obtained new multi-epochs, multi-frequencies VLBA observations using the phase-referencing mode. In subsection 3.1.2 we present the new data, in subsections 3.1.3, 3.1.4, 3.1.5, 3.1.6 and 3.1.7 we discuss the nuclear properties of this source. In subsection 3.1.8 we discuss possible origins for the peculiar radio structures.

3.1.2 New VLBA Observations: data reduction.

We obtained new VLBA observations at 1.6 GHz on 2003 August 07, at 5 GHz on 2005 July 27, and at 1.6, 5, 8.4 and 22 GHz on 2008 February 26 (see Tab.3.1). Moreover we re-reduced the data at 5 GHz of 1997 April 4 (Giovannini et al. 2005). All data were obtained using the phase referencing mode, except for the 5 GHz data of 1997, whose quality largely improved after applying the improved source position obtained from the newer data taken using phase referencing. Data at 1.6 and 5 GHz have the sensitivity and (u-v) coverage necessary to study the more extended jet structure.

Table 3.1: Calibrators list.

Epoch yy-mm-dd	Frequency GHz	Observing time hour	phase calibrators
03-08-07	1.6	1.0	J1350+3034
08-02-26	1.6	1.0	J1342+2709
97-04-06	5.0	1.0	J1350+3034
05-07-27	5.0	1.5	J1342+2709
08-02-26	5.0	1.5	J1342+2709
08-02-26	8.4	2.0	J1342+2709
08-02-26	22	3.5	J1342+2709

The observations were correlated in Socorro, NM. A total of 16 MHz bandwidth was recorded in both right and left circular polarization. Post-correlation processing used the NRAO AIPS package and the Caltech Difmap package. We followed the same scheme for the data reduction of all data sets. Using AIPS we applied ionospheric corrections and corrections to the Earth Orientation Parameters (EOPs). After this, we used the AIPS script VLBACALA to correct sampler offsets and to apply a-priori amplitude calibration. With VLBAPANG we corrected the antenna parallactic angles and with VLBAMPCL we removed the instrumental delay residuals. All calibrator data were also globally fringe-fitted and solutions were applied to the target sources with VLBAFRGP. After flagging bad visibilities, we obtained good models for the calibrators, which we used to improve the amplitude and phase calibration for the entire data set. Final maps were obtained with Difmap after averaging over IFs and in time. After editing, we applied multiple iterations of imaging and self-calibration in phase and amplitude. At last, to these improved quality data, we applied Modelfit to obtain the final set of components describing

Table 3.2: Image Parameters for natural weighting maps.

Epoch yy-mm-dd	Frequency GHz	Beam Size mas	Beam P.A. deg	Noise mJy beam^{-1}	Peak mJy beam^{-1}	Total Flux Density mJy
03-08-07	1.6	11.0×6.1	7	0.15	22.5	67.6
08-02-26	1.6	11.3×5.9	15	0.10	32.2	90.9
97-04-06	5	4.0×2.4	6	0.21	8.7	29.9
05-07-27	5	3.4×2.2	-8	0.13	10.0	42.0
08-02-26	5	3.0×1.5	-2	0.16	7.9	44.1
08-02-26	8.4	1.9×0.9	-4	0.08	7.0	25.2
08-02-26	22	1.0×0.7	-19	0.15	6.6	13.6

the data.

In Tab. 3.2 we report the image parameters for final natural weighting maps at different epochs and frequencies.

3.1.3 The parsec scale structure.

In Figs. 3.4 - 3.6 we present the full resolution images of 4C 26.42 at 1.6, 5, 8 and 22 GHz respectively. At low frequency and low resolution, the source shows two components (A and B) in the inner 15 mas (in PA $\sim 60^\circ$) and two symmetric lobes oriented North - South (N1 and S1) with a peculiar Z shaped structure (Fig. 3.4, left). The source size is $\sim$ 30 mas. At 5 GHz the two central components of the low resolution images are resolved into three components (A, C and B; see Fig.3.4 right).

The symmetric S1 and N1 lobes are still visible though with an extension of only $\sim$10 mas. We note that components A and B are coincident with the regions where the jet position angle changes by $\sim 90^\circ$. The parsec-scale structure is very symmetric. At still higher resolution (Fig.3.5), we distinguish four components in the central 10 mas (A1, A2, C and B); N1 is completely resolved out while S1 is marginally detected.

At the highest resolution, only the central components A1, A2 and C are visible (Fig. 3.6). We note that in high resolution images (8.4 and 22 GHz) because of the low signal to noise ratio the extended source structure is not visible in our images.

Comparing the parsec and kiloparsec structure (Fig.3.7), we note that two

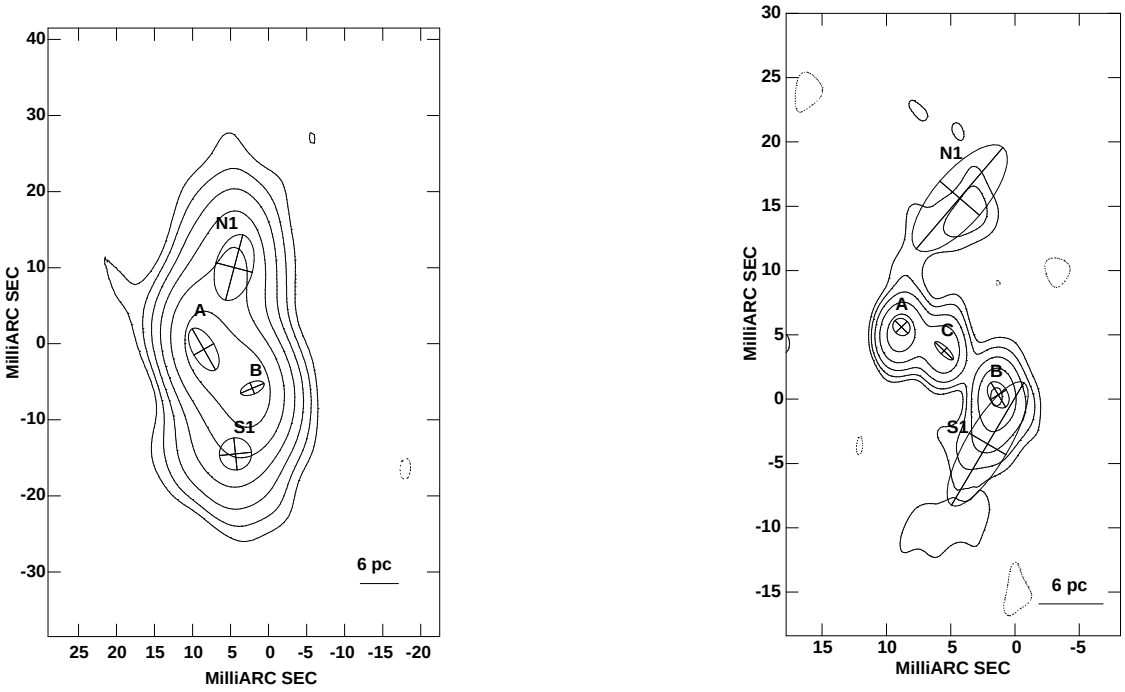

Figure 3.4: On the left: 1.6 GHz VLBA contour map obtained on 2003 August 07 with the 4 components given by modelfitting overlaid. The HPBW is 11.0 x 6.1 mas at 6.8° with a noise level = 0.15 mJy/beam . Contours are: -0.45, 0.45, 0.9, 1.8, 3.6, 7.2, 14.4 mJy/beam. On the right: 5 GHz VLBA contour map obtained on 2005 July 27 with the 5 components given by modelfitting overlaid. The HPBW is 3.4 × 2.2 mas at -8.0° with a noise level = 0.13 mJy/beam . Contours are: -0.4, 0.4, 0.8, 1.6, 3.2 and 6.4 mJy/beam.

changes in P.A. occur, one at ∼15 mas from the core where P.A. goes from 60° to −30° and the second at ∼ 2 arcsec where P.A. goes from −30° back to 60° to realign with the inner parsec-scale P.A.

3.1.4 Modelfit results.

Modelfitting was applied to all the data available for this source using elliptical, circular or delta components. The difmap modelfit program fits aggregates of various forms of model components, fitting directly to the real and imaginary parts of the observed visibilities using the powerful Levenberg-Marquardt non-linear least squares minimization technique. First we applied modelfitting to the last observations taken in 2008 independently for each frequency. All parameters of modelfit components were initially allowed to vary freely, however to facilitate comparisons between epochs, a mean shape was fixed for each frequency and only the position and flux density of the component was allowed to vary. We have also tried to describe elongated features with several small components. However, this

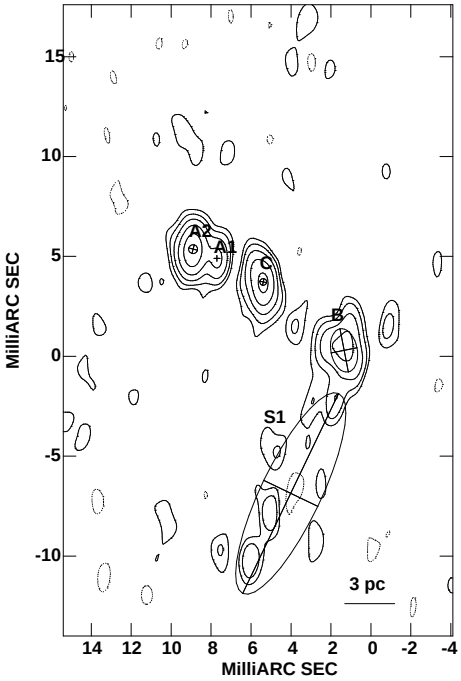

Figure 3.5: 8.4 GHz VLBA contour map at the 2008 February 26 epoch with the 5 components derived from modelfitting overlaid. The HPBW is 1.86 × 0.86 mas at -4.3° with a noise level = 0.08 mJy/beam. Contours are: -0.25, 0.25, 0.5, 1, 2, 4 mJy/beam.

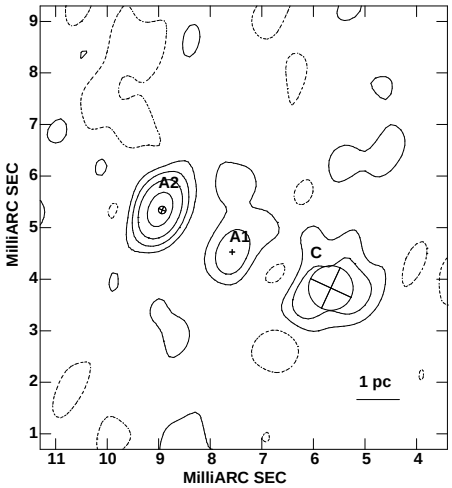

Figure 3.6: 22 GHz VLBA contour map obtained on 2008 February 26 with the 3 components derived from modelfitting overlaid. The HPBW is 1.01 x 0.65 mas at -18.5° with a noise level = 0.15 mJy/beam. Contours are: -0.45, 0.45, 1.2, 2.4, 4.8 mJy/beam

resulted in an increase of χ^2, so we retained the simplest model. For example, in the case of S1 at 5 GHz (1997 April 6), the χ^2 increases from 1.393 (one component) to 1.709 (3 components). Following this step, we supposed that only the flux density of the components can change with the time. We fixed the shape of the components and

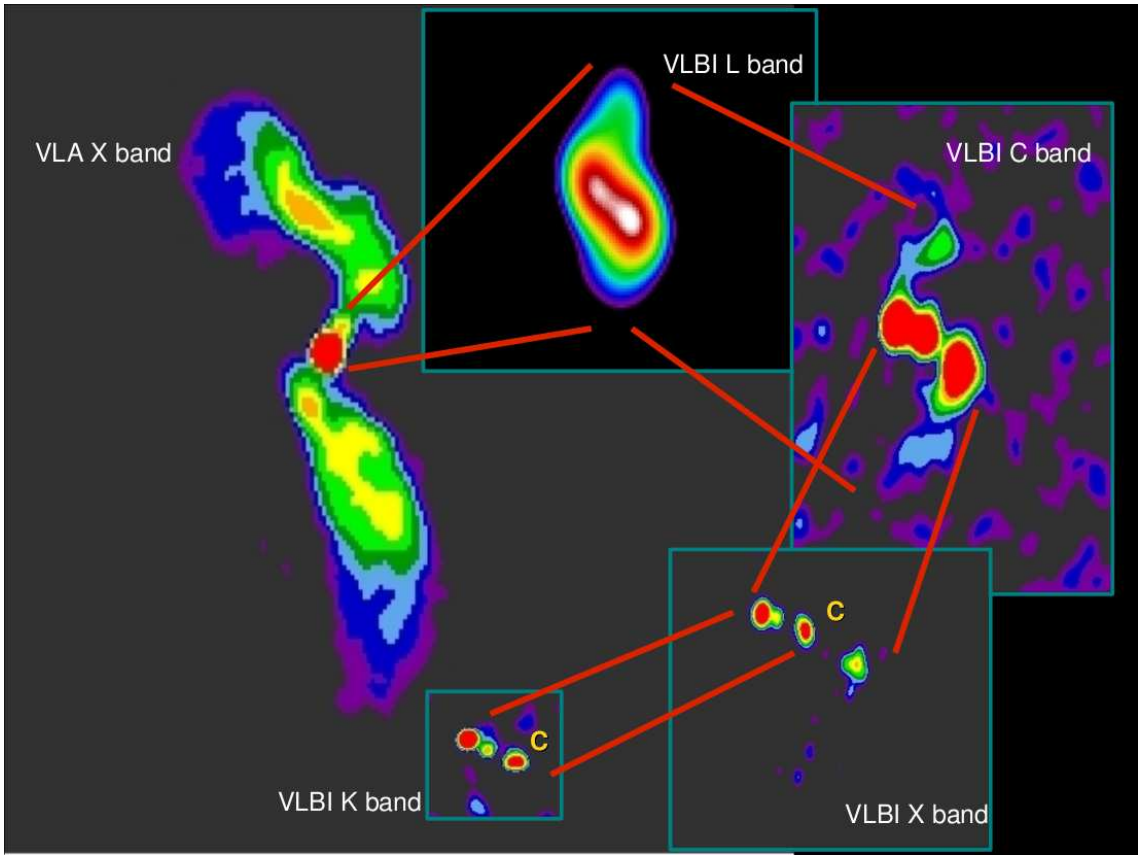

Figure 3.7: Clockwise from left to right, zooming from kiloparsec to mas scale radiostructure of 4C 26.42: color maps of VLA X band, VLBI L band, VLBI C band, VLBI X band and VLBI K band data. (C) indicates the core component.

then modelled the (u,v) data from previous epochs at the corresponding frequencies.

In Tab. 3.3, we give the frequency (col.1) and the epoch of observation (col.2), the χ^2 (col. 3) of the fit, the name of the components (col. 4), polar coordinates (r) and (θ) (col. 5 and col. 6) of the center of the component relative to the origin discussed above, with polar angle measured from the north through east, the positional uncertainty Δ (x,y) (col.7), the major axis a (col. 8), the ratio b/a of minor b and major a axes (col. 9) of the FWHM contour, the position angle Φ (col. 10) of the major axis measured from north to east and the flux density S (col. 11). Statistical errors are provided for the component parameters in Table 3. For elliptical and circular gaussian components we also calculated errors in size (a). Uncertainties in the sizes, positions and fluxes for components were derived from signal-to-noise ratios and component sizes (Fomalont 1999). True errors could be larger in the event that some components are covariant.

Table 3.3: Results of Modelfit applied to 1.6, 5, 8.4 and 22 GHz data (see text).

Frequency GHz	Epoch yy-mm-dd	χ^2	Component	r mas	θ deg	Δ (x, y) mas	a mas	b/a	Φ deg	S mJy
1.6	03-08-07	1.312	A, e	0	0	–	3.29±0.02	0.5	29.6	24.9±1.3
			N1, e	7.61	-130	0.02	6.20±0.04	0.5	-67.3	21.4±1.1
			B, e	10.58	-22	0.05	8.88±0.10	0.6	-14.7	13.1±0.7
			S1, c	14.11	-165	0.35	4.23±0.07	1	-84.2	8.2±0.4
1.6	08-02-26	1.001	A, e	0	0	–	3.29±0.01	0.5	29.6	31.9±1.6
			N1, e	8.08	-128	0.01	6.20±0.02	0.5	-67.3	31.0±1.6
			B, e	10.18	-17	0.02	8.89±0.04	0.6	-14.7	21.4±1.1
			S1, c	16.01	-178	0.03	4.23±0.06	1	-84.2	6.6±0.3
5	97-04-06	1.393	C, e	0	0	–	1.92±0.05	0.3	45.7	7.6±0.4
			A, e	4.02	64	0.15	1.43±0.03	0.9	44.7	10.4±0.6
			N1, e	11.19	-6	0.55	10.38±1.09	0.4	-40.5	2.0±0.2
			B, e	5.19	-130	0.03	2.21±0.06	0.7	30.9	7.3±0.4
			S1, e	9.4	-174	0.43	11.08±0.86	0.3	-30.6	2.7±0.2
5	05-07-27	1.205	C, e	0	0	–	1.92±0.03	0.3	45.7	8.3±0.4
			A, e	4.02	65	0.01	1.43±0.02	0.9	44.7	11.9±0.6
			N1, e	12.04	-4	0.13	10.38±0.25	0.4	-40.5	5.3±0.3
			B, e	5.07	-129	0.02	2.21±0.03	0.7	31.0	8.4±0.4
			S1, e	7.38	-158	0.09	11.08±0.18	0.3	-30.6	8.1±0.4
5	08-02-26	0.946	C, e	0	0	–	1.92±0.03	0.3	45.7	9.3±0.5
			A , e	4.02	64	0.01	1.43±0.02	0.9	44.7	11.5±0.6
			N1, e	11.10	-4	0.13	10.38±0.23	0.4	-40.5	5.9±0.3
			B, e	5.04	-127	0.02	2.21±0.04	0.7	30.9	7.7±0.4
			S1, e	6.85	-150	0.08	11.08±0.15	0.3	-30.6	9.7±0.5
8.4	08-02-26	0.890	C, c	0	0	–	0.34±0.01	1	-11.9	5.3±0.3
			A1, d	3.01	61	0.02	0	1	0	2.9±0.2
			A2, c	4.02	63	0.01	0.44±0.01	1	-14.7	8.1±0.4
			B, e	5.09	-129	0.01	2.21±0.02	0.6	11.0	7.5±0.4
			S1, c	8.89	177	0.24	11.08±0.47	0.3	-25.6	1.9±0.1
22	08-02-26	1.040	C, c	0	0	–	0.9±0.03	1	-25.0	4.6±0.3
			A1, d	2.05	71	0.01	0	1	0	2.2±0.2
			A2, c	4.04	65	0.01	0.15±0.01	1	-21.8	6.8±0.4

For high frequencies (> 1.6 GHz) we refer the component distance to component C because of symmetry reasons and its identification as the 'core' of 4C 26.42 (see Sect. 3.1.6). At 1.6 GHz where the central component C is not visible, we use component A as the reference point.

We note that the total flux density at 5 GHz, obtained by summing the different components in the 2008 epoch, is 44 mJy, therefore neglecting variability, only a small fraction ($\sim 17\%$) of the flux density is lost with respect to the sub-arcsecond core flux density (53 mJy) obtained from VLA data by van Breugel et al. (1984). Lower total flux density at 5 GHz of data carried out on 6 April 1997 are due to different not in phase referencing mode (see §2) observational analysis and it is not consequence of variability in the radioemission of the source. We compared the flux

density of components A, B and C at different epochs at 5 GHz to search for possible variability (see Table 3). The flux density is slightly different but no clear trend is present. The limit on the amount of variability is ∼0.6 mJy at 3σ level (i.e. less that 10%). Improved sampling is necessary to better constrain variability.

We also have to note that, at higher frequencies, we lost flux density measurements of some components (see Tab. 3.3). This is a consequence of steep spectral index (see Tab. 3.4), low surface brightness of these (see Tab. 3.3) combined to probably not enough sensitivity of our images (see Tab. 3.2). Improved high quality images are necessary to give a complete spectral analysis of these components.

3.1.5 The parsec-scale spectrum

We used our multifrequency data from 2008 February 26 observations to study the spectral index (defined $S_\nu \propto \nu^{-\alpha}$) distribution of the parsec-scale structure. For our analysis, we first obtained images of the source using the same maximum and minimum baseline in the (u, v) coverage, the same griding and the same restoring beam. Then, we identified the different source components, and we measured their flux densities. Finally, we derived the spectral index for each component between 1.6 GHz and 5 GHz, 5 GHz and 8.4 GHz and between 8.4 GHz and 22 GHz (see Table 4).

Between 1.6 GHz and 5 GHz owing to the low resolution, single components are not well defined. The spectrum is in general steep as expected from low brightness extended components. We note that the steepest component is component B ($\alpha = 1.8$), and that the Northern extension (N1) is steeper, and more extended than S1.

At higher resolution, component C shows a flat spectrum ($\alpha_5^{8.4}\sim0$, $\alpha_{8.4}^{22}\sim0.14$) and it appears unresolved by a gaussian fit to the self-calibrated data. For these reasons and because of the source morphology, we identify C as the center of activity for 4C 26.42 with position RA $13^h\ 48^m\ 52^s.4894321 \pm 0.0000064$, DEC $26^d\ 35^m\ 34^s.340598 \pm 0.000038$ (estimated from the high resolution observations at 22 GHz of 2008 February 26). Also component A (with subcomponents A1 and A2) shows a clear flattening in the spectrum at high frequency, while component B despite the symmetric source morphology, has a steep spectrum (1.0) between 5 and 8.4 GHz, and as expected is not detected at 22 GHz. We do not interpret this steep

Table 3.4: Spectral index for single component.

ν_1-ν_2 GHz	HPBW mas×mas, °	Component	S_{ν_1} mJy	S_{ν_2} mJy	α
1.6-5	10.0×5.0, 0	A	15.4	7.5	0.63±0.01
		B	29.0	3.6	1.82±0.01
		N1	15.4	6.1	0.82±0.02
		S1	9.4	7.3	0.66±0.03
5-8.4	3.0×3.0,0	A	6.7	6.7	0.00±0.05
		C	4.1	4.1	0.00±0.05
		B	6.2	3.7	1.03±0.06
		S1	7.7	2.6	2.12±0.06
8.4-22	1.86×0.86,-4	C	5.3	4.6	0.14±0.04
		A1	2.9	2.2	0.29±0.08
		A2	8.1	6.8	0.18±0.03

S_{ν_1} and S_{ν_2} are referred to the flux density at lower ν_1 and higher ν_2 frequency between the two considered for the spectral analysis. All flux density values are derived from 2008 February 26 observations.

spectrum as due to different synchrotron aging because the component N1 shows a steeper spectrum with respect to S1. Instead we suggest that the difference in spectral index is due to asymmetric interactions with the surrounding medium in the bending region. We note that the source is symmetric also on the kiloparsec-scale.

3.1.6 Jet dynamics

Proper Motion

We studied the apparent proper motion of components A and B using the three different epochs at 5 GHz. We have observations at two different epochs also at 1.6 GHz, but the low resolution does not allow for a reliable search for possible proper motion. At 8.4 and 22 GHz only one epoch is available. We note that components A and B are well defined and their identification is not ambiguous, while components N1 and S1 are extended with no evident substructures so that their best fit position is affected by the varying sensitivity of different observations.

No significant proper motion was detected with a limits on the motion of A and

B with respect to C of $\sim 9 \times 10^{-3}$ mas/yr ($\sim 3.6 \times 10^{-2}$c) at the 3σ level. Available data are poor (only 3 epochs) but with good time coverage (1997, 2005 and 2008 epochs). Therefore we conclude that A and B are stationary features, probably not due to moving knots in the jets but instead resulting from standing shocks in the region where the jet direction undergoes a symmetric P.A. change of about 90°.

Bulk Velocity

An estimate of the jet bulk velocity rather than pattern speed can be derived from the jet to counter-jet brightness and size ratio, and by comparison of the nuclear with the total radio power (see e.g. Giovannini et al. (1988)). The brightest component at 5 GHz at all epochs is A which is the nearest to C. The flux density ratio with respect to B at 5 GHz is $S_A/S_B \sim 1.4$. On the other hand, the distance ratio is $r_A/r_B \sim 0.8$. Moreover from an inspection of available images we note that an underlying jet connection between different structures (A, B and C) is not visible probably because of sensitivity limitations. In conclusion, there is no evidence of asymmetry in flux or position that would be expected from Doppler boosting.

In most FR I or FR II sources with good VLBI data a relatively simple nuclear-jet structure is present. The VLBI core shows a large fraction of the arcsecond core flux density, and the correlation between the core and total radio power can provide constraints on the jet velocity and orientation. In this source the arcsecond unresolved core shows a complex and extended structure in VLBI images which are not core dominated. The VLBI core is very faint and most of the flux density is from jet-like components or small regions reminiscent of radio lobes. Therefore it is not possible to estimate the jet velocity and orientation from the core dominance.

We can only note that the lack of underlying jets connecting the different knots, the source symmetry and the low power of the nuclear structure, all suggest that either the core structure of 4C26.42 is near to the plane of the sky or/and the jets are not relativistic. This conclusion reinforces the identification of mas structures as standing shocks in the jet.

3.1.7 The physical conditions at equipartition

X-ray studies have shown that the black holes at the center of galaxy groups and clusters are capable of inflating cavities or "bubbles″ in the surrounding X-ray

emitting gas (Fabian et al. 2003, 2005; Birzan et al. 2004). The core of radio emission in 4C 26.42 is clearly identified with the highest X-ray brightness region and therefore with the center of the cluster. Similar to many recent examples in literature, the correspondence between the location of the radio lobes and X-ray cavities (Johnstone et al. 2002) suggests an expansion of the radio lobes into the surrounding X-ray emitting gas. In this section we compute the magnetic field strength, internal pressure, and total energy, assuming that equipartition conditions apply.

We use the standard formulae in Pacholczyk (1970) , assuming that the relativistic particles and the magnetic field fully occupy the same volume (Φ = 1), and that the amount of energy in heavy particles equals that in electrons (k=1). We integrated over the frequency range 10^7-10^{11} Hz and we infer the extent of the source along the line-of-sight.

For the nuclear region imaged at 22 GHz (component C), we estimate a global equipartition magnetic field H_{eq} ∼0.22 Gauss. The total energy is E_{tot} ∼6.9×10^{52}erg, while the corresponding minimum internal pressure is P_{eq} ∼2.4×10^{-3} dyn/cm^2. For extended regions we used 1.6 GHz data and for the lobe on the north N1, we obtained H_{eq} ∼1.73×10^{-2} Gauss, E_{tot} ∼1.6×10^{53}erg and P_{eq} ∼1.5×10^{-5} dyn/cm^2. Instead for the lobe on the south S1, we obtained H_{eq} ∼4.28×10^{-2} Gauss, E_{tot} ∼2.9×10^{52}erg and P_{eq} ∼8.9×10^{-5} dyn/cm^2.

Birzan et al. (2004) estimated the energy required to inflate the large-scale bubbles in 4C 26.42. The energy required to create the observed bubble on the north in the X-ray emitting gas is E_{bubble}∼39 $\times10^{57}$ ergs and the age of the bubble is t_{age}∼1.8×10^7 yrs, where t_{age} is R/c_s where R is the distance of the bubble center from the black hole and c_s is the adiabatic sound speed of the gas at the bubble radius. From these values we derive the required average jet mechanical power P_{jet}= E_{bubble}/t_{age} involved in "blowing" the bubble. We find P_{jet}∼6.9×10^{43}ergs/s (∼ 6.9 $\times10^{36}$ W). Comparing the mechanical power of bubble with the heating necessary to prevent the gas from the cooling to low temperatures, Birzan et al. (2004) found that the cavities can balance the cooling if they are relativistic and non-adiabatic, and there may be further energy input if they are overpressured or produce a shock when they are formed.

We can compare P_{jet} derived above with the present parsec-scale jet power.

Assuming for the northern jet a flux density upper limit of 20 mJy at 5 GHz, its bolometric radio power is $\sim 8 \times 10^{33}$ W, significantly lower than the power estimated from the Northern cavity and therefore indicating radiatively inefficient jets (0.1% of P_{jet}). This result suggests that either the average jet power is much higher, possibly because of the presence of heavy particles, non-equipartition conditions, or an AGN activity that was higher in the past. We note that a heavy, slow jet is in agreement with the results discussed in Section 3.1.6. We also point out that low radiative efficiency seems to be a common theme for radio sources in clusters (Taylor et al. 2006; Allen et al. 2006).

3.1.8 Discussion on the parsec and kpc scale radio morphology.

The radio morphology on the parsec and kiloparsec scale of 4C 26.42 is very complex. From spectral index considerations and modelfitting results, we identify component C as the radio core. We note that the jets bend by ~ 90 ° on scales of 10s of parsecs, and are remarkably symmetric. Two possibilities can explain the observed morphology in 4C 26.42: 1) if the pc scale jets are relativistic as in most radio galaxies (see e.g. Giovannini et al. (2001, 2005)) , and as suggested by unified models, this source has to be oriented at $\sim 90°$ with respect to the line-of-sight. In this case the large symmetric change in the source PA is real and not affected by projection. We find it difficult for a highly relativistic jet to survive such a large change in its orientation. Moreover we note that for a relativistic jet in the plane of the sky the Doppler factor is much lower than 1. Any decrease in the jet velocity will increase the Doppler factor and thereby manifest as an enhancement in the surface brightness. Since no clear surface brightness discontinuity is present in our images, we conclude that the jet velocity before and after the large PA change should be roughly the same. 2) Alternatively the source morphology suggests a subsonic flow which might be expected to have entrained thermal gas. This hypothesis is in agreement with the result that data at three different epochs do not show any proper motion, and with the identification of the bright regions on both sides of the core as bright standing shocks.

The presence of non-relativistic jets in this source is in sharp contrast with the observational evidence that parsec-scale jets in FR I radio galaxies are relativistic (Giovannini et al. 2001). In FR I radio galaxies relativistic jets in the parsec-

scale region slow down because of interaction with the ISM on the sub-kiloparsec scale. However we must acknowledge the peculiar position and physical conditions of 4C26.42 at the center of a cooling flow cluster. In Brightest Cluster Galaxies (BCGs) the presence of a dense ISM in the central (parsec-scale) regions is expected since the cooling flow is related to the presence of a high density gas as confirmed by the detection of CO line emission and molecular hydrogen (Edge 2001; Edge et al. 2002). Rossi et al. (2008) showed that a jet perturbation grows because of Kelvin-Helmotz instability and produces a strong interaction of the jet with the external medium with a consequent mixing and deceleration. The deceleration is more efficient increasing the density ratio between the ambient medium and the jet. Relativistic light jets are expected in FR I sources and the above effect can produce their slowing down from the parsec to the kiloparsec scale as found in many sources (Taylor 1996; Rossi et al. 2008). However a large value of the density ratio can produce a sub-relativistic and heavy jet even on parsec-scales as suggested by our data on 4C 26.42.

A strong interaction with the ISM could also explain the large difference in the spectral index distribution of the Northern and Southern region. The symmetric radio morphology suggests that the different spectral index distribution is related to an anisotropy in the ISM. We concluded in subsection 3.4.2 that the mas structures result from standing shocks. Internal shocks can arise from sudden changes in the medium external to the jet. These shocks cause radiative losses through enhanced synchrotron radiation due to both increased particle energy density and magnetic field strength behind the shock. In particular, we note from Table 4 that the southern part (components B and S1) of 4C 26.42 is steeper than the northern part (components A and N1). This behaviour could be due to a denser ISM in the South than in the North region around our source.

We recall that in this source there are two dramatic changes in PA. A similar, but reverse change is present at about $2''$ from the nuclear region. The origin of this peculiar morphology is not clear, but in any case requires the presence of heavy slow jets. A possible origin of a large symmetric change in the jet direction could be the interaction with a rotating disk as suggested by van Breugel et al. (1984) for 3C 293. In this model, a slow jet could be bent by ram pressure of a rotational motion of the accreted gas. The ISM of the galaxy rotates supersonically, so there is a stand-off

cylindrical bow shock in the interstellar gas upstream of the jet. A result consistent with this scenario is the spectroscopic discovery in the nuclear region of 4C 26.42 of two clouds with a difference velocity of $\sim$ 330 km/sec. Their emission line ratios of Hα and Hβ are very similar and typical of Liners exceptionally weak O [III] lines (Goncalves et al. 1999). However, no clear evidence of rotating gas has been found. Moreover, the second change in direction would require two counter-rotating regions one near to the core and one at larger distance to explain the two changes in the jet direction.

An alternative possibility is that on the large scale the radio lobes rise buoyantly in the N-S direction according to the thermal gas distribution (see e.g. the radio X-ray overlay presented by Fabian et al. (2001). On intermediate scales, the jets have been heading out at P.A. -30° for a long time. Then, on the smallest scale, we can suppose that the radio jets have just been realigned recently due to the merger of a Binary Black Hole system which could produce a change in the nuclear jet ejection direction. Merritt& Ekers (2002) suggest that the orientation of a black hole's spin axis could change dramatically due to a merger event, leading to a sudden flip in the jet direction. Merger events are relatively common in cD galaxies, and in fact Johnstone et al. (1991) proposed that the structure in the envelope of the cD galaxy in A1795 is due to a merger with another giant galaxy. Alternatively the change of the jet PA on the parsec-scale could be due to a complex angular momentum of the gas accreted in the inner part of the disk of this galaxy, as proposed by Augusto et al. (2006) for B2151+174 (BCG of Abell 2390) or by rotating vortices in the cluster gas as Forman et al. (2009) suggested for the unique morphology of 3C 28, the BCG of Abell 115.

3.2 Hydra A in Abell 780.

3.2.1 Introduction.

Hydra A is the BCG of the cool core cluster A780 (z = 0.054878). This cluster is a poor cluster but however, it is an X-ray bright cluster with $L_X \sim 2 \times 10^{44}$ erg s^{-1} in the 0.5-4.5 keV range, as seen by the Einstein satellite (David et al. 1990). The total bolometric luminosity has been estimated to be 5 x 10 ^{44}erg s^{-1} from 0.4-2 keV ROSAT observations (Peres et al. 1998). In Tab.3.5 we report the value of the Mass accretion rate of Abell 780 ($\sim$ 222 $M_\odot$/yr, White et al. 1997).

Hydra A has an associated type II cooling-flow nebula (Heckman et al. 1989), characterized by high H_α and X-ray luminosities, but relatively weak [N II] and [S II] and strong [O I] (λ = 6300 Å) emission lines, usually found in LINERs. The H_α extended narrow-line emission (Baum et al. 1988) actually fills the gap between the radio lobes. The λ = 2200Å, λ=2700Å, B-band, B - V and, also, the U - I continuum colours of the centre of Hydra A have been attributed to a $\sim$10 Myr burst of star formation involving 10^{44} to 10^{44} M_{sun} (Hansen, Jorgensen & Norgaard-Nielsen 1995; McNamara 1995). This is further supported by the detection of strong absorption lines of the Balmer series in the near-UV spectrum of the nucleus (Hansen et al. 1995; Melnick et al. 1995). A strong-absorption Balmer lines are also found, which it is identified as originating in blue supergiant or giant B stars. Heckman et al. (1985) found that the stellar kinematics has negligible rotation (13 +/- 18 km s^{-1}, but their observations were limited to the region, and did not include the higher Balmer lines in absorption. On the other hand, Ekers & Simkin (1983) report very fast rotating stars in the central 20 kpc of the radio galaxy. A two-dimensional analysis of the blue spectrum shows a tilt of the Balmer absorption lines of 450 +/- 130 km s^{-1} in the central 3 arcsec, while the CaII H and K lines do not show any displacement (Melnick et al. 1997). The conclusion derived by Melnick et al. (1997) is that the young stars have formed a disc which is rotating perpendicular to the position of the radio axis. The star formation disc has also been detected in U-band images (McNamara 1995).

3.2.2 The radio structure.

Hydra A is one of the most luminous radio sources in the local Universe, only surpassed by Cygnus A. Although its radio luminosity exceeds by an order of

magnitude the characteristic FR I/FR II break luminosity, it has (Fig. 3.8) an edge-darkened FR I morphology (Ekers & Simkin 1983; Baum et al. 1988; Taylor et al. 1990).

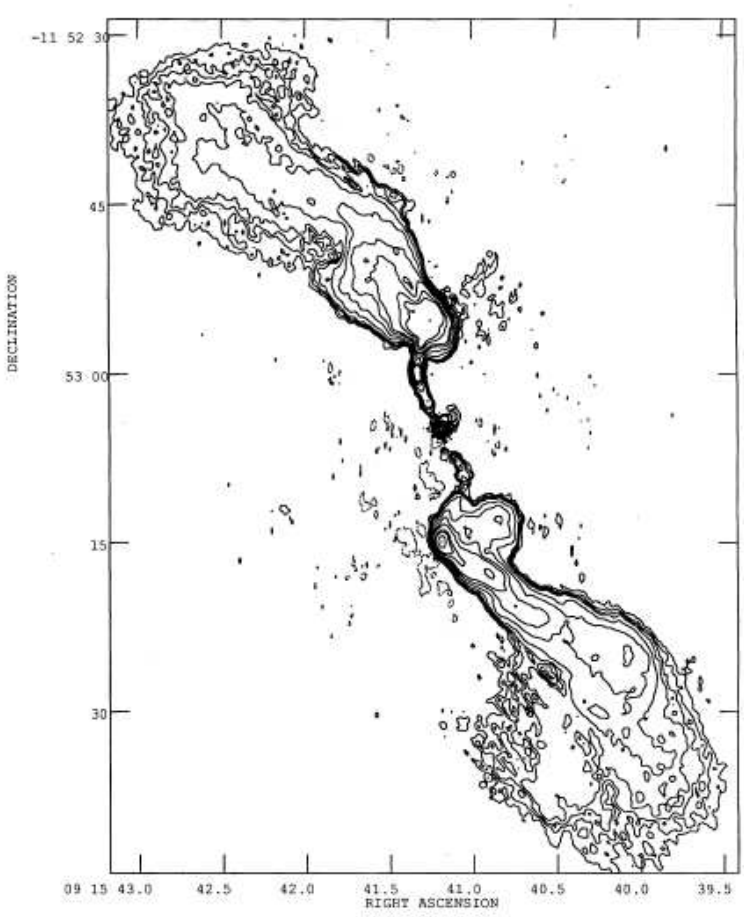

Figure 3.8: From Taylor et al. 1990: total intensity distribution of Hydra A at 4635 MHz. from A , A/B, B, C and D VLA configuration at resolution of 0.6 arcsec. Contours levels are -3.7, -1.5, 1.5, 2.7, 3.7, 5.1, 10, 21, 37, 51, 103, 154, 311, 466 mJy/arcsec^2. Negative values are indicated with dashed lines.

The total size of the radio structure extends for about 7 arcmin, such that the radio jets, which flare at 5 arcsec, are curved and display ‘ S ’ symmetry. Taylor et al. 1990 suggest that this shape may due to precession of the central engine.

The host galaxy has been identified with a cD having a double optical nucleus. Observations of nuclear optical emission lines reveal (Simkim 1979) a disk of gas with a rotation axis of 29° ±9°. This rotation axis is nearly parallel to the kpc scale jet axis of ∼26° (Taylor et al. 1990), and nearly perpendicular to the direction of the secondary nucleus, which is 10 arcmin from the primary optical nucleus at a

position angle of 125°.

Taylor & Perley (1993) have demonstrated extremely high (> 8000 radians m^{-2}) Faraday rotation measures (RMs) and a striking RM and depolarization asymmetry between the northern and the southern radio lobes, with the southern lobe having substantially greater RMs and depolarization (Fig. 3.9). They suggest the most likely mechanism to produce the high RM is a magnetized cluster gas.

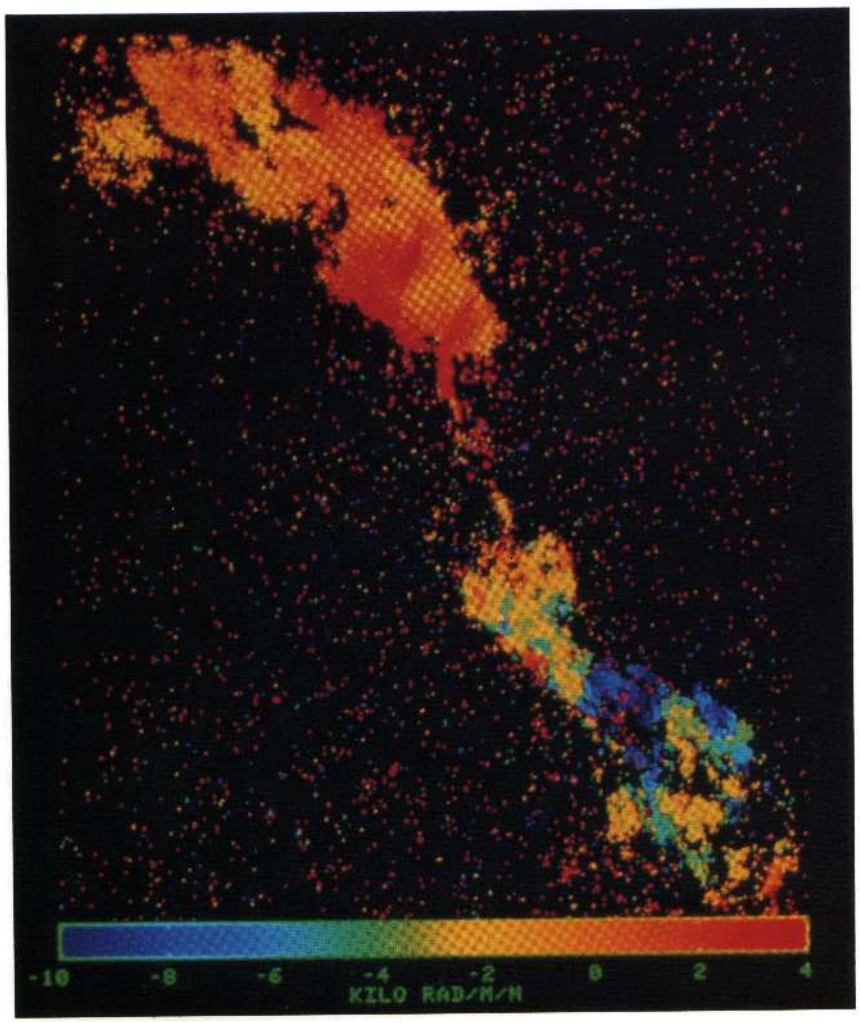

Figure 3.9: From Taylor & Pearly (1993): the RM structure of Hydra A at 0.3 arcsec of resolution. The images transition in the north lobe from the regime of -100 to +300 radians m $^{-2}$. The RM changes sign in the core. Gradients in RM and RMs are larger in the south lobe. The color indicates RM from -10000 to 4000 radians m^{-2}.

The asymmetry between the north and the south lobes can then be understood as partly due to the orientation of the radio source such that the northern lobe is closer to us and hence the radiation from it passes through a more shallow Faraday screen.

In view of this asymmetry and likely inclination of the source on the kpc scale, Hydra A appears remarkably symmetric on the parsec scale in the radio continuum. Fig. 3.10 shows the 1.3 , 5 and 15 GHz VLBA images of the nucleus of Hydra A (Taylor 1996) at 10 mas , 2 mas and 1 mas of resolution respectively. The northen side is identified as the jet being slightly stronger and the southern side is the counterjet. The jet is straight along a position angle of 23 ° and symmetric about the core with a jet/counterjet ratio of 1.2 at 1.3 GHz. This implies a $\beta\cos(\theta)\sim0.03$ for a continuous jet.

If all jet start relativistic, then the jet in Hydra A must be oriented within $\leq2^\circ$ of the plane of sky. However Taylor & Perley (1993) from rotation measures predict an inclination of 48°. Because of the good agreement between the projected pc and kpc jet axis, it is unlikely that the orientation discrepancy is due to large bend between the inner jet and the lobes. Alternatively, the inner jet could be aligned with the outer jet at 48° and the bulk jet velocity could be low (β= 0.05). Taylor (1996) suggested that the emission from the symmetric parsec-scale jets is more dependent on interactions with the surrounding material than on Doppler boosting. Other evidence supporting a fairly dense nuclear environment is free-free absorption of the inner jets and core by thermal gas with a density of 300 cm^{-3}, and HI absorption by a gas of similar density. A disk of HI is observed (Fig.3.11) with a total vertical extent $\sim$ 30 pc, and a rotation axis that is close (within 6°) to the jet axis of 23 °. This rotation is also consistent with that of the kiloparsec scale disk seen in optical emission limes.

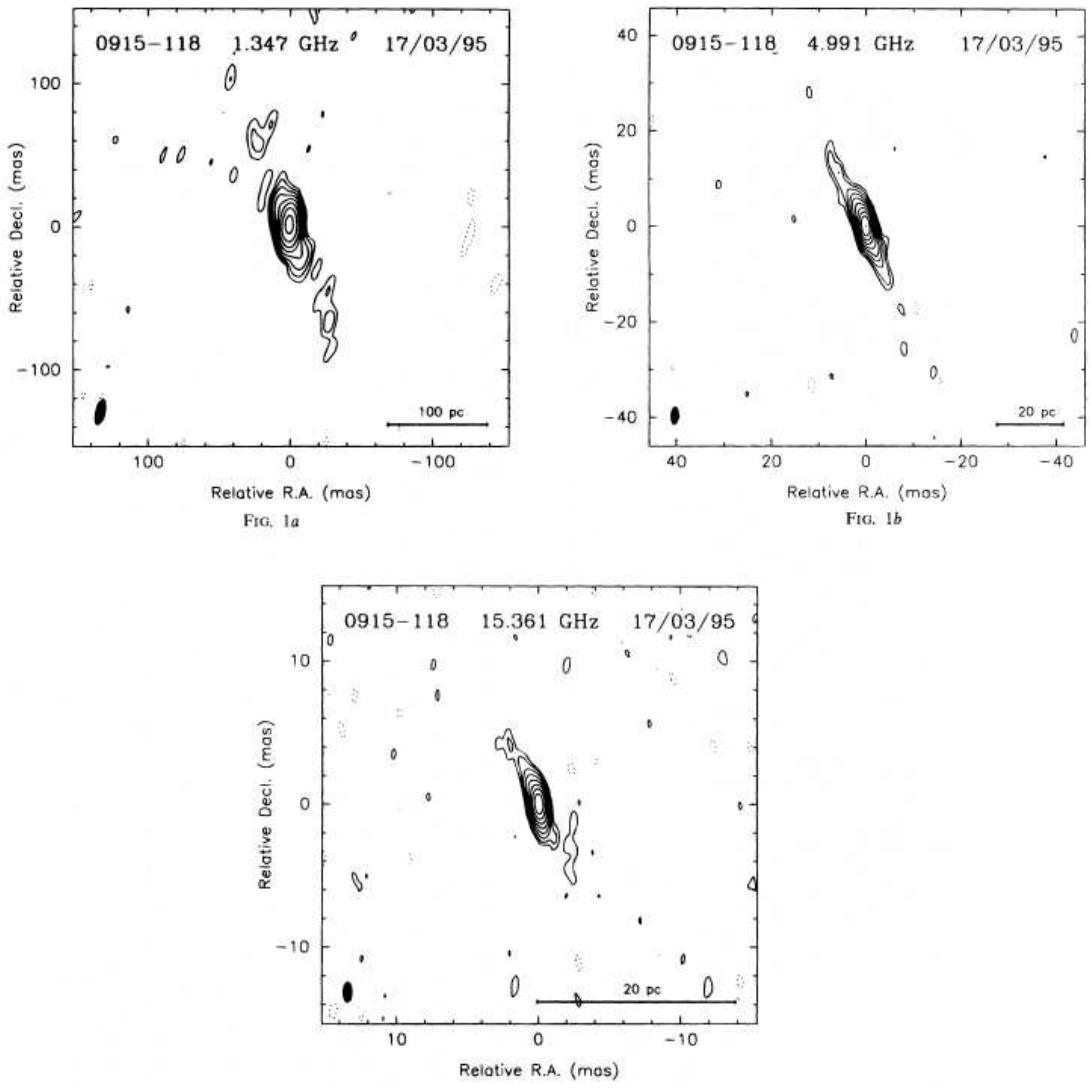

FIG. 1a FIG. 1b

Figure 3.10: From Taylor 1996: (a) The nucleus of Hydra A at 1.3 GHz. Contours are drawn at -0.5, 0.5, 1, 2, 4, 8, 16, 32 and 64 mJy/beam where the beam is 17.9 × 6.2 mas^2 in P.A. = -14 °. (b)The nucleus of Hydra A at 5 GHz. Contours are drawn at -0.3, 0.3, 0.6, 1.2, 2.4, 4.8, 9.6, 19.2, 38, 77 and 154 mJy/beam where the beam is 3.66 × 1.53 mas^2 in P.A. = -3 °. (c) The nucleus of Hydra A at 15 GHz. Contours are drawn at -0.6, 0.6, 1.2, 2.4, 4.8, 9.6, 19.2, 38 and 77 mJy/beam where the beam is 1.38 × 0.58 mas^2 in P.A. = -1 °.

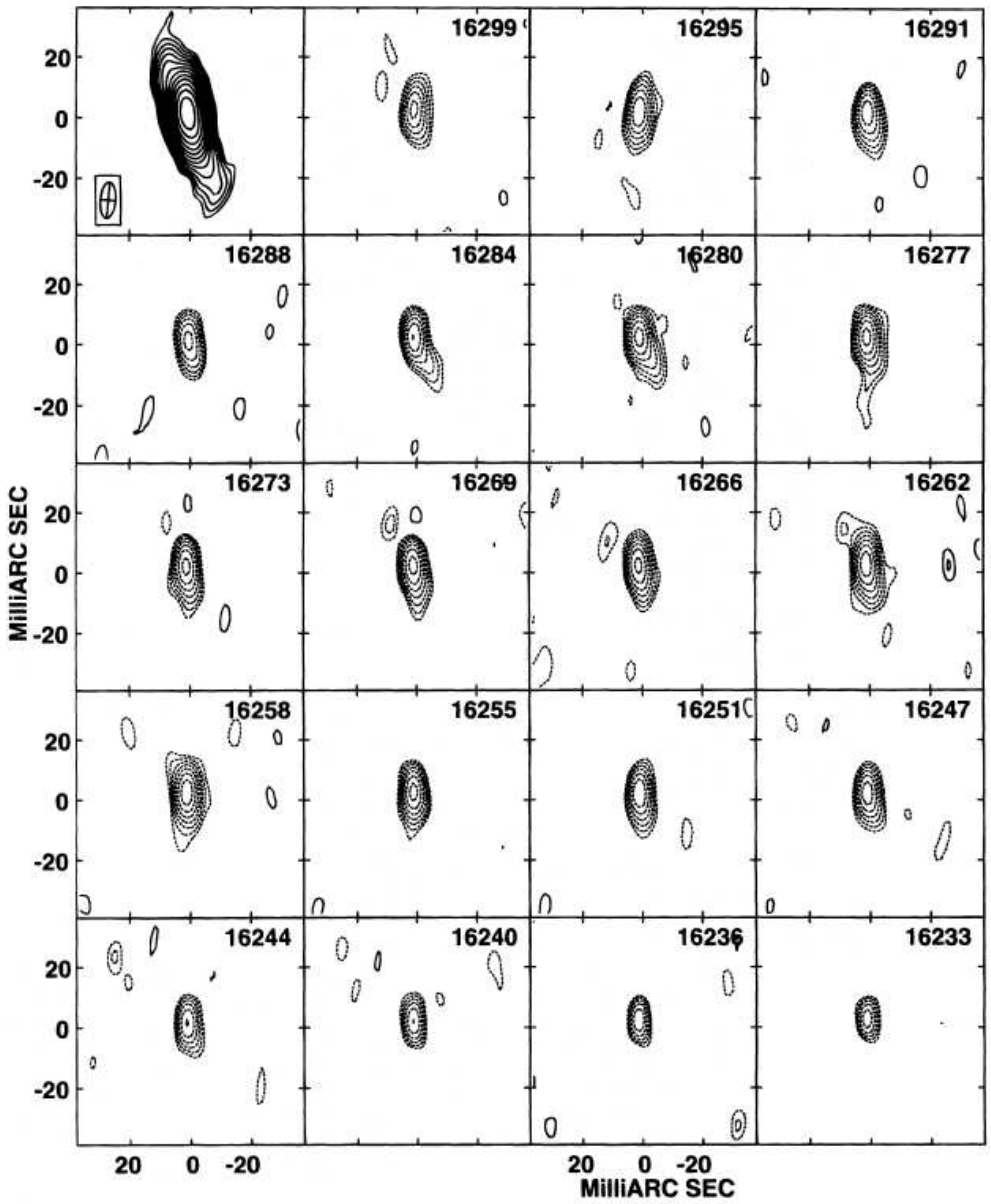

Figure 3.11: HI absoption in the central region of the spectrum in the nucleus of Hydra A. Contours are -6, -8, -11, -16, -22, and -32 mJy /beam with a beam size of 14 $\times$6 mas^2 in P.A. = -5 °. The peak absorption occurs at velocity of 16, 258 km/s. Each channel is separated by 3.67 km/s. The continuum image at the same resolution is shown in the top left of the panel with contours starting at 1 mJy/beam and increasing by a factors of root 2.

3.3 3C 84 in Abell 426 (Perseus Cluster).

3.3.1 Introduction.

The Perseus Cluster, A426, is the most X-ray luminous cluster in the nearby universe, and the prototypical cooling core cluster. Shocks and ripples are clearly evident in the deep Chandra image of Perseus (Fabian et al. 2005, 2006), and could provide steady heating of the center of the cluster (Fabian et al. 2006).

The Perseus cluster (first detected in mm by Mirabel et al. 1989) remained the only cooling flow cluster core mapped in CO for approximately 10 years. During this time the origin of the molecular emission was probed by various maps that were limited in both size and sensitivity. Reuter et al. (1993) imaged the millimetric emission of the central cluster region in CO(1-0) and CO(2-1) emission lines with the IRAM 30 m telescope and built the first map of the central $\sim 50''$. Braine et al. (1995) then observed the Perseus cluster in CO(1-0) with the IRAM Plateau de Bure interferometer (PdBI). Emission was detected around the nucleus but the continuum source made the map very noisy at the center. The authors suggested that the molecular gas could come from a source other than a cooling flow, such as a recent merger event. More recently, Inoue et al. (1996a) observed the cluster center with the Nobeyama Millimeter Array in CO(1-0) using a primary beam of $65''$ in diameter. Two peaks were identified within the inner 3 kpc (8 arcsec), which may be parts of a ring-like orbiting gas structure around the nucleus that could trace the AGN fueling by the cD galaxy. Finally, the most recent millimetric map of the central $1'$ region has been made by Bridges & Irwin (1998) with the JCMT (James Clerk Maxwell Telescope) in CO(2-1) and CO(3-2) emission lines in single dish mode. Detections out to $36''$ have been claimed, with a spatial resolution of $21''$.

Large optical nebulae are often observed within cooling flow clusters of galaxies (Crawford et al. 1999), and not detected surround galaxies in clusters where the radiative cooling time is larger than the age of the cluster. The Perseus cluster harbors a huge Hα filamentary nebula (McNamara et al. 1996a; Conselice et al. 2001; Hu et al. 1983). The origins of the optical filaments and their ionization source are not identified yet. However they do trace, in some part, the radiative cooling of the hot intracluster medium either directly or indirectly. Fabian et al. (2003) compared the X-ray structures with the optical emission and proposed that

the Hα filaments could be ionized cold gas that has been drawn up behind a rising bubbles of relativistic plasma, a picture that takes into account the role of a central radio source in cooling flows (see also Boehringer et al. 1993).

Hα also correlates with the presence of warm H_2, at $\sim$1000-2000 K (Wilman et al. 2002; Edge et al. 2002). Recent United Kingdom Infra-Red Telescope (UKIRT) observations (Hatch et al. 2005) have shown a direct association between this H_2 emission and the outer optical filaments in NGC 1275. Based on near-IR Integral Field Unit (IFU) observations of the warm H_2, Wilman et al. (2005) found a 50 pc radius ring in the central part of the galaxy. The strong Hα emission in cooling flows also traces the presence of cold molecular gas. There is a strong correlation between Hα and CO, at $\sim$10-100 K (Salomé & Combes 2003; Edge 2001), which is reinforced by a clear association, both in terms of morphology and dynamics. This is revealed as discussed before in the IRAM PdBI CO(1-0) and CO(2-1) maps of Abell 1795.

To better understand the origin of the molecular gas in Perseus A, Lim et al. 2008 have imaged this galaxy in CO(2-1) at an angular resolution of 3″ (spatial resolution of 1 kpc) with the Submillimeter Array (SMA).

The SMA map of Lim et al. 2008 (Fig. 3.12), which covers a region of radius $\sim$2″ ($\sim$10 kpc) centered on Perseus A, reveals the following:

- The molecular gas is concentrated primarily in three radial filaments that, along with several blobs, have a total mass in molecular gas of (4.2$\pm$ 0.2) $\times$ 10^9 $M_\odot$, with the three filaments alone containing $\sim$80% of the detected gas mass.

- The bulk of the molecular gas detected is aligned roughly east-west and lies between two X-ray cavities to the north and south of center. This gas is aligned approximately orthogonal to the axis of the radio jets from the AGN in Perseus A.

- Lying on the far (back) side of Perseus A, the two outer filaments are therefore flowing radially inward toward the center of the galaxy. The only known process that can naturally deposit gas in this manner is an X-ray cooling flow. Moreover, the two outer (western and eastern) filaments, and the other blobs of molecular gas, exhibit blueshifted velocities. The velocities of both

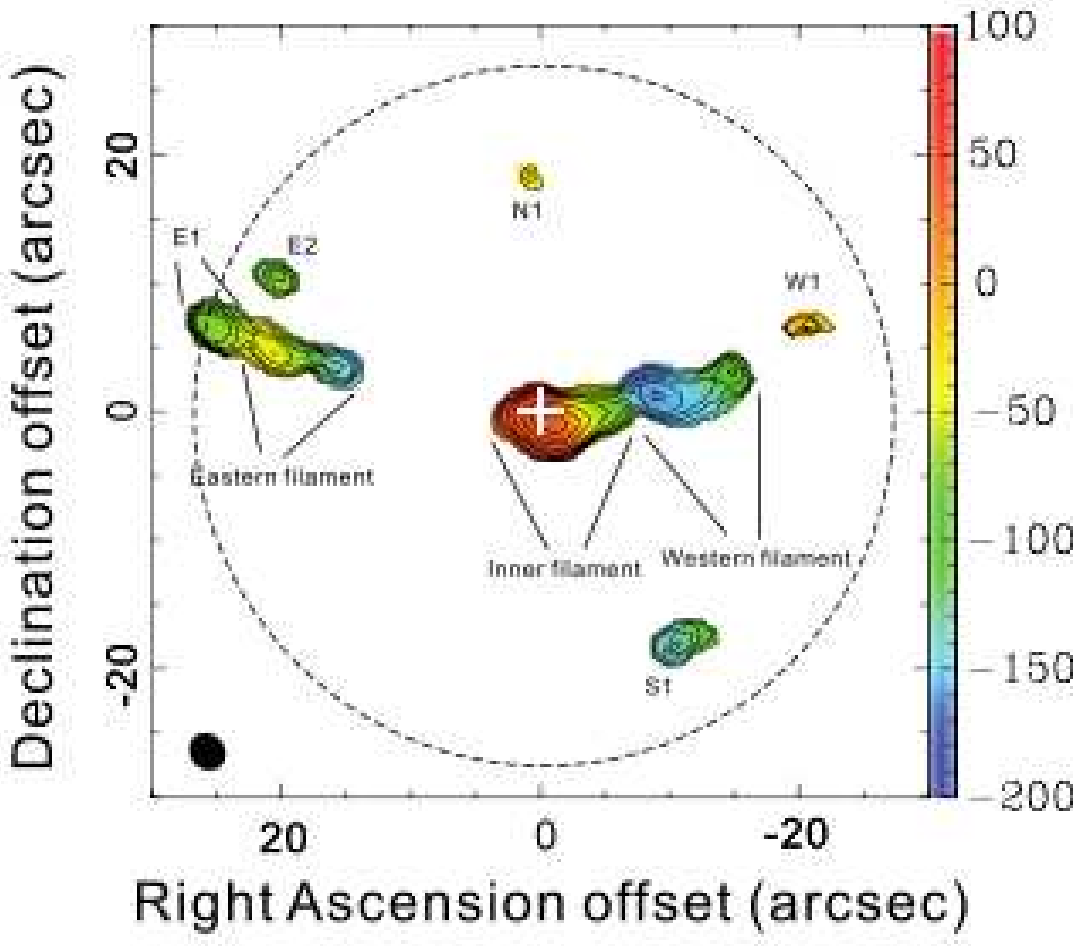

Figure 3.12: Contours of the integrated CO(2-1) intensity plotted at levels of 3, 6, 9, 12, 15, 20, 30, 40, and 50× 0.32 Jy km s^{-1} , and a color-coded map of the intensity-weighted CO(2-1) mean velocity measured with respect to the systemic heliocentric velocity of 5264± 11 km s $^{-1}$ (Huchra et al. 1999), as indicated by the right vertical bar. The FWHM of the SMA primary beam is 55″ (20 kpc), as indicated by the dotted circle. The integrated CO(2-1) intensity has been corrected for the primary beam response. The map is centered on the active nucleus of Perseus A R.A.=$03^h19^m48.16^s$, decl.=41°30′42.1″), which was detected in the continuum at the location indicated by a cross. The synthesized beam is shown as a filled ellipse at the lower left corner, and has a size of $3.0'' \times 2.7''$ with a major axis at a position angle of 39.5°. The features E1, E2, W1, N1, and S1 are discussed in Lim et al. 2008.

these filaments change linearly with radius to larger blueshifted velocities at smaller radii. The velocity pattern of the two outer filaments can be easily reproduced as free fall in the gravitational potential of Perseus A, with their outer tips lying ∼1 kpc downstream from where the cooling gas first decouples from the X-ray gas. Both filaments have a dynamical age of ∼20 Myr, implying

a total mass deposition rate into these filaments of roughly ∼75 $M_\odot$/yr (likely accurate to only a factor of a few).

- All the molecular gas detected in the east-west direction is spatially coincident with H_α gas, often lying against or close to local H_α brightenings. Where measured, specifically at the locations of the inner and western filaments, the velocities of the H_α gas are comparable with that of the molecular gas. The molecular gas also coincides spatially with a band of relatively cool X-ray gas lying between the two X-ray cavities.

3.3.2 The radio structure.

In Perseus the AGN manifests itself directly as a bright radio source known as Perseus A or 3C 84, associated with the early-type cD galaxy NGC1275 (Fig. 3.13). The feature coincident with the center of the galaxy constitutes one of the strongest compact radio sources in the sky. For these reasons, 3C 84 has been studied in some detail (Vermeulen et al. 1994; Taylor & Vermeulen 1996; Silver et al. 1998; Walker et al. 2000). Being the nearest (z=0.0178) BCG in our sample, it is the best studied also at high resolution. The radio source 3C 84 possesses well known jets which have been documented on a variety of scales (Pedlar et al. 1990; Dhawan et al. 1998; Silver et al. 1998; Walker et al. 2000). This source began a major increase in activity in about 1959. It was below 10 Jy in the earliest observations, but was already rising toward peaks in excess of 50 Jy in the 1970s and 1980s (Dent 1966; Pauliny-Toth& Kellermann 1966; Pauliny-Toth et al. 1976; O'Dea, Dent & Balonek 1984; Nesterov, Lyuty & Valtaoja 1995). It has been high ever since, although in recent years the flux density had been decaying and is currently around 20 Jy at centimeter wavelengths.

Taylor et al. (2006) found substantial Faraday RMs of ∼7000 rad m^{-2} toward 3C 84. RMs as large or larger than this have been suspected for some time due to the low observed polarization from this bright radio galaxy. The Faraday screen is most likely to be associated with the ionized gas that also produces spectacular filaments of H_α emission in the Perseus cluster. This gas may well have magnetic fields organized on small enough scales (<10 pc), to produce the observed gradient in the RM. In particular, Taylor et al. (2006) detect linear polarization from the bright jet component in south in 3C 84 at 5, 8, 15 and 22 GHz at a level of 0.8 to

7.5% increasing with frequency. Furthermore, there is some suggestion at 8.4 GHz and above that the polarization is extended. The detection of core polarization is less than 0.1% for all frequencies except for 22 GHz for which it is less than 0.2%.

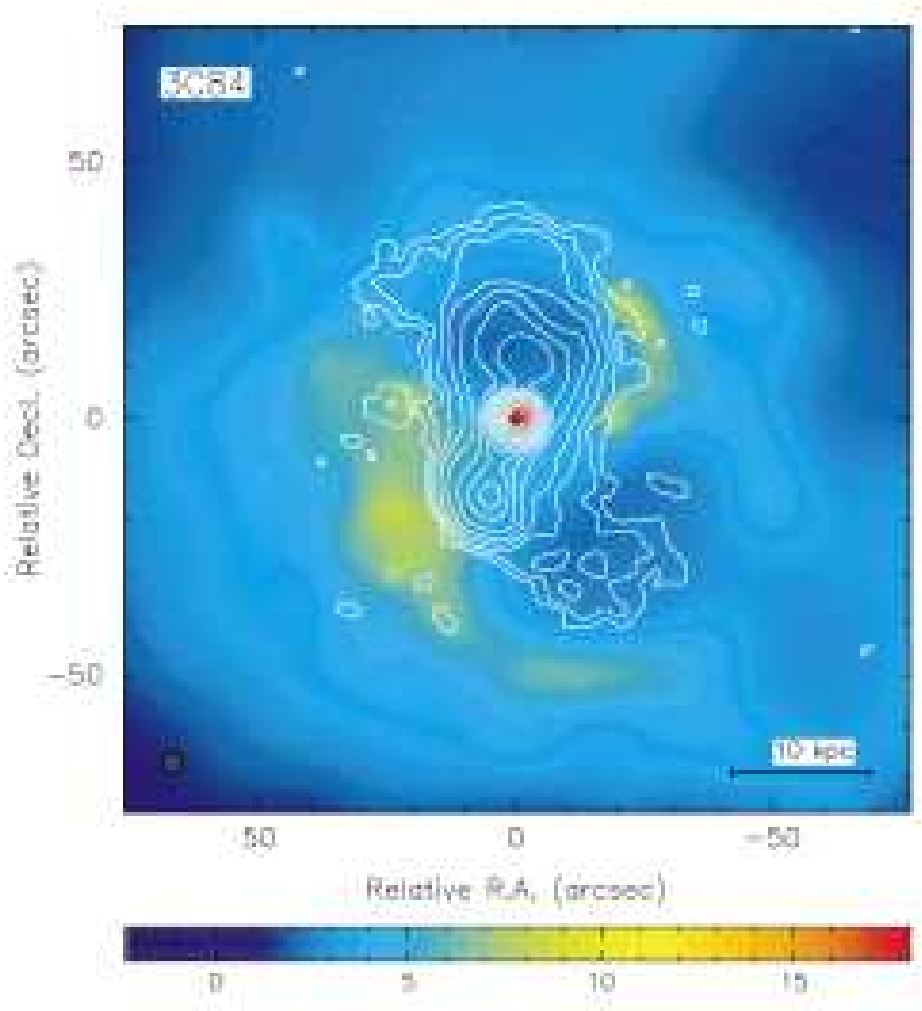

Figure 3.13: VLA observations (contour level) at a frequency of 1.4 GHz overlay to Chandra image (colour image) (Fabian et al. 2000). The radio map has a restored beam of 5 arcsec. Contour levels start at 1 mJy/beam and increase by factors of 2 to just below the peak of 21.7 Jy/beam.

.

On parsec scale, the radio morphology is quite complex (Asada et al. 2009; Lister 2001; Agudo et al. 2005) exhibiting a core with two opposite radio-jets. VLBA data show that, south of the compact core, there is a bright region of emission that has been increasing in length by about 0.3 mas/ yr. The bright region now extends (Fig. 3.14) about 15 mas south of the compact core. It is almost certainly related to a jet,

but the morphology is somewhat like the radio lobes seen in many sources on much larger scales. This, with age estimation from spectral index considerations (Asada et al. 2009; Lister 2001; Agudo et al. 2005), may indicate that the jet material from the 1959 event is not simply following earlier material down the jet channel, but is interacting strongly with either that material or the surrounding medium.

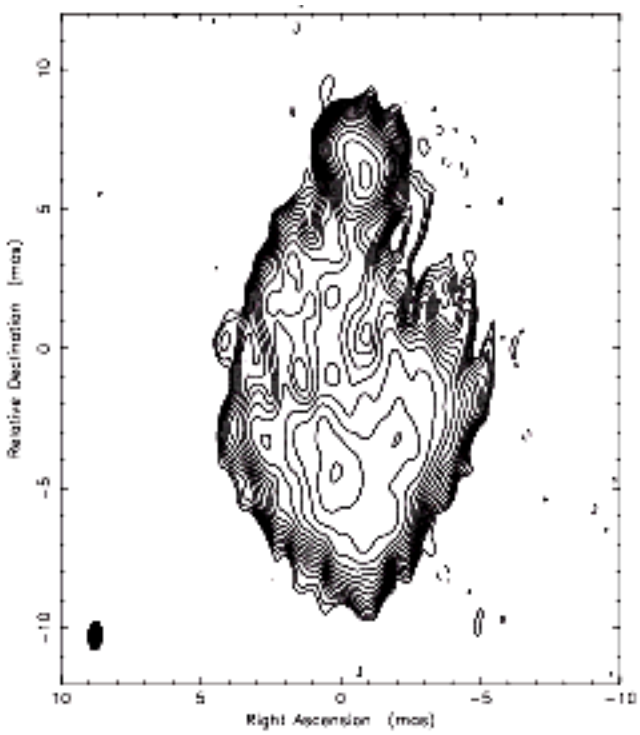

Figure 3.14: VLBA image of the total intensity of 3C 84 at 4.9 GHz (Asada et al. 2009). Contour levels are 0.000247 × (5.66, 8, 11.3, 22.6, 32, 45.3, 64, 90.5, 128, 181) Jy/beam. The restoring beam is 1.04 × 0.465 mas in P.A. = -1.88 °.

Beyond the bright southern feature, the remnants of earlier activity are clearly seen. Immediately south of the 15 mas bright feature, low-frequency VLBI observations show (Fig. 3.15) a continuation of the jet to about 100 mas (e.g., Taylor & Vermeulen 1996; Silver, Taylor & Vermeulen 1998)

Taylor, & Vermeulen 1998 also see a "millihalo" (Fig.3.16) approximately 250 mas in size at 330 MHz. On scales of arcseconds and larger, 3C 84 has weak, somewhat asymmetric twin jet structure surrounded by a diffuse halo (Pedlar et al. 1990; Sijbring 1993).

The jet morphology itself has been imaged on a variety of scales.

At high frequency (and resolution) we compared the VLBA image at 43 GHz (Lister 2001) with the 86 GHz image by Lee et al. (2008) (Figs. 3.17 and 3.18).

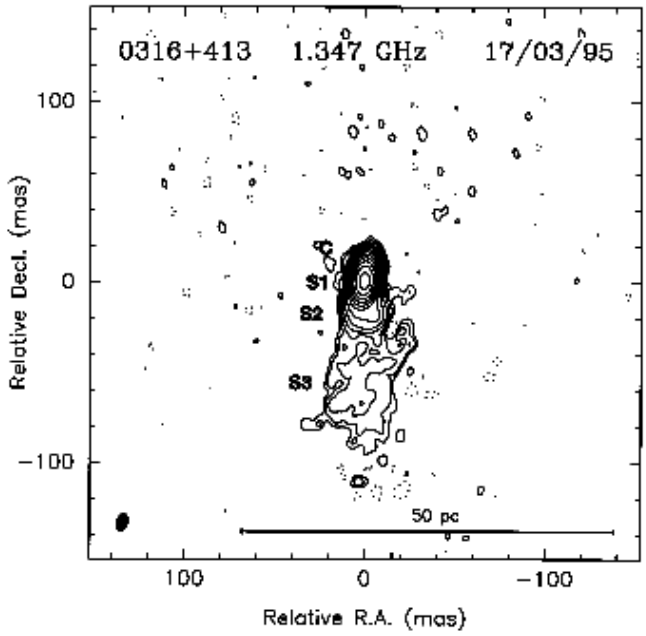

Figure 3.15: VLBA image at 1.3 GHz of 3C 84 (Taylor & Vermeulen 1996). The restoring beam has dimensions of 9.8×5.7 mas^2 in position angle of - 16 °. Contour levels are -4, 4, 8, 16, 32...8192 mJy/beam with negative values in dashed lines. For the discussion about the components C, S1, S2 , S3 see Taylor & Vermeulen 1996.

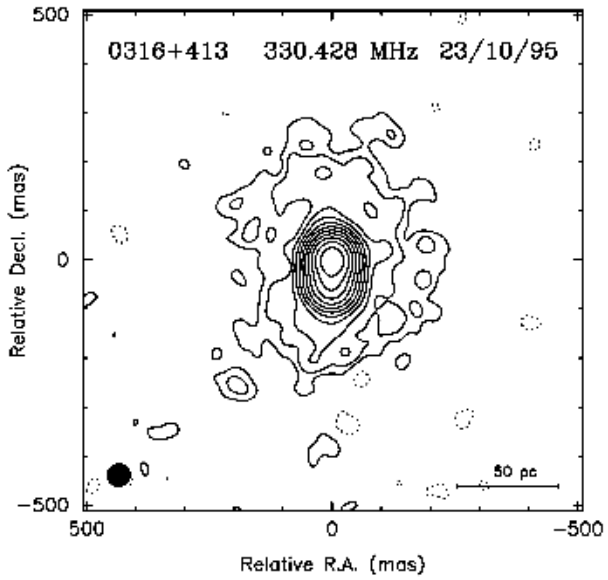

Figure 3.16: Naturally weighted and tapered image of 3C 84 at 330 MHz. The image was restored with a circular 45 mas beam. Contour levels are at -2, 2, 4, 8, 16, 2048 mJy/beam, with negative contours shown as dashed lines (Taylor & Vermeulen 1998). A "millihalo" of diffuse emission surrounding the central source is evident.

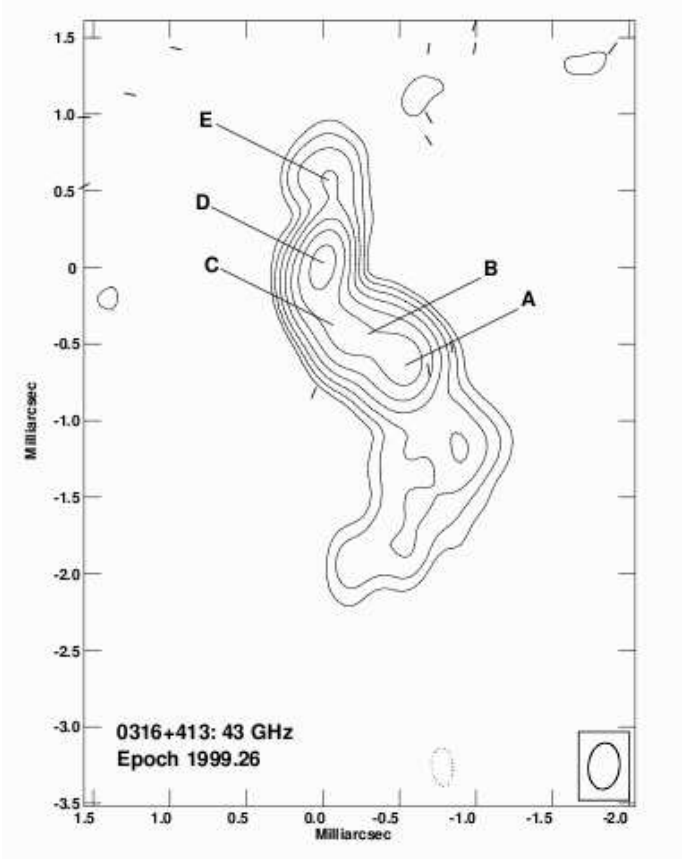

Figure 3.17: VLBA total intensity image of 3C 84 at 43 GHz, with electric vectors superimposed (Lister 2001). We identify the component E as the core.

Despite different epochs and resolutions we tentatively identify the core with component "E″ in Lister (2001) being the only self-absorbed structure (inverted spectrum) between 43 and 86 GHz. Therefore the source appears initially one-sided, and later becomes two-sided (Fig.3.19) implying that the jet interaction with the dense surrounding medium produces the slowing down of the initially relativistic jet at sub-pc scale (Taylor et al. 2006).

VLBA data at 15 GHz (Lister et al. 2009) measure proper motion in the jet and counterjet and estimate γ=0.6 and θ=11°. In VLBA data at 5 GHz (Taylor et al. 2006) the largest source angular size is $\sim$ 35 mas ($\sim$12 pc) , the core flux density is $\sim$ 3.1 Jy (P $\sim$ 2.1 $\times$ 10^{24} W/Hz) and the total flux density is 23.3 Jy (P $\sim$ 1.6 $\times$ 10^{25} W/Hz).

At lower frequency and resolution, there is a clear equivalence between the parsec-scale structure and jets seen on kiloparsec-scale (Pedlar et al. 1990). Looking through VLBA images from 22 GHz to 5 GHz, the two-sided structure starts out

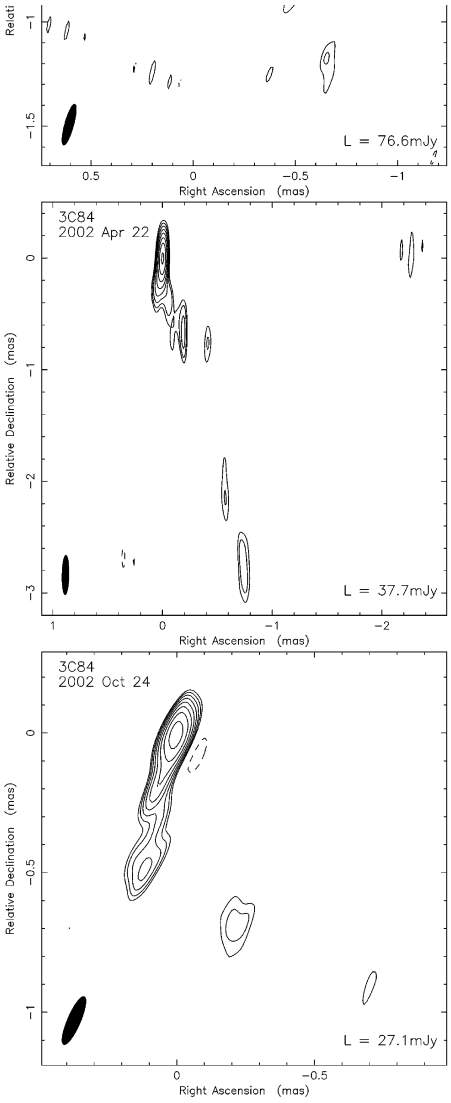

Figure 3.18: VLBA image of 3C 84 at 86 GHz (Lee et al. 2008). Minimum contour level is shown in the lower-right corner of each map. The contours have a logarithmic spacing and are drawn at 1, 1, 1.4, ..., 1.4n of the minimum contour level.

appearing more symmetric and then at lower frequencies it becomes asymmetric. Walker et al. (1998, 2000) explained this as effects of free-free absorption of the counter-jet from the surrounding torus. They show two separate epochs (Fig. 3.20) in which the absorption was observed nearly simultaneously at five frequencies.

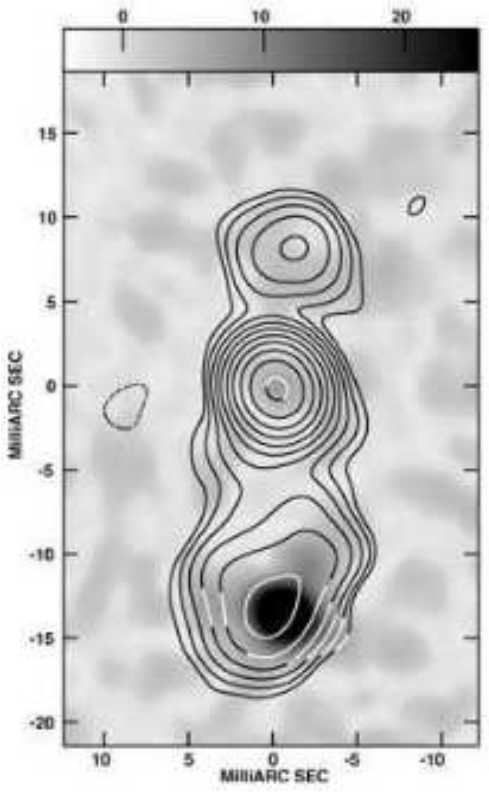

Figure 3.19: VLBA observations of 3C 84 at 15 GHz at angular resolution of 2.75 mas Taylor et al. (2006). The grey-scale represents linearly polarized intensity ranging from 4 to 2 mJy/beam. Contour levels begin at 15 mJy/ beam and increase by a factor of 2.

The observed spectral indices are sufficiently steep to preclude other absorption mechanisms.

The observed absorption is consistent with the model for which the northern feature is on the far side of the system relative to the Earth. There is an accretion disk extending to the parsec scales observed here and that accretion disk has associated ionized gas that is responsible for the absorption. The amount of ionized gas falls off fairly rapidly with core distance.

Concluding, the parsec scale morphology of 3C 84 could be interpreted as the following. The source starts one-sided (Lister 2001; Lee et al. 2008) (that means relativistic jet velocities). After, being in the center of a cool core cluster, due to strong interaction with the dense surrounding medium (Taylor et al. 2006), the jets slow down. They become mildly relativistic and 3C 84 appears two -sided in low frequency and high resolution (Walker et al. 2000; Taylor et al. 2006). See Chapter 5 for more discussion.

Finally, we have to remark that, looking at low resolution and frequency, 3C 84 shows again an asymmetric radio emission as consequence of free-free absorption (Walker et al. 2000).

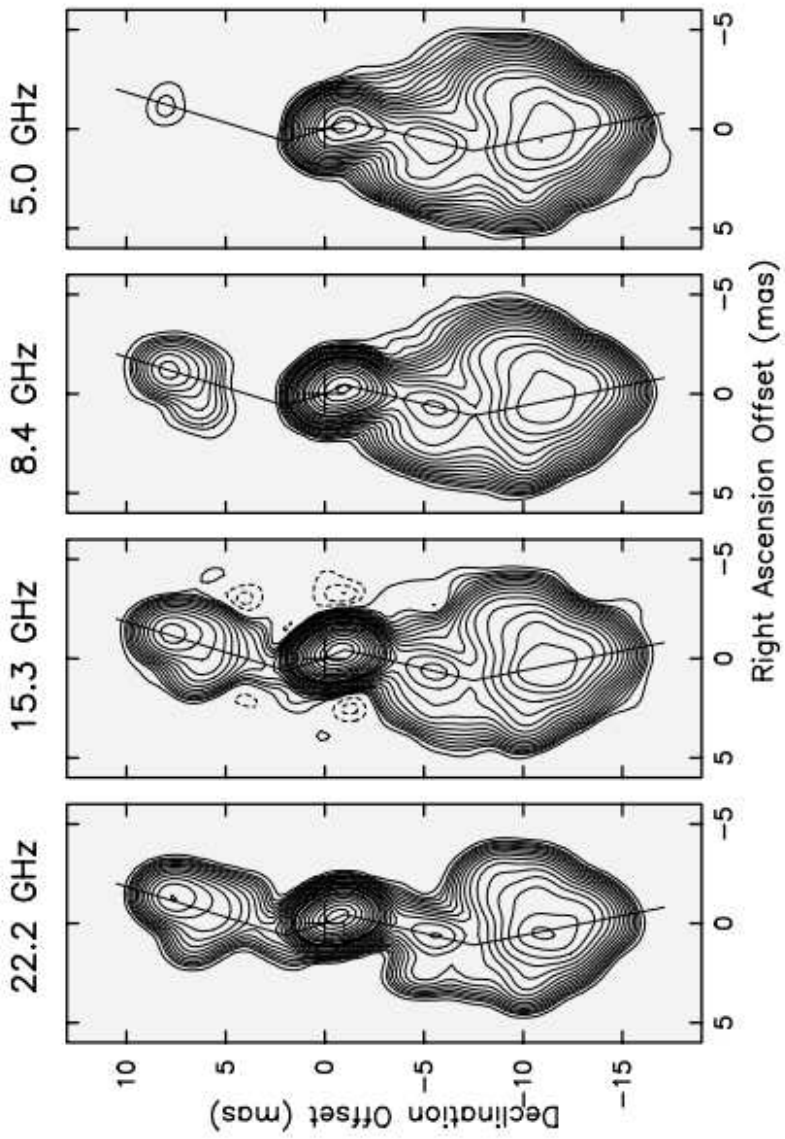

Figure 3.20: Montage of the VLBA images of 3C 84 based on data taken in 1995 January (Walker et al. 2000). The restoring beam has dimensions of 1.6 × 1.2 mas^2, elongated north-south. The contour levels start with 5, 10, 14, 20 mJy/beam and increase from there by factors of $\sqrt{2}$. The north-south segmented line shows the location of the slice along which (Walker et al. 2000) made analysis (see Walker et al. (2000)).

Chapter 4

The comparison sample: the Bologna Complete Sample.

4.1 The aim of the BCS study.

The study of the parsec scale properties of radio galaxies is crucial to obtain information on the nature of their central engine. In order to study statistical properties of different classes of sources, it is necessary to define and observe a sample that is free from selection effects. To this aim, it is important to select samples using low radio frequencies. Sources in low frequency selected samples are dominated by their extended and unbeamed (isotropic) emission, rather than the beamed compact emission that dominates in high frequency selected surveys. Low frequency selected surveys are therefore unbiased with respect to the orientation of the nuclear relativistic jet. With this purpose in mind, we initiated a project to observe a complete sample of radio galaxies selected from the B2 Catalog of Radio Sources and the Third Cambridge Revised Catalog (3CR) (Giovannini et al. 1990, 2001), with no selection constraint on the nuclear properties. We named this sample "the Bologna Complete Sample" (BCS). In the original sample, 95 radio sources from the B2 and 3CR catalogs were present, but because of the rejection of one source discussed here, we have redefined the complete sample to be 94 sources. We selected the sources to be stronger than a flux density limit of 0.25 Jy at 408 MHz for the B2 sources and greater than 10 Jy at 178 MHz for the 3CR sources (Feretti et al. 1984) and applied the following criteria:

1) declination $> 10°$;

2) Galactic latitude $|b| > 15°$;

3) redshift z<0.1;

In Giovannini et al. (2005), the sample is presented and VLBI observations for an initial group of 53 sources having bright nuclear emission are discussed. Observations were carried on with the standard VLBI technique.

Moreover a few sources have been discussed in detail and results have been presented in several papers (references are provided to these in Tab.4.1).

Here we discuss new VLBA observations that we analyze during this PhD project at 5 GHz for 26 radio galaxies with a core flux density $S_{5GHz} > 5$ mJy, 23 of them observed for the first time at mas resolution. We also present new VLBA observations at 1.6 GHz for 10 radio galaxies in order to study their extended nuclear emission. Since a few sources were observed at both frequencies, the total number of sources with new data presented here is 33. For all sources we report on parsec-scale observations and discuss in detail their structure and properties.

To complete VLBI data of the BCS sample, we asked in February 2010 VLBA and EVN observations of the remaining 18 sources. Since these sources have a very faint nuclear emission in the radio band we asked for very sensitive VLBI observations (large bandwidths, long integration times, and phase referencing).

4.2 The Sample.

In Table 4.1, we give the complete list of radio sources and summarize the most relevant information. We reported the IAU name (column 1), other name (column 2) and the redshift of the sources (column 3). For the kiloparsec morphology, we indicate if the source is a Faranoff type I or II radio galaxy (FRI/II), or a compact source, further distinguishing between flat spectrum compact sources (C), and Compact Steep Spectrum sources (CSS). Among flat spectrum compact sources, two are identified with BL-Lac type objects. Since these are well known objects (Mkn 421 and Mkn 501), in Table 1 and in the text we refer to them as BL-Lac objects. We indicate with $S_{c,5}$ the arcsecond core flux density at 5 GHz and with $\mathrm{Log\,P}_c$ the corresponding logarithm of the radio power. $\mathrm{Log\,P}_t$ is the total radio power at 408 MHz. Notes in the last column refer to the status of VLBI observations: (N) new VLBI data are given for the first time in this work, (N*) the source was previously observed with VLBI, but new data are presented here, (G) see Giovannini et al. (2001), (I) see Giovannini et al. (2005). Numbers refer to recent (post 2001) papers

where a few peculiar sources have been discussed in detail.

Table 4.1: The Complete Bologna Sample

Name IAU	Name other	z	Morphology kpc	$S_c(5.0)$ mJy	Log P_c W/Hz	Log P_t W/Hz	Notes
0034+25	UGC367	0.0321	FR I	10	22.40	23.80	N
0055+26	N326	0.0472	FR I	11	22.75	25.40	N
0055+30	N315	0.0167	FR I	588	23.57	24.24	G
0104+32	3C31	0.0169	FR I	92	22.76	24.80	G
0106+13	3C33	0.0595	FR II	24	23.30	26.42	I
0116+31	4C31.04	0.0592	C	1250	23.42	25.46	I, 1
0120+33	N507	0.0164	FR I	1.4	20.93	23.62	no VLBI
0149+35	N708	0.0160	FR I	5	21.46	23.32	N
0206+35	4C35.03	0.0375	FR I	106	23.54	25.17	G
0220+43	3C66B	0.0215	FR I	182	23.28	25.30	G
0222+36		0.0327	C	140	23.52	23.93	G,5b
0258+35	N1167	0.0160	CSS	<243	<23.14	24.35	G,5b
0300+16	3C76.1	0.0328	FR I	10	21.38	24.09	N
0326+39		0.0243	FR I	78	23.01	24.40	I
0331+39	4C39.12	0.0202	C	149	23.11	24.20	G
0356+10	3C98	0.0306	FR II	9	22.28	25.73	N
0648+27		0.0409	C	58	23.36	24.02	G,5b
0708+32		0.0672	FR I	15	23.20	24.49	N
0722+30		0.0191	Spiral?	51	22.62	23.49	N
0755+37	N2484	0.0413	FR I	195	23.82	25.36	G
0800+24		0.0433	FR I	3	22.11	24.14	no VLBI
0802+24	3C192	0.0597	FR II	8	22.83	26.01	N
0828+32AB	4C32.15	0.0507	FR II	3.3	22.29	25.41	no VLBI
0836+29-I	4C29.30	0.0650	FR I	63.0	23.79	25.19	N
0836+29-II	4C29.30	0.0790	FR I	131	24.28	25.42	G
0838+32	4C32.26	0.0680	FR I	7.5	22.91	25.32	N
0844+31	IC2402	0.0675	FR II	40	23.56	25.53	I
0913+38		0.0711	FR I	<1.0	<22.08	24.99	no VLBI
0915+32		0.0620	FR I	8.0	22.86	24.63	N
0924+30		0.0266	FR I	<0.4	<20.80	24.44	no VLBI
1003+35	3C236	0.0989	FR II	400	24.97	26.16	I
1037+30	4C30.19	0.0909	C	<84	<24.22	25.36	I
1040+31		0.0360	C	55	23.21	24.70	I
1101+38	Mkn 421	0.0300	BL Lac	640	24.11	24.39	G
1102+30		0.0720	FR I	26	23.50	25.07	I
1113+29	4C29.41	0.0489	FR I	41	23.27	25.35	N
1116+28		0.0667	FR I	30	23.50	25.05	I, N*
1122+39	N3665	0.0067	FR I	6	20.77	22.45	N
1142+20	3C264	0.0206	FR I	200	23.28	25.17	G, 3

Table 4.1: continued.

Name IAU	Name other	z	Morphology kpc	$S_c(5.0)$ mJy	Log P_c W/Hz	Log P_t W/Hz	Notes
1144+35		0.0630	FR I	250	24.37	24.49	G, 7
1204+24		0.0769	FR I	8	23.05	24.58	N
1204+34		0.0788	FR II?	23	23.53	25.17	I
1217+29	N4278	0.0021	C	162	21.20	21.75	G, 5
1222+13	3C272.1	0.0037	FR I	180	21.74	23.59	G
1228+12	3C274	0.0037	FR I	4000	23.30	25.38	G
1243+26B		0.0891	FR I	<1.8	<22.54	25.23	no VLBI
1251+27	3C277.3	0.0857	FR II	12	23.33	26.05	N
1254+27	N4839	0.0246	FR I	1.5	21.31	23.45	9
1256+28	N4869	0.0224	FR I	2.0	21.31	24.22	no VLBI
1257+28	N4874	0.0239	FR I	1.1	21.15	23.81	9
1316+29	4C29.47	0.0728	FR I	31	23.58	25.59	I
1319+42	3C285	0.0797	FR I/II	6	22.95	25.92	N
1321+31	N5127	0.0161	FR I	21	22.09	24.32	I
1322+36	N5141	0.0175	FR I	150	23.01	24.07	G
1339+26	UGC8669	0.0722	FR I	<55	<23.83	25.19	N
1346+26	4C26.42	0.0633	FR I	53	23.70	25.47	I, N*, 8
1347+28		0.0724	FR I	4.8	22.78	24.81	no VLBI
1350+31	3C293	0.0452	FR I	<100	<23.67	25.68	I, N*, 4
1357+28		0.0629	FR I	6.2	21.97	24.81	N
1414+11	3C296	0.0237	FR I	77	22.98	24.93	I
1422+26		0.0370	FR I	25.0	22.89	24.80	I
1430+25		0.0813	FR I	<1.0	<22.20	25.34	no VLBI
1441+26		0.0621	FR I	<0.7	<21.81	24.78	no VLBI
1448+63	3C305	0.0410	FR I	29	23.05	25.44	I
1502+26	3C310	0.0540	FR I	80	23.73	26.20	I, N*
1512+30		0.0931	C	<0.4	<21.92	24.75	no VLBI
1521+28		0.0825	FR I	40	23.81	25.40	I
1525+29		0.0653	FR I	2.5	22.40	24.64	no VLBI
1528+29		0.0843	FR I	4.5	22.89	25.10	no VLBI
1529+24	3C321	0.0960	FR II	30	23.83	26.20	I
1549+20	3C326	0.0895	FR II	3.5	22.83	26.27	no VLBI
1553+24		0.0426	FR I	40	23.22	23.92	I
1557+26	IC4587	0.0442	C	31	23.42	24.05	I
1610+29	N6086	0.0313	FR I	<6.0	<22.12	23.85	no VLBI
1613+27		0.0647	FR I	25	23.40	24.65	I
1615+35B	N6109	0.0296	FR I	28	22.75	25.13	N
1621+38	N6137	0.0310	FR I	50	23.03	24.30	I
1626+39	3C338	0.0303	FR I	105	23.33	25.57	G, 6
1637+29		0.0875	FR I	13	23.38	25.17	N
1652+39	Mkn 501	0.0337	BL-Lac	1250	24.51	24.36	G, 2
1657+32A		0.0631	FR I	2.5	22.37	25.07	no VLBI
1658+30	4C30.31	0.0351	FR I	84	23.36	24.63	I

Table 4.1: continued.

Name IAU	Name other	z	Morphology kpc	$S_c(5.0)$ mJy	Log P_c W/Hz	Log P_t W/Hz	Notes
1736+32		0.0741	FR I	8	23.01	24.89	N
1752+32B		0.0449	FR I	12	22.74	24.17	N
1827+32A		0.0659	FR I	26	23.43	24.88	I
1833+32	3C382	0.0586	FR II	188	24.18	26.04	G
1842+45	3C388	0.0917	FR II	62	24.10	26.47	I
1845+79	3C390.3	0.0569	FR II	330	24.39	26.30	G
1855+37		0.0552	C	<100	<23.85	24.75	I
2116+26	N7052	0.0164	FR I	47	22.46	23.29	I
2212+13	3C442	0.0262	FR I?	2.0	21.49	25.21	no VLBI
2229+39	3C449	0.0181	FR I	37	22.44	24.68	I
2236+35	UGC12127	0.0277	FR I	8.0	22.14	24.12	N
2243+39	3C452	0.0811	FR II	130	24.30	26.64	G
2335+26	3C465	0.0301	FR I	270	23.74	25.61	G

$S_c(5.0)$ is the arcsecond core flux density at 5.0 GHz;

Log P_c is the corresponding logarithm of the radio power;

Log P_t is the logarithm of the total radio power at 408 MHz;

Morphology: C = flat spectrum compact core, CSO = Compact Symmetric Object,

CSS = Compact Steep Spectrum source,

FRI or II = Fanaroff type I or II;

Notes refer to the status of VLBI observations:

G: Giovannini et al. 2001; I: Giovannini et al. 2005; N, N* new data are given in this work;

1: Giroletti et al. 2003a,b; 2: Giroletti et al. 2004, 2008 3: Lara et al. 2004 4: Beswick et al. 2004

5: Giroletti et al. 2005 5b: Giroletti et al. 2005b 6: Gentile et al. 2007;

7: Giovannini et al. 2007; 8: Liuzzo et al. 2009a; 9: Liuzzo et al. 2010

For a reference to the extended structure see Fanti et al. 1987 for B2 sources

and Leahy et al. at the URL: http://www.jb.man.ac.uk/atlas).

For all sources, high-quality images at arcsecond resolution obtained with the Very Large Array (VLA) of the NRAO[1] are available in the literature, allowing a detailed study of the large-scale structure. According to the kiloparsec scale morphology, the sample contains 65 FRI radio galaxies, 16 FRII sources, and 13 compact sources. According to the optical and large-scale radio structure, one source (0722+30) has been classified as a spiral galaxy and therefore should not be included in this sample. Because of its peculiarity it will be discussed in Giroletti et al. (in preparation). The source is reported in Table 4.1, but has not been considered in

[1]The National Radio Astronomy Observatory is operated by Associated Universities, Inc., under cooperative agreement with the National Science Foundation.

the statistical considerations and will not be considered in the future.

We refer to the "arcsecond core" for the measure of the nuclear emission at arcsecond resolution provided by VLA observations at 5 GHz (see e.g. Giovannini et al. (1988)), while we use the term "VLBI core" to refer to the unresolved compact component visible in the VLBI images at milliarcsecond resolution.

4.3 New observations and Data Reduction.

4.3.1 VLBA Observations at 5 GHz

We obtained Very Long Baseline Array (VLBA) observing time at 5 GHz to produce high-resolution images for 26 sources of the BCS. For these observations, we selected sources with an estimated nuclear flux density $S_c(5.0)$ at arcsecond resolution > 5 mJy.

Because in most cases the VLBA target source is not sufficiently strong for fringe-fitting and self-calibration, we used the phase referencing technique. Moreover, calibration of atmospheric effects for either imaging or astrometric experiments can be improved by the use of multiple phase calibrators that enable multi-parameter solutions for phase effects in the atmosphere. We therefore adopted a multi-calibrator phase calibration. In addition, a relatively long integration time for each source has been used to obtain good (u, v)-coverage, necessary to properly map complex faint structures.

Observations were made with the full VLBA. Each source was observed with short scans at different hour angles to ensure good (u, v)-coverage. We observed in full polarization (RCP and LCP) with 4 IFs (central frequency 4.971 GHz, 4.979 GHz, 4.987 GHz and 4.995 GHz). Both right- and left-circular polarizations were recorded using 2 bit sampling across a bandwidth of 8 MHz. The VLBA correlator produced 16 frequency channels for a total aggregate bit rate of 256 Mbs. In order to improve the VLBI astrometric accuracy and image quality of a target source, we observed more than one reference calibrator along with the target. We scheduled the observation so as to use the AIPS task ATMCA, which combines the phase or multi-band delay information from several calibrators. Each pointing on a target source was bracketed by a phase calibrator scan using a 4 minute duty cycle (2.5 minutes on source, 1.5 minutes on phase calibrator). After 4 scans of target and phase calibrators we introduced one ATMCA calibrator scan (1.5 minutes on each ATMCA calibrator). The total observing time on each target

Table 4.2: Sources and Calibrators list

Name IAU	Core Absolute Position $RA_{(J2000)}$ $(^h\,^m\,^s)$	DEC_{J2000} $(^\circ\,'\,'')$	phase calibrator	ATMCA calibrators
0034+25	00 37 05.488	25 41 56.331	J0046+2456	J0106+2539, J0057+3021, J0019+2602
0055+26	00 58 22.630	26 51 58.689	J0046+2456	J0106+2539, J0057+3021, J0019+2602
0149+35	01 52 46.458	36 09 06.494	J0152+3716	J0137+3309, J0205+3212
0300+16	03 03 15.014	16 26 18.978	J0305+1734	J0256+1334, J0321+1221
0356+10	03 58 54.437	10 26 02.778	J0409+1217	J0407+0742, J0345+1453
0708+32B	07 11 47.669	32 18 35.946	J0714+3534	J0646+3041
0722+30	ND	ND	J0736+2954	J0646+3041
0802+24	08 05 35.005	24 09 50.329	J0802+2509	J0813+2542,J0805+2106
0836+29-I	08 40 02.352	29 49 02.529	J0839+2850	J0827+3525,J0852+2833,J0823+2928
0838+32	08 41 13.097	32 24 59.712	J0839+2850	J0827+3525,J0852+2833,J0823+2928
0915+32B	09 18 59.406	31 51 40.636	J0919+3324	J0915+2933
1113+29	11 16 34.619	29 15 17.121	J1125+2610	J1130+3031,J1103+3014,J1102+2757
1116+28	11 18 59.366	27 54 07.003	J1125+2610	J1130+3031,J1103+3014,J1102+2757
	11 18 59.366	27 54 07.002	J1125+2610	1.6 GHz data
1122+39	11 24 43.624	38 45 46.278	J1130+3815	J1104+3812,J1108+4330
1204+24	12 07 07.365	23 54 24.886	J1209+2547	J1150+2417,J1212+1925
1251+27B	12 54 12.007	27 37 33.961	J1300+2830	J1230+2518
1319+42	13 21 17.867	42 35 14.989	J1327+4326	J1324+4048,J1254+4536
1339+26B	ND	ND	J1342+2709	J1327+2210 J1407+2827,J1329+3154
1346+26	13 48 52.489	26 35 34.341	J1342+2709	J1327+2210,J1407+2827,J1329+3154
	13 48 52.489	26 35 34.337	J1350+3034	1.6 GHz data
1350+31	13 52 17.801	31 26 46.463	J1350+3034	1.6 GHz data
1357+28	14 00 00.854	28 29 59.801	J1342+2709	J1327+2210, J1407+2827,J1329+3154
1422+26	14 24 40.529	26 37 30.476	J1436+2321	1.6 GHz data
1448+63	14 49 21.61	63 16 14.3	J1441+6318	1.6 GHz data
1502+26	15 04 57.120	26 00 58.455	J1453+2648	J1522+3144,J1516+1932
	15 04 57.109	26 00 58.473	J1453+2648	1.6 GHz data
1529+24	15 31 43.47	24 04 19.1	J1539+2744	1.6 GHz data
1557+26	15 59 51.614	25 56 26.319	J1610+2414	1.6 GHz data
1613+27	16 15 31.360	27 26 57.335	J1610+2414	1.6 GHz data
1615+35B	16 17 40.537	35 00 15.201	J1613+3412	J1635+3808, J1642+2523
1621+38	16 23 03.119	37 55 20.552	J1640+3946	1.6 GHz data
1637+29	16 39 20.117	29 50 55.855	J1653+3107	J1635+3808, J1642+2523
1736+32	17 38 35.770	32 56 01.524	J1738+3224	J1735+3616, J1753+2848
1752+32B	17 54 35.503	32 34 17.192	J1748+3404	J1735+3616, J1753+2848
2236+35	22 38 29.421	35 19 46.872	J2248+3718	J2216+3518, J2236+2828

is about 110 minutes. Calibrators were chosen from the VLBA calibrator list to be bright and close to the source; in Table 4.2, we report the list of the selected calibrators. Short scans on strong sources were interspersed with the targets and the calibrators as fringe finders.

The observations were correlated in Socorro, NM. Postcorrelation processing used the NRAO AIPS package (Cotton 1993) and the Caltech Difmap packages (Pearson et al. 1994). We produced also images of the calibrators in order to obtain and apply more accurate phase and gain corrections to the multi-sources file during the initial calibration steps; then we determined the absolute position of the sources. We give the coordinates of the core candidate of each source in Table 4.2. Initial images were derived using phase-referencing, then self-calibrated depending on SNR. The signal-to-noise allowed for phase self-calibration on a very few sources.

Final images were obtained using the AIPS and Difmap packages. We produce images with natural and uniform weights. The important parameters for the final images of the observed sources are summarized in Table 4.3. The VLBI core properties have been estimated by using Modelfit in Difmap. The total VLBI flux is the sum of all fitted components. The noise level was estimated from the final images.

4.3.2 VLBA Observations at 1.6 GHz

Observation of 10 objects were also obtained in phase reference mode with the VLBA on 2003 August 07 and 2003 August 30 as part of projects BG136A, and B. Observations were performed in full polarization (RCP and LCP) with two IFs (central frequencies 1659.49 MHz and 1667.49 MHz). Both right- and left-circular polarizations were recorded using 2 bit sampling across a bandwidth of 8 MHz. The VLBA correlator produced 16 frequency channels for a total aggregate bit rate of 128 Mbs.

Each pointing on a target source was bracketed by a calibrator scan in a 5 min. duty cycle (3 min. on source, 2 min. on the calibrator). Two groups of (typically) 11 duty cycles were executed for each source at different hour angles, resulting in a total of $\sim$66 minutes per target, with a good coverage of the $(u, v)-$plane. Calibrators were chosen from the VLBA Calibrators List to be bright and close to the source; a list of sources with their relative calibrator is reported together with the 5 GHz

calibrators used in Table 4.2 .

The correlation was performed in Socorro and the initial calibrations were done within AIPS. Global fringe fitting was performed on all calibrators and the solutions were applied to the targets using a two-point interpolation. We then produced images of the calibrators in order to obtain and apply more accurate phase and gain corrections to the sources; we also determined from preliminary maps the absolute position of the sources, which we used thereafter. The final calibrated single-source datasets were exported to Difmap, for imaging and self-calibration. We produced images with the same procedure described for the 5 GHz data, and the relevant parameters are summarized in Table 4.3.

Table 4.3: VLBA Observations

Epoch gg-mm-yy	target	HPBW mas×mas, °	noise mJy/beam	S_{tot} mJy	core/jet mJy	notes
2005-06-22	0034+25	3.3× 1.6 (-15)	0.1	3.6	3.6	C
2005-06-22	0055+26	3.3× 1.6 (-14)	0.09	7.5	7.5	C
2005-07-20	0149+35	3.0× 1.4 (0)	0.08	3.2	3.2	C
2005-07-20	0300+16	3.2× 1.7 (-1)	0.1	6.1	6.1	C
2005-07-20	0356+10	3.3× 1.6 (-4)	0.12	2.2	2.2	C
2005-07-20	0708+32B	1.5× 1.5 (-)	0.08	10.5	5.9	double:A
					4.6	double:B
2005-07-20	0722+30		0.1	ND	ND	-
2005-07-02	0802+24	3.5× 3.5 (-)	0.05	3.6	2.1	two-sided:C
					1.5	two-sided:J
2005-07-02	0836+29-I	1.4× 1.4 (-)	0.08	47.8	24.2	one-sided:C
					5.8	one-sided:J1
					17.1	one-sided:J2
2005-07-02	0838+32	3.0× 1.7 (12)	0.09	7.0	7.0	C
2005-06-17	0915+32	2.9× 1.6 (-6)	0.1	13.6	13.6	C
2005-07-02	1113+29	4 × 4 (-)	0.06	40.0	36.8	one-sided:C
					3.2	one-sided:J
2005-07-02	1116+28	3.3× 1.5 (5)	0.09	11.5	11.5	C at 5 GHz
2003-08-07	1116+28	10.8 × 5.5 (28)	0.13	9.5	9.5	C at 1.6 GHz
2005-06-17	1122+39	2.6× 1.8 (-1)	0.10	8.8	8.8	C
2005-06-17	1204+24	3.0× 1.7 (-4)	0.09	5.3	5.3	C
2005-06-17	1251+27B	2× 2 (-)	0.06	10.4	6.2	two-sided:C
					4.2	two-sided:J
2005-06-17	1319+42	2.3×1.4 (0)	0.1	5.0	3.0	two-sided:C
					2.0	two-sided:J
2005-06-27	1339+26		0.1	ND	ND	-
2005-06-27	1346+26	see Chapter 3				Z structure
2003-08-07	1350+31	12 × 10, (24)	0.1	235	17.2	at 1.6 GHz:C
					2.5	J
					2.0	CJ
					192	E1 see Sect.4.1.2
					11.9	E2
					11.2	E3
2005-06-27	1357+28	3× 2 (0)	0.15	5.6	3.8	two-sided:C
					1.8	two-sided:J
2003-08-07	1422+26	10.1 × 4.5 (	0.15	9.3	5.1	one-sided:C? 1.6 GHz
					4.2	J?
2003-08-30	1448+63	9.8× 4.5 (-5)	0.15	ND	ND	1.6 GHz,see text
2005-06-17	1502+26	2× 2 (-)	0.06	7.8	0.5	5GHz two-sided:C
					3.1	two-sided:E1
					4.2	two-sided:W1
2003-08-07	1502+26	10.2 × 4.5 (-20)	0.2	27.1	0.3	C 1.6 GHz
					6.0	W
					11.3	E1
					4.1	N
2003-08-07	1529+24	11.0×11.0 (-)	0.1			1.6 GHz,see text
2003-08-30	1557+26	9.8 × 4.5 (2)	0.12	10.5	10.5	C 1.6 GHz
2003-08-30	1613+27	9.9 × 4.5 (3)	0.12	9.3	9.3	C 1.6 GHz
2005-06-27	1615+35B	2.8×1.8 (-17)	0.06	23.6	17.1	one-sided:C
					6.5	one-sided:J
2003-08-07	1621+38	7×7 (-)	0.09	17.9	15.5	1.6GHz,one-sided:C
					2.4	one-sided:J

Table 4.3: continued.

Epoch gg-mm-yy	target	HPBW mas×mas, °	noise mJy/beam	S_{tot} mJy	core/jet mJy	notes
2005-06-27	1637+29	2.8× 1.8 (-12)	0.1	7.8	7.8	C
2005-06-22	1736+32	2.9× 1.2 (-32)	0.14	7.6	7.6	C
2005-06-22	1752+32B	2 × 2 (-)	0.08	9.2	6.1	two-sided:C
					3.1	two-sided:J
2005-06-22	2236+35	3.3× 1.6 (-19)	0.09	8.8	8.8	C

In column 7 (notes) we indicate the component for which flux density is reported in column 6 (core/jet). C = core component; j = jet. We also report the observing frequency when at 1.6 GHz, in all other cases the observations are at 5 GHz.

4.4 Notes on sources.

We present here new observations for 33 sources (including the spiral galaxy 0722+30, see above). We detected all sources except 0722+30 and 1339+26 at 5 GHz, and 1448+63 (3C305) at 1.6 GHz. Among detected sources a few exhibit an extended structure that we will discuss in detail below. For all the other sources we give a short note and for all resolved sources we present an image. A summary of results are reported in Table 4.3.

4.4.1 Sources of special interest

0836+29-I (4C 29.30)

This source ($z = 0.0647$, also referred to as B2 0836+29A) has been often confused in the literature with the cD galaxy B2 0836+29 (0836+29-II, at $z = 0.079$), the brightest galaxy in Abell 690, which was studied by Venturi et al. (1995).

0836+29-I was studied in detail by van Breugel et al. (1986), and recently by Jamrozy et al. (2007). It is a possible merger system (van Breugel et al. 1986). On the large scale (Fig. 4.1) the source shows clear evidence of intermittent radio activity. There is a large scale structure about $9''$ in size, with an estimated age of about 200 Myr (Jamrozy et al. 2007); a more compact structure shows a central core and two bright spots and an extended emission about $1''$ in size with an age lower than 100 Myr. The inferred spectral age for the inner double is 33 Myr (Jamrozy et al. 2007). At higher resolution (van Breugel et al. 1986) the core source (component C_2) is visible (Fig. 4.2)along with a bright one-sided jet about $3''$ in size, which terminates with a bright spot (C1).

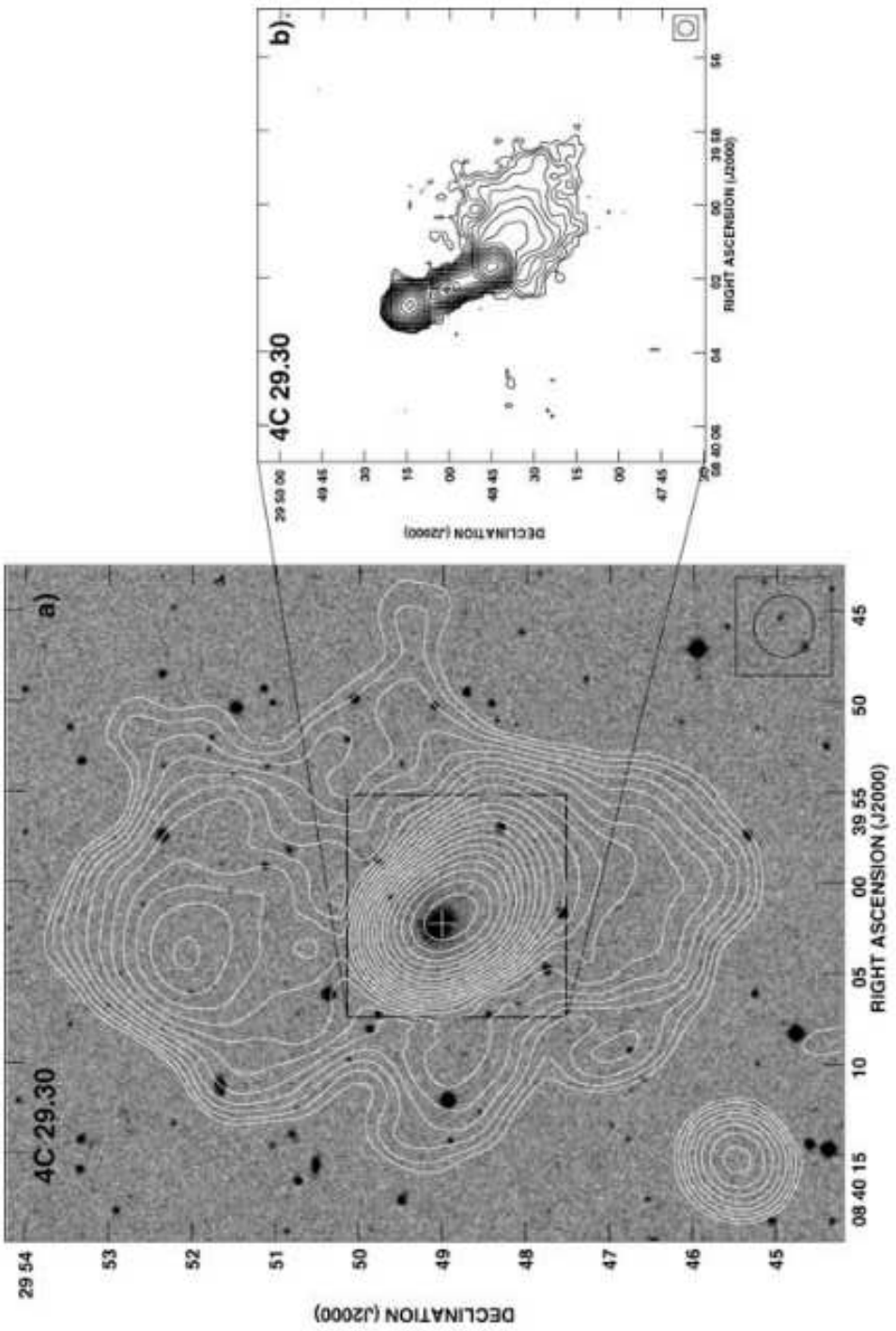

Figure 4.1: 1400-MHz VLA images of 4C 29.30 (Jamrozy et al. 2007). (a) D-array contour map of the entire source overlayed on the optical field from the Digital Sky Survey (DSS). The contour levels are spaced by factors of $\sqrt{2}$, and the first contour is 0.3 mJy/beam. (b) B-array contour map of the central part of the source from FIRST. The contour levels are spaced by factors of $\sqrt{2}$ and the first contour is 0.45 mJy/beam. The size of the beam is indicated by an ellipse in the bottom right corner of each image. The cross marks the position of the radio core.

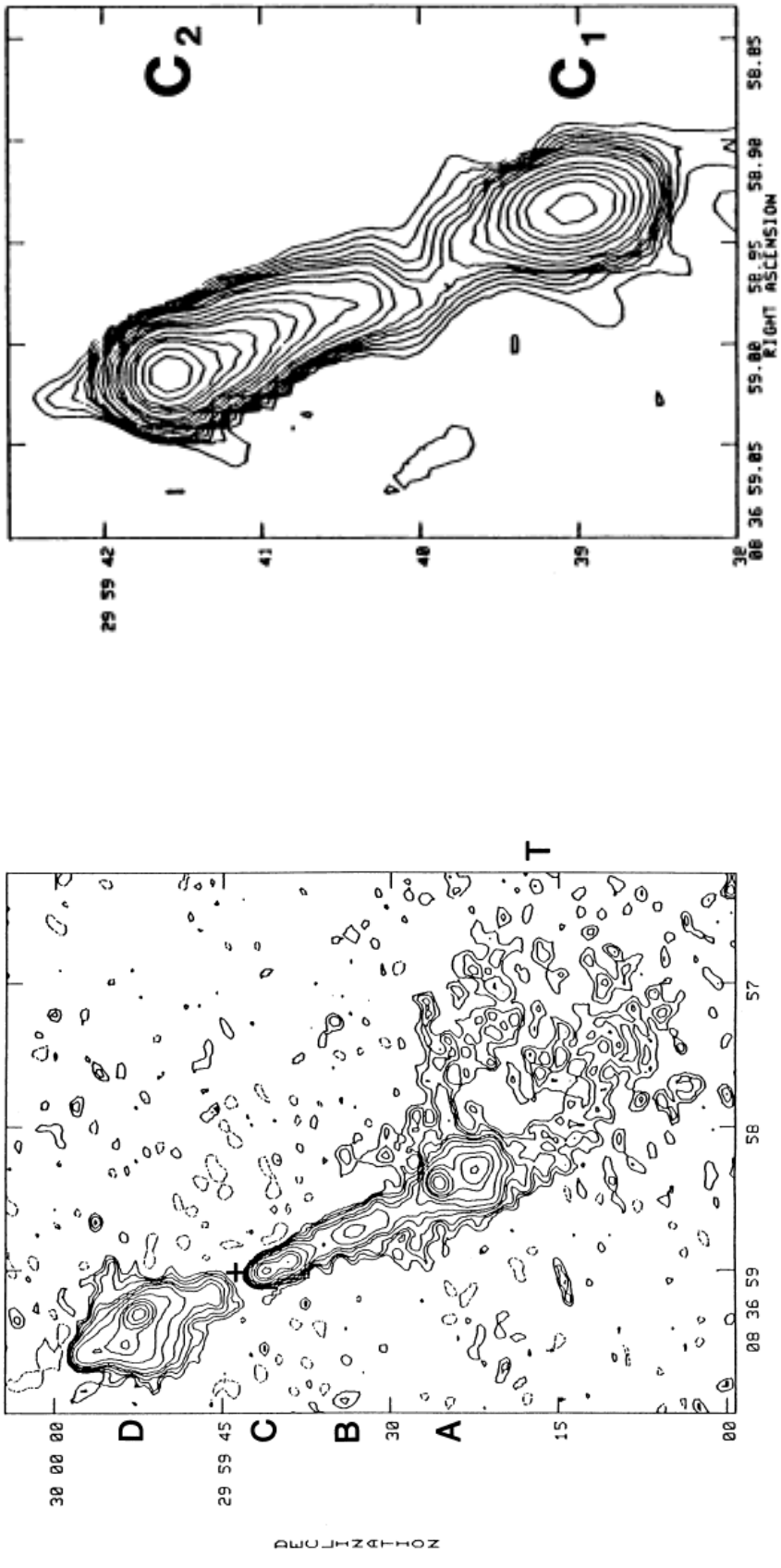

Figure 4.2: On the left: Contour representation (van Breugel et al. 1986) of the total intensity of 4C 29. 30 at 6 cm (0.3 $''$ × 0.3 $''$ of resolution). Contour value are 0.05 × (-3. 3, 5, 7, 10, 16, 25, 40, 60 and 100 mJy/beam. Negative values appear as a dashed lines. On the right: Detail of the map at 6 cm (van Breugel et al. 1986) to show the components C_1 and C_2. Contour values are 0.06 × (3, 4, 5, 6, 7, 8, 10, 12, 16, 20, 25, 30, 50, 60, 80, 100, 150 and 200) mJy/beam. Coordinates are at 1950.

In our low resolution VLBA image (Fig. 4.3 left), the parsec scale structure looks like a scaled version of the arcsecond scale structure shown by van Breugel et al. (1986). At higher resolution (Fig. 4.3 right) the Northern component is resolved into a core-jet structure, and the Southern component is resolved into a bright knot in the most external region.

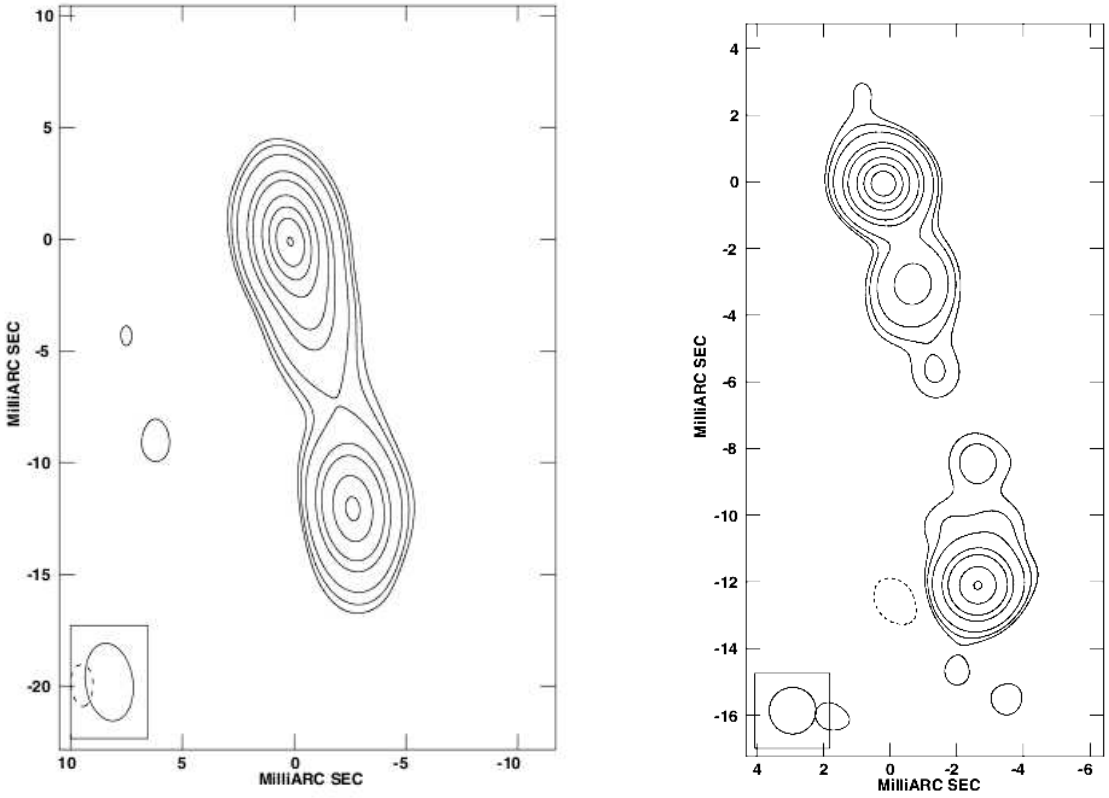

Figure 4.3: On the left: VLBA image at 5 GHz of 0836+29-I at low resolution (HPBW = 35×21 mas^2 in PA= 8°). The noise level is 0.1 mJy/beam. Levels are -0.3, 0.3, 0.5, 1, 3, 5, 10, 15, 20 and 25 mJy/beam. On the right: VLBA image at 5 GHz of 0836+29-I at high resolution (HPBW = 1.4 mas). The noise level is 0.08 mJy/beam and contours are: -0.3, 0.3, 0.5, 1, 5, 10, 15 and 20 mJy/beam. The nuclear source has been identified with the Northern compact component (see text).

Although we lack spectral information, we can identify the nuclear source as the Northern parsec scale component, since it is the only unresolved structure by a Gaussian fit and because of homogeneity with the arcsecond scale. From the jet to counter-jet ratio (> 50) we estimate that the orientation angle has to be $\theta < 49°$ and the jet velocity $\beta > 0.65$. Assuming a high jet velocity with a Lorentz factor in the range 3 to 10 (Giovannini et al. 2001) and an orientation angle $\theta \sim 40°$, we can derive the intrinsic jet length and age of single components. In this scenario the

first knot after the core (right panel in Fig. 4.3), is $\sim$ 15 yrs old and the Southern knot is $\sim$ 70 yrs old.

The structure of this source is in agreement with a quasi-periodic activity visible in the small as well as on the large scale. Assuming the same orientation angle and velocity of the jet on the arcsecond scale $\sim$ 0.6 c (in agreement with the jet sidedness) we can estimate an age $\sim 10^4$ yrs for the one-sided jet structure present in van Breugel et al. (1986). We note that Jamrozy et al. (2007) discussed the evidence of a strong outburst in between 1990 and 2005, which could be related to the presence of the new VLBI component with an estimated age of 15 yrs. In Table 4.1 and 4.4 we report the more recent arcsecond core flux density from Jamrozy et al. (2007). It is important to note that during the long time range of the activity of this source with many periods of restarting activity the jet position angle was constant in time.

1350+31 (3C 293)

This peculiar source has been studied in detail in the radio and optical bands. Recent results are presented in Beswick et al. (2004) and Floyd et al. (2006), where the source structure is discussed from the sub-arcsec to the arcminute scale. In Giovannini et al. (2005), we presented a VLBI image at 5 GHz where a possible symmetric two-sided jet structure is present at mas resolution.

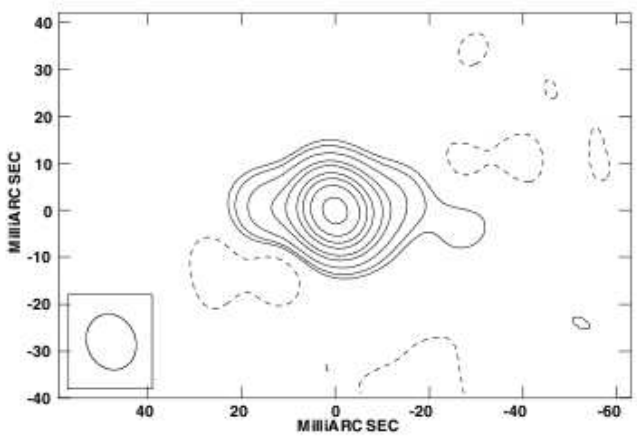

Figure 4.4: 1.6 GHz VLBA image of 1350+31 (3C 293). The HPBW is 12 × 10 mas in PA 24°. The noise is 0.1 mJy/beam, contours are −0.3, 0.3, 0.5, 1, 2, 3, 5, 7, 10 and 15 mJy/beam

Because of the complex nature of the inner structure, we re-observed the source with the VLBA at 1.6 GHz in phase reference mode. We show the new 1.6 GHz image of the core in Fig. 4.4. In agreement with the 5 GHz VLBA image, we have a two-sided structure with symmetric jets. The jet emission is detected on both sides up to ~ 20 mas from the core, with the eastern jet being slightly brighter. Hereafter, we refer to it as the main jet(J), and to the western one as the counterjet (CJ). This is also in agreement with the indication discussed by Beswick et al. (2004), although their suggested jet orientation and velocity are in contrast with the high symmetry of the VLBA jet. From visibility model fitting, we derive total flux densities for the core and the jets of $S_c = 17$ mJy, $S_j = 2.5$ mJy, and $S_{cj} = 2.0$ mJy. The core spectral index is $\alpha^5_{1.6} = 0.05$.

On the shortest baselines, we clearly detect a significant amount of extended flux ($S \sim 200$ mJy) and we were able to image the MERLIN knots E1, E2, and E3 (see Fig. 3 in Beswick et al. (2004)), while components on the west side are not revealed (data are reported in Table 4.4). We then reduced archival VLA data in

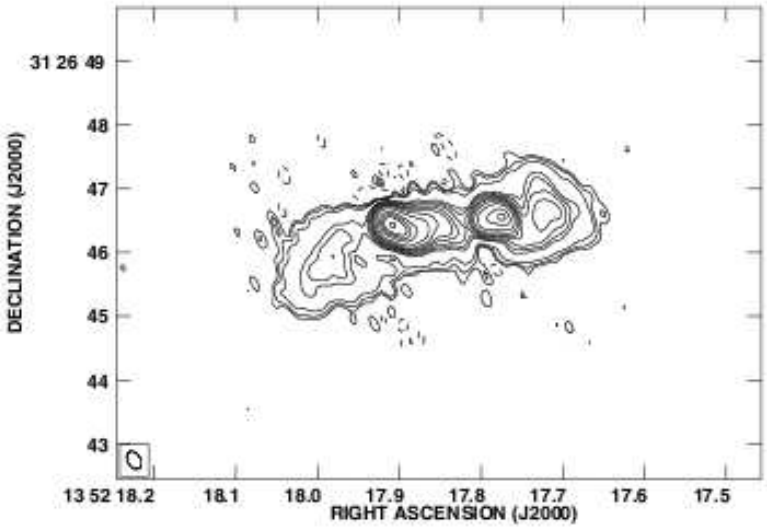

Figure 4.5: 5 GHz image of 1350+31 (3C 293) obtained with VLA+PT. The HPBW is 0.3" × 0.2" in PA 30°. The noise level is 0.06 mJy/beam and levels are: −0.3, 0.3, 0.5, 1, 5, 7, 10, 15, 20, 30, 50, 100, 150, 200 and 300 mJy/beam.

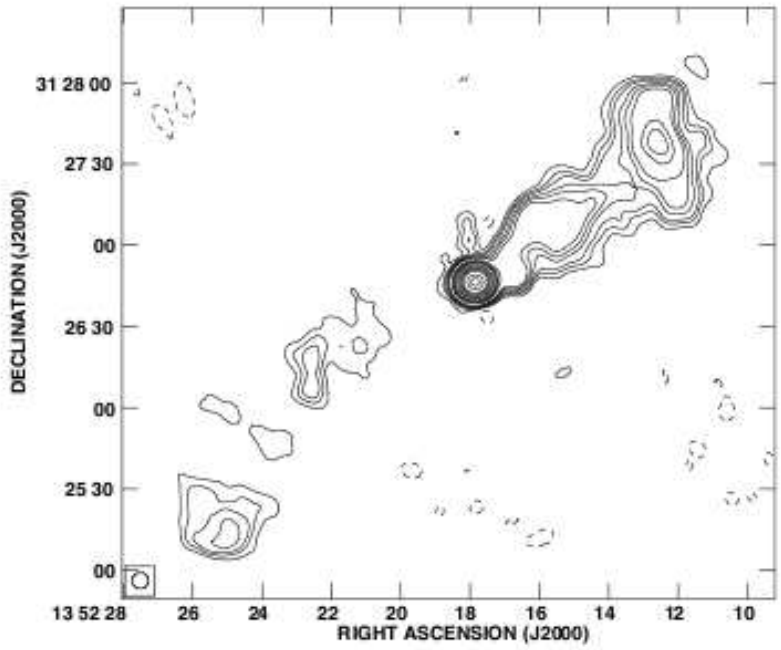

Figure 4.6: VLA image at 1.4 GHz of 3C293. The HPBW is 6″ ; the noise level is 0.26 mJy/beam, and levels are: -1, 1, 2, 3, 5, 7, 10, 30, 50, 70, 100, 200, 300, 500, 700, 1000, 2000 and 3000 mJy/beam.

order to better study the connection between the sub-arcsecond and the arcsecond structure. In Fig. 4.5, we show a 5 GHz sub-arcsecond VLA+PT image. This reveals the inner two-sided jet structure with a fainter diffuse emission. On even larger scales (Fig. 4.6), VLA 1.4 GHz data reveal more extended, fainter emission along a different PA.

From a comparison between different images we infer that the sub-arcsecond structure in the E-W direction is related to restarted activity of the central AGN. The large change in PA with respect to the extended lobes, however, is not due to a PA change from the restarted nuclear activity but appears constant in time and is most likely produced by the jet interaction with a rotating disk as discussed in van Breugel & Fomalont (1984). In this scenario we expect that the jet at $\sim$ 2.5 kpc from the core is no longer relativistic.

1502+26 (3C 310)

This source is identified with a magnitude 15 elliptical galaxy at $z = 0.0538$ having clearly extended X-ray emission, first detected with the Einstein satellite by **?**. In the radio band at low resolution (Fig. 4.7), it appears as a relaxed double van Breugel & Fomalont (1984) with a steep radio spectrum ($\alpha^{26}_{750} = 0.9$; $\alpha^{0.75}_{10.7} = 1.4$). The low brightness lobes exhibit a complex structure with filaments and bubbles. There is an unresolved radio core with a faint extension from the core to the North, extended 5″ , possibly identified as a weak jet (van Breugel & Fomalont 1984).

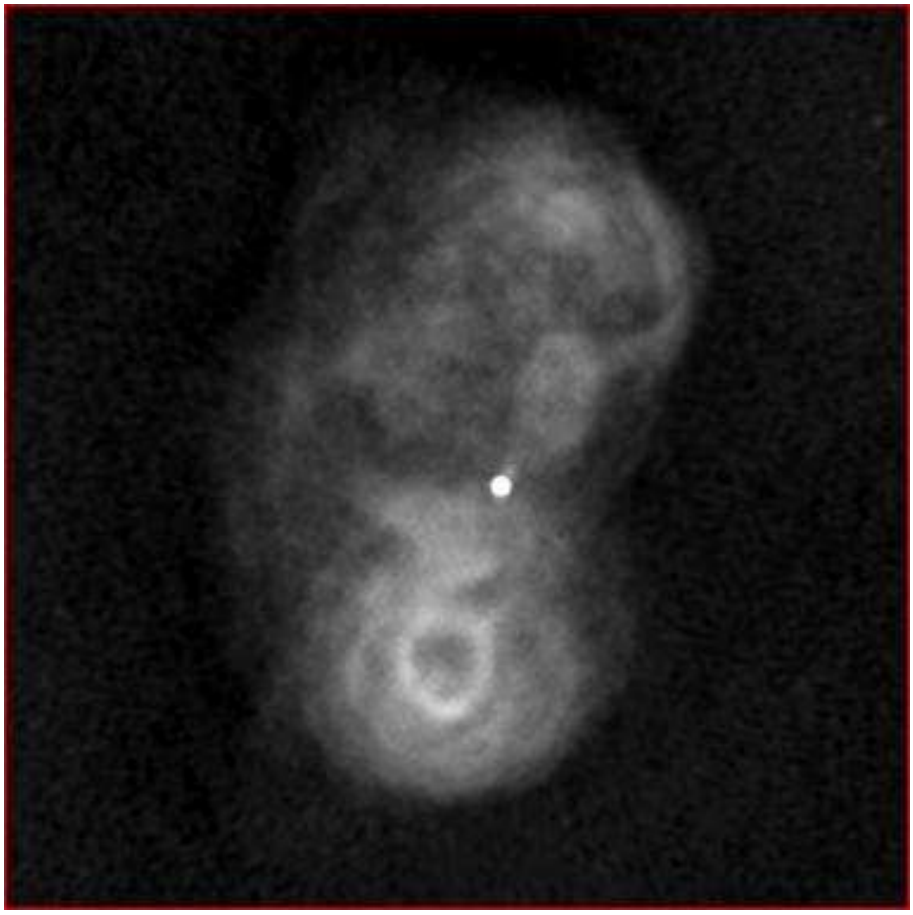

Figure 4.7: VLA map (grey colour) at 20 cm (van Breugel & Fomalont 1984).

The parsec scale images are complex. In Giovannini et al. (2005), we showed a structure interpreted as one-sided emission, in contrast with an image by Gizani et al. (2002). Because of this discrepancy and the short exposure and low flux density, we re-observed this source at 5 and 1.6 GHz in phase reference mode. In Fig. 4.8 we show a 5 GHz image at full resolution, where an extended complex structure

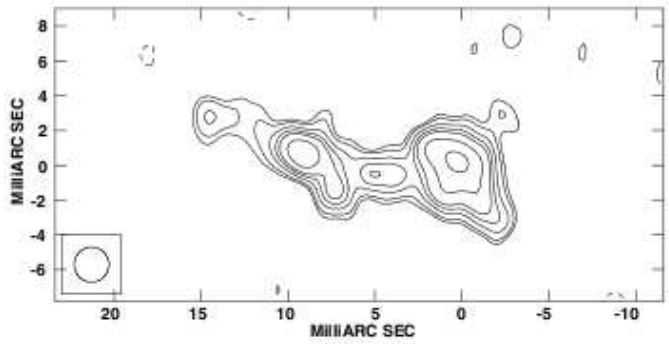

Figure 4.8: VLBA image of 1502+26 (3C 310) at 5 GHz. The HPBW is 2 mas. The noise level is 0.06 mJy/beam and levels are: −0.2, 0.15, 0.2, 0.3, 0.4, 0.5, 0.7 and 1 mJy/beam.

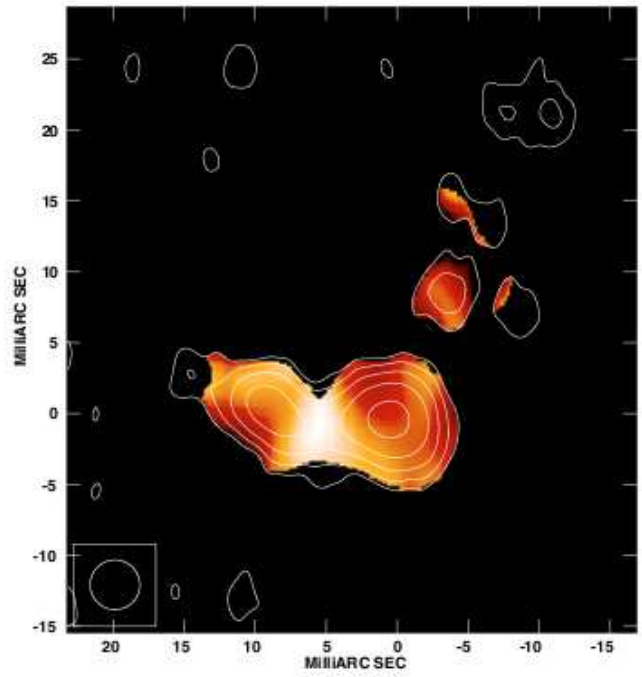

Figure 4.9: VLBA image of 1502+26 (3C 310) at 5 GHz with a HPBW = 3.5 mas superimposed to the spectral index image (colour) between 1.6 and 5 GHz. The greyscale range in the colour image is from −0.3 (white) to 2.0 (dark red). The noise level in the contour image is 0.04 mJy/beam and levels are: 0.1, 0.2, 0.4, 0.8 and 1.6 mJy/beam.

oriented in the E-W direction, almost perpendicular to the kiloparsec scale structure is present. The symmetry of this structure suggests the presence of a nuclear central emission with two almost symmetrical lobes connected by a bridge (jets?). At lower resolution (Fig. 4.9) the double E-W structure is confirmed, moreover some emission on the top (North) of the brightest lobe is visible. At 1.6 GHz (Fig. 4.10) the source presents two main components along the East-West direction plus a low brightness

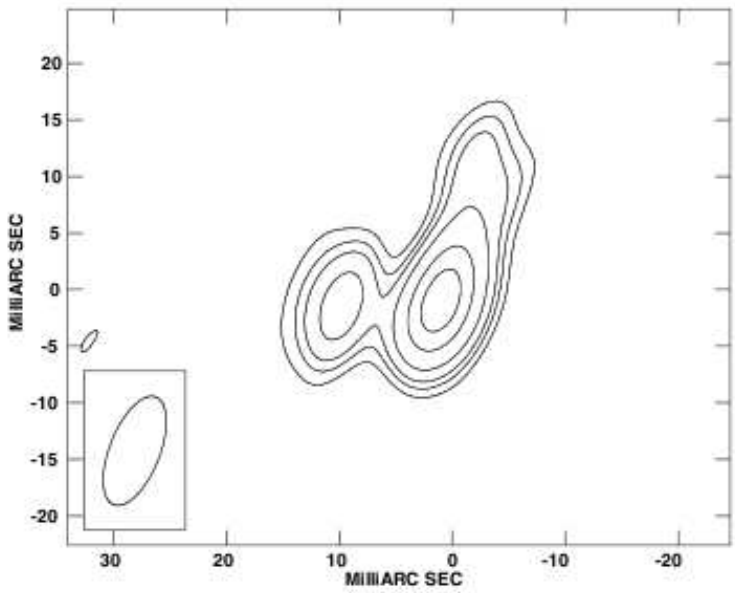

Figure 4.10: VLBA image at 1.7 GHz of 1502+26 (3C 310), with a HPBW = 10.2 × 4.5 mas in PA= -22 °. The noise is 0.2 mJy/beam, and levels are: -1, 1, 1.5, 2, 3, 5 and 7 mJy/beam.

emission extending to the North, in agreement with the low resolution 5 GHz image, and with Gizani et al. (2002). In all images the source brightness is very low, at the mJy level at 5 GHz and with a peak flux density of 8.5 mJy at 1.6 GHz.

In order to discuss the nature of the components, we produced a map of the spectral index (defined as $S_\nu \propto \nu^{-\alpha}$) distribution, using images at 5 and 1.6 GHz with the same angular resolution. The spectral index is inverted in the central region of the E-W structure (-0.3) and steep in the two symmetric lobes (on the average 0.9 at E and 1.1 at W). Despite the low signal to noise ratio we are able also to estimate the spectral index in the North region which is still steep (~ 1.3), albeit with a large uncertainty (see Fig. 4.9). Therefore we confirm the identification of the core with the faint emission at the center of the parsec scale structure. The morphology is quite peculiar: we have a symmetric two-sided emission in the E-W direction, i.e. almost perpendicular to the kiloparsec-scale emission. After about five milliarcseconds we have a symmetric change in the direction of the radio emission of about 80° which then becomes aligned with the kiloparsec scale axis. A possible explanation for this **Z-shaped** structure so near to the core will be discussed in Sect. 4.5.3.

4.4.2 Notes on other observed sources.

The remaining sources of these new observations have simpler structures. They can be unresolved, have short jet-like features, or even remain undetected. Below we summarize the results on these sources, together with some information on the large-scale structure. We only skip 1346+26 (4C 26.42), a very peculiar radio source with a **Z** shaped morphology from sub-parsec to kiloparsec scales), since it is presented a detailed discussion with more data Chapter 3.

0034+25 (UGC367) – This radio galaxy, identified with an E galaxy at $z = 0.032$, shows a wide angle tail morphology (Fig.4.11) with an inner symmetric jet structure in P.A. $= 90°$.

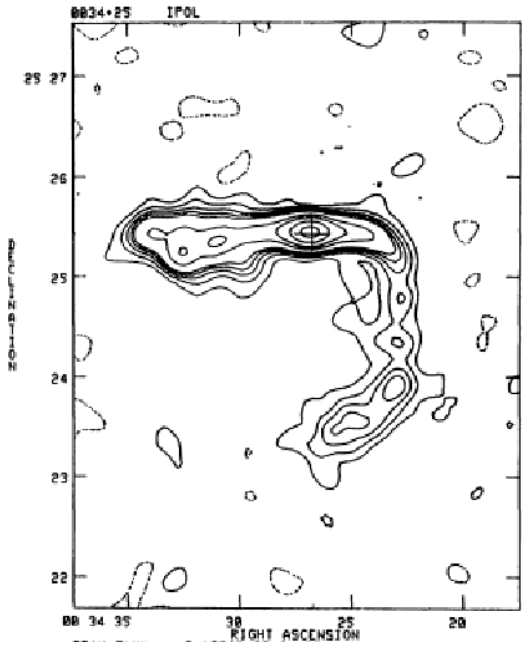

Figure 4.11: Contours map of 0034+25 at 20 cm in C- VLA configuration. The restoring beam is 13 arcsec, Contour levels are 2.139 × (-2, 2, 4, 6, 8, 10, 20, 30, 50, 75 and 100) mJy/beam. The cross marks the position of the optical identification (de Ruiter et al. 1986). Coordinates are at 1950.

It belongs to the Zwicky cluster 0034.4+2532. The host galaxy has an inner stellar disk perpendicular to the radio jet that has been interpreted as the signature of merging in the past (Gonzalez-Serrano et al. 1993). In our VLBA observation the source appears unresolved with total flux density ∼3.6 mJy. As the ratio $S_{\rm VLBA}/S_c$ is only 36%, most of the arcsecond flux is still missing on the milliarcsecond scale.

0055+26 (NGC326) – This galaxy is the Brightest Cluster Galaxy (BCG) of the Zwicky cluster 0056.9+2636. It appears as a dumbbell galaxy with two equally bright nuclei with projected separation of $7''$. The large scale radio emission shows (Fig. 4.12) twin jets along direction P.A.= 135° (Murgia et al. 2001).

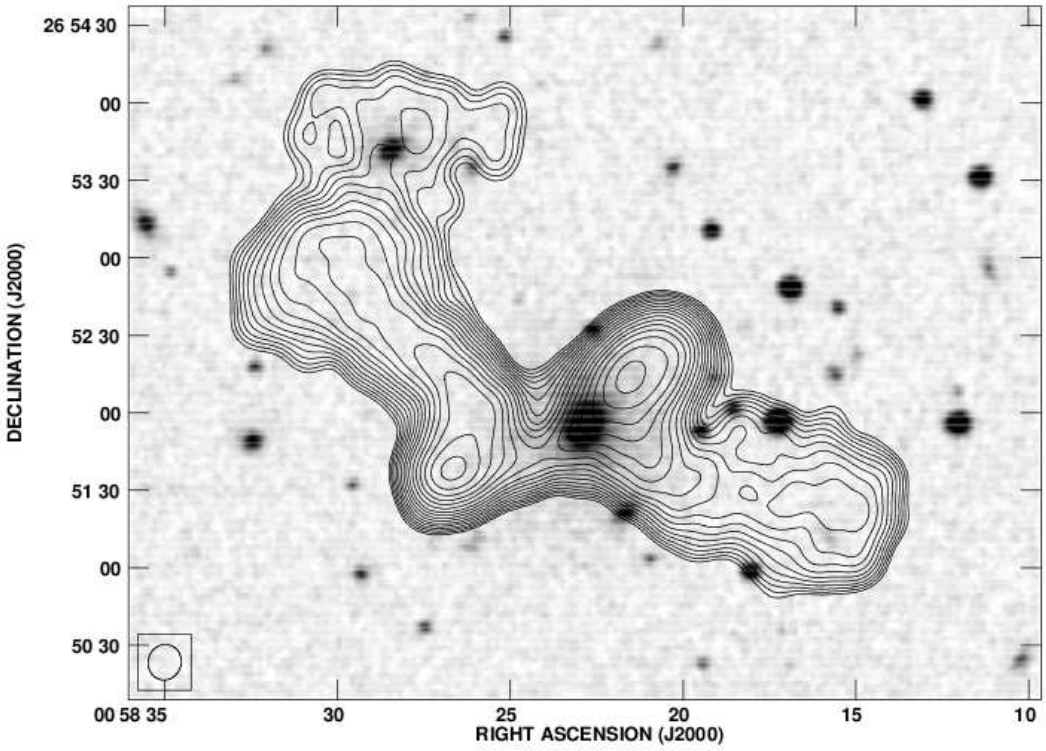

Figure 4.12: 1.4 GHz C array (contours) overlayed onto the optical image of NGC326 from the red Palomar Digitized Sky Survey. The contour levels are 0.5, 0.71, 1, 1.4, 2, 2.8, 4, 5.7, 8, 11, 16, 23, 32, 45, 64, 91, 130, 180 mJy/(beam area) and the restoring beam is $13\overset{''}{.}8 \times 12\overset{''}{.}8$ with PA= $-16.9°$ (Murgia et al. 2001).

There is a peak in X-ray emission consistent with the location of the radio galaxy core. In our VLBA data , we found nuclear emission with a possible slight extension in the same PA as the kiloparsec-scale jets, with a total flux density of 7.5 mJy.

0149+35 (NGC 708) – This galaxy is the BCG of the cooling cluster A262 (see also Chapter 2). At optical wavelengths, it is a low brightness galaxy whose nuclear regions are crossed by an irregular dust lane and patches of dust (Capetti et al. 2000). Feedback between the radio activity and the surrounding thermal gas is discussed by Blanton et al. (2004). In our VLBA image, this source appears unresolved with a total flux density $S_5 = 3.2$ mJy. Some of the arcsecond core flux is lost on the parsec scale ($S_{\rm VLBA}/S_c \sim 64\%$).

0300+16 (3C 76.1) – On kiloparsec scales, 3C 76.1 is classified as an FR I radio galaxy (Fig. 4.13); it was imaged at 6 cm by Vallèe (1982), and at 20 cm by Leahy & Perley (1991).

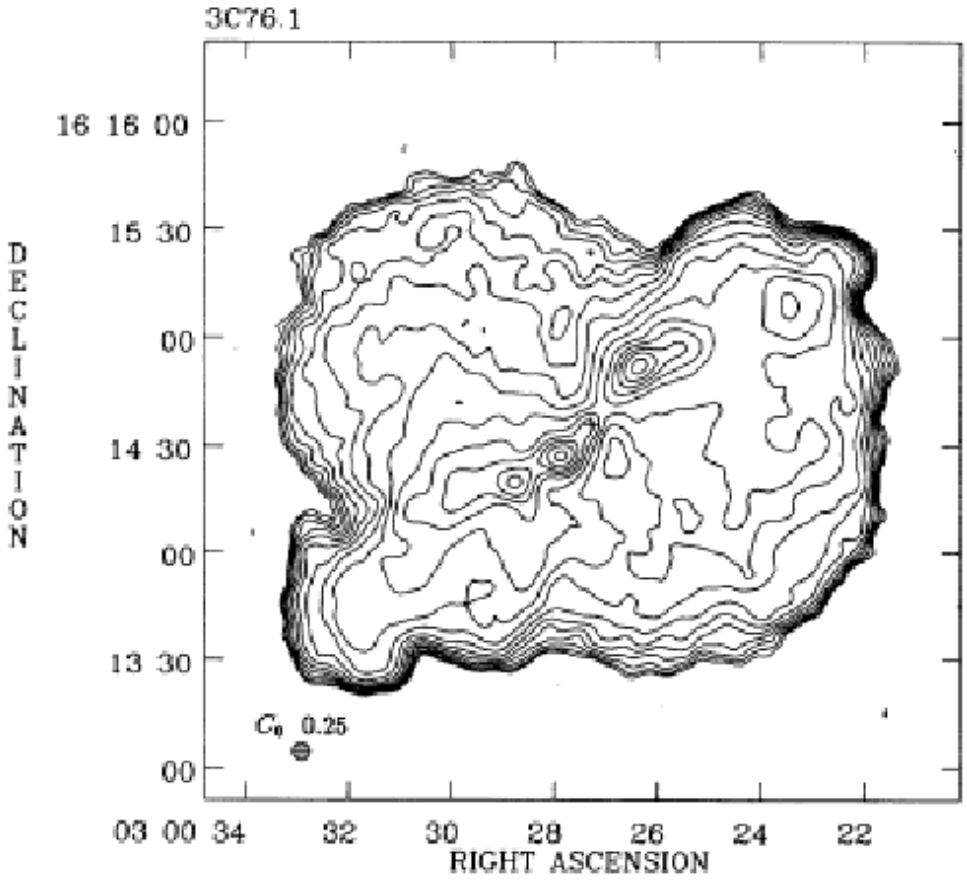

Figure 4.13: VLA total intensity of 3C 76.1 at 20 cm. Contour level are logarithmic with a ratio of $\sqrt{2}$ between levels starting from C $_0$ $\times 1$ where C_0 is given in the left of the panel (Leahy & Perley 1991).

The source has twin jets with a faint ($\sim$ 8 mJy) radio core surrounded by an extended low brightness radio halo. In our VLBA image, we found an unresolved core with the total flux density $S_5 = 6.1$ mJy. Some arcsecond core flux is lost on the parsec scale ($S_{VLBA}/S_c \sim 60\%$).

0356+10 – (3C 98) – The host galaxy is a typical narrow-line radio galaxy (NLRG), with extended emission lines studied by Baum et al. (1988, 1990). On kiloparsec scales, 3C 98 shows a double-lobe FRII radio structure which spans 216 arcsec at 8.35 GHz, with a radio jet that crosses the northern lobe and terminates in a bright hotspot (Fig. 4.14). There is little evidence of a southern jet, but a twin hotspot in the southern lobe is present (Hardcastle et al. 1998).

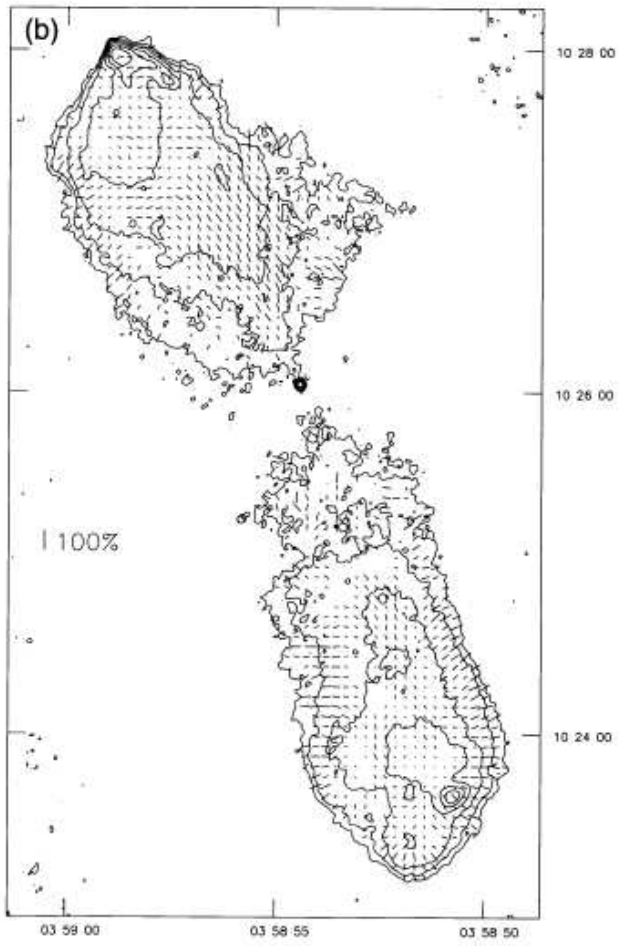

Figure 4.14: VLA map of 3C98 at 2 arcsec resolution (Leahy et al. 1997) at 3.6 cm. Contour levels are 0.2 × (-2. -1, 1, 2, 4, ...) mJy/beam. Negative contours are dashed.

The core of this symmetric FRII radio galaxy is pointlike in our VLBI image, with the total flux density ∼2.2 mJy. Most of the arcsecond core flux is missing on the parsec scale ($S_{\rm VLBA}/S_c \sim 24\%$), suggesting the presence of faint jets below our noise level and invisible because they are oriented in the plane of the sky.

0708+32B. This source is classified as a low power compact source. In VLA images at 20 cm (Fanti et al. 1986) it shows a nuclear emission with two symmetric lobes $< 10''$ ($\sim$ 10 kpc) in size oriented in the N-S direction (Fig. 4.15). .

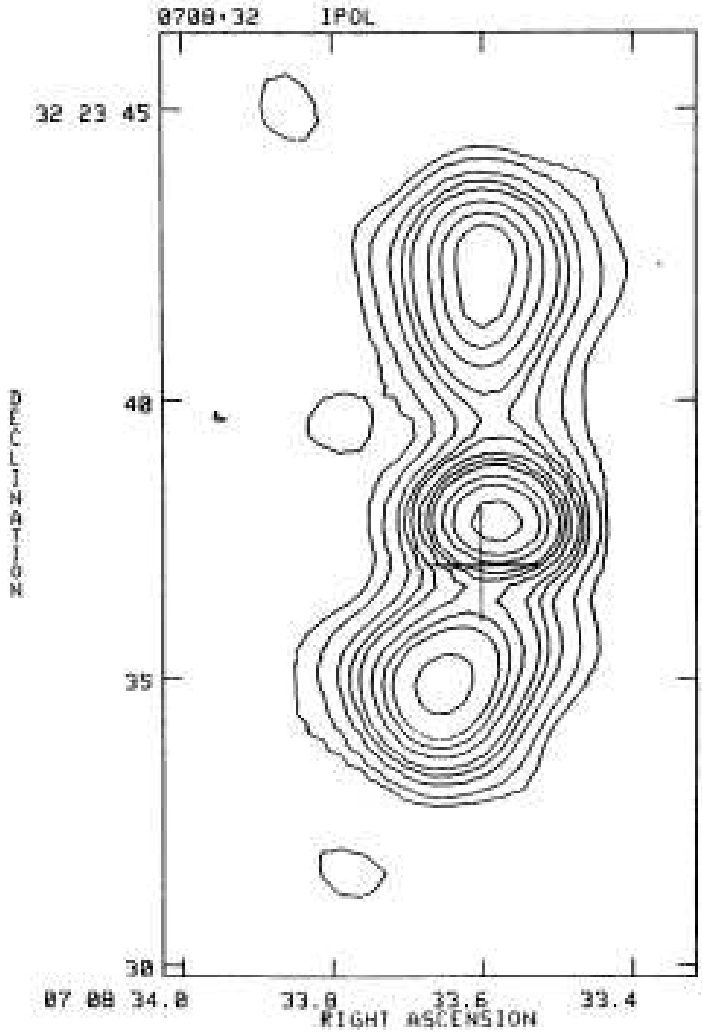

Figure 4.15: VLA Contour map of 0708+32B at 20 cm (Fanti et al. 1986). The cross marks the position of the optical identification. Contour level are 0.25 $\times$ (-2, 1, 2, 4, 6, 8, 12, 16, 20, 30, 60 and 80) mJy/beam. Coordinates are at 1950.

Higher resolution VLA data will be presented in Giroletti et al. (2010) to address the kiloparsec-scale structure of this source.

In our VLBA images (Fig. 4.16 and Fig. 4.17), we detected a double structure oriented along PA $\sim 150^\circ$ and extended ~ 4 mas. Since no spectral index information is available we are not able to identify the nuclear source, but the high degree of symmetry suggests an identification as a CSO with recurrent radio activity. The

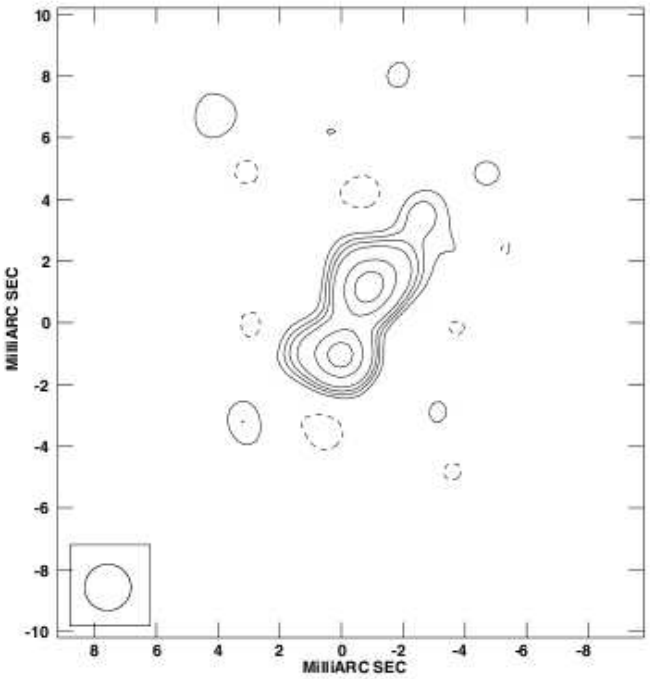

Figure 4.16: VLBA image at 5 GHz of 0708+32B. The HPBW is 1.5 mas, the noise level is 0.08 mJy/beam and levels are: -0.3, 0.3, 0.5, 0.7, 1, 2 and 3 mJy/beam.

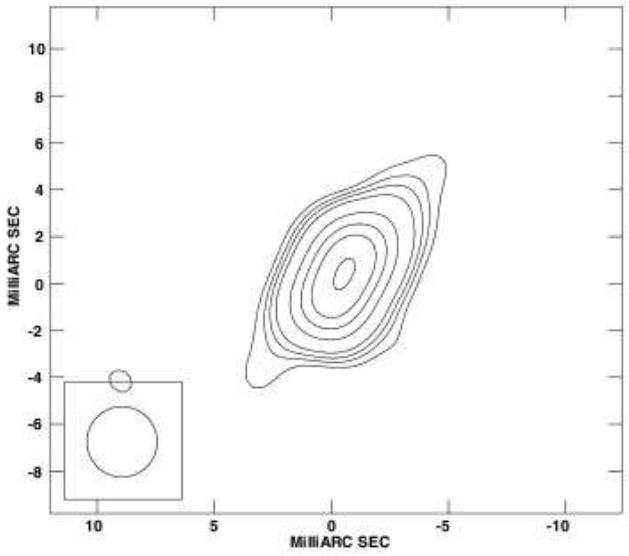

Figure 4.17: VLBA image at 5 GHz of 0708+32B. The HPBW is 3 mas, the noise level is 0.09 mJy/beam and levels are: -0.3, 0.3, 0.5, 0.7, 1, 2, 3, 4 and 5 mJy/beam

correlated VLBI flux density is 9.5 mJy- about 70% of the arcsecond core flux density.

0722+30 This radio source at $z = 0.0188$ is the only one identified with a spiral galaxy (see Capetti et al. (2000)). It is a highly inclined galaxy with a strong absorption associated with the disk and a bulge-like component. The radio emission (Fig. 4.18) is quite peculiar showing two symmetric jet-like features at an angle of about 45° from the disk (see Fanti et al. (1986)).

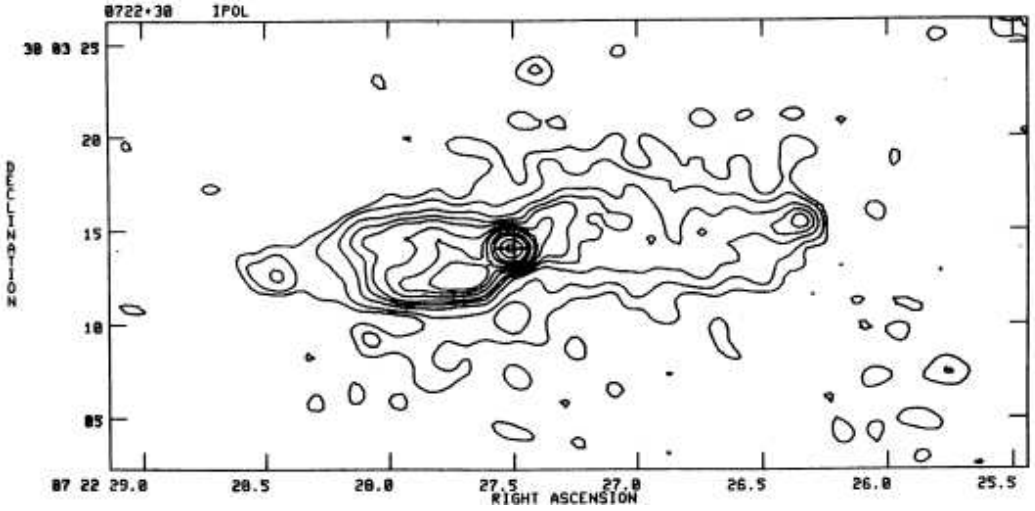

Figure 4.18: VLA contour map of 0722+30 at 20 cm (Fanti et al. 1986). Contour levels are 0.25 × ((-2, 1, 2, 4, 6, 8, 12, 16, 20, 30, 60 and 80) mJy/beam. The cross marks the position of the optical identification.

New high resolution VLA images will be discussed in Giroletti et al. (2010). The source is undetected in our VLBA image, with a $S_{\rm peak} < 0.3$ mJy/beam at 5 GHz. Because of the optical identification this source will not be considered in the following discussion.

0802+24 (3C 192) – On large scale (Fig. 4.19), this radio source shows an 'X' symmetric double-lobe structure which extends ∼200 arcsec at 8.35 GHz, showing bright hotspots at the end of the lobes (Baum et al. 1988; Hardcastle et al. 1998).

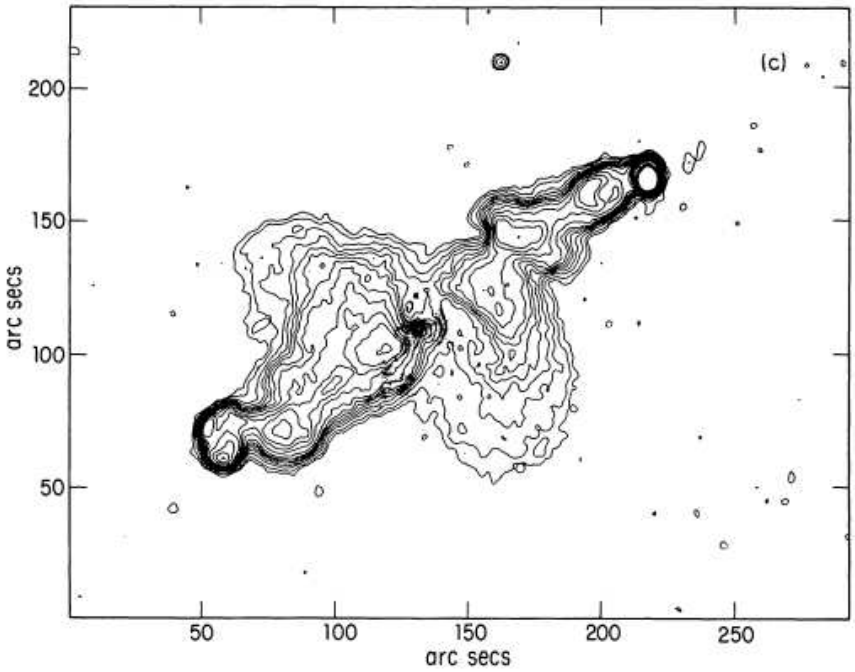

Figure 4.19: VLA map at 18 cm of 3C 192 (Baum et al. 1988). Contour levels are (-0.5, 0.5, 1, 2, 3, 4, 5, 6, 7.5, 10, 12.5, 15, 20, 30, 40, 50) mJy/beam. The resolution of the map is 3.9 $''$.

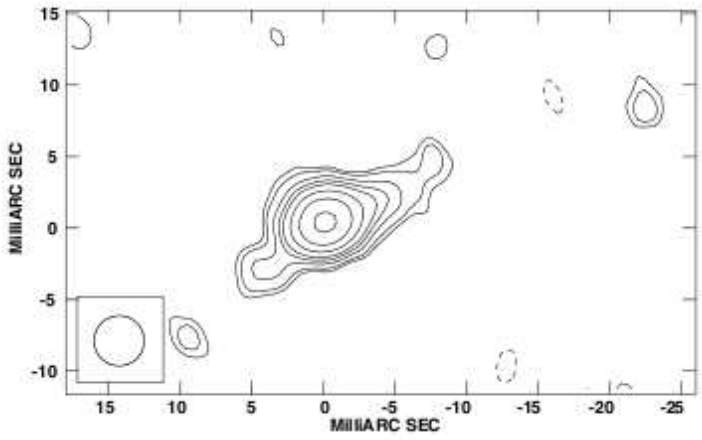

Figure 4.20: The VLBA image at 5 GHz of 0802+24 (3C192). Contour levs are −0.2, 0.15, 0.2, 0.3, 0.4, 0.5, 0.7, 1 and 1.5 mJy beam^{-1}, and the HPBW is 3.5 mas. The noise level is 0.05 mJy/beam

Extended narrow line emission has been detected in this galaxy. In our VLBA image (Fig. 4.20), the source appears two-sided, with jets at the same orientation as the kiloparsec-scale jets (P.A. $\sim$ - 80°). The core flux density is $\sim$2.1 mJy and the total flux density is $\sim$ 3.6 mJy. The correlated VLBI flux density is $\sim$ 50% of the arcsecond core flux.

0838+32 (4C 32.26) – This radio source is associated with a dumbbell galaxy identified as the brightest galaxy in Abell 695, although recent works claim that it is at the centre of a group unrelated and much closer than the Abell cluster it was originally identified with (Jetha et al. 2008). At low resolution (Valentijn 1979; Jetha et al. 2008) it appears to be a Wide Angle Tailed (WAT) source (Fig. 4.21), but at high resolution it shows a compact FRII structure with core flux density $S_{c,1.4}$ ∼7.5 mJy (Machalski 1998).

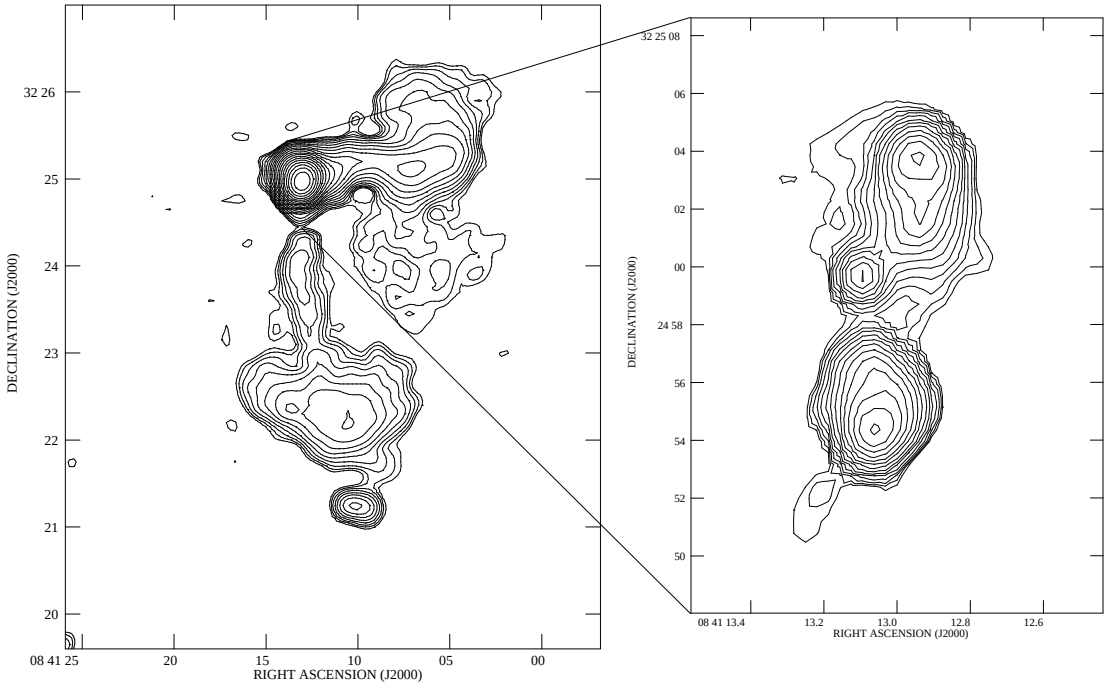

Figure 4.21: 1.4 GHz VLA image of 4C 32.26 (main image) of resolution arcsec^2, showing the large-scale radio lobes; the inner lobes appear unresolved in this image. The inset image is a arcsec^2, 4.9 GHz image that shows the inner core and lobes. Contours are in steps with the lowest contour at 0.31 mJy/beam for both images (Jetha et al. 2008).

The radio structure suggests a possible restarting activity and X-ray data suggest that the currently active lobes are expanding supersonically (Jetha et al. 2008). In our VLBA image, the source is unresolved with total flux density $S_5 = 7.0$ mJy, with little or no arcsecond core flux missing on parsec scales ($S_{\rm VLBA}/S_c \sim 90\%$).

0915+32 – The VLA radio map by Fanti et al. (1987) shows a two-sided jet in P.A. = 28° with mirror symmetry (Fig. 4.22). The radio structure could be due to gravitational interactions with a nearby spiral galaxy (Parma et al. 1985).

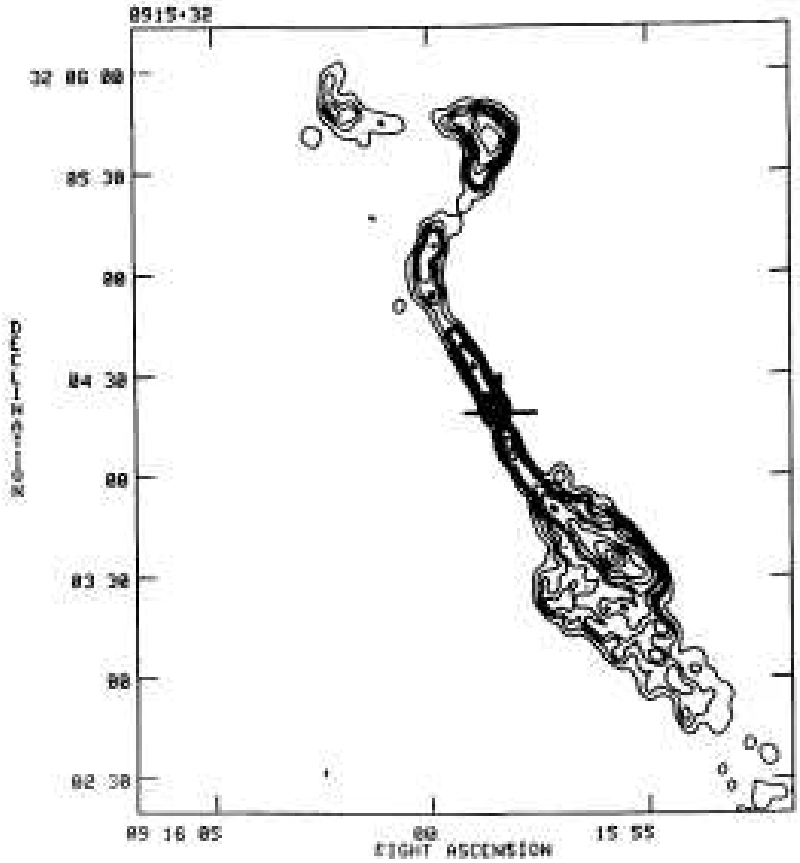

Figure 4.22: Contour plot of the radio map at 20 cm of 00915+32 (Fanti et al. 1987). Contour levels are 0.2 × (-1, 1, 2, 4, 6, 8, 12, 16, 20, 28, 40, 80) mJy/beam. The cross marks the position of the optical identification. The beam is 4.5 × 3.8 arcsec ^{2}, P.A. = 9 °. The noise level is 0.08 mJy/beam. Coordinates are at 1950.

In our VLBA image, the source appears unresolved with a total flux density of $S_5 \sim 13.6$ mJy. No arcsecond core flux is lost on the mas scale ($S_{\rm VLBA}/S_c \sim 100\%$).

1113+29 (4C 29.41) – This radio source is associated with the BCG of Abell 1213, which is part of a double system of galaxies close to the center of the cluster (Trussoni et al. 1997). At radio frequencies (Fig. 4.23), it shows a double structure with linear size ~ 61 kpc and a total radio power at 1.4 GHz Log $P_{1.4} = 24.7$ (Fanti et al. 1986).

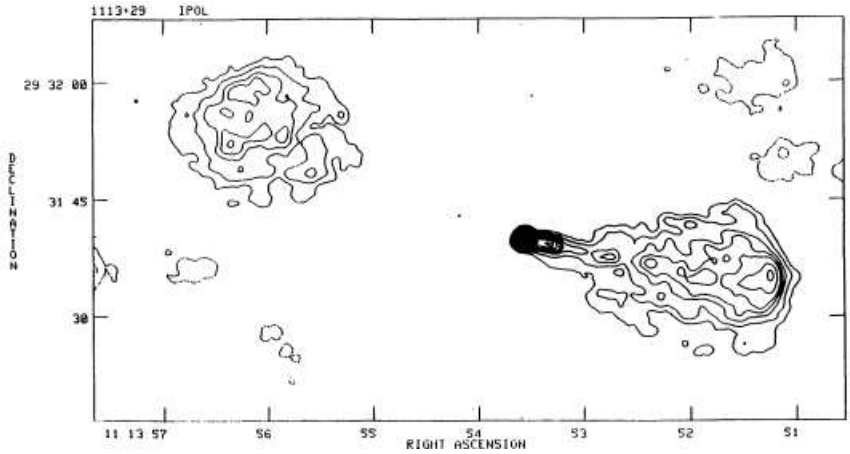

Figure 4.23: Contour plot of the radio map at 20 cm of 1113+29 (Fanti et al. 1986). Contour levels are 0.5 × (-2, -1, 1, 2, 4, 6, 8, 12, 16, 20, 30, 40, 50, 60) mJy/beam. The cross marks the position of the optical identification. The beam is 1.44 × 1. 25 arcsec^2, P.A. = 60 deg. The noise level is 0.15 mJy/beam. Coordinates are at 1950.

An extended weak X-ray emission has been found to be associated with the cluster (Ledlow et al. 2003).

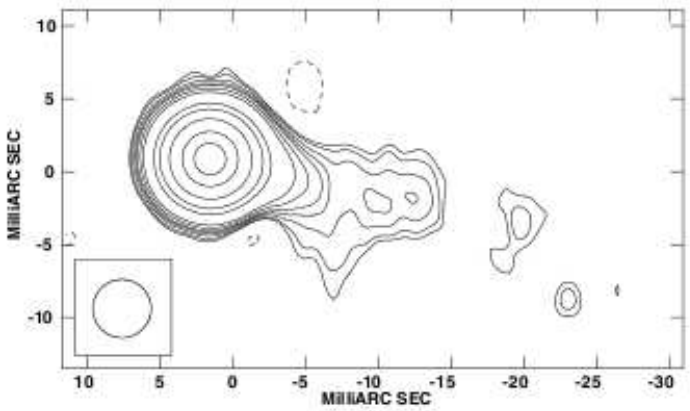

Figure 4.24: VLBA image of 1113+29 at 5 GHz. The HPBW is 4 mas, the noise level is 0.06 mJy/beam and levels are: −0.2, 0.15, 0.2, 0.3, 0.4, 0.5, 0.7, 1, 3, 5, 10, 20 and 30 mJy/beam.

In our VLBA image, the source shows an extended one-sided jet (Fig. 4.24),

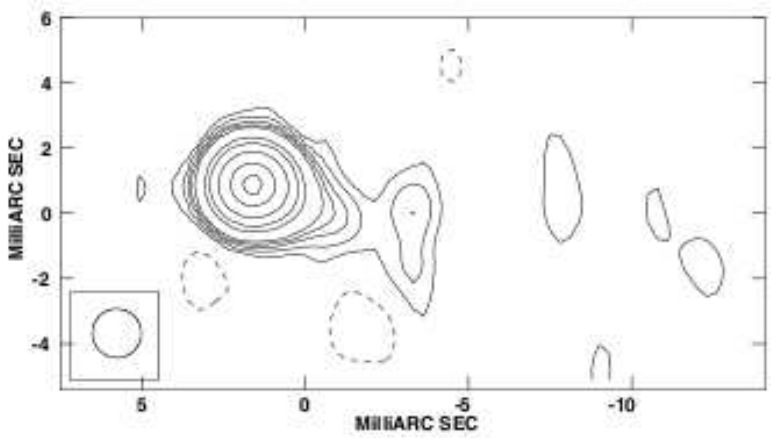

Figure 4.25: VLBA image of 1113+29 at 5 GHz. The HPBW is 1.5 mas, the noise level is 0.07 mJy/beam, and levels are: -0.2, 0.15, 0.3, 0.5, 0.7, 1, 3, 5, 10, 20 and 30 mJy/beam.

resolved in the high resolution image and suggestive of a limb-brightened structure (Fig. 4.25). The parsec-scale jet is on the same side as the main kiloparsec scale jet. The total correlated flux in the VLBA image is $\sim$ 40 mJy, and therefore no arcsecond core flux is missing on the parsec scale.

1116+28 – The galaxy associated with this radio source is a double system at a distance of $z = 0.0667$. At arcsecond resolution (Fanti et al. 1987), the radio source shows a Narrow Angle Tail (NAT) structure with two symmetric jets (Fig. 4.26).

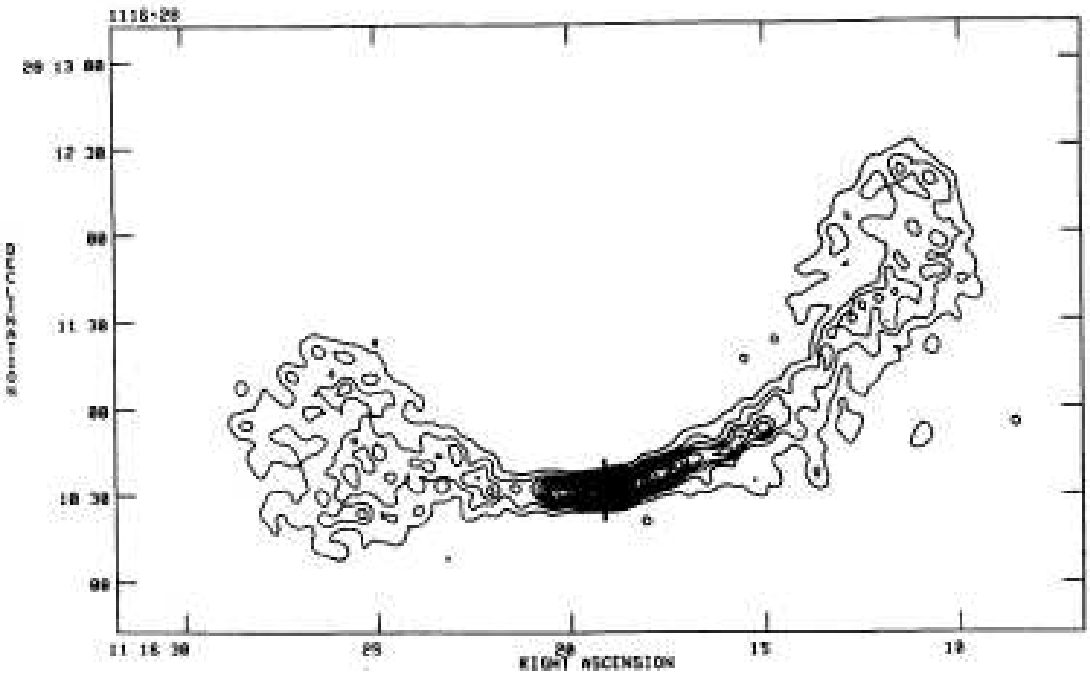

Figure 4.26: Contour plot of the radio map at 20 cm of 1116+28 (Fanti et al. 1987). Contour levels are 0.5 × (-1, 1, 2, 3, 4, 5, 6, 7, 8, 10, 12, 14, 16, 20, 25, 30, 40, 50, 60. 80, 100, 120) mJy/beam. The cross marks the position of the optical identification. The beam is 5.5 × 4.4 arcsec ^{2}, P.A. = 15 deg. The noise level is 0.12 mJy/beam. Coordinates are at 1950.

? showed a slightly resolved parsec-scale structure with two-sided jets oriented in the same direction as the kpc-scale jets. Because of the large fraction of missing flux in the VLBI image we re-observed this source at 5 and 1.6 GHz. We do not confirm the two-sided jets previously reported. We consider therefore this source to be unresolved with total flux densities $S_{1.6} = 9.5$ mJy, $S_5 = 11.5$ mJy, and a slightly inverted spectral index $\alpha^5_{1.6} = -0.17$. Most of the arcsecond core flux is still missing on the milliarcsecond scale at both frequencies ($S_{\rm VLBA}/S_c \sim 40\%$).

1122+39 (NGC 3665) – At arcsecond resolution (Fig. 4.27), this appears to be a core plus twin-jet radio source (Parma et al. 1986).

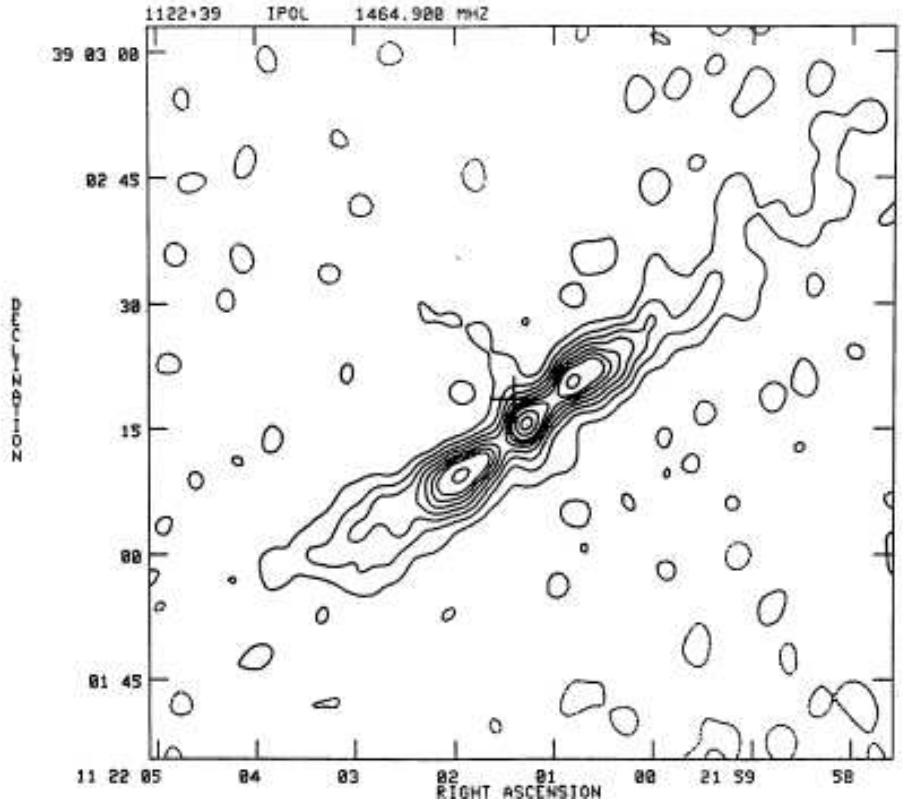

Figure 4.27: Contour plot of the radio map at 20 cm of 1122+39 (Parma et al. 1986). Contour levels are 0.9 × (-2, 2, 6, 12, 20, 30, 40, 50, 70, 90 and 100) mJy/beam. The cross marks the position of the optical identification. The resolution is 3.5 arcsec. Coordinates are at 1950.

In our VLBA image, it shows a pointlike structure with a total flux density $S_5 =$ 8.8 mJy. No arcsecond core flux is missing on the parsec-scale ($S_{\rm VLBA}/S_c \sim 100\%$)

1204+24 – In the VLA image (Fig. 4.28), this source appears as a FRI with faint symmetric lobes and a bright core (Fanti et al. 1986).

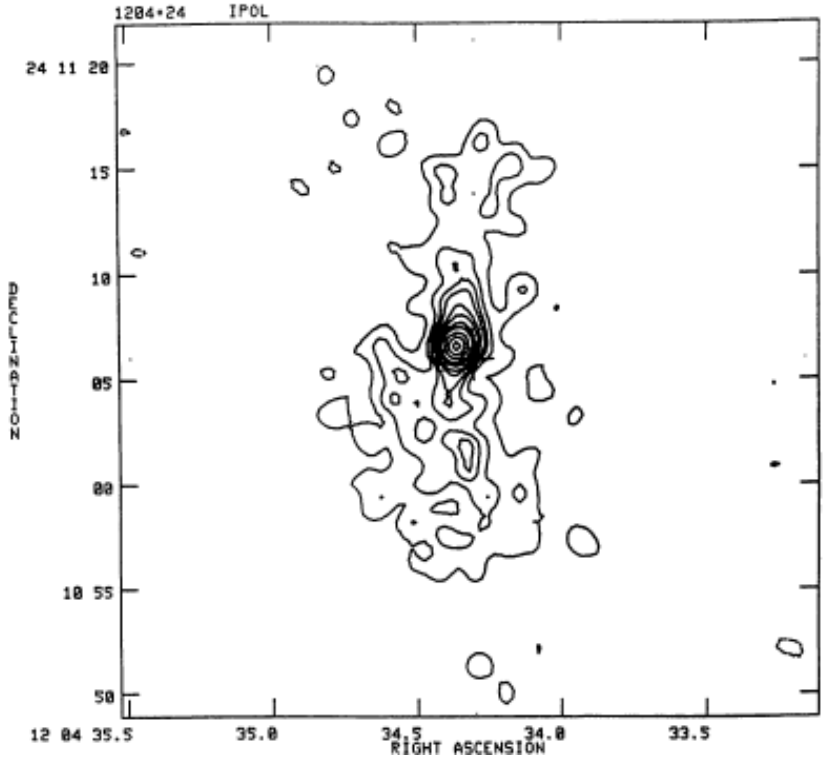

Figure 4.28: Contour plot of the radio map at 20 cm of 1204+24 (Fanti et al. 1986). Contour level are 10 × (-0.25, 0.25, 0.5, 0.75, 1, 1.5, 2, 3, 4, 6, 8 and 10) mJy/beam. The cross marks the position of the optical identification. The beam is 1.4 × 1.1 arcsec^2, P.A. = 41 °. The noise level is 0.15 mJy/beam. Coordinates are at 1950.

In our VLBA image, it appears unresolved with a total flux density $S_5 = 5.3$ mJy, corresponding to a fraction of the VLA core $S_{\rm VLBA}/S_c \sim 66\%$.

1251+27B (3C 277.3) – The radio and optical properties of 3C 277.3 are described in detail by van Breugel et al. (1985). The elliptical host galaxy of 3C 277.3 is very smooth and regular; on kiloparsec-scale (Fig. 4.29), the radio source extends <60 kpc and it has two wide and diffuse lobes with a few brightness enhancements (southern jet and northern hot spot).

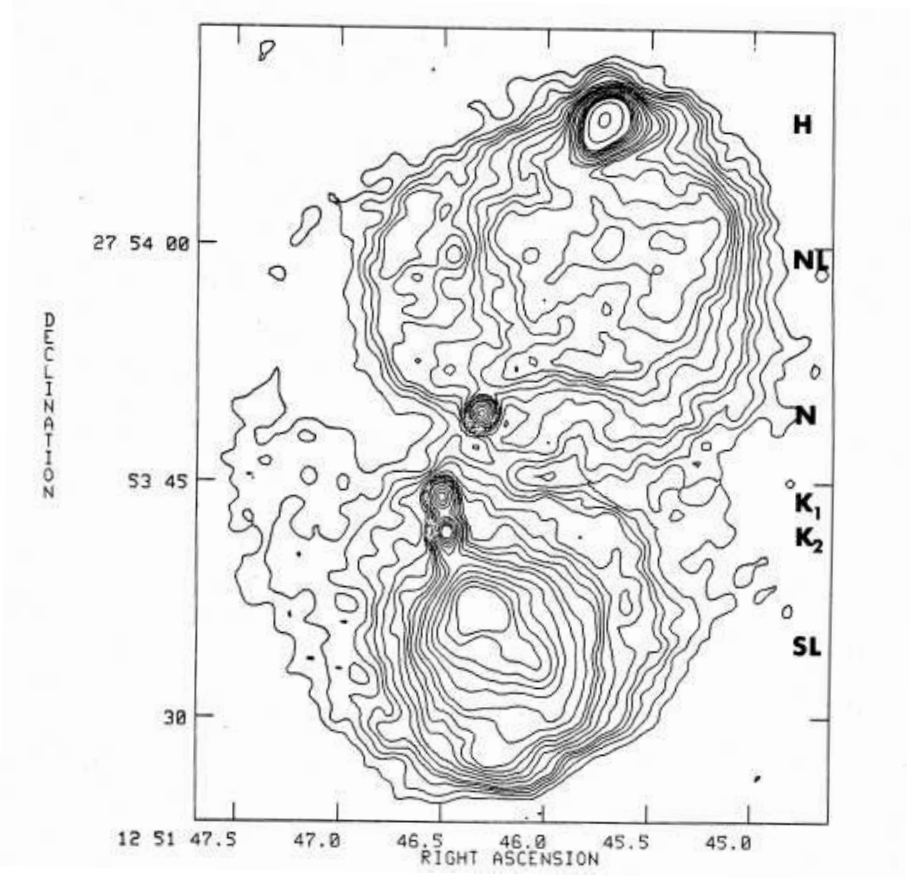

Figure 4.29: Contour plot of the radio map at 20 cm of 3C277.3 (van Breugel et al. 1985). The resolution is 1.2 arcsec. Various features are labeled (see van Breugel et al. (1985)). Contour values are 0.57 × (-0.9, 0.9, 1.5, 2, 2.5, 3, 4, 5, 6, 7, 8, 10, 12, 16, 20, 24, 28, 32, 50, 90) mJy/beam. Negative values appear dashed.

In our VLBA image (Fig. 4.30), this source shows a possible two-sided structure with total flux density ∼10.4 mJy and a jet orientation quite similar to the kiloparsec-scale jet (ΔPA∼20°). The core flux density is ∼6.2 mJy and only ∼ 10% of the arcsecond flux is lost on the mas scale.

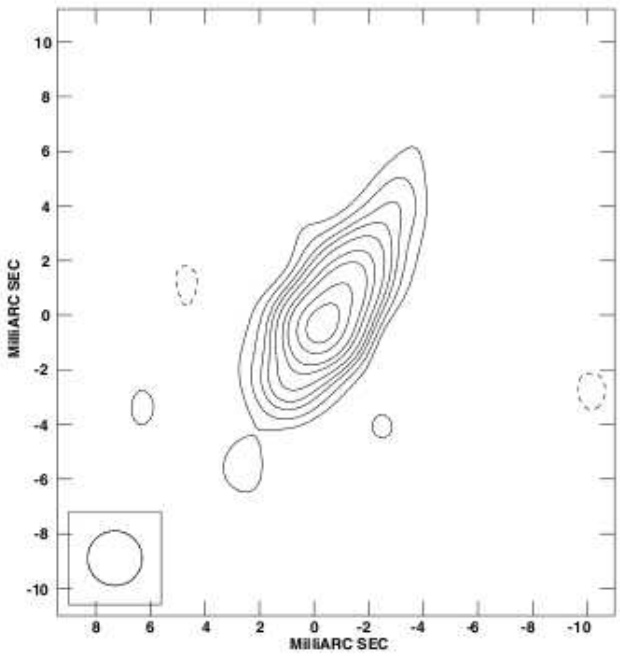

Figure 4.30: VLBA image of 1251+27B (3C277.3). The HPBW is 2 mas, the noise is 0.06 mJy/beam, and levels are: -0.2, 0.15, 0.3, 0.5, 0.7, 1, 1.5, 2, 3 and 4 mJy/beam.

1319+42 (3C 285) – The host galaxy of 3C 285 has been identified with the BCG of a group of galaxies (Sandage 1972). 3C 285 is a classical double-lobed radio galaxy (Fig. 4.31) of 190 arcsec total extension at 4.86 GHz, with two hotspots and an eastern ridge showing curvature roughly along the line to the optical companion (Leahy & Williams 1984; Hardcastle et al. 1998).

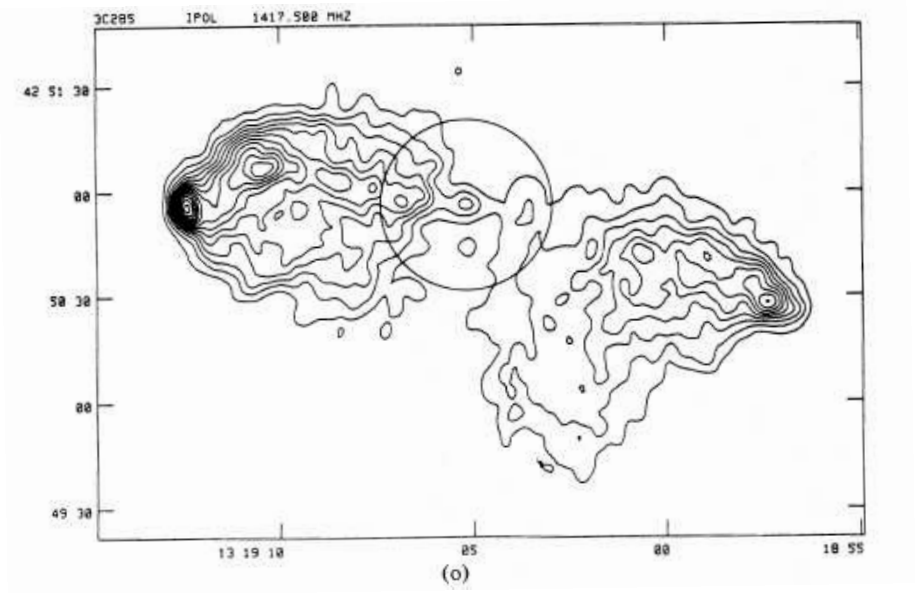

Figure 4.31: VLA Contour map of 3C285 at 21 cm (Leahy & Williams 1984). The circle indicates the 25 kpc region around the galaxy center. The peak is 0.029 Jy/beam. Contours are -2, 2, 4, ...28 mJy/beam.

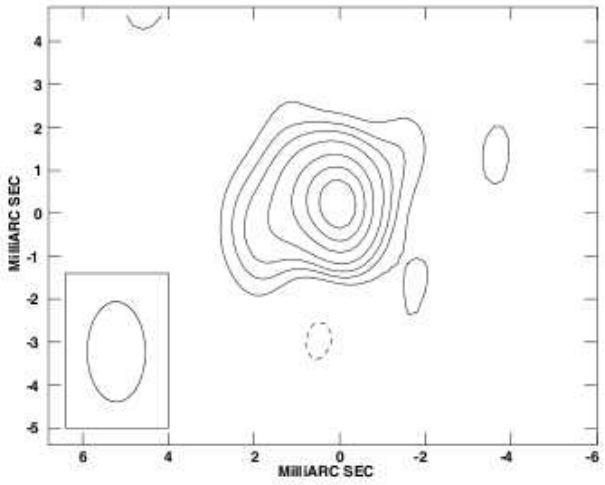

Figure 4.32: VLBA image at 5 GHz of 1319+42 (3C 285). The HPBW is 2.3 × 1.4 mas in PA = 0°. The noise level is 0.1 mJy/beam and levels are: −0.3, 0.3, 0.5, 0.7, 1, 1.5, 2 and 2.5 mJy/beam.

In our VLBA image, the source is slightly resolved at the same PA as the kiloparsec-scale jets (Fig. 4.32) with a symmetric structure. The total flux density is ∼4.7 mJy; very little arcsecond core flux is lost on the milliarcsecond-scale (S_{VLBA}/S_c∼80%)

1339+26 (UGC 08669) – This radio galaxy has a head-tail morphology (Fig. 4.33).

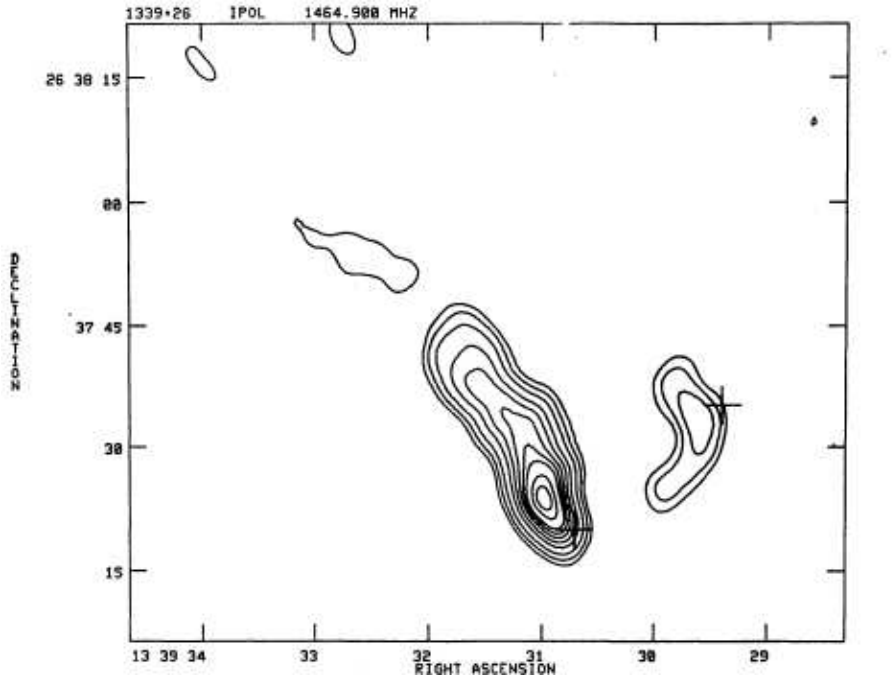

Figure 4.33: Contour plot of the radio map at 20 cm of 1339+26 (Parma et al. 1986). Contour levels are 0.44 × (-2, 2, 4, 8, 16, 25, 35, 45, 55, 75 and 90) mJy/beam. The cross marks the position of the optical identification. The resolution is 3.5 arcsec. Coordinates are at 1950.

It is the easternmost of a double system identified with the dominant member of the cluster Abell 1775. A small dark nuclear band (P.A.∼ 0°) characterizes this otherwise regular galaxy (Capetti et al. 2000). In our VLBA image, this source is not detected above 0.3 mJy/beam.

1357+28 – The host of this radio source is a round elliptical galaxy with a small dust lane (P.A. $\sim 90°$) bisecting the nuclear region (Capetti et al. 2000). The radio map by Fanti et al. (1987) shows a two-sided inner jet in P.A. = 0.5° that decollimates and bends at 30 arcsec from the core (Fig. 4.34).

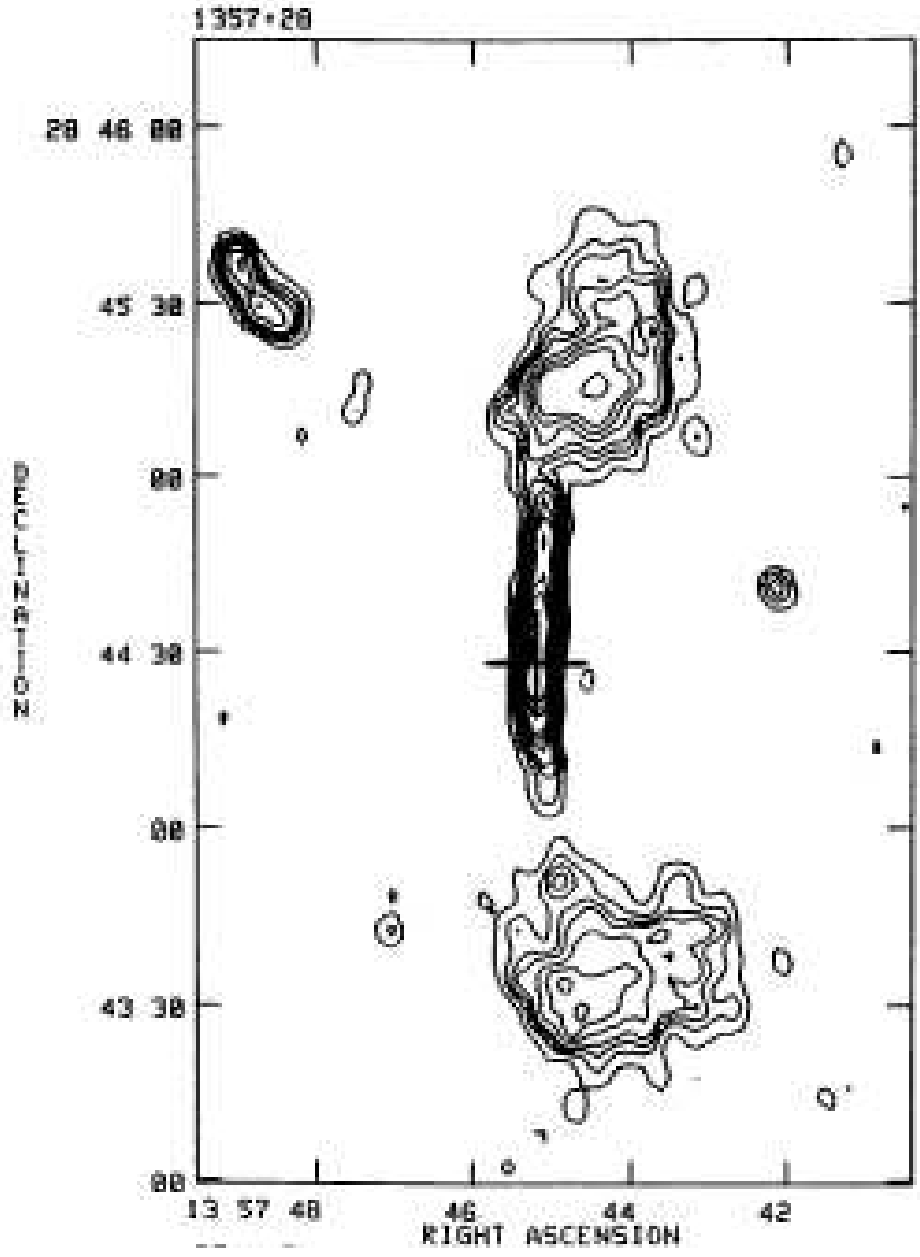

Figure 4.34: Contour plot of the radio map at 20 cm of 1357+28 (Fanti et al. 1986). Contour levels are 0.25 × (-1, 1, 2, 4, 6, 8, 10, 15, 20, 40, 60, 100, 150 and 200) mJy/beam. The cross marks the position of the optical identification. The beam is 4.2 × 3.7 arcsec^2, P.A. =5 °. The noise level is 0.09 mJy/beam. Coordinates are at 1950.

Our VLBA image (Fig. 4.35) shows a slightly extended core suggesting a two-

sided structure in PA $\sim 20°$. The VLBA core flux density is 5.6 mJy and some of the arcsecond core flux is missing on the milliarcsecond scale ($S_{\rm VLBA}/S_c \sim 60\%$).

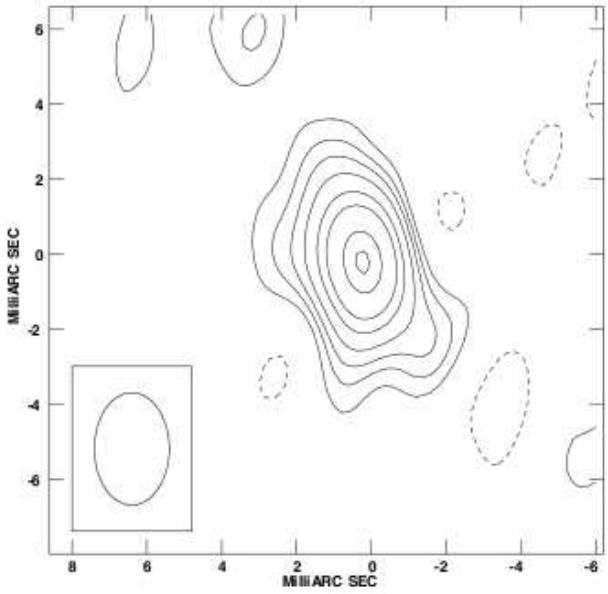

Figure 4.35: VLBA image at 5 GHz of 1357+28. The HPBW is 3×2 mas in PA 0°. The noise is 0.15 mJy/beam, and levels are: -0.3 0.3 0.5 0.7 1 1.5 2 3 3.5 mJy/beam.

1422+26 – An extended FR I galaxy (Fig. 4.36), with two symmetric jets oriented east-west at arcsecond resolution. At 5 GHz, Giovannini et al. (2005) detect a weak (3 mJy) milliarcsecond scale source. The 1.6 GHz observations presented in this work detect a larger flux density ($S_{1.6} \sim 9.3$ mJy), distributed in a misaligned and distorted structure (see Fig. 4.37).

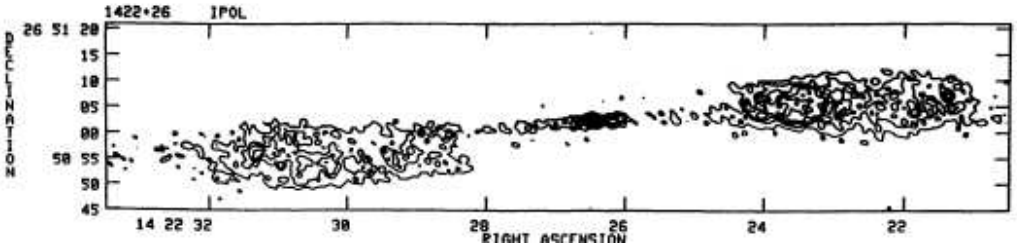

Figure 4.36: Contour plot of the radio map at 20 cm of 1422+26 (Fanti et al. 1986). Contour levels are 0.1144 × (-5, 3, 5, 7, 9, 12, 15, 20, 25, 50, 75 and 90) mJy/beam. The cross marks the position of the optical identification. Levels are in mJy/beam. The beam is 1.4 × 1.2 arcsec^2, P.A. =54 °. The noise level is 0.1 mJy/beam. Coordinates are at 1950.

We tentatively identify the peak in the 1.6 GHz image with the nuclear source detected also at 5 GHz. In this scenario the spectral index is ~ 0 and the extended 1.6 GHz structure is a one-sided, distorted jet. More data are necessary to understand the nature of this source.

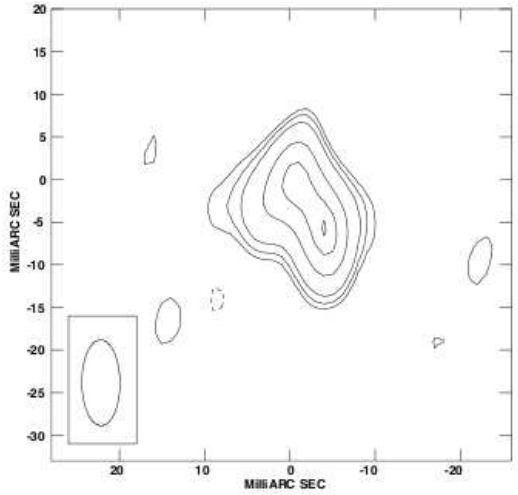

Figure 4.37: VLBA image of 1422+26 at 1.6 GHz. The HPBW is 10.1 × 4.5 mas in PA 0°. The noise is 0.15 mJy/beam and levels are: −0.5 0.7 0.7 1 2 3 3.5 mJy/beam.

1448+63 (3C 305) – A well known double source (Fig. 4.38), recently studied in detail by Massaro et al. (2009), it was only marginally detected in previous VLBA 5 GHz observations (Giovannini et al. 2005).

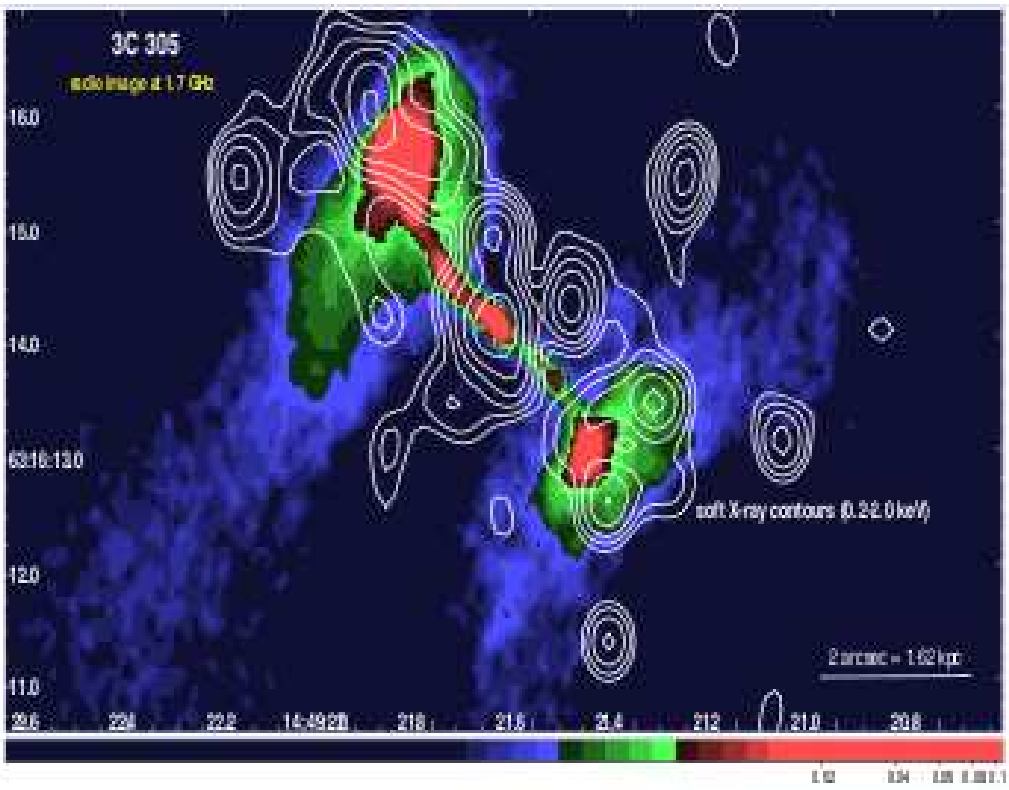

Figure 4.38: The radio image of 3C 305 at 1.7 GHz obtained combining MERLIN and VLA data retrieved from the Web site: http://www.jb.man.ac.uk/. An Atlas of DRAGNs with soft X-ray contours overlaid (0.2-2.0 keV, smoothed 0.5). There is a clear evidence that the extended X-ray emission lies beyond the radio structure (Massaro et al. 2009)

In our new observations at 1.6 GHz the nuclear source is not detected, but there is a clear detection on the shortest baselines. The visibilities are well described by a two component model, separated by $\sim 1.5''$. These are probably the two hot spots visible in the MERLIN images (see Massaro et al. (2009)).

1529+24 (3C 321) – An extended FR II narrow line radio galaxy, with optical evidence of double nuclei. The two components are clearly merging galaxies with evidence for a merger-triggered starburst activity (Roche & Eales 2000). The kiloparsec-scale nuclear emission (Fig. 4.39) has been discussed by Baum et al. (1988).

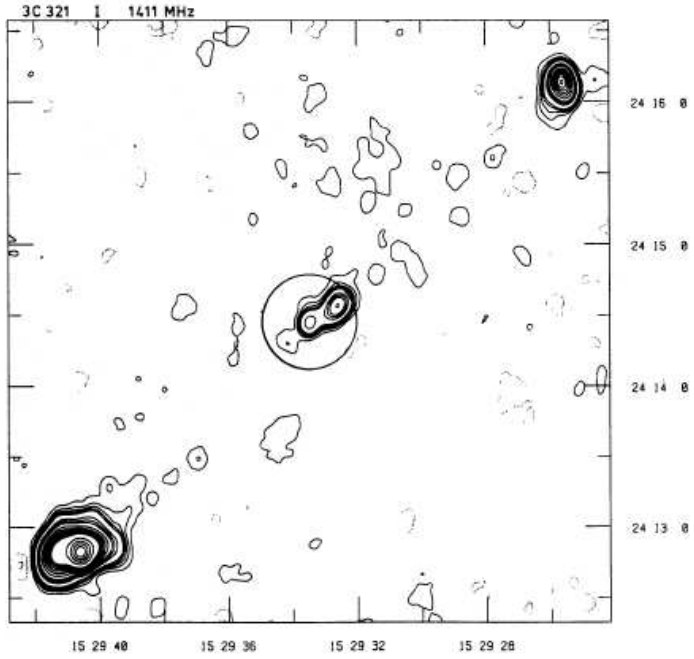

Figure 4.39: VLA Contour map of 3C321 at 21 cm (Leahy & Williams 1984). The circle indicates the 25 kpc region around the galaxy center. The peak is 1.21 Jy/beam. Contours are -6, -3, 3, 6...15, 30, 40, 50, 75, 100, 200, 40, ...1000 mJy/beam.

With the VLBA we detect at 1.6 GHz some faint, diffuse emission, difficult to either clean or modelfit. A tentative visibility model fit reveals ~ 7 mJy at 1.6 GHz, in two nearly equal components separated by $0.03''$ (see Fig. 4.40).

A faint and complex structure is expected from the large difference between the point-like mas structure at 5 GHz (~ 3 mJy) and at 1.6 GHz (~ 7 mJy) and the arcsecond core flux density at 5 GHz (~ 30 mJy).

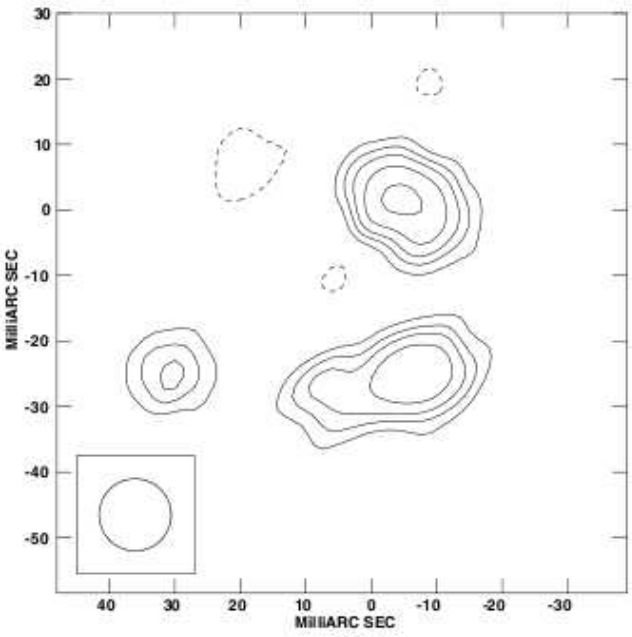

Figure 4.40: VLBA image of 1529+24 at 1.6 GHz. The HPBW is 11.0 mas. The noise is 0.1 mJy/beam and levels are: -0.3, 0.3 0.5 0.7 1 1.5 mJy/beam.

1557+26 – This is an unresolved source on arcsecond scale, with $S_5 = 30$ mJy. Our 1.6 GHz image recovers ~ 10 mJy in a relatively compact component. The spectral index with respect to the 5 GHz data by Giovannini et al. (2005) is $\alpha^5_{1.6} = 0.1$ in agreement with the core dominated one-sided structure found at 5 GHz. Visibility phases and amplitudes on the LA-PT baseline suggest that there could also be a more extended component, but it is not possible to constrain it with the present data.

1613+27 – A symmetric double on kiloparsec scales (Parma et al. 1986), with a 25 mJy core at 5 GHz (Fig. 4.41).

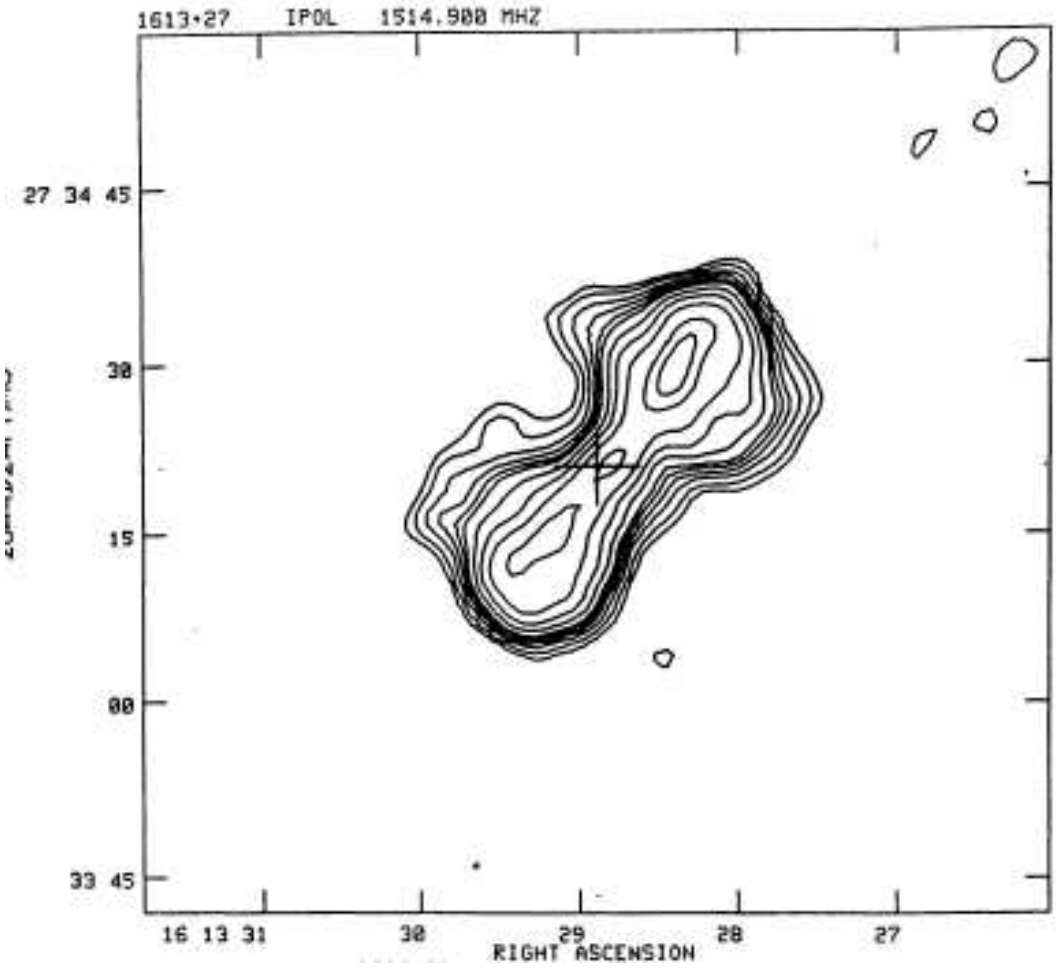

Figure 4.41: Contour plot of the radio map at 20 cm of 1613+27 (Parma et al. 1986). Contour levels are 0.15 × (-4, 4, 6, 9, 12, 15, 18, 25, 35, 50, 75 and 90) mJy/beam. The cross marks the position of the optical identification. The resolution is 3.5 arcsec. Coordinates are at 1950.

Our 1.6 VLBA image reveals an unresolved core, with $S_{\rm VLBA,1.6} = 9.3$ mJy, in

agreement with VLBA at 5 GHz (Giovannini et al. 2005); the non simultaneous spectral index is $\alpha^{5}_{1.6} = 0.15$. The large fraction of missing flux could imply that the VLA core flux is overestimated, or that the source is variable.

1615+35B (NGC6109) – This is a very extended Head Tail (HT) radio source (Fig. 4.42) with a structure more than 10′ in size, oriented N-S. It is associated with an elliptical galaxy of m_{pg}=14.9 at a redshift of 0.0296.

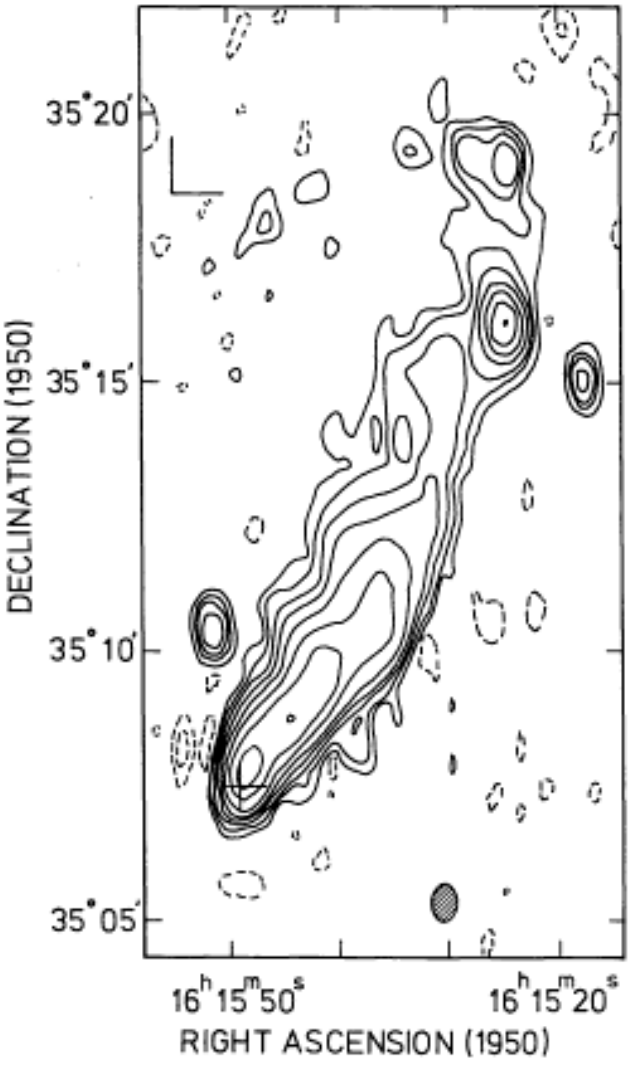

Figure 4.42: Contour plot of the radio map at 1.4 GHz of 1615+35B (Ekers et al. 1978). The cross marks the position of the optical identification. Contour levels are -3, -1.5 (dashed), 1.5, 3, 6, 12, 24, 48, ...mJy/beam. The cross indicates the position of the optical identification. The dashed ellipse is the half power cross section for the beam.

In our VLBA image (Fig. 4.43), the nuclear emission is seen with a jet on the same side as the kiloparsec-scale jet. The total flux density detected in our map is $\sim$ 23.6 mJy, the core flux is $\sim$17.1 mJy and the ratio between the VLBA correlated flux and the arcsecond core flux density at 5 GHz is 85%. At 1.2 mas from the nucleus, the jet/counter-jet surface brightness ratio is $\geq$30.

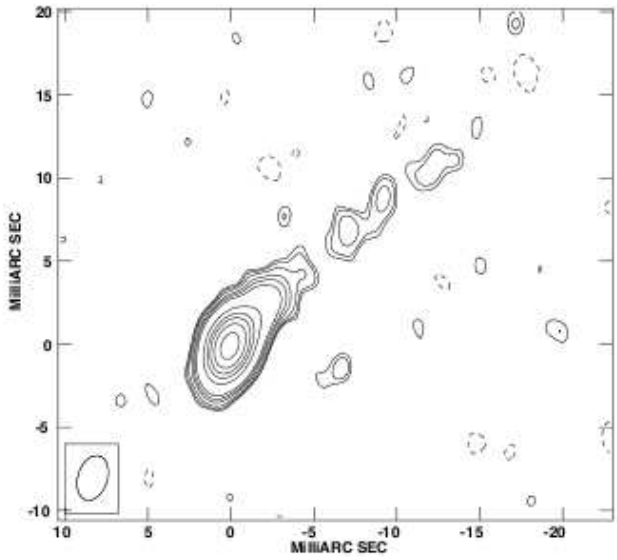

Figure 4.43: VLBA image of 1615+35B at 5 GHz. The HPBW is 2.8 × 1.8 mas^2 in PA=-17°. The noise level is 0.06 mJy/beam and levels are −0.15 0.15 0.2 0.3 0.5 0.7 1 3 5 7 10 15 mJy/beam.

1621+38 – A head-tail radio galaxy (Fanti et al. (1986), Fig. 4.44).

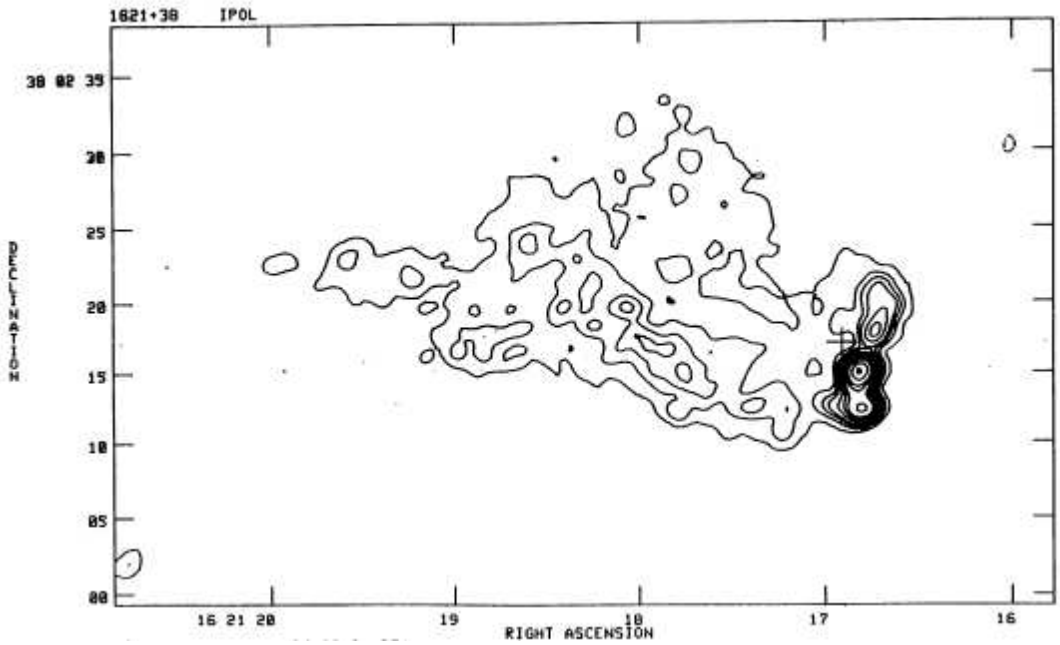

Figure 4.44: Contour plot of the radio map at 20 cm of 1621+38 (Fanti et al. 1986). Contour levels are 0.5 × (-2, 1, 2, 3, 4, 6, 8, 10, 15, 20, 30 and 40) mJy/beam.The cross marks the position of the optical identification. The beam is 1.38 × 1.33 arcsec^2, P.A. = - 52 °. The noise level is 0.27 mJy/beam. Coordinates are at 1950.

In our VLBA 1.6 GHz data it shows a core-jet structure in PA $\sim 160°$ (Fig. 4.45) in agreement with the 5 GHz image of Giovannini et al. (2005). The core spectral index is $\alpha^5_{1.6} = 0.25$ and a significant fraction of core flux density is missing.

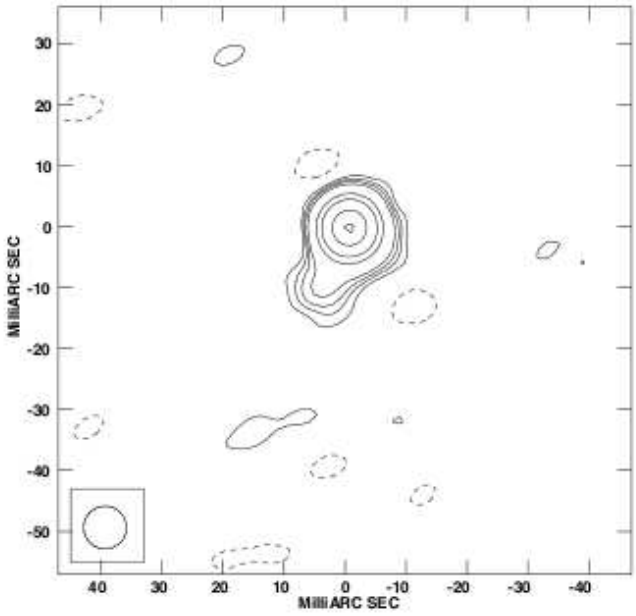

Figure 4.45: VLBA image of 1621+38 at 1.7 GHz. The HPBW is 7 mas, the noise 0.09 mJy/beam and levels are: -0.3, 0.3, 0.5, 0.7, 1, 3, 5, 10 and 15 mJy/beam.

1637+29 – This peculiar source displays a head-tail morphology (Fig. 4.46) associated with a poor group of galaxies (de Ruiter et al. 1986).

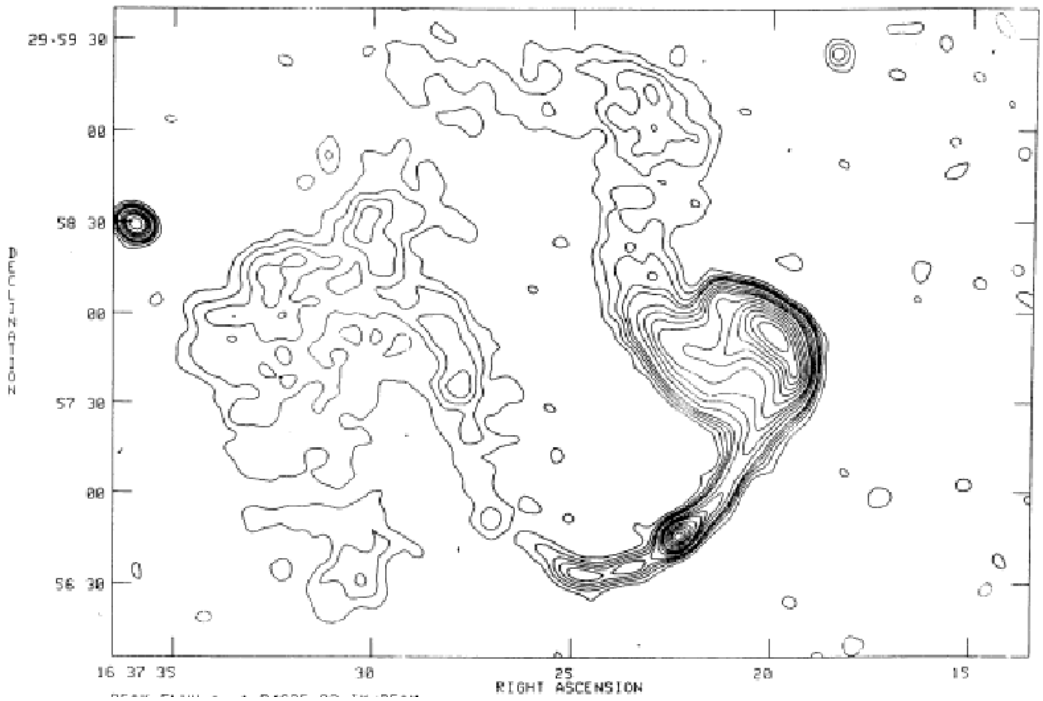

Figure 4.46: Contour plot of the radio map at 20 cm of 1637+29 (de Ruiter et al. 1986). The resolution is 6.5 arcsec.Contour levels are -0.2 (dashed line), 0.2, 0.4, 0.6, 0.8, 1.0, 1.5, 2, 2.5, 3, 4, 6, 7, 8, 9 mJy/beam . Coordinates are at 1950.

The radio source consists of twin bent jets, with the main jet ending in a very bright lobe and two radio tails showing conspicuous oscillations. Our VLBA image shows an unresolved component with total flux density $S_5 \sim= 7.8$ mJy. The ratio between the VLBA correlated flux and the arcsecond core flux density at 5 GHz is 60%.

1736+32 – The B2 source is resolved in two unrelated radio sources (Fig. 4.47). The main source (the Northern one) has a FR I structure, the secondary (Southern) appears as a background FR II source projected onto the SE lobe of the FR I galaxy (Fanti et al. 1986).

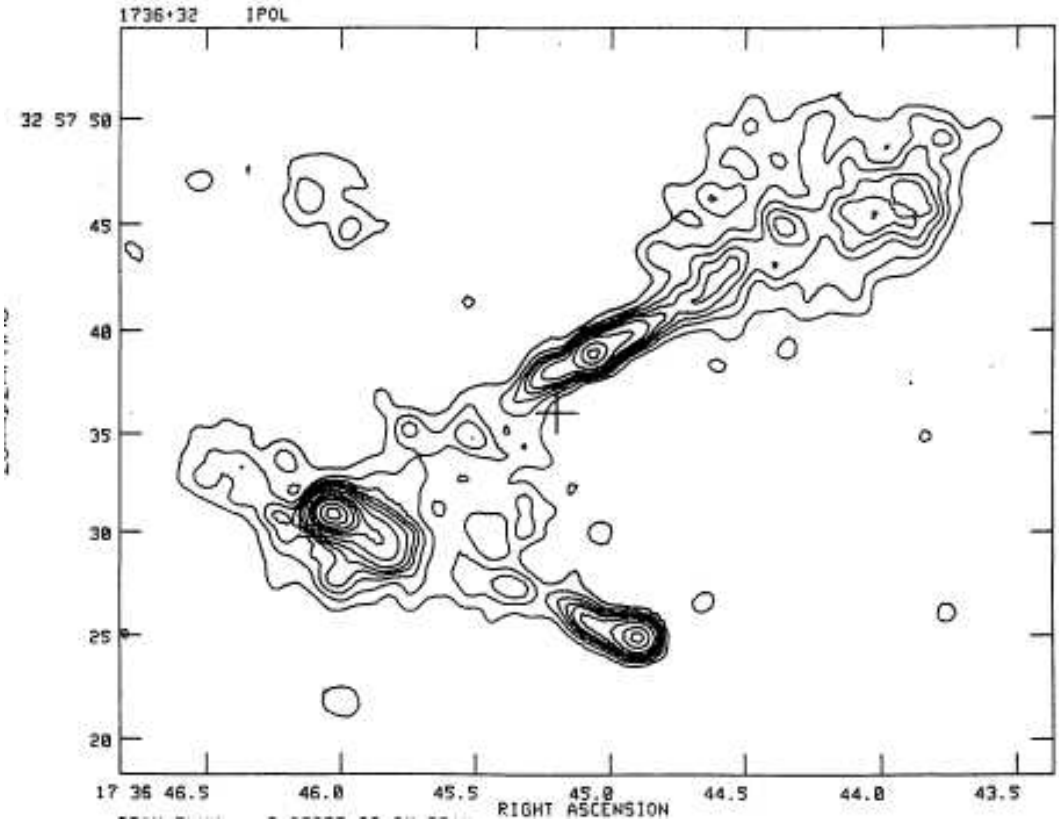

Figure 4.47: Contour plot of the radio map at 20 cm of 1736+32 (Fanti et al. 1986). Contour levels are 1× (0.3, 0.6, 0.9, 1.2, 1.5, 2, 3, 5, 7, 10, 15 and 20) mJy/beam. The cross marks the position of the optical identification. The beam is 1.27 × 1.27 arcsec^2, P.A. =0 °. The noise level is 0.24 mJy/beam.

In our VLBA image of the main source, we found an unresolved structure with a total flux density $\sim$ 7.6 mJy. No arcsecond core flux is missing on the milliarcsecond scale.

1752+32B: In VLA images (Fig. 4.48), this source appears as a FRI source (Capetti et al. 1993).

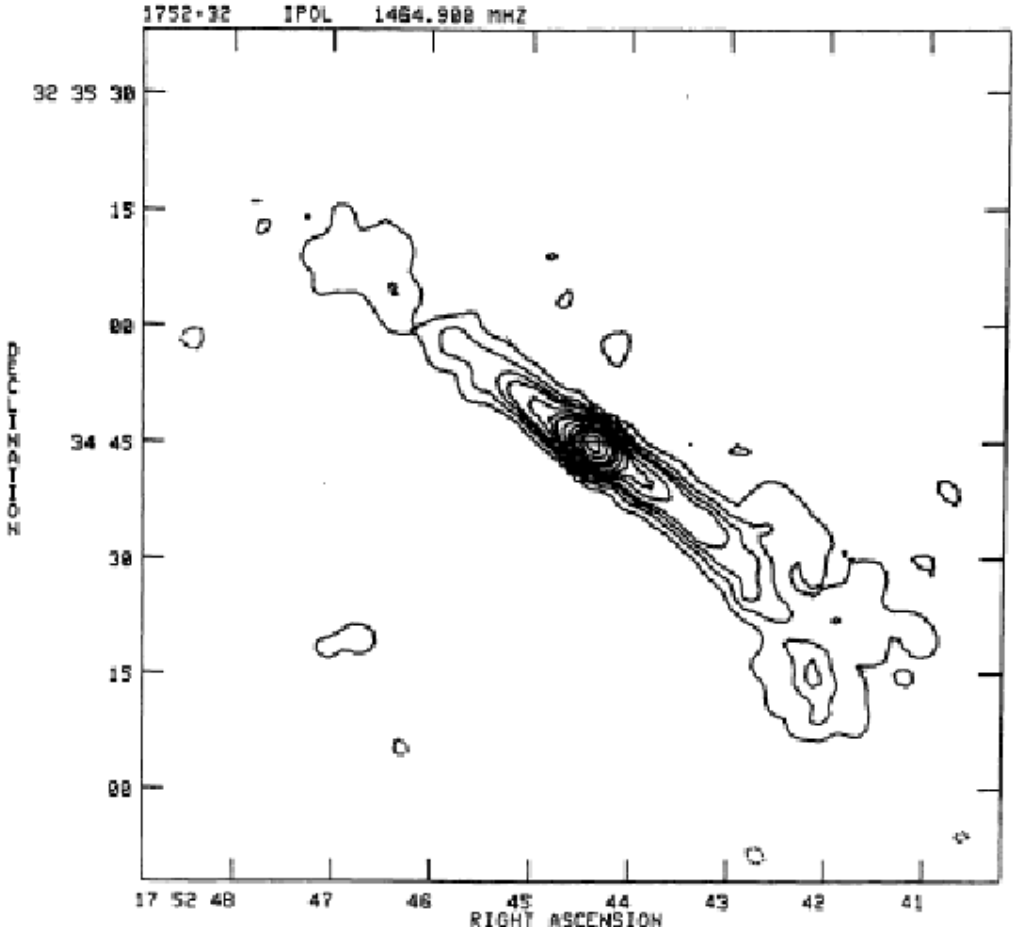

Figure 4.48: Contour plot of the radio map at 20 cm of 1752+32B (Fanti et al. 1986). Contour levels are 0.4 × (-1, 1, 2, 3, 4, 6, 8, 10, 14, 20, 25, 30, 40, 50 and 60) mJy/beam. The cross marks the position of the optical identification. The beam is 1.41 × 1.3 arcsec^2, P.A. = - 69 °. The noise level is 0.13 mJy/beam. Coordinates are at 1950.

Our VLBA image shows nuclear emission with a two-sided emission at the same PA as the kiloparsec-scale jet (Fig. 4.49). The total flux density detected in our map is ∼9.3 mJy, the core flux is ∼7.4 mJy and the ratio between the VLBA correlated flux and the arcsecond core flux density at 5 GHz is 77%.

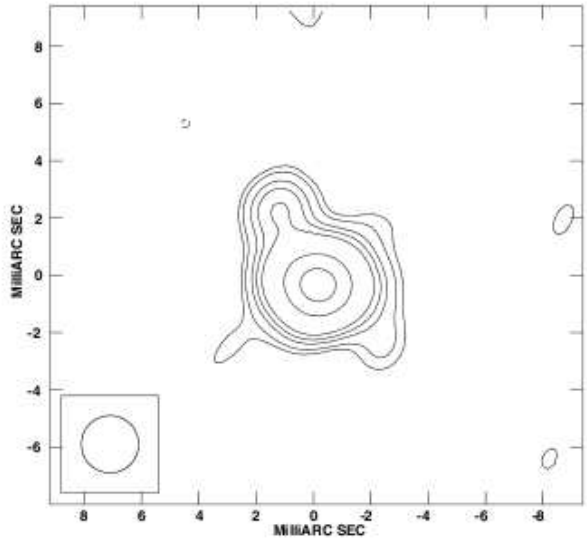

Figure 4.49: VLBA image of 1752+32B at 5 GHz. The HPBW is 2 mas, the noise level 0.08 mJy/beam. Contours are: −0.2 0.2 0.3 0.5 0.7 1 3 5 mJy/beam.

2236+35 (UGC 12127) – This source has a large-scale double radio jet (Fig. 4.50) embedded in a low-surface-brightness region with S symmetry (Fanti et al. 1986).

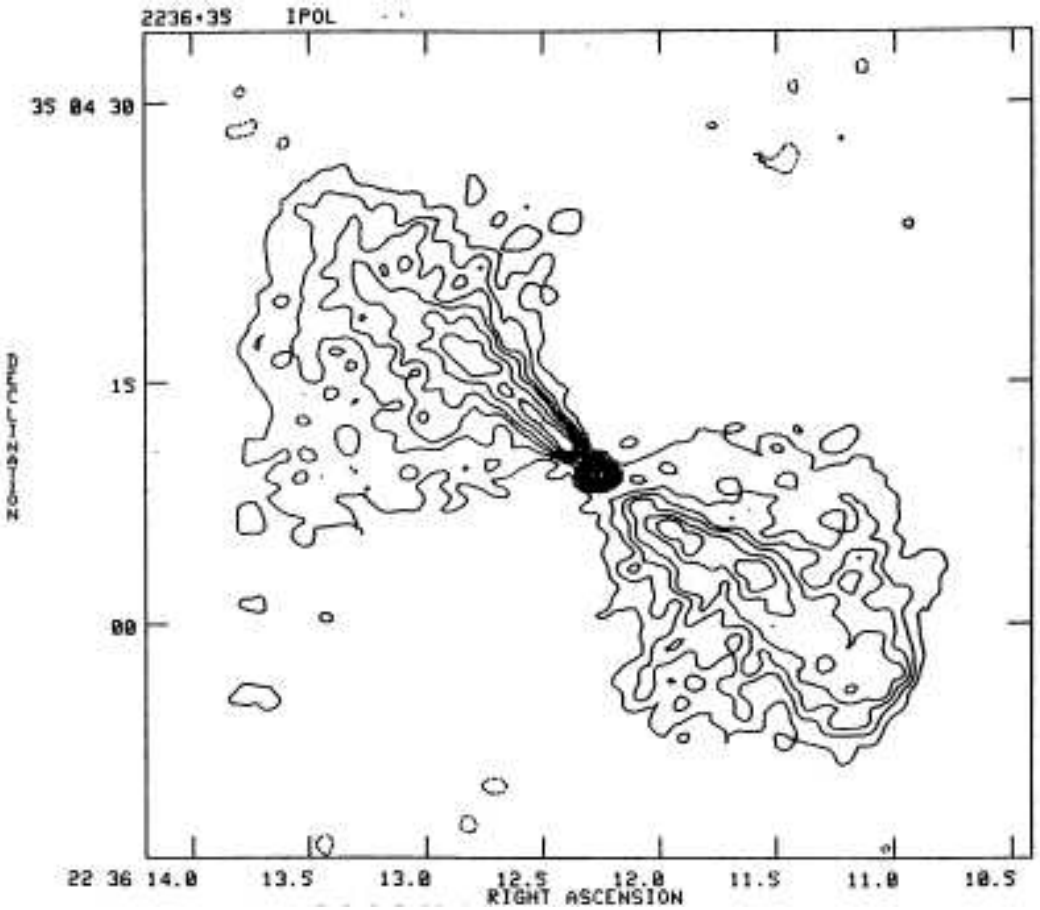

Figure 4.50: Contour plot of the radio map at 20 cm of 2236+25 (Fanti et al. 1986). Contour levels are 0.25 × (-2, 1, 2, 3, 4, 6, 8, 12, 16, 20 and 24) mJy/beam. The cross marks the position of the optical identification. The beam is 1.14 × 1.09 arcsec^2, P.A. =35 °. The noise level is 0.13 mJy/beam. Coordinates are at 1950.

In our VLBA image, the source is unresolved with total flux density ∼8.8 mJy and no arcsecond core flux is missing on the milliarcsecond scale.

4.5 Results for the BCS sample.

Considering previous (Giovannini et al. 2005) and these new observed BCS sources, here we present some statistical results for the BCS sample.

4.5.1 Source Morphology

Among sources with VLBI data, we have the following kiloparsec-scale structures: (a) 51 FRI radio galaxies; (b) 13 FRII radio galaxies; (c) 11 compact sources with a flat spectrum (including two BL-Lac objects), and 1 compact steep-spectrum source (CSS). The observed sample is not yet complete, but representative of a sample of sources at random angles to the line of sight. In fact, in a randomly oriented sample of radio galaxies, the probability that the source is at an angle θ_1 and θ_2 with respect to the line of sight is

$$P(\theta_1,\theta_2) = \cos\theta_1 - \cos\theta_2$$

In the observed sample, the percentage of FR I plus FR II radio sources is 84% that corresponds to sources oriented at angles greater than 33°. We note also that among sources that are compact at arcsecond resolution 3 (27%) show a two-sided pc scale structure, 5 (45%) are one-sided, 1 (9%) is a CSO and 2 (18%) have not been detected. This result confirms that low power compact sources with a flat spectrum have sub-kpc scale structure, but their small size is not always due to projection effects of beamed objects as in the case of the two BL-Lac sources and possibly the other three radio galaxies with one-sided parsec-scale structure.

The total number of sources with a two-sided jet morphology on the parsec-scale is 23, corresponding to 30% of the sample. This percentage is higher than that found in previous samples in the literature: indeed, there are 11% (7/65) symmetric sources in the PR (Pearson-Readhead) sample Pearson and Readhead (1988) and 4.6% (19/411) in the combined PR and Caltech-Jodrell (CJ) samples Taylor et al. (1994); Polatidis et al. (2003). The difference in the percentage of two-sided jet sources can be even larger if we consider that there are two separate classes of two-sided objects: CSOs and core jets. The CSOs do not strongly depend on orientation since most of the flux comes from the hot spots moving at (0.10.3)c. Nearly all symmetric sources in the PR and CJ sample are young CSO sources, while very few

of them are expected in the local (z < 0.1) universe. We note that in our sample there is only one CSO (4C 31.04; Giroletti et al. 2003), and it was not classified as a two-sided jet source. The main difference between the percentage of symmetric sources in the present sample and in previous samples is naturally explained in the framework of unified scheme models by the fact that the present sources show relatively faint cores and they are less affected by orientation bias. In particular, all two-sided FR II radio galaxies are narrow-line objects that confirm that broad-line radio galaxies are oriented at least as close to the line of sight as quasars.

It is difficult to estimate the expected number of sources in our sample that should show two-sided structure, since the detection of both the jet and the counterjet depends not only on the Doppler effect but also on the sensitivity needed to detect the counterjet. The values of the jet-to-counterjet ratios R for the sources of our sample are given in Table 4.4. The high values derived for 0055+30 (NGC 315) and 0220+43 (3C 66B) are related to the presence of high-brightness jets and very deep radio observations of these sources (Giovannini et al. (2001)). In the other two-sided sources, the values of R are in the range 15. Most of the lower limits to R are much larger than 5, thus confirming that the sensitivity in our maps is generally good enough to detect as two sided the sources that are at large angles to the line of sight. The sources with a two-sided structure in our sample are about 30%. This percentage implies that sources with two-sided jets are oriented at angles greater than 70°. This is consistent with a jet-to-counterjet ratio $\leq$5 if the jet velocity is (0.90.99)c.

We note that a jet-to-counterjet ratio $\leq$5 in two-sided sources implies also that a counterjet is easily detected only if the jet brightness is at the level of about 15 rms (using a map detection limit of 3 rms). We find that 27% (14) of the FR I radio galaxies and 46% (6) of the FR II radio galaxies are two sided on the parsec scale. The higher fraction of symmetric sources among the FR II galaxies could suggest that the jets in FR II galaxies are intrinsically stronger than those in FR I galaxies (assuming that the velocities are the same). No correlation is found between the jet-to-counterjet ratio and the total or arcsecond core radio power.

Table 4.4: Parameters for Observed Sources

Name	Type Kpc	Type pc	S_{cVLBI} mJy	$S_{totVLBI}$ mJy	S_{cVLA} mJy	$S_{totVLBI}/S_{cVLA}$ %	j/cj ratio %	core dominance
0034+25	FR I	C	3.6	3.6	10	36	...	1.10
0055+26	FR I	C	7.5	7.5	11	68	...	0.26
0055+30	FR I	two-sid	296	477	588	81	42	8.71
0104+32	FR I	one-sid	72	90	92	98	>16	0.60
0106+13	FR II	two-sid	11.0	30	24	100	2	0.21
0116+31	C	CSO	20.0	1250	–	100	...	1.07
0149+35	FR I	C	3.2	3.2	5	64	...	0.25
0206+35	FR I	one-sid	75	87	106	82	>14	2.14
0220+43	FR I	two-sid	105	180	182	99	10	0.98
0222+36	C	two-sid	58.2	120	140	86	...	12.02
0258+35	CSS	one-sid	7.4	243	<243	100	...	<2.75
0300+16	FR I	C	6.1	6.1	10	61	...	0.07
0326+39	FR I	one-sid	55.5	74	78	95	>25	1.91
0331+39	C	one-sid	90	104	149	70	>12	3.24
0356+10	FR II	C	2.2	2.2	9	24	...	0.05
0648+27	C	one-sid	4.4	12.8	58	22	>8	7.41
0708+32B	FR I	CSO?	?	10.5	15	70	...	2.63
0755+37	FR I	one-sid	138	216	195	100	>20	3.16
0802+24	FR II	two-sid	2.1	3.6	8	45	1	0.13
0836+29-II	FR I	one-sid	146	167	131	100	>20	8.32
0836+29-I	FR I	one-sid	24.2	47.8	63	76	>50	...
0838+32	FR I	C	7.0	7.0	7.5	93	...	0.41
0844+31	FR II	two-sid	27.0	32	40	80	1	1.35
0915+32	FR I	C	13.6	13.6	8.0	100	...	0.98
1003+35	FR II	one-sid	152.8	466	400	100	>45	14.13
1037+30	C	ND	ND	<2	<84	–	...	<10
1040+31	C	two-sid	37.6	48	55	87	5	2.00
1101+38	BL Lac	one-sid	335	448	640	70	>110	24.55
1102+30	FR I	two-sid	14.3	17	26	65	1.7?	2.29
1113+29	FR I	one-sid	36.8	40.0	41	98	> 5	0.89
1116+28	FR I	C	11.5	11.5	30	38	...	2.34
1122+39	FR I	C	8.8	8.8	6	100	...	0.18
1142+20	FR I	one-sid	125	172	200	86	>24	1.17
1144+35	FR I	two-sid	50.1	?	–	–	...	..
1204+24	FR I	C	5.3	5.3	8	66	...	4.57
1204+34	FR II	one-sid	33.7	39	23	100	>2	2.09
1217+29	C	two-sid	31.5	121	162	75	>2	<2.75
1222+13	FR I	one-sid	105	126	180	70	>10	0.32
1228+12	FR I	one-sid	450	1600	4000	40	>150	0.91
1251+27B	FR II	two-sid	6.2	10.4	12	87	2	0.38
1257+28	FR I	one-sid	0.79	1.07	1.1	97	>2	0.06
1316+29	FR I	two-sid	5.3	23	31	74	1	1.29
1319+42	FR II	two-sid	3.0	5.0	6	83	2	0.19
1321+31	FR I	two-sid	3.7	11	21	52	1?	0.26
1322+36	FR I	one-sid	45	60	150	40	>20	3.09
1339+26	FR I	ND	–	–	<55	–	...	<4.07
1346+26	FR I	two-sid	4.1	44	53	83	...	2.04
1350+31	FR I	two-sid	14.4	23	–	–	2	<1.42

Table 4.4: continued.

Name	Type Kpc	Type pc	S_{cVLBI} mJy	$S_{totVLBI}$ mJy	S_{cVLA} mJy	$S_{totVLBI}/S_{cVLA}$ %	j/cj ratio %	core dominance
1357+28	FR I	two-sid	3.8	5.6	6.2	90	1?	0.10
1414+11	FR I	two-sid	65.1	86	77	100	2	0.95
1422+26	FR I	one-sid	1.7	3	25.0	12	>20?	0.81
1448+63	FR I	C?	1.1	2	29	7	...	0.48
1502+26	FR I	two-sid	0.5	7.8	80	10	1	0.78
1521+28	FR I	one-sid	39.5	44	40	100	>17	2.88
1529+24	FR II	C	3.4	3	30	10	...	0.98
1553+24	FR I	one-sid	40.7	46	40	100	>20	6.17
1557+26	C	one-sid	7.8	9	30	30	> 4	8.13
1613+27	FR I	C	7.8	8	25	32	...	3.31
1615+35B	FR I	one-sid	17.1	23.6	28	84	>15	0.37
1621+38	FR I	one-sid	12.9	20	50	40	> 5	2.29
1626+39	FR I	two-sid	29	91	105	87	1.1	0.76
1637+29	FR I	C	7.8	7.8	13	60	...	1.48
1652+39	BL-Lac	one-sid	450	1000	1250	80	>1250	64.54
1658+30	FR I	one-sid	60.0	76	84	90	>8.5	3.09
1736+32	FR I	C	7.6	7.6	8	95	...	0.95
1752+32B	FR I	two-sid	6.1	9.2	12	77	2	1.41
1827+32A	FR I	one-sid	5.9	15	26	58	>7.5	2.51
1833+32	FR II	one-sid	105	131	188	70	>20	2.75
1842+45	FR II	one-sid	34.0	52	62	84	>10	1.23
1845+79	FR II	one-sid	??	??	330	–	>100	3.02
1855+37	C	ND	ND	<2	<100	–	...	<7.94
2116+26	FR I	two-sid	?	?	47	–	1	2.63
2229+39	FR I	C	25.9	30	37	81	...	0.35
2236+35	FR I	C	8.8	8.8	8.0	100	...	0.39
2243+39	FR II	two-sid	18	125	130	96	1.1	1.51
2335+26	FR I	one-sid	168	234	270	87	>10	1.82

VLBI data are at 5 GHz

One-sided sources are found in 31/76 sources (41%) confirming that this structure is the most frequent pc scale structure because of Doppler boosting.

The number of unresolved sources in our VLBI images is 15 (20%). Most of them (14) are FR I radio galaxies, and 1 is a FR II source (1529+24). In most cases these are sources with faint relativistic jets in the plane of the sky, and therefore their jets are de-boosted.

We observed sources with a low core flux density at 5 GHz at arcsecond resolution (> 5 mJy), but only 3 sources (4 %) have not been detected in our VLBI observations. Two of them are C-shaped sources as discussed before, and the

other one is a FR I radio galaxy. This result confirms that also in low power sources and in radio sources with a low radio nuclear activity a compact nuclear radio source is present.

Finally we would like to discuss the two radio sources where a **Z**-shaped structure is present on the parsec-scale. At present among BCS sources these are 1502+26 (3C310), and 1346+26 (4C26.42). A few other are present in literature as e.g. the CSO 1946+708 (Taylor et al. 2009). The presence of this symmetric and large change in the jet direction so near the core cannot be due to projection or relativistic effects. The large symmetry present in these sources imply that are oriented close to the plane of the sky, moreover a change in the jet velocity and/or orientation would produce a change in the Doppler factor that should be revealed by the observations of the jet properties. As discussed in more detail in Chapter 3, for 1346+26 the source morphology strongly suggests that in these sources the jets are not highly relativistic even at a few pc distance from the core. A slow and possibly high density jet could more easily interact with a turbulent surrounding medium in rotation near the central Black Hole to show this peculiar symmetric structure.

4.5.2 Missing flux in parsec scale structures

We compared the total flux at VLBA scale with the core arcsecond flux density (Tab. 4.4). Over all data, among 76 sources, we find that 47 (62 %) have a correlated flux density larger than 70% of the arcsecond core flux density. This means that in these sources we mapped most of the mas scale structure and so we can properly connect the parsec to the kiloparsec structures. Instead, for 19 (38%) sources, a significant fraction of the arcsecond core flux density is missing in the VLBA images. This suggests variability or the presence of significant structures between ∼30 mas and 1 arcsec that the VLBA can miss due to a lack of short baselines. In particular among the 6 sources where the VLBA flux density is less than 10% of the arcsecond core flux density measured by the VLA, we have evidence of a complex structure in agreement with an intermediate-scale structure lost in our images. Variability should be also considered. To properly study these structures, future observations with the EVLA at high frequency or with the e-MERLIN array will be necessary.

4.5.3 Jet velocity and orientation

For 51 sources we can estimate the ratio between the jet and counter-jet brightness or provide a lower limit to the ratio (Table 4.4). Among the 25 sources with a ratio $\gtrsim$ 10 we have one-sided sources with the exception of 0055+30 and 0220+43 where deep observations allowed us to detect a counterjet structure despite a large brightness ratio. The presence of large ratios confirms the presence of relativistic jets.

We estimated the core dominance also of new observed sources (Table 4.4). According to Giovannini et al. (1994) and references therein, a correlation is present between the core and total radio power and we can use the core dominance to estimate the jet velocity and orientation. In Table 4.4 we present the core dominance defined as the ratio between the observed and the estimated core radio power according to the relation given in Giovannini et al. (1994).

A ratio larger than 1 implies a source with a boosted core, therefore oriented at an angle smaller than 60°. For a value of the core dominance in the range 0.25 - 1, the core radio power is lower than the value expected from the correlation therefore the nuclear observed power is de-boosted and the source is oriented at an angle larger than 60°. These values are in general in agreement with the ratio between the jet and counterjet brightness and can give useful constraints on the jet velocity and orientation. Three sources show a core dominance larger than 10: two BL Lacs and 0222+36, a symmetric source in VLBI images but with evidence of restarted activity (Giroletti et al. 2005a,b).

If the core dominance is smaller than 0.25 no solution can be found from the correlation. Such a strong deboosting cannot be obtained even if the source is in the plane of the sky and the jets are strongly relativistic. We interpret such a result as a possible nuclear variability with the core in a low activity regime and/or the evidence that the nuclear activity is now stopped and the total radio power is related to a previous episode of greater nuclear activity, i.e. the AGN is dying. We have 8 sources with a such low core dominance. Four of them are FR I radio galaxies (0300+16, 1122+39, 1257+28, 1357+28) characterized by a faint nuclear emission in VLA observations at 5 GHz not only with respect to the total low frequency flux density, but also with respect to the source total flux density at the same frequency. The remaining four sources are narrow line extended and powerful FR

II radio galaxies (0106+13, 0356+10, 0802+24, 1319+42), lobe dominated and with evidence of spectral steepening at high frequency. Also in these sources the extended radio lobes suggest a previous episode of greater nuclear activity.

Chapter 5

Conclusions

5.1 BCG versus BCS sample.

A comparison between BCG and BCS samples is necessary to confirm the achieved statistical results on BCGs properties.

Main results from the study of the BCS are:

- The detection rate is high: only 3 sources (4%) out of 76 have not been detected, even though we observed sources with an arcsecond core flux density as low as 5 mJy at 5 GHz. This result confirms the presence of compact radio nuclei at the center of radio galaxies.

- As expected in sources with relativistic parsec-scale jets, the one-sided jet morphology is the predominant structure present in our VLBI images. However, 22% of the observed sources show evidence of a two-sided structure. This result is in agreement with a random orientation and a high jet velocity ($\beta \sim 0.9$).

- We find 2/76 sources ($\sim$3%) with a **Z**-shaped structure on the parsec-scale suggesting the presence of low velocity jets in these peculiar radio sources. Note that one of these is 4C 26.42, the BCG in a cool core cluster Abell 1795 (see Chapter 3).

- In 8 ($\sim$10%) sources the low core dominance suggests that the nuclear activity is now in a low activity state. The dominance of the extended emission implies a greater activity of the core in the past. However in these sources a parsec-scale core and even jets are present. In this scenario the nuclear activity may be in a low or high state but is not completely quiescent. This result is in

agreement with the evidence that a few sources show evidence of a recurring or re-starting activity. This point can be better addressed when observations are available for the full sample so that we can discuss the time-scale of the recurring activity.

- In most cases, the parsec and the kiloparsec scale jet structures are aligned and the main jet is always on the same side with respect to the nuclear emission. This confirms the idea that the large bends present in some BL Lacs sources are amplified by the small jet orientation angle with respect to the line-of-sight.

- In 62% of the sources, there is good agreement between the arcsecond-scale and the VLBI correlated flux density. For the other 38% of the sources, at the milliarcsecond scale more than 30% of the arcsecond core flux density is missing. This suggests the presence of variability, or of a significant sub-kiloparsec-scale structure, which will be better investigated with the EVLA at high frequency or with the e-MERLIN array.

Concerning the BCG sample (Chapter 2), the main statistical results are:

- the final detection rate is 60 %. The non detections of the BCG sample are more than these of the BCS sample, but we have to note that, differently to the BCS, the BCG sample is composed also by radioquiet sources at kpc scale. If we consider only radioloud objects on large scale, the detection rate arise to 76%.

- The presence of a clear dichotomy between relaxed and non relaxed clusters is evident (Table 2.5). At mas scale, one-sided structures are only in BCGs in non cool core clusters, instead two-sided morphologies are only in BCGs in cool core clusters.

- As for the BCS sample, the majority (70%) of sources has a correlated flux density larger than 80 % of the arcsecond flux density. Only for 30% a significant fraction of the arcsecond core flux density is missing in the VLBA images suggesting the same conclusion reported for BCS sample.

- In most cases, the parsec and the kiloparsec scale jet structures are aligned and the main jet is always on the same side with respect to the nuclear emission.

- We estimated the core dominance also for the BCG sample. As expected, among the BCGs with low core dominance we find 4 sources (UGC6086, NGC3842, UGC10143, UGC10187) undetected in our VLBA maps being radioquiet core in radio galaxies. Moreover, two (3C 84 and 2C 338) evidences of restarted activity in the radioemission associated to the BCG are found, with 3C 84 showing the higher core dominance value of the sample.

From this comparison we note that:

- BCG and FRI radio galaxies show a similar radio structure on mas resolution. In both samples, we have evidence of a sub (kpc) scale structure in some sources. No large binding is observed from parsec to kpc with a few exceptions.
- A marginal evidence is present that restarted and/or intermittent activity is more often in BCG sources.
- On parsec scale, a clear dichotomy is found between BCGs in cool core (two-sided) and non cool core clusters (one-sided). Only one-sided BCGs have similar kinematic properties with FRIs (see next section).

5.2 Jet velocity for one sided structures.

Based on conclusions for the BCS sample that one-sided jet morphology is the predominant structure and only 22% of FRI radio galaxies have two-sided jets, in agreement with expectations based on a random orientation for sources with relativistic jets, we suggest that all FRIs not in cool cores have similar parsec-scale properties regardless of their host galaxy classification (BCG or non BCG). One-sided structures in non cool core clusters are due to Doppler boosting effects in relativistic, intrinsically symmetric jets.

5.3 Jet velocity for two-sided structures.

Two-sided structures can be due either to relativistic jets in the plane of the sky or to mildly relativistic jets. For our BCGs, we exclude the first hypothesis as a consequence of statistical considerations in comparison with the BCS results. The percentage of tow-sided structure is too high respect the 22 % found in a BCS sample, a random oriented sources with relativistic and symmetric jets. It is not

possible that all BCGs in cool core clusters discussed here with resolved jets are oriented in the plane of sky. Therefore we conclude that BCGs in cool core clusters have mildly relativistic jets on the parsec-scale. To further test this hypothesis, in Fig.5.1 we plot the observed total arcsecond radio power at 408 MHz versus the observed arcsecond core radio power at 5 GHz for all the sources of our extended sample.

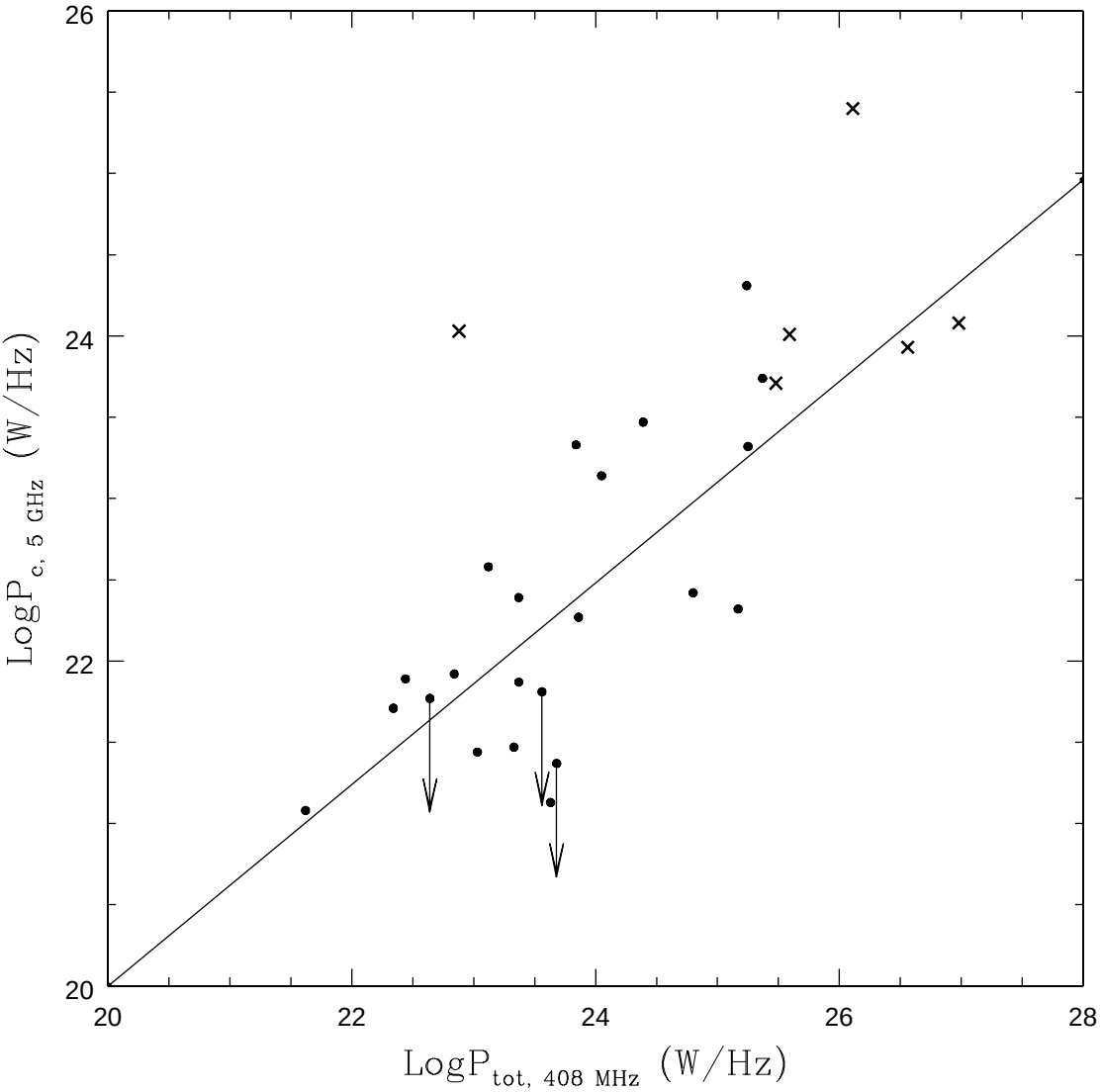

Figure 5.1: Total arcsecond radio power at 408 MHz versus observed arcsecond core radio power at 5 GHz for all BCGs of our complete sample with available information. The solid line is the relation found by Giovannini et al. (2001). Crosses (x) represent BCGs with two-sided pc scale jets and dots, one-sided sources.

The solid black line is the correlation found by Giovannini et al. (2001) for

sources randomly oriented with relativistic jets. According to the Table 2.3, for UGC10143, UGC10187 and NGC6086 we draw the upper limits of the observed arcsecond core radio power at 5 GHz. Despite the low number of sources discussed here we note that two-sided sources (crosses in the plot) detected in cooling clusters, and expected to show mildly relativistic jets, are not in agreement with the correlation found by Giovannini et al. (2001), while BCG with one-sided jets (dots in the figure) are in good agreement with the general correlation confirming the presence of relativistic jets in these BCGs.

5.4 Mildly relativistic jets: how to produce them?

In the center of cool core clusters, it is well known to be a very dense surrounding medium. Mildly relativistic jets in BCGs that lie in cool core clusters could be produce as consequence of jet interaction with this dense surrounding medium. We think that in these objects works at pc scale the same mechanism of deceleration due to the strong interaction of the jet with the surrounding medium that occurs in FRI radio sources at kpc scale. Because of the dense ISM of BCGs in cool core clusters, we suggest that in BCGs in cool core clusters the jet interaction with the ISM is already relevant on the parsec-scale.

We note (see Table 2.4) that two-sided jets are present only in BCGs at the center of clusters with a central mass accretion rate > 90 $M_{\odot}$/yr. A future speculation about a possible correlation between nuclear radio emission and X -ray properties (e.g. cooling rate) seem to be interesting.

In details, we suggest that jets in BCGs in cool core clusters start relativistic . In the same way as jet velocities of FRIs slow down at kpc scale, they decelerate thanks to the interaction with the surrounding medium but for these BCGs this happens yet at (sub-)parsec scale as stronger interaction due to denser environment in the center of these clusters. 3C 84 and Hydra A (see Chapter 3) are two observational evidences of BCGs in cool core for which our explanation seems to work.

5.4.1 The jet propagation model of Rossi et al. 2008.

We show here a model proposed by Rossi et al. 2008 to reproduce the jet propagation deceleration that occurs in FRI radio sources at kpc scale.

Strong observational evidence indicates that all extragalactic jets associated with AGNs move at relativistic speed up to 100 pc^{-1} kpc scales from the nucleus. At greater distances, reflecting the Fanaroff-Riley radio source classification, it is observed an abrupt deceleration in FR-I jets while relativistic motions persist up to Mpc scale in FR-II. More recently a large body of evidence has accumulated showing that jets are relativistic at their base, not only in FR-II radio sources but also in FR-I.

Superluminal motions are observed on milliarcsecond scales in several FR-I jets (Giovannini et al. 2001) and on arcsecond scales in M87 and Cen A (Biretta et al. 1995; Hardcastle et al. 2003). Finally on small scales, there are also observations

of one-sidedness and brightness asymmetry between jet and counter-jet, most likely due to Doppler boosting effects (Laing et al. 1999).

Relativistic motions from the inner regions all the way to larger scales, with Lorentz factors of about ten, appear to be present in powerful FR-II jet. Instead sub-relativistic velocities are found on kpc scales (Bicknell 1994) in low power radio sources, and the decrease in brightness asymmetry along the jet suggests that a deceleration must occur (Laing et al. 1999; Laing & Bridle 2002; Canvin et al. 2005).

Rossi et al. 2008 investigated this phenomenon by means of high-resolution three-dimensional relativistic hydrodynamic simulations using the PLUTO code for computational astrophysics.

Jet deceleration can be obtained by redistributing the bulk momentum through some form of mass entrainment (Bicknell 1994, 1995). Velocity shear instabilities are the most likely triggering mechanisms of entrainment (De Young 1996, 2005). The nonlinear development of velocity shear or Kelvin-Helmholtz instabilities leads to an exchange of mass, momentum and energy at contact discontinuities between fluids in relative motion (Bodo et al. 1994, 1995, 1998). Understanding the details of this process is essential for modeling the jet dynamics and for giving clues on the determination of the jet physical parameters. Perturbations grow as a consequence of the velocity shear instabilities and lead to entrainment of the external medium and to jet deceleration. Rossi et al. 2008 in their model assume that the jet is in pressure equilibrium with the outside medium, although this choice is not critical for the final results.

In non-relativistic regime, they found that: (i) lighter jets exhibit fatter, nearly spherical cocoons (see also Krause & Camenzind 2003) as a consequence of the reduced head propagation velocity and bulk momentum of the beam; (ii) heavier jets advance at higher velocities generating cylindrical, thinner cocoons; (iii) high Mach numbers have the same effect as low density contrasts in producing elongated (spearhead) cocoons, while low Mach numbers jets form fatter cocoons (see also Massaglia et al. (1996)). A similar behavior is found for relativistic jets, the main difference being that, increasing the Lorentz factor, jets, even at low density, tend to form cocoons that resemble those of the heavy non-relativistic case due to their increased inertia. In addition, in relativistic fluid dynamics, different Mach

numbers correspond to different jet internal energies rather than beam velocities, this leaves the density contrast η (ratio between ambient to beam density) as the main parameter defining the shape of the cocoon.

Rossi et al. 2008 focus their attention on the entrainment properties as a possible source of the jet deceleration. The entrainment process takes place from the interaction between the jet beam and the cocoon, promoted by the development of Kelvin-Helmholtz instabilities (KHI) at the beam interface. The entrained material is composed of jet backflowing material mixed with the shocked ambient medium through the contact discontinuity. The process is therefore quite complex and is determined by many different factors, the behavior of KHI of course being one of the most relevant. The linear analysis of the KHI for relativistic flows (Hardee et al. 1998; Hardee 1987, 2000) shows that the growth rate of unstable modes depends on the Mach number, density ratio η between jet and external medium and Lorentz factor.

Rossi et al. 2008 conclude that the main parameter governing the jet behavior and the entrainment properties turns out to be the density ratio η, while the Mach number plays a minor role even though it contributes to the determination of the KHI modes linear growth rates

Recently several authors, e.g. (Piner & Edwards 2004; Chiaberge et al. 2000; Giroletti et al. 2004), have proposed that observational properties of FR-I radio sources and their beamed counterparts (BL Lac objects) are produced by jets characterized by a velocity structure in which an inner core maintains a highly relativistic velocity and is surrounded by material that has been slowed down by the interaction with the ambient medium. A structure of this type is called the "spine-layer". The appearance of a jet with a spine-layer configuration is different when viewed at different angles. In fact, the two velocity components have different Doppler factors and the spine dominates the emission when the jet is observed at small angles with respect to the line of sight (BL Lac objects with strong Doppler boosting), while the prevailing contribution at larger angles is due to the entrained layer at low Lorentz factors (FR-I radio sources)

In Rossi et al. 2008 calculations, a "spine-layer" velocity structure has been obtained self-consistently as the result of a well defined physical process, i.e. the interaction of the outer jet layers with the ambient material, driven by jet

instabilities. In particular they have found that, in the strongly underdense case $\eta = 10^4$, the jet acquires a velocity structure in which the inner core maintains a highly relativistic velocity and is surrounded by material that has been slowed down by the interaction with the ambient medium.

In their study, assuming Lorentz factor equal to 10, they explore the parameter plane (M, η), finding that the deceleration becomes more efficient with increasing η. A preliminary analysis of the parameter space suggests that only jets with a high density ratio ($\eta > 10^2$) can undergo appreciable deceleration, while the Mach number does not seem to play a fundamental role in this respect.

With their model, they can simulate and reproduce for example the radio emission of M 87. Fig. 5.2 is the synthetic maps with the jet in case of η= 10 ^{4}, Mach number M=3 with an inclination of 20° with respect to the line of sight. Fig. 5.3 is the VLBI radio image at 2 cm of M87 (Kovalev et al. 2007). They concluded that the VLBA map of M87 can be compared with the synthetic map at low inclination angle, which agrees with observational estimates.

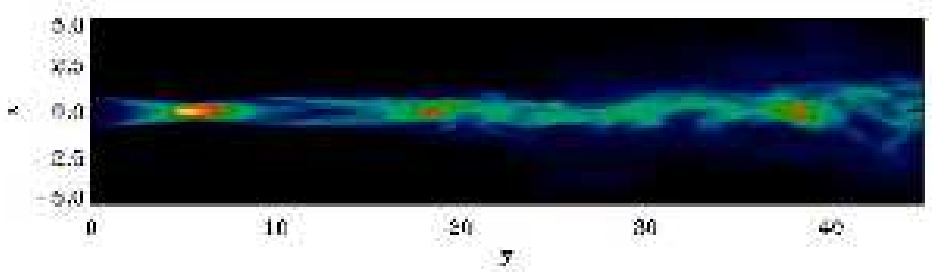

Figure 5.2: Synthetic map for the jet in case of η= 10 ^{4}, Mach number M=3 and with an inclination of 20° with respect to the line of sight (γ is the direction of the jet propagation).

In conclusion, Rossi et al. (2008) discussed the interaction between relativistic jets and the surrounding ISM. The deceleration becomes more efficient as the density ratio between the ambient medium and the jet increases. Light, relativistic jets are expected in FR I sources, so the above effect can slow them down from the parsec to the sub-kiloparsec-scale as found in many sources (Taylor 1996; Rossi et al. 2008). Since light jet beams imply reduced jet kinetic powers, the model of Rossi et al. (2008) leaves the density contrast as the most likely candidate to account for the discrepancies in the efficiency of the deceleration process.

In this scenario, we suggest that the jet begin relativistic as for sources in non

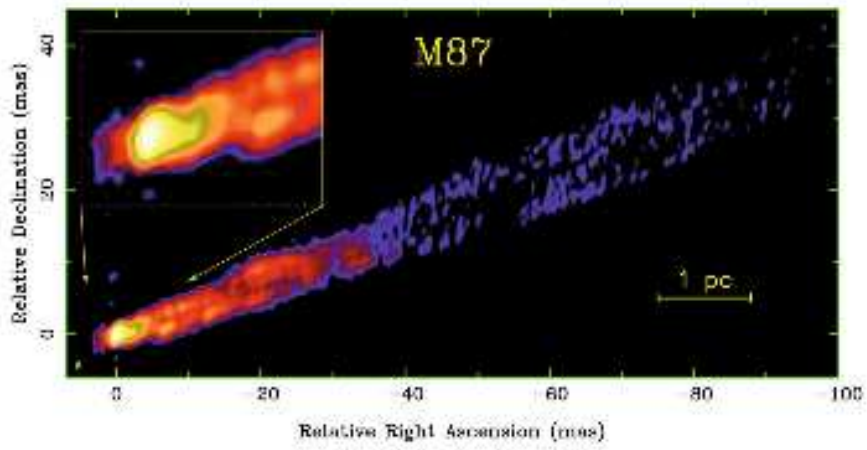

Figure 5.3: VLBA radio image at 2 cm of M87 (Kovalev et al. 2007).

cool core clusters,(and thus appears one-sided at the base) but a large value of the density ratio can produce a sub-relativistic (and therefore two-sided) heavy jet at a much shorter distance from the central engine as compared to "normal" FR I radio galaxies.

5.4.2 Dense surrounding medium in cool core clusters.

In the following, we report some evidences that high density surrounding medium is present in the center of cool core clusters.

Over the past few years, observations of hot gas in galaxy clusters with the XMM-Newton and Chandra X-ray observatories have radically altered the concept of X-ray cooling flows. Spectra taken with XMM-Newton at high energy resolution and sensitivity indeed show a decrease in gas temperature toward the cluster center, but fail to reveal any detectable gas at temperatures below about one-third of the bulk ambient temperature (Peterson et al. 2003; Peterson & Fabian 2006). These results provide no evidence for a cooling flow, and imply that any gas cooling to temperatures $\sim$1 $3\times$ 10^7 K has a mass deposition rate at least 10 times lower than that previously inferred. Furthermore, images taken with Chandra at high angular resolutions reveal that the X-ray gas at the centers of putative cooling-flow clusters is usually disturbed (e.g., Fabian et al. 2000; McNamara et al. 2000, 2001; Blanton et al. 2001; Mazzotta et al. 2002). X-ray cavities are commonly seen, and spatially coincident with radio jets from the central galaxy where detectable (Dunn et al. 2005 and references therein), indicating that energetic particles injected from an

active galactic nucleus (AGN) are responsible for the observed disturbances. The work needed to inflate these X-ray cavities implies that the energy output of AGNs is more than sufficient to balance radiative losses from the X-ray gas, and can therefore greatly diminish if not quench the cooling flow (Churazov et al. 2002; Bîrzan et al. 2004).

Among the results of several studies, the ICM appears to be probably multi-phase (e.g. Ferland et al. 1994). Numerous searches have been made for the predicted mass sink from X-ray cooling flows. These searches cover a broad range of temperatures, from ionized gas at temperatures of $\sim 10^{5.5}$ K (e.g., through the O[VI] line in the ultraviolet; Bregman et al. 2006 and references therein) down to $\sim 10^4$ K (e.g., H_α, [N II], and [S II] lines in the optical; Crawford & Fabian 1992 and references therein), to neutral gas at temperatures $\sim 10^3$ K in atomic hydrogen (21 cm line; O'Dea et al. 1998 and references therein), hot molecular hydrogen (near-IR vibrational lines; Edge et al. 2002 and references therein). None of these searches have found gas at quantities anywhere near the above-mentioned predicted levels (prior to the era of the XMM-Newton satellite as explained below) in putative cooling-flow clusters (see, e.g., reviews by Fabian 1994; Mathews & Brighenti 2003).

Searches have been made also for cool molecular hydrogen. The intracluster medium is enriched in heavy elements with a metallicity of up to 0.3 solar making possible the formation of CO molecules. The first detection of CO emission has been made in Perseus A by Lazareff et al. (1989), but the corresponding H_2 is not strongly identified as coming from the cooling flow rather than from the galaxy itself.

CO emission lines have been detected in several cooling flows at millimeter wavelengths, with the IRAM 30 m telescope, the James Clerk Maxwell Telescope (JCMT) and the Caltech Submillimeter Observatory (CSO) (Salomé & Combes 2003; Edge 2001). The presence of very cold molecular gas within these environments has been revealed. The Owens Valley Radio Observatory (OVRO) and the Plateau de Bure (PdB) interferometers have even produced the first maps of the molecular emission and confirmed the peculiar morphology and dynamics of the cold component (Salomé & Combes 2004; Edge & Frayer 2003). The gas masses derived from these CO observations are also consistent with the cold residual gas expected to cool out of the X-ray band (from Chandra and XMM-Newton mass

deposition rates), making it possible that the long searched for cool gas has indeed been detected.

High angular resolution CO observation could reveal an ordered spatial-kinematic pattern in this molecular gas.

In Chapter 3, we report in details CO observations for 4C 26.42 (Abell 1795) and 3C 84 (Perseus cluster).

A final note is important on the ISM in cool core and non cool core clusters.

In the scenario that wants to connect the parsec scale radio emission and X-ray properties of BCGs, we have to comment the connection with the X-ray cool cores. The X-ray work we used (Tab. 2.4) for cool cores defined cool cores at $>$ 10 kpc scales. We know that it appears tricky to connect with what we observe at pc scales. Although even Chandra cannot do much within 0.1 kpc scale, the better X-ray data with Chandra have shown the existence of small cool cores (coronae) in most (if not all) non cool core clusters defined at $\geq$ 10 kpc scales. Many non cool core clusters with one sided jet at pc scales have dense cool cores at $\sim$ kpc scales (so high pressure)(Sun et al. 2007, 2009). It seems that the cool core / non-cool-core defined at $\geq$ 10 kpc scales has no connection with the X-ray gas properties at $\sim$ kpc scales as most of them (if not all) have small, dense ISM cool cores remained.

However, we think that at parsec scale what it is important in BCGs in cool core cluster is not the presence of the hot coronae but the warm/cold gas. In fact, "small cool cores (coronae)" are present not only in BCG but in many (most) giant E galaxies identified as FR I radio galaxies. Most of these radio galaxies are in small groups as 3C31 , 3C 449 and more (Balmaverde et al. 2008). We suggest that giant E galaxies BCG in cool core and non cool core clusters could be similar in the inner region if we look at the hot gas. But if we take into account the warm gas we note that BCGs in large cooling cores have larger H_α and more gas at T=10^4 K (Crawford et al. 2005, Fabian et al. 2003, Salomé et al. 2003, 2006, Donoghue 2007). We propose that in the interaction of the jet with the surrounding medium, it could be that the different amount of warm gas rather than the hot gas plays in BCG in cooling clusters the main important role in the jet velocity deceleration on (sub) pc scales.

5.5 Final conclusions for BCG sample.

BCGs are a unique class of objects. To study their properties on the parsec-scale, we defined a complete sample selecting all BCGs in nearby Abell clusters (DC<3) and declination >0°. We obtained VLBA observations at 5 GHz for these objects without radio data at mas resolution available from literature. We find a different behavior between BCGs in cool core and non cool core clusters. Undetected and point like sources are found in BCGs of both types of clusters. Undetected sources are generally a consequence of low radio activity at the epoch of the observations (radio quiet core), or no radio emission whatsoever (radio quiet source). Point source morphologies may indicate insufficient sensitivity of our data and/or core dominance effects.

To better understand their properties, we added to our complete sample other BCGs with detailed information about the radio emission at parsec-scale and X-ray properties of the cluster. The extended sample is composed of 34 BCGs: 11 in cool core clusters and 23 in non cool core clusters. A dichotomy is found between the parsec-scale structures of BCGs in cool core and non cool core clusters: all the resolved objects (56%) in non cool core clusters show a one-sided jet, instead in cool core clusters, all the resolved BCGs (64%) show a two-sided morphology. Using the BCS sample as a comparison sample, we suggest that one sided structure in non cool core clusters is due to Doppler boosting effects in relativistic, intrinsically symmetric jets. Furthermore, the dominance of two-sided jet structures only in cooling clusters suggests sub-relativistic jet velocities. The different jet properties can be related to a different jet origin or to the interaction with a different ISM. In BCGs at the center of a cooling core cluster the gas density in the ISM region is expected to be higher. Therefore we can assume a strong interaction of the jet at parsec resolution with the environment. However, a large value of the density ratio (par. 5.4.1) of the medium to the jet, can produce entrainment leading to a sub-relativistic and heavy jet at a much shorter distance (pc scale). This suggestion is supported by data from the literature on Hydra A and 3C 84 (see Chapter 3), BCGs of two cool core clusters (A780 and A426 respectively). We also found episodic jet activity from the central engine of AGN in a few objects (Chapter 2). The recurrent activity of the radio source in cool core clusters is of great interest to the study of AGN feedback in clusters (Chapter 1).

Appendix

A.1: The VLBA instrument.

The Very Long Baseline Array (VLBA) is a system of ten radio telescopes controlled remotely from the Array Operations Center in Socorro, New Mexico (USA) by the National Radio Astronomy Observatory. The array works together as the world's largest dedicated, full-time astronomical instrument using the technique of very long baseline interferometry. Its construction began in February 1986, and was completed in May 1993. The first observation using all ten sites occurred in May 29, 1993.

Each VLBA station consists of an 25 m diameter dish antenna and an adjacent control building which houses the station computer, tape recorders and other equipment associated with collecting the radio signals gathered by the antenna. Each antenna weighs 218 t and is nearly as tall as a ten story building when pointed straight up. The longest baseline in the array is 8,611 kilometres.

The VLBA radio telescopes are located at (Fig. A.1): Mauna Kea (Hawaii), Brewster(Washington),Owens Valley (California)), Kitt Peak (Arizona), Pie Town (New Mexico), Los Alamos(New Mexico), Fort Davis (Texas), North Liberty (Iowa), Hancock (New Hampshire), St. Croix (United States Virgin Islands).

Four other sites are brought online for as much as 100 hours per four-month trimester. In this configuration, the entire array is known as the High-Sensitivity Array. These sites are as follows: Arecibo (Puerto Rico), Green Bank (West Virginia), Very Large Array(New Mexico), Effelsberg (Germany).

The VLBA working is based on the VLBI (Very Long Baseline Interferometry) technique.

Data received at each antenna in the array is paired with timing information, usually from a local atomic clock, and then stored for later analysis on magnetic tape or hard disk. At that later time, the data are correlated with data from other antennas similarly recorded, to produce the resulting image The angular resolution

Fig. A.1: The ten radio-telescope antennas of the Very Long Baseline Array (VLBA)

for VLBA is given by:

$$\theta_{\rm HPBW} \sim 2063 \times \frac{\lambda^{\rm cm}}{B^{\rm km}_{\rm max}} \ \ {\rm mas},$$

where B^{km}_{max} is the maximun baseline between the VLBA antennas and $\lambda^{\rm cm}$ is the receiver wavelength in cm (Wrobel 1995). In Tab. A.1, it is reported the angular resolution θ_{HPBW} of VLBA at different wavelength. For example, at 6 cm, at the longest VLBA baseline, θ_{HPBW}∼1.4 mas.

The VLBI technique enables this distance to be much greater than that possible with conventional interferometry, which requires antennas to be physically connected by coaxial cable, waveguide, optical fiber, or other type of transmission line. The greater telescope separations are possible in VLBI due to the development of the closure phase imaging technique by Roger Jennison in the 1950s, allowing VLBI to produce images with superior resolution.

In VLBI interferometry, the digitized antenna data are usually recorded at each of the telescopes (in the past this was done on large magnetic tapes, but nowadays it is usually done on large RAID arrays of computer disk drives). The antenna signal is sampled with an extremely precise and stable atomic clock (usually a hydrogen maser) that is additionally locked onto a GPS time standard. Alongside the astronomical data samples, the output of this clock is recorded on the tape/disk media. The recorded media are then transported to a central location. More recently experiments have been conducted with "electronic" VLBI (e-VLBI) where

Tabl. A.1: Angular resolution of VLBA at different wavelengths.

Wavelength (cm)	90	50	21	18	13	6	4	2	1	0.7
θ_{HPBW} (mas)	22	12	5.0	4.3	3.2	1.4	0.85	0.47	0.32	0.17

the data are sent by fibre-optics and not recorded at the telescopes, speeding up and simplifying the observing process significantly. Even though the data rates are very high, the data can be sent over normal Internet connections taking advantage of the fact that many of the international high speed networks have significant spare capacity at present.

At the location of the correlator the data are played back. The timing of the playback is adjusted according to the atomic clock signals on the (tapes/disk drives/fibre optic signal), and the estimated times of arrival of the radio signal at each of the telescopes. A range of playback timings over a range of nanoseconds are usually tested until the correct timing is found. Playing back the data from each of the telescopes in a VLBI array. Great care must be taken to synchronize the play back of the data from different telescopes. Atomic clock signals recorded with the data help in getting the timing correct.

Each antenna will be a different distance from the radio source, and as with the short baseline radio interferometer the delays incurred by the extra distance to one antenna must be added artificially to the signals received at each of the other antennas. The approximate delay required can be calculated from the geometry of the problem. The tape playback is synchronized using the recorded signals from the atomic clocks as time references, as shown in Fig. A.2.

If the signal from antenna A is taken as the reference, inaccuracies in the delay will lead to errors ε_B and ε_C in the phases of the signals from tapes B and C respectively (see Fig. A.3.).

If the position of the antennas is not known to sufficient accuracy or atmospheric effects are significant, fine adjustments to the delays must be made until interference fringes are detected. This is the aim of the data reduction process to produce images that in our thesis were made with (AIPS Astronomical Image Processing System) and Difmap. For more details see AIPS Cookbook and Difmap manual.

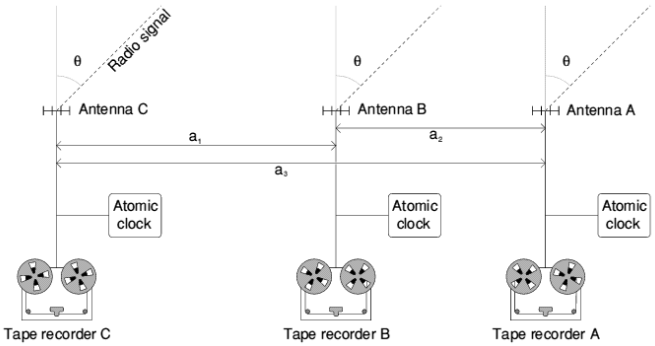

Fig. A.2: Recording data at each of the telescopes in a VLBI array. Extremely accurate high-frequency clocks are recorded alongside the astronomical data in order to help get the synchronization correct.

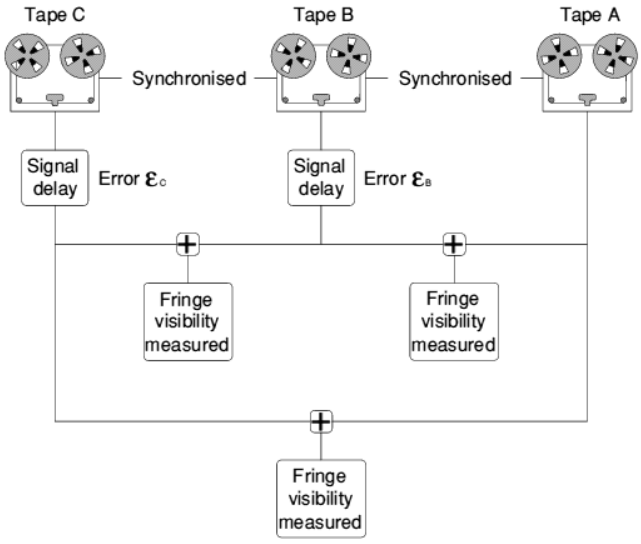

Fig. A.3: Playing back the data from each of the telescopes in a VLBI array. Great care must be taken to synchronize the play back of the data from different telescopes. Atomic clock s signals recorded with the data help in getting the timing correct

A.2: Jet Sidedness.

Assuming that the jets are intrinsically symmetric and relativistic, the jet velocity (βc) and orientation (θ) can be constrained from the jet to counterjet brightness ratio R, according to the formula

$$R = (1 + \beta\cos\theta)^{2+\alpha} \ (1 - \beta\cos\theta)^{-(2+\alpha)}$$

as the observed surface brightness is $S_{obs} = S_{em}\ D^{2+\alpha}$ where S_{em} is the emitted (intrinsic) surface brightness and $D = 1/(\gamma\ (1\pm\ \beta\cos\theta))$ with γ the Lorentz factor,(+) for the jet and (-) for the receding counterjet.

We assume a jet spectral index $\alpha = 0.5$ with $S \propto \nu^{-\alpha}$. The validity of this formula depends on the degree of isotropy of the intrinsic synchrotron emissivity in the jets. Here we assume that the parsec-scale jet emissivity is isotropic (see also Giovannini et al. 1994 for a more detailed discussion).

A.3: Core Dominance.

Giovannini et al. (1988) found a general correlation between the core and total radio power in radio galaxies. Since the total radio power was measured at low frequency and is therefore not affected by Doppler boosting, the core emission derived by the total radio power is not boosted. Assuming that sources are oriented at random angles, the best-fit value corresponds to the average orientation angle (60°), and the observed dispersion of the core radio power around the best-fit line reflects the different orientation angles (see Giovannini et al. 1994 for a more detailed discussion). We can use this correlation to derive the expected intrinsic core radio power from the total galaxy radio power and, comparing it with the observed core radio power, estimate $\beta\cos\theta$ of the source.

In Giovannini et al. (2005) the correlation given in Giovannini et al. (1988) is reanalyzed to take into account new better quality data of the core flux density at 5 GHz. Moreover, radio quasars are added with the same selection criteria used for radio galaxies, since all sources with θ in the range 0°-90° should be included, to derive the correct correlation. The new correlation is

$$\log P_c = (0.62 \pm 0.04)\ \log P_t + (\ 7.6 \pm 1.1).$$

where P_c is the arcsecond core radio power at 5 GHz, and P_t is the total radio power at 408 MHz. To take into account the core variability, the have allowed the core flux density to vary within a factor of 2 from the measured one.

Bibliography

Agudo, I., et al. 2005, arXiv:astro-ph/0510850

Allen, S. W. 1998, MNRAS, 296, 392

Allen, S. W., Ettori, S., & Fabian, A. C. 2001, MNRAS, 324, 877

Allen, S. W., Dunn, R. J. H., Fabian, A. C., Taylor, G. B., & Reynolds, C. S. 2006, MNRAS, 372, 21

Anton, K. 1993, A&A, 270, 60

Aragon-Salamanca, A., Baugh, C. M., & Kauffmann, G. 1998, MNRAS, 297, 427

Asada, K., Nagai, H., Kameno, S., Shen, Z.Q., Shinji, H., Gabuzda D. c., & Inoue, M. 2009, contribution in a conference Approaching Micro-arcsecond resolution with VSOP-2: Astrophysics and Technology.

Ashman, K. M., & Carr, B. J. 1988, MNRASs, 234, 219

Ashman, K. M., & Carr, B. J. 1991, MNRAS, 249, 13

Athanassoula, E., Makino, J., & Bosma, A. 1997, MNRAS, 286, 825

Augusto, P., Edge, A. C., & Chandler, C. J. 2006, MNRASS, 367, 366

Baldwin, J. A., Phillips, M. M., & Terlevich, R. 1981, PASP, 93, 5

Balmaverde, B., Baldi, R. D., & Capetti, A. 2008, A&A, 486, 119

Barnes, J. E., & Hernquist, L. 1992, ARA&A, 30, 705

Barnes, J. E., & Hernquist, L. 1996, ApJ, 471, 115

Baum, S. A., Heckman, T. M., Bridle, A., van Breugel, W. J. M., & Miley, G. K. 1988, ApJS, 68, 643

Baum, S. A., Heckman, T., & van Breugel, W. 1990, ApJS, 74, 389

Baum, S. A., & O'Dea, C. P. 1991, MNRAS, 250, 737

Baum, S. A., Heckman, T. M., & van Breugel, W. 1992, ApJ, 389, 208

Baum, S. A., et al. 1997, ApJ, 483, 178

Bell, E. F., et al. 2004, ApJL, 600, L11

Bell, E. F., et al. 2004, ApJj, 608, 752

Becker, R. H., White, R. L., & Helfand, D. J. 1995, ApJ , 450, 559

Beers, T. C., & Geller, M. J. 1983, ApJ, 274, 491

Benson, A. J., Bower, R. G., Frenk, C. S., Lacey, C. G., Baugh, C. M., & Cole, S. 2003, ApJ, 599, 38

Bernardi, M., et al. 2003, AJ, 125, 1817

Bernardi, M., et al. 2003, AJ, 125, 1849

Bernardi, M., et al. 2003, AJ, 125, 1866

Bernardi, M., et al. 2003, AJ, 125, 1882

Bernardi, M., Nichol, R. C., Sheth, R. K., Miller, C. J., & Brinkmann, J. 2006, AJ, 131, 1288

Bernardi, M., Hyde, J. B., Sheth, R. K., Miller, C. J., & Nichol, R. C. 2007, AJ, 133, 1741

Best, P. N., Kauffmann, G., Heckman, T. M., & Ivezić, Ž. 2005, MNRAS, 362, 9

Best, P. N., Kaiser, C. R., Heckman, T. M., & Kauffmann, G. 2006, MNRAS, 368, L67

Best, P. N., von der Linden, A., Kauffmann, G., Heckman, T. M., & Kaiser, C. R. 2007, MNRAS, 379, 894

Beswick, R. J., Peck, A. B., Taylor, G. B., & Giovannini, G. 2004, MNRAS, 352, 49

Bicknell, G. V. 1994, The Physics of Active Galaxies, 54, 231

Bicknell, G. V. 1995, ApJS, 101, 29

Binggeli, B., Sandage, A., & Tarenghi, M. 1984, AJ, 89, 64

Bird, C. M., Davis, D. S., & Beers, T. C. 1995, AJ, 109, 920

Biretta, J. A., Zhou, F., & Owen, F. N. 1995, ApJ, 447, 582

Birzan, L., Rafferty,D. A., McNamara, B. R., Carilli, C. L., Wise, M. W., & Nulsen, P. E. J. 2004, Bulletin of the American Astronomical Society, 36, 905

Bîrzan, L., McNamara, B. R., Nulsen, P. E. J., Carilli, C. L., & Wise, M. W. 2008, ApJ, 686, 859

Blandford R. D., Icke V., 1978, MNRAS 185 527

Blanton, E. L., Sarazin, C. L., McNamara, B. R., & Wise, M. W. 2001, ApJ, 558, L15

Blanton, E. L., Sarazin, C. L., McNamara, B. R., & Clarke, T. E. 2004, ApJ, 612, 817

Bliton, M., Rizza, E., Burns, J. O., Owen, F. N., & Ledlow, M. J. 1998, MNRAS, 301, 609

Bode, P. W., Berrington, R. C., Cohn, H. N., & Lugger, P. M. 1994, ApJ, 433, 479

Bodo, G., Massaglia, S., Ferrari, A., & Trussoni, E. 1994, A&A, 283, 655

Bodo, G., Massaglia, S., Rossi, P., Rosner, R., Malagoli, A., & Ferrari, A. 1995, A&A, 303, 281

Bodo, G., Rossi, P., Massaglia, S., Ferrari, A., Malagoli, A., & Rosner, R. 1998, A&A, 333, 1117

Boehringer, H., Voges, W., Fabian, A. C., Edge, A. C., & Neumann, D. M. 1993, MNRAS, 264, L25

Böhringer, H., et al. 2001, A&A, 365, L181

Boylan-Kolchin, M., Ma, C.-P., & Quataert, E. 2006, MNRAS, 369, 1081

Bower, R. G., Benson, A. J., Malbon, R., Helly, J. C., Frenk, C. S., Baugh, C. M., Cole, S., & Lacey, C. G. 2006, MNRAS, 370, 645

Bonamente, M., Lieu, R., Joy, M. K., & Nevalainen, J. H. 2002, ApJ, 576, 688

Bondi, M., Gregorini, L., Padrielli, L., & Parma, P. 1993, A&AS, 101, 431

Braine, J., & Dupraz, C. 1994, A&A, 283, 407

Braine, J., Wyrowski, F., Radford, S. J. E., Henkel, C., & Lesch, H. 1995, A&A, 293, 315

Bregman, J. N., Otte, B., Miller, E. D., & Irwin, J. A. 2006, ApJ, 642, 759

Bridges, T. J., & Irwin, J. A. 1998, MNRAS, 300, 967

Brighenti, F., & Mathews, W. G. 2006, ApJ, 643, 120

Brüggen, M., Kaiser, C. R., Churazov, E., & Enßlin, T. A. 2002, MNRAS, 331, 545

Brüggen, M. 2003, ApJ, 593, 700

Brüggen, M., Ruszkowski, M., & Hallman, E. 2005, ApJ, 630, 740

Burns, J. O., White, R. A., & Hough, D. H. 1981, AJ, 86, 1

Burns, J. O., & Balonek, T. J. 1982, ApJ, 263, 546

Burns, J. O. 1990, AJ, 99, 14

Burns, J. O., Rhee, G., Owen, F. N., & Pinkney, J. 1994, ApJ, 423, 94

Capelato, H. V., de Carvalho, R. R., & Carlberg, R. G. 1995, ApJ, 451, 525

Capetti, A., Morganti, R., Parma, P., & Fanti, R. 1993, A&*A*PS, 99, 407

Capetti, A., de Ruiter, H. R., Fanti, R., Morganti, R., Parma, P., & Ulrich, M.-H. 2000, AAP, 362, 871

Canvin, J. R., Laing, R. A., Bridle, A. H., & Cotton, W. D. 2005, MNRAS, 363, 1223

Carilli, C. L., Perley, R. A., & Harris, D. E. 1994, MNRAS, 270, 173

Cattaneo, A., Dekel, A., Devriendt, J., Guiderdoni, B., & Blaizot, J. 2006, MNRAS, 370, 1651

Celotti, A., & Fabian, A. C. 1993, MNRAS, 264, 228

Clarke, T. E., Blanton, E. L., Sarazin, C. L., Anderson, L. D., Gopal-Krishna, Douglass, E. M., & Kassim, N. E. 2009, ApJ, 697, 1481

Chandrasekhar, S. 1943, ApJ, 98, 54

Chen, Y., Reiprich, T. H., Böhringer, H., Ikebe, Y., & Zhang, Y.-Y. 2007, A&A, 466, 805

Chiaberge, M., Celotti, A., Capetti, A., & Ghisellini, G. 2000, A&A, 358, 104

Churazov, E., Brüggen, M., Kaiser, C. R., Böhringer, H., & Forman, W. 2001, ApJ, 554, 261

Churazov, E., Sunyaev, R., Forman, W., Böhringer, H. 2002, MNRAS, 332, 729

Collins, C. A., & Mann, R. G. 1998, MNRAS, 297, 128

Condon, J. J., Cotton, W. D., Greisen, E. W., Yin, Q. F., Perley, R. A., Taylor, G. B., & Broderick, J. J. 1998, AJ, 115, 1693

Conselice, C. J., Gallagher, J. S., III, & Wyse, R. F. G. 2001, AJ, 122, 2281

Conselice, C. J., Bundy, K., Ellis, R. S., Brichmann, J., Vogt, N. P., & Phillips, A. C. 2005, ApJ, 628, 160

Cotton, W. D. 1993, AJ, 106, 1241

Cowie, L. L., Hu, E. M., Jenkins, E. B., & York, D. G. 1983, ApJ, 272, 29

Crawford, C. S., & Fabian, A. C. 1992, MNRAS, 259, 265

Crawford, C. S., Allen, S. W., Ebeling, H., Edge, A. C., & Fabian, A. C. 1999, MNRAS, 306, 857

Crawford, C. S., Hatch, N. A., Fabian, A. C., & Sanders, J. S. 2005, MNRAS, 363, 216

Cross, N. J. G., et al. 2004, AJ, 128, 1990

Croton, D. J., et al. 2006, MNRAS, 365, 11

Dalla Vecchia, C., Bower, R. G., Theuns, T., Balogh, M. L., Mazzotta, P., & Frenk, C. S. 2004, MNRAS, 355, 995

David, L. P., Arnaud, K. A., Forman, W., & Jones, C. 1990, ApJ, 356, 32

David, L. P., Nulsen, P. E. J., McNamara, B. R., Forman, W., Jones, C., Ponman, T., Robertson, B., & Wise, M. 2001, ApJ, 557, 546

De Lucia, G., Springel, V., White, S. D. M., Croton, D., & Kauffmann, G. 2006, MNRAS, 366, 499

Dekel, A., & Cox, T. J. 2006, MNRAS, 370, 1445

Desroches, L.-B., Quataert, E., Ma, C.-P., & West, A. A. 2007, MNRAS, 377, 402

de Ruiter, H. R., Parma, P., Fanti, C., & Fanti, R. 1986, A&AS, 65, 111

De Young, D. S. 1996, Energy Transport in Radio Galaxies and Quasars, 100, 261

De Young, D. S. 2005, X-Ray and Radio Connections (eds. L.O. Sjouwerman and K.K Dyer) Published electronically by NRAO, http://www.aoc.nrao.edu/events/xraydio Held 3-6 February 2004 in Santa Fe, New Mexico, USA, (E7.01) 7 pages,

de Vaucouleurs, G. 1948, Annales d'Astrophysique, 11, 247

Dickey, J. M. 1997, AJ, 113, 1939

Di Matteo, T., Johnstone, R. M., Allen, S. W., & Fabian, A. C. 2001, ApJ, 550, L19

Djorgovski, S., & Davis, M. 1987, ApJ, 313, 59

Dhawan, V., Kellerman, K. I., & Romney, J. D. 1998, ApJ, 498, L111

Donnelly, R. H., Markevitch, M., Forman, W., Jones, C., David, L. P., Churazov, E., & Gilfanov, M. 1998, ApJ, 500, 138

Dressler, A. 1979, BAAS, 11, 633

Dubinski, J. 1998, ApJ, 502, 141

Dunn, R. J. H., Fabian, A. C., & Taylor, G. B. 2005, MNRAS, 364, 1343

Dunn, R. J. H., Fabian, A. C., & Celotti, A. 2006, MNRAS, 372, 1741

Dunn, R. J. H., Allen, S.W., Taylor, G.B., Shurkin, K.F., Gentile, G., Fabian, A. C., & Reynolds, C.S. 2009, MNRAS, submitted

Ebneter, K., & Balick, B. 1985, AJj, 90, 183

Edge, A. C. 2001, MNRAS, 328, 762

Edge, A. C., Wilman, R. J., Johnstone, R. M., Crawford, C. S., Fabian, A. C., & Allen, S. W. 2002, MNRAS, 337, 49

Edge, A. C., & Frayer, D. T. 2003, ApJL, 594, L13

Edwards, L. O. V., Hudson, M. J., Balogh, M. L., & Smith, R. J. 2007, MNRAS, 379, 100

Eilek, J. A., Burns, J. O., O'Dea, C. P., & Owen, F. N. 1984, ApJ, 278, 37

Eilek, J. A., & Owen, F. N. 2002, ApJ, 567, 202

Ekers, R. D., & Simkin, S. M. 1983, ApJ, 265, 85

Ensslin, T. A., & Biermann, P. L. 1998, A&A, 330, 90

Ettori, S., Fabian, A. C., Allen, S. W., & Johnstone, R. M. 2002, MNRASs, 331, 635

Faber, T., & Visser, M. 2006, MNRAS, 372, 136

Fabian, A. C. 1994, ARA&A, 32, 277

Fabian, A. C., Canizares, C. R., & Boehringer, H. 1994, ApJ, 425, 40

Fabian, A. C., et al. 2000, MNRAS, 318, L65

Fabian, A. C., Sanders, J.-S., Ettori, S., Taylor, G.B., Allen, S.W., Crawford, C.S., Iwasawa, K., Johnstone, R.M. 2001, MNRAS, 321, L33

Fabian, A. C., Celotti, A., Blundell, K. M., Kassim, N. E., & Perley, R. A. 2002, MNRAS, 331, 369

Fabian, A. C., Sanders, J. S., Crawford, C. S., Conselice, C. J., Gallagher, J. S., & Wyse, R. F. G. 2003, MNRAS, 344, L48

Fabian, A. C., Sanders, J. S., Taylor, G. B., & Allen, S. W. 2005, MNRAS, 360, L20

Fabian, A. C., Sanders, J. S., Taylor, G. B., Allen, S. W., Crawford, C. S., Johnstone, R. M., & Iwasawa, K. 2006, MNRAS, 366, 417

Falcke, H., Rieke, M. J., Rieke, G. H., Simpson, C., & Wilson, A. S. 1998, ApJl, 494, L155

Fanaroff, B. L., & Riley, J. M. 1974, MNRAS, 167, 31P

Fanti, C., Fanti, R., de Ruiter, H. R.,

Fanti, C., Fanti, R., de Ruiter, H. R., & Parma, P. 1987, A&AS, 69, 57

Feldmeier, J. J., Mihos, J. C., Morrison, H. L., Rodney, S. A., & Harding, P. 2002, ApJ, 575, 779

Feretti L., Giovannini G., Gregorini L., Parma P., Zamorani G., 1984, A&A 139, 55

Feretti, L., & Giovannini, G. 1985, A&A, 147, L13

Feretti, L., & Giovannini, G. 1987, A&A, 182, 15

Feretti, L., & Giovannini, G. 1988, A&A, 191, 21

Feretti, L., Comoretto, G., Giovannini, G., Venturi, T., & Wehrle, A. E. 1993, ApJ, 408, 446

Feretti, L., & Giovannini, G. 1994, A&A, 281, 375

Ferrarese, L., & Merritt, D. 2000, ApJL, 539, L9

Flin, P., Trevese, D., Cirimele, G., & Hickson, P. 1995, A&AS, 110, 313

Flin, P., & Krywult, J. 2006, A&A, 450, 9

Floyd, D. J. E., Perlman, E., Leahy, J. P., Beswick, R. J., Jackson, N. J., Sparks, W. B., Axon, D. J., & O'Dea, C. P. 2006, ApJ, 639, 23

Fisher, D., Illingworth, G., & Franx, M. 1995, ApJ, 438, 539

Fomalont, E. B. 1999, Synthesis Imaging in Radio Astronomy II, 180, 301

Forman, W. R., et al. 2009, American Astronomical Society Meeting Abstracts, 213, #448.18

Fujita, Y., & Suzuki, T. K. 2005, ApJL, 630, L1

Gavazzi, G., & Jaffe, W. 1987, A&A, 186, L1

Gebhardt, K., et al. 2000, ApJL, 539, L13

Ge, J. P., & Owen, F. N. 1993, AJ, 105, 778

Ge, J., & Owen, F. N. 1994, AJ, 108, 1523

Gentile, G., Rodríguez, C., Taylor, G. B., Giovannini, G., Allen, S. W., Lane, W. M., & Kassim, N. E. 2007, ApJ, 659, 225

Giovannini, G., Feretti, L., Gregorini, L., & Parma, P. 1988, AAP, 199, 73

Giovannini G., Feretti L., Comoretto G., 1990, ApJ 358, 159

Giovannini, G., Feretti, L., Venturi, T., Cotton, W. D., Lara, L., Marcaide, J., & Wehrle, A. E. 1994, The Physics of Active Galaxies, 54, 263

Giovannini, G., Cotton, W. D., Feretti, L., Lara, L., & Venturi, T. 1998, ApJ, 493, 632

Giovannini, G., Cotton, W. D., Feretti, L., Lara, L., & Venturi, T. 2001, ApJ, 552, 508

Giovannini, G., Taylor, G. B., Feretti, L., Cotton, W. D., Lara, L., & Venturi, T. 2005, ApJ, 618, 635

Giovannini, G., Giroletti, M., & Taylor, G. B. 2007, A&A, 474, 409

Giovannini G.et al. in preparation.

Girardi, M., Escalera, E., Fadda, D., Giuricin, G., Mardirossian, F., & Mezzetti, M. 1997, ApJ, 482, 41

Giroletti M., Giovannini G., Taylor G.B., Conway J.E., Lara L., Venturi T. 2003, A&A 399, 889

Giroletti, M.,Giovannini, G., Taylor, G. B., & Conway, J. E. 2003, New Astronomy Review, 47, 613

Giroletti, M., et al. 2004, ApJ, 600, 127

Giroletti, M., Taylor, G. B., & Giovannini, G. 2005, ApJ, 622, 178

Giroletti, M., Giovannini, G., & Taylor, G. B. 2005, A&AP, 441, 89

Giroletti, M., Giovannini, G., Cotton, W. D., Taylor, G. B., Pérez-Torres, M. A., Chiaberge, M., & Edwards, P. G. 2008, A&AP, 488, 905

Giroletti, M. et al. in preparation.

Gitti, M., Ferrari, C., Domainko, W., Feretti, L., & Schindler, S. 2007, A&A, 470, L25

Gizani, N. A. B., Garrett, M. A., Morganti, R., Cohen, A., Kassim, N., Gonzalez-Serrano, J. I., & Leahy, J. P. 2002, evn..conf, 163

Gomez, P. L., Ledlow, M. J., Burns, J. O., Pinkey, J., & Hill, J. M. 1997, AJ, 114, 1711

Goncalves, A. C., Véron-Cetty, M.-P., & Véron, P. 1999, AAPS, 135, 437

Gonzalez-Serrano, J. I., Carballo, R., & Perez-Fournon, I. 1993, AJ, 105, 1710

Govoni, F., Murgia, M., Markevitch, M., Feretti, L., Giovannini G., Taylor, G.B., Carretti, E., arXiv:0901.1941v1, submitted on 2009 January 14.

Granato, G. L., De Zotti, G., Silva, L., Bressan, A., & Danese, L. 2004, ApJj, 600, 580

Gregory, S. A., & Thompson, L. A. 1984, ApJ, 286, 422

Grillmair, C. J., Faber, S. M., Lauer, T. R., Baum, W. A., Lynds, R. C., O'Neil, E. J., Jr., & Shaya, E. J. 1994, AJ, 108, 102

Hatch, N. A., Crawford, C. S., Fabian, A. C., & Johnstone, R. M. 2005, MNRAS, 358, 765

Hansen, L., Jorgensen, H. E., & Norgaard-Nielsen, H. U. 1995, A&A, 297, 13

Hardcastle, M. J., Alexander, P., Pooley, G. G., & Riley, J. M. 1998, MNRAS, 296, 445

Hardcastle, M. J., Worrall, D. M., Kraft, R. P., Forman, W. R., Jones, C., & Murray, S. S. 2003, ApJ, 593, 169

Hardcastle, M. J., Sakelliou, I., & Worrall, D. M. 2005, MNRAS, 359, 1007 bibitem[Hardee(2000)]2000ApJ...533..176H Hardee, P. E. 2000, ApJ, 533, 176

Hardee, P. E. 1987, ApJ, 313, 607

Hardee, P. E., Rosen, A., Hughes, P. A., & Duncan, G. C. 1998, ApJ, 500, 599

Hardee, P. E. 2000, ApJ, 533, 176

Hausman, M. A., & Ostriker, J. P. 1978, ApJ, 224, 320

Heckman, T. M., Illingworth, G. D., Miley, G. K., & van Breugel, W. J. M. 1985, ApJ, 299, 41

Heckman, T. M., Baum, S. A., van Breugel, W. J. M., & McCarthy, P. 1989, ApJ, 338, 48

Hernquist, L. 1990, ApJ, 356, 359

Hoessel, J. G., Borne, K. D., & Schneider, D. P. 1985, ApJ, 293, 94

Holtzman, J. A., et al. 1996, AJ, 112, 416

Hopkins, P. F., Hernquist, L., Cox, T. J., Di Matteo, T., Robertson, B., & Springel, V. 2006, ApJS, 163, 1

Hu, E. M., Cowie, L. L., & Wang, Z. 1985, ApJS, 59, 447

Hu, E. M., Cowie, L. L., & Wang, Z. 1985, ApJS, 59, 447

Huchra, J. P. 1999, The Low Surface Brightness Universe, 170, 45

Hudson, D.S., Mittal, R., Reiprich, T.H., Nulsen, P.E.J., Andrnach, H., Sarazin, C.L. 2009, A&A, in press - arXiv:0911.0409

Jamrozy, M., Konar, C., Saikia, D. J., Stawarz, Ł., Mack, K.-H., & Siemiginowska, A. 2007, MNRAS, 378, 581

Jetha, N. N., Hardcastle, M. J., Ponman, T. J., & Sakelliou, I. 2008, MNRAS in press (arXiv:0809.2534)

Johnstone, R. M., Fabian, A. C., & Nulsen, P. E. J. 1987, MNRAS, 224, 75

Johnstone, R. M., Allen, S. W., Fabian, A. C., & Sanders, J. S. 2002, MNRAS, 336, 299

Johnstone, R. M., Naylor, T., & Fabian, A. C. 1991, MNRAS, 248, 18P

Jones, C., & Forman, W. 1999, ApJ, 511, 65

Kaastra, J. S., et al. 2001, X-ray Astronomy 2000, 234, 351

Kaiser, C. R., & Binney, J. 2003, MNRAS, 338, 837

Kauffmann, G., et al. 2003, MNRAS, 341, 54

Kauffmann, G., White, S. D. M., Heckman, T. M., Ménard, B., Brinchmann, J., Charlot, S., Tremonti, C., & Brinkmann, J. 2004, MNRAS, 353, 713

Kellerman, K. I., & Pauliny-Toth, I. 1968, AJ, 73, 874

King, I. R. 1978, ApJ, 222, 1

Kormendy, J. 1977, ApJ, 217, 406

Kormendy, J. 1989, ApJL, 342, L63

Kovalev, Y. Y., Lister, M. L., Homan, D. C., & Kellermann, K. I. 2007, ApJL, 668, L27

Krause, M. G. H., & Camenzind, M. 2003, arXiv:astro-ph/0307152

Krichbaum, T. P., et al. 1992, A&A, 260, 33

Laine, S., van der Marel, R. P., Lauer, T. R., Postman, M., O'Dea, C. P., & Owen, F. N. 2003, AJ, 125, 478

Laing, R. A., Parma, P., de Ruiter, H. R., & Fanti, R. 1999, MNRAS, 306, 513

Laing, R. A., & Bridle, A. H. 2002, MNRAS, 336, 328

Lara, L., Cotton, W. D., Feretti, L., Giovannini, G., Venturi, T., & Marcaide, J. M. 1997, ApJ, 474, 179

Lara, L., Feretti, L., Giovannini, G., Baum, S., Cotton, W. D., O'Dea, C. P., & Venturi, T. 1999, ApJ, 513, 197

Lara, L., Giovannini, G., Cotton, W. D., Feretti, L., & Venturi, T. 2004, A&AP, 415, 905

Lauer, T. R. 1988, ApJ, 325, 49

Lauer, T. R., & Gunn, J. E. 1985, BAAS, 17, 516

Lauer, T. R., et al. 2007, ApJ, 662, 808

Lazareff, B., Castets, A., Kim, D.-W., & Jura, M. 1989, ApJL, 336, L13

Leahy, J. P., & Williams, A. G. 1984, MNRAS, 210, 929

Leahy, J. P., & Perley, R. A. 1991, AJ, 102, 537

Leahy, J. P., Black, A. R. S., Dennett-Thorpe, J., Hardcastle, M. J., Komissarov, S., Perley, R. A., Riley, J. M., & Scheuer, P. A. G. 1997, MNRAS, 291, 20

Ledlow, M. J., & Owen, F. N. 1995, AJ, 110, 1959

Ledlow, M. J., Voges, W., Owen, F. N., & Burns, J. O. 2003, AJj, 126, 2740

Lee, S.-S., Lobanov, A. P., Krichbaum, T. P., Witzel, A., Zensus, A., Bremer, M., Greve, A., & Grewing, M. 2008, AJ, 136, 159

Lester, D. F., Zink, E. C., Doppmann, G. W., Gaffney, N. I., Harvey, P. M., Smith, B. J., & Malkan, M. 1995, ApJ, 439, 185

Lim, J., Ao, Y., & Dinh-V-Trung 2008, ApJ, 672, 252

Lin, Y.-T., & Mohr, J. J. 2004, ApJj, 617, 879

Lister, M. L. 2001, ApJ, 562, 208

Lister, M. L., et al. 2009, arXiv:0909.5100

Liuzzo, E., Taylor, G. B., Giovannini, G., & Giroletti, M. 2009, A&A, 501, 933

Liuzzo, E., Giovannini, G., Giroletti, M., & Taylor, G. B. 2009, A&A, 505, 509

Liuzzo, E., Giovannini, G., Giroletti, M., & Taylor, G. B. 2010, arXiv:1002.1380v1

Loken, C., Roettiger, K., Burns, J. O., & Norman, M. 1995, ApJ, 445, 80

Machalski, Astronomy and Astrophysics Supplement, 1998, v.128, p.153-178.

Malumuth, E. M., & Kirshner, R. P. 1981, ApJ, 251, 508

Malumuth, E. M., & Kirshner, R. P. 1985, ApJ, 291, 8

Magorrian, J., et al. 1998, AJ, 115, 2285

Massaro, F., et al. 2009, ApJl, 692, L123

Mathews, W. G., & Brighenti, F. 2003, ApJ, 599, 992

Mathews, W. G., Faltenbacher, A., & Brighenti, F. 2006, ApJ, 638, 659

Matthews, T. A., Morgan, W. W., & Schmidt, M. 1964, ApJ, 140, 35

Mazzotta, P., Fusco-Femiano, R., & Vikhlinin, A. 2002, ApJL, 569, L31

McNamara, B. R., & O'Connell, R. W. 1989, AJ, 98, 2018

McNamara, B. R. 1992, BASS, 24, 1143

McNamara, B. R. 1995,ApJ 443, 77

McNamara, B. R., O'Connell, R. W., & Sarazin, C. L. 1996, AJ, 112, 91

McNamara, B. R., Jannuzi, B. T., Elston, R., Sarazin, C. L., & Wise, M. 1996, ApJ, 469, 66

McNamara, B. R., et al. 2000, ApJ, 534, L135

McNamara, B. R., et al. 2001, ApJ, 562, L149

McNamara, B. R. 2004, The Riddle of Cooling Flows in Galaxies and Clusters of galaxies, 177

McNamara, B. R., Nulsen, P. E. J., Wise, M. W., Rafferty, D. A., Carilli, C., Sarazin, C. L., & Blanton, E. L. 2005, 433, 45

Meier, D. L., Ulrich, M.-H., Fanti, R., Gioia, I., & Lari, C. 1979, ApJ, 229, 25

Melnick, J., Gopal-Krishna, & Terlevich, R. 1997, A&A, 318, 337

Merritt, D. 1984, ApJL, 280, L5

Merritt, D. 1985, ApJ, 289, 18

Merritt, D., & Ekers, R. D. 2002, Science, 297, 1310

Mihos, J. C., & Hernquist, L. 1996, ApJ, 464, 641

Mirabel, I. F., Sanders, D. B., & Kazes, I. 1989, ApJL, 340, L9

Morganti, R., Killeen, N. E. B., & Tadhunter, C. N. 1993, MNRAS, 263, 1023

Morris, R. G., & Fabian, A. C. 2005, MNRAS, 358, 585

Mohr, J. J., Geller, M. J., Fabricant, D. G., Wegner, G., Thorstensen, J., & Richstone, D. O. 1996, ApJ, 470, 724

Murante, G., et al. 2004, ApJL, 607, L83

Murgia, M., Parma, P., de Ruiter, H. R., Bondi, M., Ekers, R. D., Fanti, R., & Fomalont, E. B. 2001, A&AP, 380, 102

Naab, T., & Burkert, A. 2003, ApJ, 597, 893

Nagai, H., Asada, K., Doi, A., Kameno, S., & Inoue, M. 2009, Astronomische Nachrichten, 330, 161

Nesterov, N. S., Lyuty, V. M., & Valtaoja, E. 1995, A&A, 296, 628

Nipoti, C., Londrillo, P., & Ciotti, L. 2003, MNRAS, 342, 501

Nusser, A., Silk, J., & Babul, A. 2006,MNRAS, 373, 739

O'Dea, C. P., & Owen, F. N. 1987, ApJ, 316, 95

O'Dea, C. P., Payne, H. E., & Kocevski, D. 1998, AJ, 116, 623

O'Donoghue, A. A., Owen, F. N., & Eilek, J. A. 1990, ApJS, 72, 75

Oegerle, W. R., & Hoessel, J. G. 1991, ApJ, 375, 15

Oegerle, W. R., & Hill, J. M. 1994, AJ, 107, 857

Oegerle, W. R., & Hill, J. M. 2001, AJ, 122, 2858

Oemler, A., Jr. 1976,ApJ, 209, 693

Omma, H., Binney, J., Bryan, G., & Slyz, A. 2004, MNRAS, 348, 1105

Owen, F. N., Burns, J. O., & White, R. A. 1984, Clusters and Groups of Galaxies. International Meeting held in Trieste, Italy, September 13-16, 1983. Editors, F. Mardirossian, G. Giuricin, M. Mezzetti; Publisher, D. Reidel Pub. Co., Dordrecht, Holland, Boston, MA, Hingham, MA, U.S.A. Sold and distributed in the U.S.A. and Canada by Kluwer Academic Publishers, 1984. LC # QB858.7 .C58 1984. ISBN # 9027717729. P.295, 1984, 295

Owen, F. N., O'Dea, C. P., Inoue, M., & Eilek, J. A. 1985, ApJ, 294, L85

Owen, F. N., & Ledlow, M. J. 1997, ApJS, 108, 41

Pacholczyk, A. G. 1970, Series of Books in Astronomy and Astrophysics, San Francisco: Freeman, 1970,

Padmanabhan, N., et al. 2004, New Astronomy, 9, 329

Parma, P., Ekers, R. D., & Fanti, R. 1985, A&*A*PS, 59, 511

Parma, P., de Ruiter, H. R., Fanti, C., & Fanti, R. 1986, A&AS, 64, 135

Parma, P., de Ruiter, H. R., & Cameron, R. A. 1991, AJ, 102, 1960

Pearson T. J., Readhead A. C. S., 1988, ApJ 328, 114

Pearson, T. J., Shepherd, M. C., Taylor, G. B., & Myers, S. T. 1994, Bulletin of the American Astronomical Society, 26, 1318

Pedlar, A., Ghataure, H. S., Davies, R. D., Harrison, B. A., Perley, R., Crane, P. C., & Unger, S. W. 1990, MNRAS, 246, 477

Peterson, J. R., et al. 2001, A&A, 365, L104

Peterson, J. R., Ferrigno, C., Kaastra, J. S., Paerels, F. B. S., Kahn, S. M., Jernigan, J. G., Bleeker, J. A. M., & Tamura, T. 2002, arXiv:astro-ph/0202108

Peterson, J. R., Kahn, S. M., Paerels, F. B. S., Kaastra, J. S., Tamura, T., Bleeker, J. A. M., Ferrigno, C., & Jernigan, J. G. 2003, ApJ, 590, 207

Peterson, J. R., & Fabian, A. C. 2006, PhR, 427, 1

Peres, C. B., Fabian, A. C., Edge, A. C., Allen, S. W., Johnstone, R. M., & White, D. A. 1998, MNRAS, 298, 416

Piner, B. G., & Edwards, P. G. 2004,ApJ, 600, 115

Pinkney, J. 1995, Ph.D. Thesis,

Polatidis A. G., Wilkinson P.N., Xu W., Readhead A.C.S., Pearson T. J., Taylor G. B., Vermeulen R. C., 1995, ApJS, 98, 1

Porter, A. C., Schneider, D. P., & Hoessel, J. G. 1991, AJ, 101, 1561

Quilis, V., Bower, R. G., & Balogh, M. L. 2001, MNRAS, 328, 1091

Rafferty, D. A., McNamara, B. R., Nulsen, P. E. J., & Wise, M. W. 2006, ApJ, 652, 216

Rees, M. J., & Ostriker, J. P. 1977, MNRAS, 179, 541

Rhee, G. F. R. N., & Latour, H. J. 1991, A&A, 243, 38

Reuter, H. P., Pohl, M., Lesch, H., & Sievers, A. W. 1993, A&A, 277, 21

Ricker, P. M., & Sarazin, C. L. 2001, ApJ, 561, 621

Roche, N., & Eales, S. A. 2000, MNRAS, 317, 120

Roettiger, K., Burns, J. O., Clarke, D. A., & Christiansen, W. A. 1993, BAAS, 25, 1444

Rossi, P., Mignone, A., Bodo, G., Massaglia, S., & Ferrari, A. 2008, A&A, 488, 795

Ruszkowski, M., Brüggen, M., & Begelman, M. C. 2004, APJ, 611, 158

Sakelliou, I., & Merrifield, M. R. 1999, MNRAS, 305, 417

Sakelliou, I., & Merrifield, M. R. 2000, MNRAS, 311, 649

Salomé, P., & Combes, F. 2003, A&A, 412, 657

Salomé, P., & Combes, F. 2004, A&A, 415, L1

Salomé, P., et al. 2006, A&A, 454, 437

Sandage A., 1972, ApJ 178, 25

Sarazin, C. L., Burns, J. O., Roettiger, K., & McNamara, B. R. 1995, ApJj, 447, 559

Schombert, J. M. 1986, ApJS, 60, 603

Schombert, J. M. 1987, ApJS, 64, 643

Schombert, J. M. 1988, ApJ, 328, 475

Extragalactic astronomy and cosmology: an introduction Di Peter Schneider, 2006, Springer edition

Scodeggio, M., Solanes, J. M., Giovanelli, R., & Haynes, M. P. 1995, ApJ, 444, 41

Seigar, M. S., Lynam, P. D., & Chorney, N. E. 2003, MNRAS, 344, 110

Silk, J. 1977, ApJ, 211, 638

Silver, C. S., Taylor, G. B., & Vermeulen, R. C. 1998, ApJ, 502, 229

Simkin, S. M. 1979, ApJ, 234, 56

Sjibring, L. G. 1993, Groningen: Rijksuniversiteit, —c1993,

Struble, M. F., & Rood, H. J. 1984, AJj, 89, 1487

Sun, M., Jones, C., Forman, W., Vikhlinin, A., Donahue, M., & Voit, M. 2007, ApJ, 657, 197

Sun, M. 2009, ApJ, 704, 1586

Tamura, T., et al. 2001, A&A, 365, L87

Taylor, G. B., Perley, R. A., Inoue, M., Kato, T., Tabara, H., & Aizu, K. 1990, BAAS, 22, 802

Taylor, G. B., & Perley, R. A. 1993, ApJ, 416, 554

Taylor, G. B., Vermeulen, R. C., Pearson, T. J., Readhead, A. C. S., Henstock, D. R., Browne, I. W. A., & Wilkinson, P. N. 1994, ApJS, 95, 345

Taylor, G. B., Barton, E. J., & Ge, J. 1994, AJ, 107, 1942

Taylor, G. B. 1996, ApJ, 470, 394.

Taylor, G. B., & Vermeulen, R. C. 1996, ApJ, 457, L69

Taylor, G. B., & Vermeulen, R. C. 1997,ApJl, 485, L9

Taylor, G. B., O'Dea, C. P., Peck, A. B., & Koekemoer, A. M. 1999, ApJ, 512, L27

Taylor, G. B., Fabian, A. C., & Allen, S. W. 2002, MNRAS, 334, 769

Taylor, G. B., Gugliucci, N. E., Fabian, A. C., Sanders, J. S., Gentile, G., & Allen, S. W. 2006, MNRAS, 368, 1500

Taylor, G. B., Sanders, J. S., Fabian, A. C., & Allen, S. W. 2006, MNRAS, 365, 705

Taylor G.B., Charlot P., Vermeulen R.C., Pradel N., 2009, ApJ in press; arXiv:0904.1879

Thomas, P. 1988, MNRAS, 235, 315

Thomas, P. A., & Fabian, A. C. 1990, MNRAS, 246, 156

Thuan, T. X., & Romanishin, W. 1981, ApJ, 248, 439

Toomre, A., & Toomre, J. 1972, ApJ, 178, 623

Tonry, J. L. 1984, ApJ, 279, 13

Tonry, J. L. 1987, Structure and Dynamics of Elliptical Galaxies, 127, 89

Tran, K.-V. H., van Dokkum, P., Franx, M., Illingworth, G. D., Kelson, D. D., & Schreiber, N. M. F. 2005, ApJL, 627, L25

Tremaine, S. 1990, Dynamics and Interactions of Galaxies, 394

Tremaine, S., et al. 2002, ApJ, 574, 740

Trussoni, E., Massaglia, S., Ferrari, R., Feretti, L., Fanti, R., & Parma, P. 1997, Memorie della Societa Astronomica Italiana, 68, 295

Valentijn, E. A. 1979, A&AP, 78, 367

Valentijn, E. A., & Bijleveld, W. 1983,A&A, 125, 223

Vallee, J. P., Wilson, A. S., & van der Laan, H. 1979, A&A, 77, 183

Vallèe, J. P. 1982, AJ, 87, 486

Vallee, J. P., & Roger, R. S. 1987, AJ, 94, 1

van Breugel, W., & Fomalont, E. B. 1984, ApJl, 282, L55

van Breugel W., Miley G., Heckman T., Butcher H., Bridle A., 1985, ApJ 290, 496

van Breugel, W. J. M., Heckman, T. M., Miley, G. K., & Filippenko, A. V. 1986, ApJ, 311, 58

van Breugel, W., Heckman, T., & Miley, G. 1984, ApJ, 276, 79

van Dokkum, P. G., Franx, M., Fabricant, D., Kelson, D. D., & Illingworth, G. D. 1999, ApJL, 520, L95

Venturi, T., Readhead, A. C. S., Marr, J. M., & Backer, D. C. 1993, ApJ, 411, 552

Venturi, T., Castaldini, C., Cotton, W. D., Feretti, L., Giovannini, G., Lara, L., Marcaide, J. M., & Wehrle, A. E. 1995, ApJ, 454, 735

Venturi, T., Dallacasa, D., & Stefanachi, F. 2004, A&A, 422, 515

Verdoes Kleijn, G. A., Baum, S. A., de Zeeuw, P. T., & O'Dea, C. P. 1999, AJ, 118, 2592

Vermeulen, R. C., Readhead, A. C. S., & Backer, D. C. 1994, ApJ, 430, L41

Vermeulen, R. C., Readhead, A. C. S., & Backer, D. C. 1994, Compact Extragalactic Radio Sources, 115

von der Linden, A., Best, P. N., Kauffmann, G., & White, S. D. M. 2007, MNRAS, 379, 867

Walker, R. C., Romney, J. D., & Benson, J. M. 1994, ApJ, 430, L45

Walker, R. C., Kellermann, K. I., Dhawan, V., Romney, J. D., Benson, J. M., Vermeulen, R. C., & Alef, W. 1998, IAU Colloq. 164: Radio Emission from Galactic and Extragalactic Compact Sources, 144, 133

Walker, R. C., Dhawan, V., Romney, J. D., Kellermann, K. I., & Vermeulen, R. C. 2000, ApJ, 530, 233

Weil, M. L., & Hernquist, L. 1996, ApJ, 460, 101

West, M. J. 1994, MNRAS, 268, 79

White, S. D. M. 1983, Internal Kinematics and Dynamics of Galaxies, 100, 337

White, S. D. M., & Frenk, C. S. 1991, ApJ, 379, 52

White, D. A., Jones, C., & Forman, W. 1997, MNRAS, 292, 419

Willman, B., Governato, F., Wadsley, J., & Quinn, T. 2004, MNRAS, 355, 159

Wilman, R. J., Edge, A. C., Johnstone, R. M., Fabian, A. C., Allen, S. W., & Crawford, C. S. 2002, MNRAS, 337, 63

Wilson, A. S., & Ulvestad, J. S. 1982, ApJ, 263, 576

Wise, M. W., McNamara, B. R., Nulsen, P. E. J., Houck, J. C., & David, L. P. 2007, ApJ, 659, 1153

Xu, C., Baum, S. A., O'Dea, C. P., Wrobel, J. M., & Condon, J. J. 2000, AJ, 120, 2950

Acknowledgments

Just technical thanks and acknowledgments here, that I would like to address to the people who have been important during these three years of PhD.

My honor mentions goes to Gabriele Giovannini and Marcello Giroletti who have been patient, motivating and helpful advisers for this period. Thank also to Greg Taylor for the fundamental collaboration in various works and the hospitality during the period at University of New Mexico.

Thank to all persons that I have met at IRA for the many helps that I received and not only. Thanks guys, it has been an extremely enjoyable period!

Grazie.
Elisabetta.